NIGERIAN JOURNAL OF SPACE RESEARCH

(ISSN 0794-4489)
VOLUME 8
March 30, 2010

Funded by
National Space Research and Development Agency (NASRDA), Abuja, Nigeria.

(*Centre for Basic Space Science, Nsukka*)
E-Mail: cbss_unn@yahoo.com
Website: www.cbssonline.com

DEUTCHETZ Publishers

THE NIGERIAN JOURNAL OF SPACE RESEARCH

From the Editor-in-Chief

This edition of Nigerian Journal of Space Research is dedicated to the International Heliophysical Year IHY African Regional School, which was held at Enugu, Nigeria from 10th to 22th November, 2009. The School was hosted by NASRDA Centre for Basic Space Science on behalf of Nigerian government.

This volume consists of peer-reviewed lecture notes from various instructors, who participated in the school. The topics covered during the school were in areas of Space Science known as heliospace and geospace. The School also featured hands-on laboratory classes on Mathlab. AFRIS2009 was poised at setting the pace for intensive capacity building in Space Science and Technology in Africa – an aim that was greatly achieved.

The International Heliophysical Year (IHY) 2007 was a 70-country scientific programme, which involved thousands of scientists across the globe. This collaboration spanned from February 2007 to February 2009. The mission of the progamme was to enhance research, outreach, and historical preservation of the International Geophysical Year of 1957. Activities of IHY 2007 included the deployment of new instrumentation arrays especially in developing countries, and an extensive education and public outreach component.

*IHY Schools were organized at different regions of the world. The IHY African Regional School took place at the historical city of Enugu, Nigeria. The IHY School was a huge success as forty-one graduate students and postdocs from 12 African countries participated in the Regional School. Fifteen seasoned experts from United States of America, Japan, France, Norway, Cote D'Ivoire, South Africa and Nigeria taught in the School. Countries with delegates were Algeria, Cote D'ivoire, Democratic Republic of Congo, Egypt, Ethiopia, Ghana, Kenya, Mozambique, Nigeria, Republic of South Africa, Uganda and Zambia. The Conveners were Professors Pius N. Okeke (Centre for Basic Space Science, Nigeria) and Maurius Potigieter (North West University, South Africa); while Nat Gopalswamy (*National Aeronautics and Space Administration, United States*) and Babatunde Rabiu (Federal University of Technology, Akure, Nigeria) were Directors of the School.*

The organizers of the School acknowledged the travel grants received from the International Secretariat of IHY at National Aeronautics and Space Administration of the United States*; Abdus Salam International Center for Theoretical Physics, Trieste, Italy; North West University, South Africa; University of Bergen, Norway; and Space Environment Research Center, Kyushu University, Japan. The host Institution - Centre for Basic Space Science- bore the heavy costs of lodging and logistics for the meeting. The coordinating support of United Nations Office for Outer Space Affairs, Vienna, is greatly appreciated.*

The articles in this edition represent current states of developments in different areas of heliophysics and shall for long remain reference materials for research and teaching in Space Science. Nigerian Journal of Space Research is known for publication of dedicated research articles in the field of Space Science and applications.

Prof. P. N. Okeke

Editor-in-Chief & Director, CBSS

Origin:

The Nigerian Journal of Space Research (NJSR) was founded in 2005 by the Centre for Basic Space Science, National Space Research and Development Agency, Federal Ministry of Science and Technology, Abuja.

Number of publications per year

NJSR is published twice in a year, March and September.

Aims and objectives

NJSR serves as a medium or channel for the publication/dissemination of the works, findings and discoveries of researchers in Nigeria and other parts of the world in various areas of space science. Currently, NJSR is the only such important publication medium in Nigeria. Scientists/researchers themselves, during the workshop organised by CBSS in July 2004, identified the urgent need to have this journal. The journal publishes original papers, editorials, news, conference proceedings and career/professional information that are relevant to space scientists/researchers in Nigeria.

Scope and areas of coverage*:*

The Journal accepts for publication articles/papers that will serve the useful purpose of disseminating new research findings in various areas of the space science, such as:

- Environmental Science
- Satellite/Communication/Remote Sensing Physics.
- Astrophysics and Cosmology.
- Atmospheric/Ionospheric Physics.

- Meteorology.
- Geophysics and Geodesy.
- Observational Astronomy
- Instrumentation, Electronics and software development

***Instructions to authors*:**

NJSR publishes papers in all aspects of Space Science and fields closely related to them. Papers should contain the results of original works, which have neither been previously published nor are to be published elsewhere. Manuscripts must be written in English, and preferably **typeset** with **Microsoft Word**. It should be one and half-spaced.

***Format of Manuscript*:**

Manuscripts should be in the following order: (1) Title Page (2) Abstract (3) Text (4) Appendices, if any (5) References (6) Figure captions and (7) Tables. The pages should be numbered consecutively beginning with the title page.

Title page: Title of the paper should be concise and informative. This should be followed by:
The initial(s) and name(s) of the author(s): The full institutional address of all authors should be marked by superscripts and in italics.
Abstract: The paper must include a brief abstract that states clearly the principal conclusions of the article. The abstract should be complete, concise and continuous and be 3-5% of the length of the paper.

***Key words*:** A maximum of 4 key words should be provided after the abstract.

Review Article: NJSR may publish reviews from time to time, but these are by invitation only.

Research notes: Publications just referring briefly to already published papers may be submitted.

Letter to NJSR: New important results which deserve faster publication should be submitted as Letters provided they are shorter than 3 printed pages.

Length of articles: A maximum of fifteen pages including tables, graphs and illustrations will be accepted. Only summary of procedure, analysis and results are important. Manuscripts should be written in font size 12, 1.5 spacing on A4.

***Sections in the text**:* These should be numbered using Arabic numerals. Subsections should be numbered 1.1, 1.2, e.t.c. and sub-subsections 1.2.1, 1.2.2, e.t.c.

References: The references should be typed on separate page(s) of the text in alphabetical order. Citation should for example read (Okeke, *et al.*, 2004).

Tables: Each table should be typed on a separate page and numbered on top sequentially with Arabic numerals. They should be understandable without reference to the text. Units should appear at the top of the column. The tables should be compressed as much as possible, but should not be less than font size 8.

Figures: Figures and graphs should be mentioned in the text and their appropriate positions should be indicated. These should also be numbered beneath using Arabic numerals.

Equations: Equations should be numbered sequentially in bracketed Arabic numerals on the right hand side.

Submission of manuscripts: Manuscripts should be submitted to our editorial office in two possible ways: as an attachment by e-mail or by posting the diskette to the address below via courier. In addition to this, authors should send three (3) hardcopies of their manuscript by surface mail. Submitted manuscripts will not be reviewed without the hardcopies. Authors should also send us a notification through our e-mail address that they have sent us their manuscript by post. All subsequent communications between us and authors shall be by e-mail or phone.

Our address is:

Postal: The Editor-in-Chief

The Nigerian Journal of Space Research

Centre for Basic Space Science

University of Nigeria, Nsukka

E-mail: cbss_unn@yahoo.com
cc: okekepius@yahoo.com
Website: www.cbssonline.com

Telephone: 08035509530, 08069327779, 08038714158.

Funding: Publication of this journal is funded by National Space Research and Development Agency (NASRDA), Abuja, Nigeria.

Request for the Journal:

Since the Journal is produced in May and November every year, interested scientists members of the public and libraries are invited to make their request for the journal well in advance, between January and February of every year, to be sure that copies are reserved for them. The journal will be posted to them as a registered surface mail. The journal will also be available at the Centre's website.

TABLE OF CONTENT

NIGERIAN JOURNAL OF SPACE RESEARCH **8**: 1-32, 2009 September 1

Solar Eruptions

Nat Gopalswamy PhD
Solar Physics Laboratory, Heliophysics Division, NASA Goddard Space Flight Center, Greenbelt, MD 20771, USA. Email: nat.gopalswamy@nasa.gov

Table of Contents

1.0. Introduction

One of the consequences of solar activity is the sudden release of energy known as solar eruption in the form of heating and mass motion from localized magnetic regions on the Sun. The primary characteristic of a magnetic region that leads to eruption is that the region is magnetically closed – i.e., they have one or more polarity inversion lines at the photospheric level. Such magnetic regions can be tiny bright points to large active regions containing sunspots. The sudden localized release of thermal energy is recognized as a solar flare, while

the energy released in the form of mass motion is identified as coronal mass ejections (CMEs). Solar flares are classified as eruptive (associated with CMEs) and compact (no CME association). Flares are observed as enhanced thermal emission in soft X-rays, extreme ultraviolet (EUV), H-alpha, and even white light. Nonthermal emission is also observed in radio, hard X-rays, and gamma rays. Electrons and ions accelerated during the energy release process are basically responsible for both thermal and nonthermal emissions during flares. Mass ejections come in various shapes and sizes, ranging from the small-scale jets to the large-scale CMEs. CMEs are also observed at various wavelengths, but white light images provide the most complete picture over large distances from the Sun. Both flares and CMEs have important consequences in the heliosphere. X-ray and EUV radiation from flares produce extra ionization in the terrestrial ionosphere causing sudden ionospheric disturbances (SIDs) that seriously affect radio communication and navigation. Energetic CMEs drive fast mode shocks that accelerate the particles from the corona and interplanetary medium to high energies. CMEs arriving at Earth can produce intense geomagnetic storms. Several review articles exist on these topics (see the articles in the recent Geophysics Monographs by Kunow et al., 2006; Gopalswamy et al., 2006). A more detailed description of the eruption events can be found in (Gopalswamy, 2007; 2009).

2.0. Overview of Eruptions

Solar flares and CMEs occur from closed magnetic regions, where magnetic free energy is stored and released in the eruptions. In this section, examples of the closed magnetic field regions are provided. Examples of flares, CMEs and the associated phenomena are also discussed.

2. 1. Eruption Regions

The two types of solar source regions that result in eruptions are illustrated in Figure 1 using a photospheric magnetogram obtained by the Solar and Heliospheric Observatory (SOHO) mission's Michelson Doppler Imager (MDI) instrument and the corresponding H-alpha picture from the Kanzelhoehe Solar Observatory. Compact regions like A with high magnetic field

intensity (100s to 1000s of G) are active regions, which contain sunspots and thin filaments overlying the polarity inversion line. Extended regions like B have weaker magnetic field spread over a larger area with a long filament overlying the neutral line. Both types of magnetic regions are potential sources of CMEs and flares. Filaments consist of cool material (~8000 K) suspended in the hot (~2 MK) corona. The ends of filaments are rooted in opposite polarity patches seen in the magnetogram. Filaments reside in filament channels, which appear as cavities in coronal images. The filaments appear dark because they absorb H-alpha line emission from the chromosphere. When viewed above the limb, the filaments appear as bright features against the cold sky and therefore are referred to as prominences. Filaments and prominences have similar appearance in microwaves. During an eruption, the filament is ejected from the Sun (wholly or partially) including the surrounding coronal material. Thus a CME typically contains multithermal plasma.

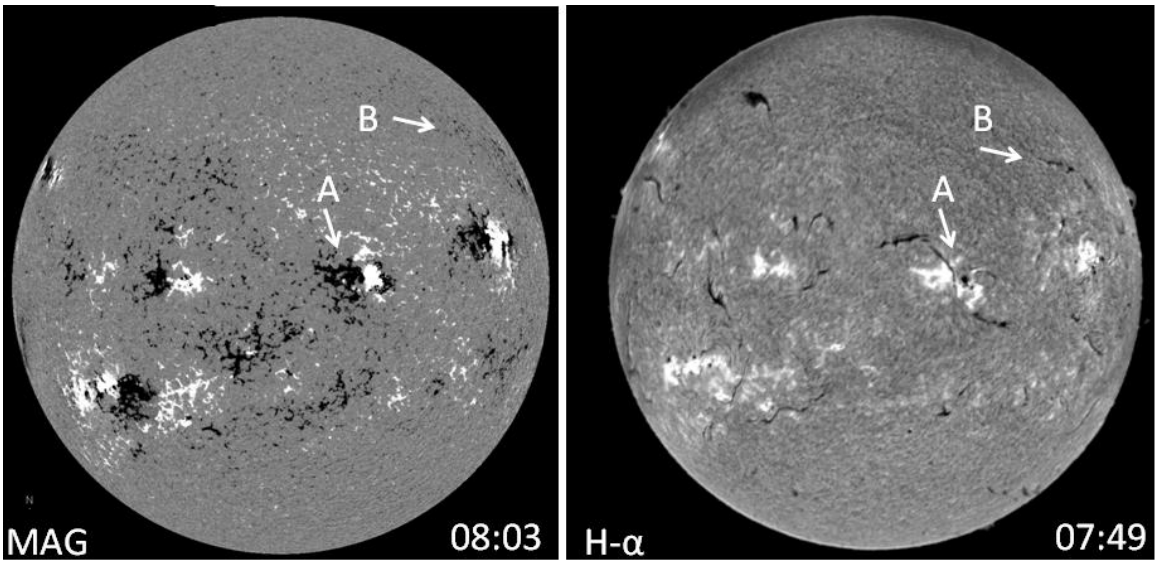

Figure 1. *A line of sight magnetogram from SOHO/MDI taken at 08:03 UT (left) and an H-alpha image from the Kanzelhoehe observatory taken at 07:49 UT (right) both on 2001 November 4. In the magnetogram, white and dark represent positive (north) and negative (south) magnetic polarities, respectively. The elongated dark features in the H-alpha image are the filaments. One of the active regions (AR 9684) is marked "A". A large-scale weak field region is marked "B". In both regions, the filaments overly the polarity inversion lines. The active region magnetic fields are intense and the filaments are generally thin. In the filament regions, the magnetic field is also enhanced compared to the quiet Sun.*

2. 2. Eruption from a Quiescent Filament Region

Figure 2 shows an eruption imaged in H-alpha wavelengths from a region similar to B in Figure 1, but from a different day (2003 February 18). In the pre-eruption image, one can see a dark filament (F) in EUV (from SOHO/EIT) overlying the photospheric polarity inversion line that divides the positive and negative polarity patches of the extended magnetic region (from SOHO/MDI obtained at 19:17 UT on 2003 February 17). The filament appears dark because it is cool and hence absorbs the 195 Å emissions from the underlying corona. In the 02:00 UT image on February 18, the filament can be seen lifted from its initial location and can be seen above the limb in projection. At this stage the filament is said to be eruptive. Directly beneath the eruptive filament, one can see two thin bright patches parallel to each other, which are referred as flare ribbons. The ribbons indicate energy input to the chromosphere, thought to be due to electrons from the energy release site just beneath the erupting filament in the corona. The ribbons expand with bright loops connecting them as the eruption progresses (Fig.1d). These "post-eruption" loops are roughly perpendicular to neutral line, while the flare ribbons are roughly parallel to the neutral line (located on either side of the neutral line). The loops are known as flare loops and the entire structure as post eruption arcade (PEA) formed due to reconnection above. PEAs can be seen in coronal images obtained in many wavelengths: EUV, X-ray, and microwave. The centroid of the PEA is usually referred to as the solar source of the eruption.

Figure 3 shows a set of coronal images obtained by SOHO/LASCO. Only a portion of the FOV containing the CME is shown. Running difference images are used so changes can be readily detected. In the image at 02:08 UT, the eruptive filament can be seen just above the limb. Overlying the filament is a dark region, which indicates the outward movement of coronal material overlying the filament. At this time, the coronal material is hidden by the occulting disk of the coronagraph. In the image at 2:42 UT, the leading edge of the CME can be seen at a heliocentric distance of 3.25 solar radii (Ro). The connection to the solar source region can be

seen via the EUV disturbance. In the image at 03:42 UT, the parts of the CME leading edge have already left the coronagraph FOV, whose outer edge is at 6 Ro. The large-scale dark feature is the location of the CME in the previous frame (effect of the running difference). The bright feature inside the dark region is the filament material seen earlier in EUV. The CME speed is determined by tracking the leading edge in every frame in which the CME is observed and fitting a straight line or second order fit to the height – time (h – t) measurements. In this case, the h – t measurements gives a linear speed of 888 km/s, which is an average speed within the LASCO FOV. Since the CME was accelerating within the LASCO FOV, the h – t measurements fit better to a second order fit, giving a constant acceleration of 11.3ms^{-2}. The

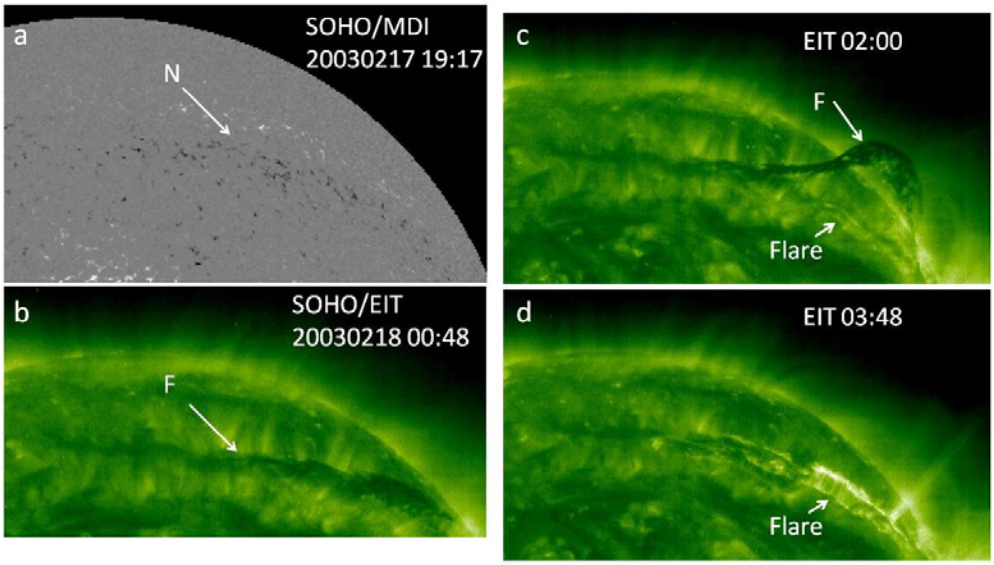

Figure 2. *A filament eruption from a non-sunspot region (also known as quiescent filament region). a) a patch of the photospheric magnetogram from the northwest quadrant of the Sun obtained by SOHO/MDI showing the extended magnetic region with positive (white) and negative (dark) polarities separated by a polarity inversion line that runs east-west (marked N). b) A dark filament (F) overlying the neutral line as seen in absorption at 195 Å by SOHO/EIT. c) The filament F has lifted from its equilibrium position, with an arch shape seen above the limb in projection and two bright ribbons (marked "Flare") forming near the surface. d) The ribbons have expanded with thin loops connecting the two ribbons, while the filament has long moved past the EIT field of view (FOV). These loops are called flare loops and the entire structure as flare (see Fig. 3).*

angular width of the CME measured as the position angle (PA) difference between the two edges of the CME is 93^o. PA is measured from the north in the counterclockwise direction. For the CME in Fig. 3, the two edges are at PA = 265^o and 358^o yielding an angular width of 93^o in the sky plane. The central PA (CPA) is the mid angle between the two edges, which is 312^o. The speed, width, and central position angle are the basic attributes of a CME.

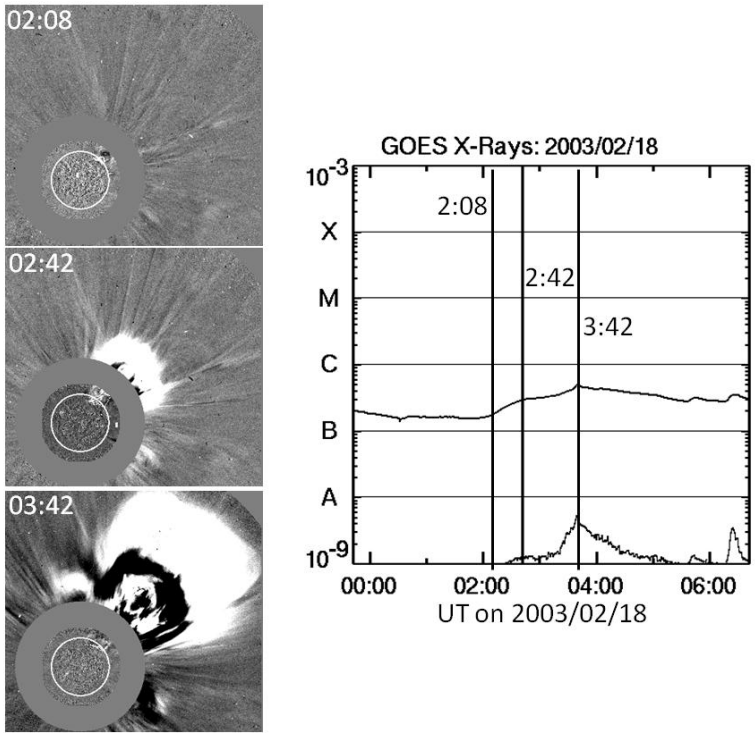

Figure 3. *Three snapshots of the CME on 2003 February 18 (left) and the GOES soft X-ray light curve. The white circle represents the optical limb of the Sun. The gray disk is the coronagraph occulting disk, on which the EIT difference image is superposed to show the activity taking place on the Sun. This figure also illustrates the flare-CME relationship.*

Figure 3 also shows the flare light curve obtained by the Geostationary Operational Environmental Satellites (GOES) in two soft X-ray wavelength channels (1 – 8 Å upper curve and 0.5 – 4 Å lower curve). The times of the three coronagraph images are marked on the GOES light curve by the three vertical lines. No flare was reported by the Solar Geophysical Data (SGD), but we can identify a weak flare in association with the filament eruption. However, the filament eruption itself was reported as a "Disappearing Solar Filament" or DSF

starting at 01:23 UT and continuing beyond 02:53 UT based on H-alpha observations made at the Learmonth observatory in Australia. Clearly the flare starts after the filament erupts. When the flare reaches its peak at 03:42 UT, the CME has moved beyond 6 Ro. The PEA remains visible for several hours more before fading to the background level. The flare in this case is extremely weak. The peak soft X-ray flare intensity is used to designate the flare size. In this case, the flare size is B5.0, which means the peak soft X-ray flux during the flare is 5.0×10^{-7} Wm^{-2}. This is said to be a B-class flare. The Y-axis shows that flares in general can have intensity varying over several orders of magnitude, starting below A class (1.0×10^{-8} Wm^{-2}) and beyond X class (1.0×10^{-4} Wm^{-2}). Flares stronger than X class are expressed using X but with a larger suffix. For example, the largest flare during cycle 23 was reported by NOAA at X17.4 on 2003 November 4. The detector was saturated at this intensity, so the actual flare size must have been larger. The GOES detector has no spatial resolution, so the light curve is a summation of all events taking place on the Sun including the background X-ray emission from the corona. The background itself varies between solar minimum (A class) and maximum (C class) by about two orders of magnitude. Traditionally, the flare size is measured as the total area of the flare ribbons in H-alpha. The flare size is given on a scale of 1-4, with each number subscripted by the letters F (faint), N (normal) and B (brilliant). In addition, flares below 1 are classified as subflares (SF). Details on the flare classification can be found in Gopalswamy (2007) at various wavelength regimes such as soft X-rays, H-alpha, and microwaves**.**

2. 3 Eruption from an Active Region

Figure 4 shows another CME, which seems to surround the occulting disk of the coronagraph. Such CMEs are known as halo CMEs (Howard et al., 1982), which are like any other CME, but are moving close to the Sun-Earth line. One can imagine this CME to be cone shaped with its apex at the Sun and its base is moving towards or away from the observer. Projection of the cone base on the sky plane gives the “halo” appearance. No EIT images were available for this CME, so it is impossible to tell whether the CME is frontsided or backsided from the LASCO images alone. Fortunately, soft X-ray images from the Yohkoh satellite were available, which

show a PEA centered at the heliographic coordinates N08W18 (Fig.4). The eruption occurred in the active region marked A (AR 9684) in Fig. 1on 2001 November 4. The CME was very fast, with an average speed of 1810 km/s within the LASCO FOV. The h – t measurements fit to a second order polynomial (constant acceleration of - 63ms^{-2}), suggesting that the CME was rapidly decelerating within the LASCO FOV. This is a characteristic property of fast CMEs because of the drag caused by the ambient medium (Gopalswamy et al., 2001). The flare is also relatively big in this case, with an X-ray importance of X1.0 (peak flux is 1.0x10^{-4} Wm^{-2}).

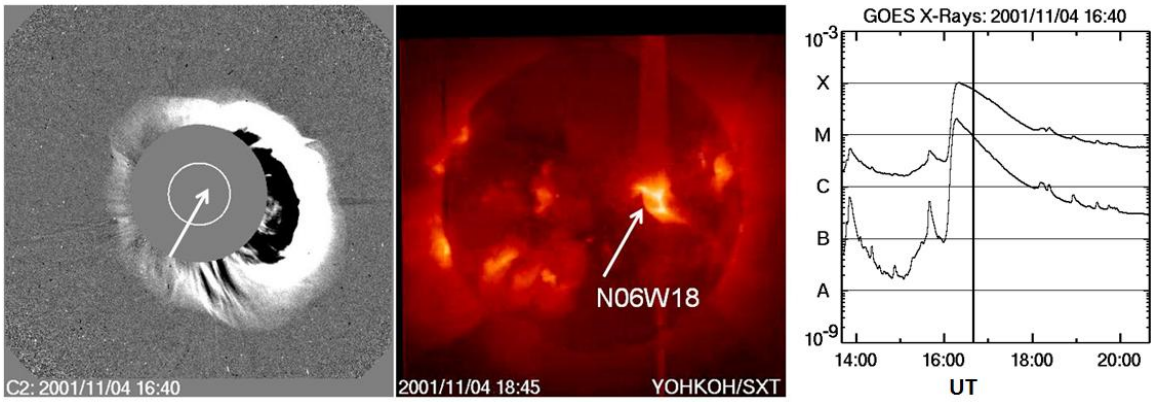

Figure 4. *The halo CME of 2001 November 4 at 16:40 UT as observed by LASCO/C2 (left), its solar source in the soft X-ray image obtained by Yohkoh (middle), and the GOES light curves (right). The eruption occurred in AR 9634 in association with an X1.0 flare that had a start time of 16:03 UT. The CME first appeared in LASCO/C2 FOV at 16:25 UT and became halo in the next frame at 16:35 UT.*

2. 4. CMEs and Shocks

Figure 5 shows a large-scale disturbance in the corona surrounding the flaring region revealed by EUV images for the 2005 May 13 CME. Such disturbances are coronal waves (MHD fast mode waves or shocks depending on the speed) surrounding the erupting CME. The EUV disturbance has a size of ~0.4 Ro at 16:37 UT. The disturbance spreads over the entire solar disk by 17:07 UT as can be seen in Fig. 5. In this event, the disturbance is most likely a shock because the CME was rather fast (1689 km/s). Detection of such large-scale EUV disturbances has become one of the standard techniques of identifying the solar source of CMEs. The white-light image in Fig. 5 taken about 15 min after the EUV image clearly shows the close

connection between the EUV disturbance and the CME in white light. The diffuse feature surrounding the main body of the CME (marked S for shock in Fig. 5) can be identified with the EUV disturbance. The main body of the CME is thought to be a flux rope whose legs are rooted in the dimming regions D1 and D2, located on either side of the neutral line. The flare reconnection process is thought to create the flux rope (or builds upon a pre-existing one), whose outward motion causes the disturbance seen in white light as the CME with the surrounding shock.

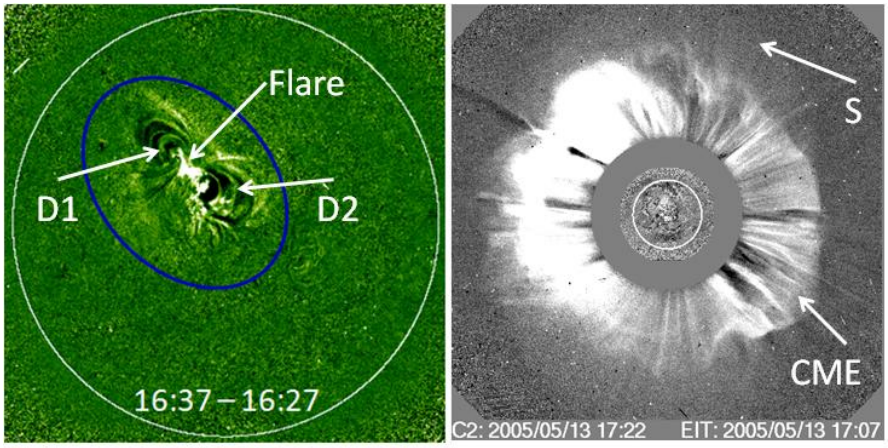

Figure 5. *(left) SOHO/EIT 195 Å difference image on 2005 May 13 at 16:37 UT showing the flare (PEA), dimming regions (D1, D2) and a large-scale disturbance surrounds the active region. (right) The corresponding white-light CME at 17:12 UT. Superposed on this image is a EUV difference image from SOHO/EIT at 17:07 UT. Note that the EUV disturbance has spread over the entire solar disk compared to the image at 16:37 UT. The disturbance is seen as the diffuse feature marked as that surrounds the CME.*

The shock can also be inferred from a type II radio burst, which is caused by ~10 keV electrons accelerated at the shock front. The escaping electrons form a beam that is unstable to Langmuir waves in the background plasma. The Langmuir waves are then converted into electromagnetic radiation at the fundamental and harmonic of the local plasma frequency by the plasma emission mechanism. Figure 6 shows an intense type II burst associated with the 2001 November 4 CME discussed earlier (see Fig. 4). The radio dynamic spectrum shows a type III burst indicative of electron beams from the eruption site, supposed to be accelerated at the flare reconnection. The type II burst, on the other hand, is due to nonthermal electrons accelerated at

the CME-driven shock. Thus the radio data provide a simple means of probing two acceleration mechanisms: the flare and shock acceleration. Both types of bursts are due to the plasma emission mechanism and hence occur at progressively lower frequencies as the electron beam and the shock propagate away from the eruption site. Thus, one can track the electron beams and shocks in the corona as they move away from the Sun. When the shocks reach the observer near Earth (e.g., at the spacecraft located at Sun-Earth L1), one can observe the type II burst, Langmuir waves, and the electron beams all at once at the shock front, thus confirming the plasma emission mechanism (Bale et al., 1999).

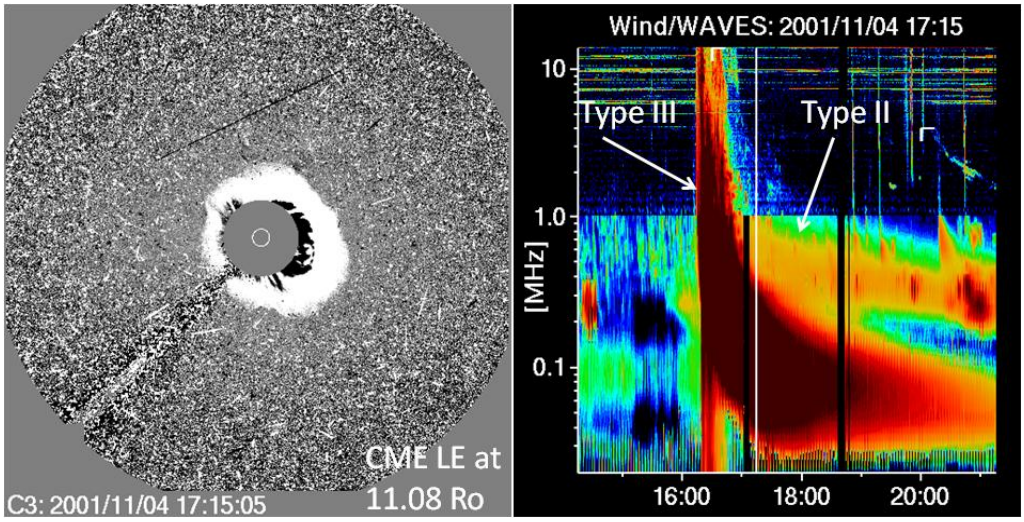

Figure 6. *(left) The 2001 November 4 CME. (right) Wind/WAVES Dynamic spectrum showing the type III and type II bursts associated with the CME. The type II radio emission occurs at ~1 MHz when the CME is at 11 Ro (indicated by the vertical line). The streaks in the background corona are actually secondary particles hitting the SOHO detector produced by primary SEPs arriving at the SOHO spacecraft*

2. 5. Consequences of CMEs

CME-driven shocks accelerate ions (protons and heavier ions) and high energy electrons that can be detected when they arrive at Earth in tens of minutes. These particles are collectively known as solar energetic particles (SEPs). Shocks continue to accelerate SEPs as they propagate into the IP medium, so they are continuously detected until the shock reaches the observing spacecraft, when a sudden increase in SEP intensity is observed. The intensity increase at the shock is referred to as an energetic storm particle (ESP) event. SEPs also reach

the detector when the shock moves past Earth if there is magnetic connectivity. The onset phase of the SEP event associated with the 2001 November 4 CME is shown in Fig. 7. The onset time (17:05:30 UT) is within an hour of the CME lift off time (16:17 UT). If one accounts for the propagation time of the 13 MeV protons along the Parker spiral (typical length ~1.2 AU), the particle release time at the Sun can be placed immediately after the CME lift off because this is a fast CME and drives shock early on. Statistical studies indicate that SEPs are released near the Sun when the associated CMEs are at a heliocentric distance of ~7 Ro (Gopalswamy, 2008a).

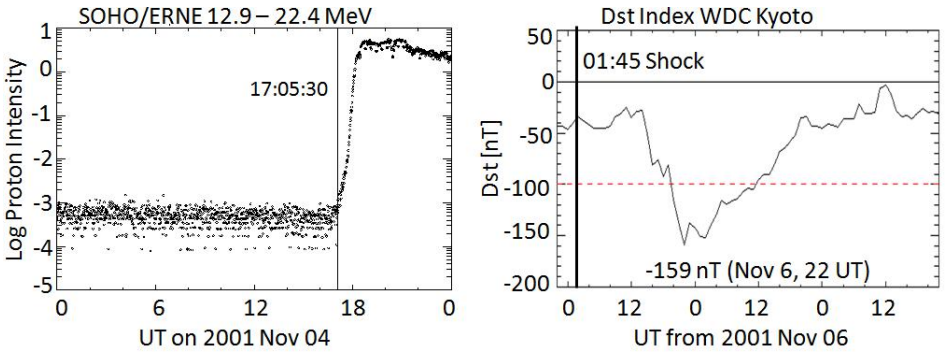

Figure 7. *The SEP event (left) and the geomagnetic storm (right) associated with the 2001 November 4 CME (Figs. 4 and 6). The SEP data are from SOHO/ERNE in the 12.9 – 22.4 MeV energy channel. The SEP onset time at Earth is at17:05:30 UT, right after the CME liftoff. The geomagnetic storm reaches its maximum intensity (i.e., minimum Dst) at 22:00 UT on November 6. The shock ahead of the 2001 November 4 CME arrived at Earth at 1:45 UT on November 6 as indicated by the vertical line in the Dst plot. The horizontal line at -100 nT indicates the intense storm level. Dst > -100 nT storms are considered moderate to weak.*

The shock arrival at Earth is also recognized in the ground-based magnetometer data as a sudden increase in the horizontal component of Earth's magnetic field. The Disturbance storm time (Dst) index is a measure of this magnetic field change. The sudden increase in Dst index is referred to as storm sudden commencement (SSC) because usually a geomagnetic storm follows the SSC. The ESP event is so called because of its association with the geomagnetic storm. The Dst plot in Fig. 7 shows that the 2001 November 4 CME resulted in a sudden commencement (shock) followed by an intense (Dst < -100 nT) geomagnetic storm. The occurrence of a storm following the SSC depends on the magnetic structure in the shock sheath

and the interplanetary counterpart of the CME (ICME) that drives the shock. The magnetic structure must contain a south pointing field, which reconnects with Earth's magnetic field to initiate the storm process. Geomagnetic storms can also happen without the SSC because some ICMEs do not drive a shock.

The above discussion introduced various phenomena associated with solar eruptions: flares (H-alpha and soft X-ray), filament eruptions, EUV waves, white-light CMEs, type II and type III radio bursts (metric and IP), SEPs, ICMEs with shock, and geomagnetic storms. Of these, the SEP and geomagnetic storm effects have important practical consequences because they cause severe weather in the space environment. Such "space weather" is hazardous to space and ground based technological systems, radio communication and navigation, and to human health. These are CME related space weather. The rest of the article will focus on CMEs.

3.0. General Structure of the Magnetosphere

CMEs have been studied extensively using data from several spaceborne coronagraphs since the early 1970s and the ground-based Mauna Loa K-coronameter (see e.g., Howard et al., 1985; Hundhausen, 1993; Gopalswamy, 2004; 2006a,b; Kahler et al., 2006). SOHO observations provided the most extensive information on CMEs as summarized below:

1. The CME speed is obtained by tracking the leading edge until it reaches the edge of the coronagraphic FOV. A linear fit to the height – time (h – t) measurements gives the average speed within the FOV. Since the h – t measurements are made in the sky plane, the speed is a lower limit. Figure 8 shows that the speed varies over two orders of magnitude from 20 km/s to more than 3000 km/s, with an average value of 475 km/s (see Fig. 8).
2. The CME angular width ranges from $<5^o$ to 360^o (halo CMEs). The average width of CMEs with width $<120^o$ is $\sim 44^o$. The widths shown in Fig.8 have been measured after the CME has reached a height of ~8 Ro because the speed changes with time when the CME is close to the Sun. Almost 90% of the CMEs have width $<120^o$, and only ~3.5% have an apparent width of 360^o. About 11% of CMEs have width $\geq 120^o$ (see Fig. 8). There is actually a correlation

between CME speed (V km/s) and width (W in degrees) indicating that faster CMEs are generally wider: V = 360 + 3.64W (Gopalswamy et al., 2009a).

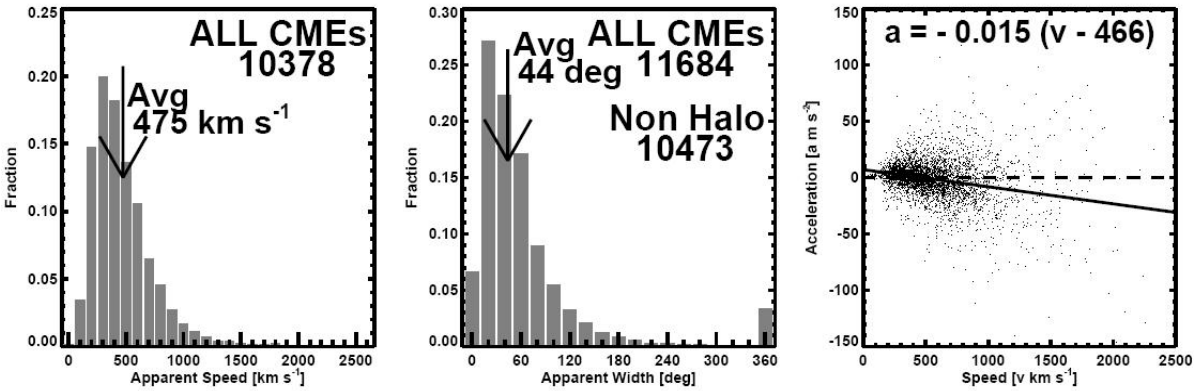

Figure 8. *Speed, width, and acceleration of CMEs measured in the sky plane for all CMEs detected until the end of 2006. The acceleration is shown as a function of the measured speed. The average width is computed for CMEs with width <120^o because the width of halo CMEs is unknown.*

3. The linear fit is not a good approximation for many CMEs. A second order (constant acceleration) fit often represents the h – t measurements better. The scatter plot shown in Fig. 8 is between the constant acceleration and linear speed obtained from the same h – t measurements. We see that CMEs moving faster than the slow solar wind decelerate, while the lower speed ones accelerate. CMEs with speeds close to that of the slow solar wind move with constant speed. A scatter plot between the observed acceleration and the CME linear speed shows a weak correlation with the regression line a = - 0.015 (V - 466), where V is the CME speed and a is the acceleration (see Fig. 8). One can associate the 466 km/s as the slow solar wind speed (see Gopalswamy et al., 2000). This is only approximate because the CME propulsion and gravity may still be playing a role in the coronagraphic FOV.

4. CME mass ranges from a few times 10^{12} g to more than 10^{16} g with an average value of 3.4×10^{14} g (Gopalswamy, 2004). Wider CMEs generally have a greater mass content (M): logM = 12.6 + 1.3 logW (Gopalswamy et al. 2005a). The corresponding kinetic energies range from ~10^{27} erg to more than 10^{33} erg, with an average value of 2.9×10^{29}erg.

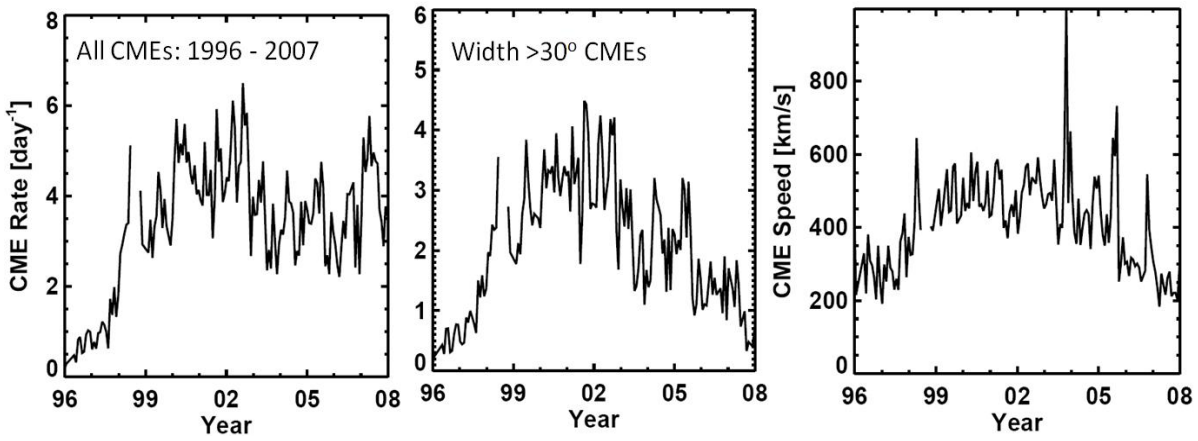

Figure 9. *CME rate (left two) and speed (right) averaged over Carrington rotation periods (27.4 days). The left panel includes all the CMEs detected manually. The middle panel shows only CMEs wider than 30°. The spikes in the speed plot are due to super active regions.*

5. CMEs occur at a rate (averaged over Carrington Rotation periods) of ~0.5 per day (solar minimum) to >6 per day (solar maximum). During solar maximum, manual detection of faint and narrow CMEs is difficult. This causes a change in the contribution to the total CME rate from such CMEs over the solar cycle, as illustrated in Fig. 9. Considering only CMEs wider than 30°, one sees that the CME rate is similar to the sunspot number.

6. The sunspot number (SSN) and the CME daily rate are reasonably correlated (Gopalswamy et al., 2009b and references therein): CME rate = 0.02SSN + 0.9 with a correlation coefficient r =0.84. However, there is a clear solar-cycle variation of this correlation. The correlation is high during the rise (r = 0.90) and declining (r = 0.73) phases of the solar cycle, but is lower during the maximum phase (r = 0.64). This has been attributed to the fact that CMEs also originate from non-spot regions, which occur in large numbers during the maximum phase (e.g., polar crown filament regions, which occur exclusively outside the sunspot zone).

7. The average speed of CMEs (averaged over Carrington Rotation periods) also varies in phase with the solar cycle: it increases by a factor of 2 from ~250 km/s during solar minimum to ~550 km/s during solar maximum. Occasionally, the average speed reaches very high values because of some super active regions that produce energetic CMEs in quick succession (see Fig. 9).

8. CMEs contain coronal material at a temperature of ~ a few MK in the outer structure with cool filament material (~8000 K) in the core. When the CME is shock-driving, the compressed sheath behind the shock can have higher temperature than in the ambient corona.
9. CMEs moving faster than the coronal magnetosonic speed drive shocks, which accelerate solar energetic particles (SEPs) to GeV energies. The shocks also accelerate electrons, which produce nonthermal radio emission (type II radio bursts) throughout the inner heliosphere. EUV waves maybe another manifestation of the CME-driven waves that surround CMEs.
10. Each CME eruption is accompanied by a solar flare. The soft X-ray peak flux is correlated with the CME kinetic energy (Hundhausen, 1997; Yashiro and Gopalswamy, 2009: Gopalswamy et al., 2009a). However, more than half of the flares are not associated with CMEs. There are even X-class flares without CMEs (Gopalswamy et al., 2009c).
11. There is a close temporal and spatial connection between CMEs and flares: CMEs move radially away from the eruption region (Yashiro et al., 2008), except for small deviations that depend on the phase of the solar cycle (Gopalswamy et al., 2003).
12. Statistical studies (Kay et al., 2003) indicate that flares without CMEs are generally much hotter (18.4 MK compared to 11.7 MK for flares with CMEs).

4.0. Interplanetary CMEs

The idea of interplanetary CMEs and shocks (Parker, 1957; Gold, 1962) precedes the discovery of white-light CMEs in 1971 (Tousey, 1973). Interplanetary shocks were first detected by Mariner 2 (Sonnet et al., 1964). The picture that a magnetic bottle moves from the Sun into the IP space driving a shock proposed by Gold (1962) is now the standard picture of ICMEs, except that the magnetic bottle is replaced by a flux rope. Koomen et al. (1974) recognized the similarity between the Gold magnetic bottle and CMEs observed by OSO-7 coronagraph. Burlaga et al. (1981) reported a complete ICME structure with shock, sheath, and the driving magnetic cloud using observations made by five spacecraft. Various signatures are used to identify ICMEs: solar wind plasma signatures (temperature, plasma beta, flow speed), magnetic signatures (field strength, field rotation), compositional and charge state signatures (average Fe

charge state, O7+/O6+ ratio, alpha to proton ratio), and particle (thermal and nonthermal) flux signatures (see Gosling, 1990; Neugebauer and Goldstein, 1997 for a review). Arrival of shocks at the spacecraft is also a good indicator of the impending ICME arrival except when the associated CME propagates at a large angle to the Sun-spacecraft line. Space observations made by a large number of spacecraft over the past several decades have shown that ICMEs can be found throughout the heliosphere (see e.g., Wang et al., 2005). Techniques such as IP scintillation observations (see e.g., Tokumaru et al., 2007), IP type II radio burst observations (see e.g., Gopalswamy et al., 2005a), and solar energetic particle events (see e.g., Gopalswamy et al., 2008a) also provide information on parts of CMEs in the heliosphere.

4.1. Magnetic Clouds

The magnetic cloud signatures defined by Burlaga et al. (1981) combine magnetic (enhanced field, smooth rotation of the field) and plasma signatures (reduced proton temperature). The smooth rotation is thought to be due to the flux-rope (helical) structure of the ICME. MCs can be classified into four types based the orientation of the MC axis with respect to the ecliptic. If the axis is close to the ecliptic plane, the MC is known as a low-inclination cloud. The out-of-the ecliptic component at the leading edge of the MC can be north or south pointing. As one approaches the axis and crosses it, the direction of the out-of-the ecliptic component flips from one direction in the leading edge to the opposite in the trailing edge. Thus the MCs are called NS and SN for north-south and south-north rotation, respectively. When the MC axis makes an angle $> 45^{o}$ with the ecliptic, the MC is referred to as a high-inclination cloud. The out-of-the-ecliptic component in this case points either to the south or to the north throughout the cloud. For the high-inclination MCs, the rotation is in the east-west direction. i.e., the leading edge of the MC has east or west pointing field with the opposite sense in the trailing edge. If the axial field of the high-inclination MC points to the north (south) it is said to be of FN (FS) type. Each MC type will have two subtypes based on the handedness of the MC. For example, the NS MC can be NES or NWS depending on the direction of the axial field in the east (E) or west (W) direction (Bothmer and Schwenn, 1994). Similarly, an FN MC can be of ENW WNE

depending on the direction of the east-west component at the leading edge. Figure 10 illustrates the four MC types using the out-of-the ecliptic (Z component in GSE coordinates) component of the magnetic field (B_z). All the MCs shown in Fig. 10 are shock-driving, so there is a sheath region between the MC and the shock as indicated. The magnitude of the field component is large (>10 nT) compared to the solar wind field (~5 nT). The statistical properties of MCs can be summarized as follows: 1. The total magnetic field in MCs has an average value of 17 nT, which is about three times the solar wind value. 2. The density inside MCs is ~8.5 cm^{-3}, which is not too different from the solar wind value. 3. The mean speed of MCs (478 km/s) is only slightly larger than the typical slow solar wind speed (437 km/s—see Gopalswamy, 2006c). At the Sun, the CMEs associated with MCs have a much larger average speed (~1000 km/s). The speed reduction is due to the interaction with the ambient solar wind. Depending on the initial speed V, the CME undergoes an acceleration a = - 0.0054 (V – 406), where V is in km/s and a is in m/s^2. For high initial speeds, the relation is quadratic (Gopalswamy, 2009). 4. The average MC duration is ~21 h, which implies a spatial scale of ~0.25 AU for the thickness of the MC (see Lepping and Berdichevski, 2000; Gopalswamy, 2006c). 5. Although both SN and SN MCs are observed during every solar cycle, there is a predominance of one type during a given cycle. The predominance seems to be decided by the global magnetic field of the Sun. The global field of the Sun reverses during solar maxima, so the predominance switches around this time. For example, when the north pole of the Sun has positive polarity, there was the predominance of the NS MCs. After the polarity reversal in 2002, the SN MCs started appearing in larger numbers (see Echer et al., 2005; Gopalswamy, 2008b).

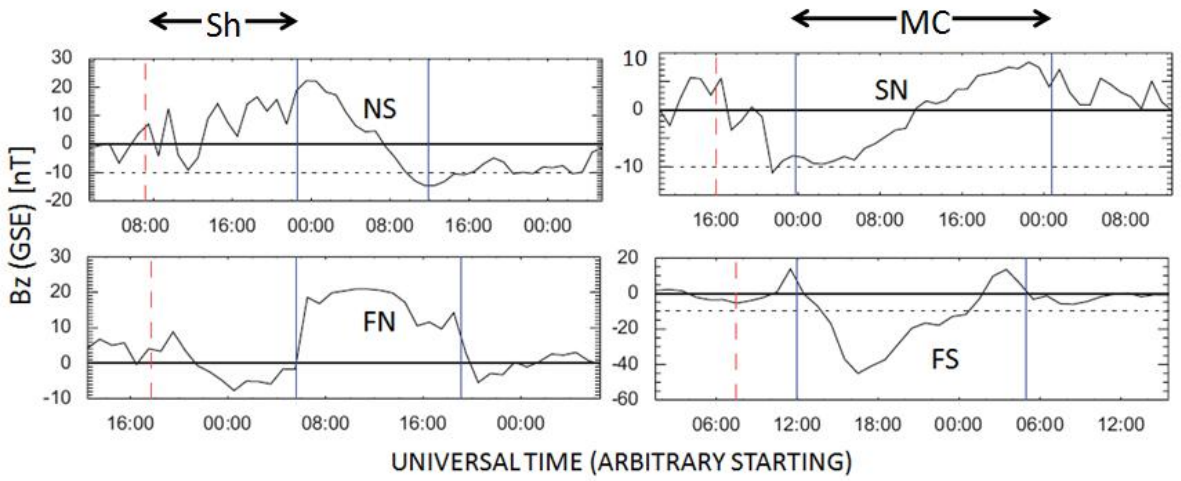

Figure 10. *The four MC types defined based on the direction of the leading field from the B_z component in GSE coordinates: North-south (NS), south-north (SN), fully north (FN), and fully south (FS). The vertical dashed line denotes the shock. The MC interval is between the two vertical solid lines. The region between the shock and MC is the sheath region.*

4.2. ICMEs without MC Structure

Not all ICMEs have flux rope structure at 1 AU. Only about a third of the ICMEs were found to be MCs (Zhang and Burlaga, 1988). Counting only shock driving ICMEs, Gopalswamy et al. (2009d) found that out of 180 ICMEs, 57 were MCs and the rest were non-cloud ejecta, which confirms earlier statistics. However, the MC fraction depends on the phase of the solar cycle. During solar minimum, the fraction of MCs is very high, close to 100%, whereas during solar maximum, the fraction decreases to ~20% (Riley et al., 2006). One of the reasons is that during solar minimum the global dipolar field of the Sun is strong so CMEs are generally channeled towards the equator, even though the source regions are at relatively higher latitudes during the beginning of solar cycles. This can be seen from the solar source locations MCs shown in Fig. 11. First of all we note that the source longitudes are within ±30^o from the central meridian. The same is true for latitudes also with a few exceptions during the rise phase. In the rise phase of a solar cycle, active regions typically emerge at higher latitudes, but the CMEs move toward lower latitudes because of the strong global dipolar field. During the maximum and declining phases, the MC sources progressively appear closer to the equator, which resembles the sunspot

butterfly diagram. This is consistent with the fact that only active regions contain high enough free energy to power the CMEs that become MCs.

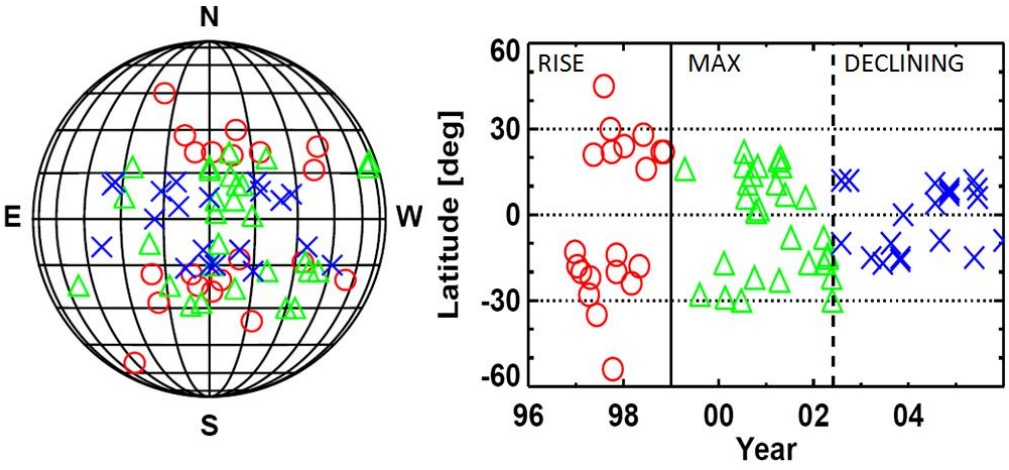

Figure 11. *Solar sources of CMEs associated with MCs shown as heliographic coordinates (left) and latitude distribution (right). The three phases of the solar cycle 23 are distinguished.*

The latitude distribution of non-cloud ICMEs is nearly identical to that of the MCs, but the longitude distribution is quite different. The source longitudes of non-cloud ICMEs are generally farther from the central meridian. This means CMEs responsible for the non-cloud ICMEs are ejected at larger angles to the Sun-Earth line and hence typically make a glancing impact on Earth. On the other hand the MC-associated CMEs are mostly ejected close to the Sun-Earth line. In the extreme case, CMEs ejected orthogonal to the Sun-Earth line may be observed purely as a shock with the driving ejecta not arriving at Earth. This geometrical difference may be responsible for observing non-cloud ICMEs even though they possess the flux rope structure. In other words, all ICMEs may be flux ropes if viewed appropriately. This point is illustrated in Fig. 12, which shows two magnetic clouds, one driving a shock and the other not. When the observing spacecraft passes through the nose of the flux rope, it observes an MC. When it is away from the nose, it observes ejecta. In the extreme case, the spacecraft observes just the sheath. The source locations of MCs and non-MCs overlap significantly, so there may be factors other than geometry. Interaction with other CMEs and nearby coronal

holes may alter the trajectory of ICMEs (Gopalswamy et al., 2009e). It is also not clear if some CMEs inherently lack flux rope structure (Gosling, 1990).

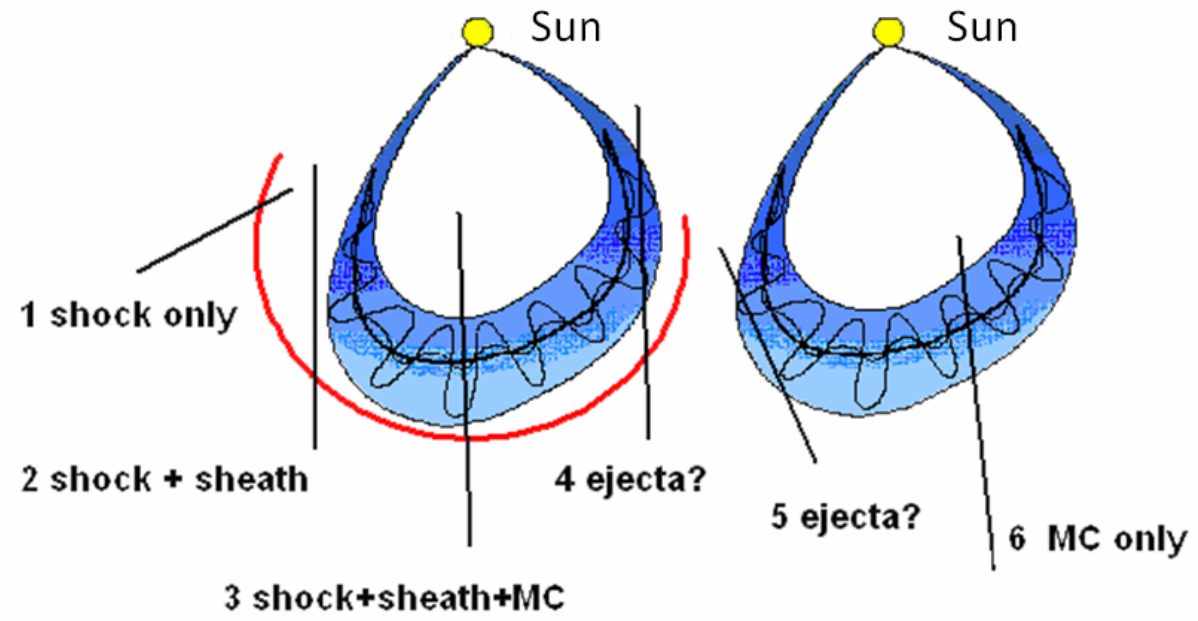

Figure 12. *A shock-driving magnetic cloud (left) and another without a shock (right). Various possible spacecraft paths (labeled 1 to 6) shown and the corresponding structures observed. Paths 3 and 6 observe the ICMEs as MCs.*

It must be pointed out that the vast majority of CMEs are not distinctly observed as ICMEs at 1AU. If we count just the shock driving ICMEs, they amount to about ~2% of all CMEs (230 IP shocks were detected at 1 AU even though ~13000 CMEs were observed during solar cycle 23). It is estimated that about 10% all CMEs are energetic enough to make a significant impact on Earth's atmosphere and the heliosphere in general.

5.0. Solar Eruptions and Space Weather

Both flares and CMEs affect space weather. Flares cause excess ionization of the subsolar ionosphere for the duration of the flare (minutes to hours). This primarily causes changes in the ionospheric electron density resulting in communication and navigation problems. CMEs cause

two key space weather effects: SEPs and geomagnetic storms, illustrated schematically in Fig. 13. CMEs responsible for SEPs and magnetic storms have different longitude distributions, with some overlap. SEP production typically starts when the CME-driven shock is within a few solar radii (~7 Ro on the average) from the Sun (Gopalswamy, 2008a). The CME-driven shock continues to produce SEPs in the IP medium on the way to Earth. When the shock arrives at the observing spacecraft, a sudden increase in SEP intensity is observed, which is known as the ESP event. Production of geomagnetic storms, on the other hand, happens only upon the arrival of the southward magnetic field component (Bs) in the CME and/or the sheath at Earth's magnetosphere. Thus, Bs in the CME is the crucial aspect of storm-causing CMEs. The shock-driving ability of a CME, on the other hand, is crucial for the production of SEPs. The CME speed need to exceed the sum of the solar wind speed (V_{sw}) and the Alfven speed (V_A) of the ambient medium to drive a shock. In addition, the shock must be supercritical to be efficient in accelerating particles. It has been shown that about 35% of shocks observed at 1 AU are radio quiet (lack of type II radio bursts), which also lack large SEP events (Gopalswamy et al., 2009d). The shock strength is not only determined by the CME speed, but also by the coronal and interplanetary environment through which the shock propagates. For example, the Alfven speed can vary by a factor of 4 in the region where the SEP production starts (Gopalswamy et al., 2008a,b). The shock is often produces what is known as a storm sudden commencement (SSC) an indicator of impending geomagnetic storm, provided the ICME that follows the SSC has Bs. Thus the magnetic structure of the ICME is important for geomagnetic storms, but not for SEPs. For example an FN MC does not produce a geomagnetic storm, even though the shock driven by it may be producing SEPs.

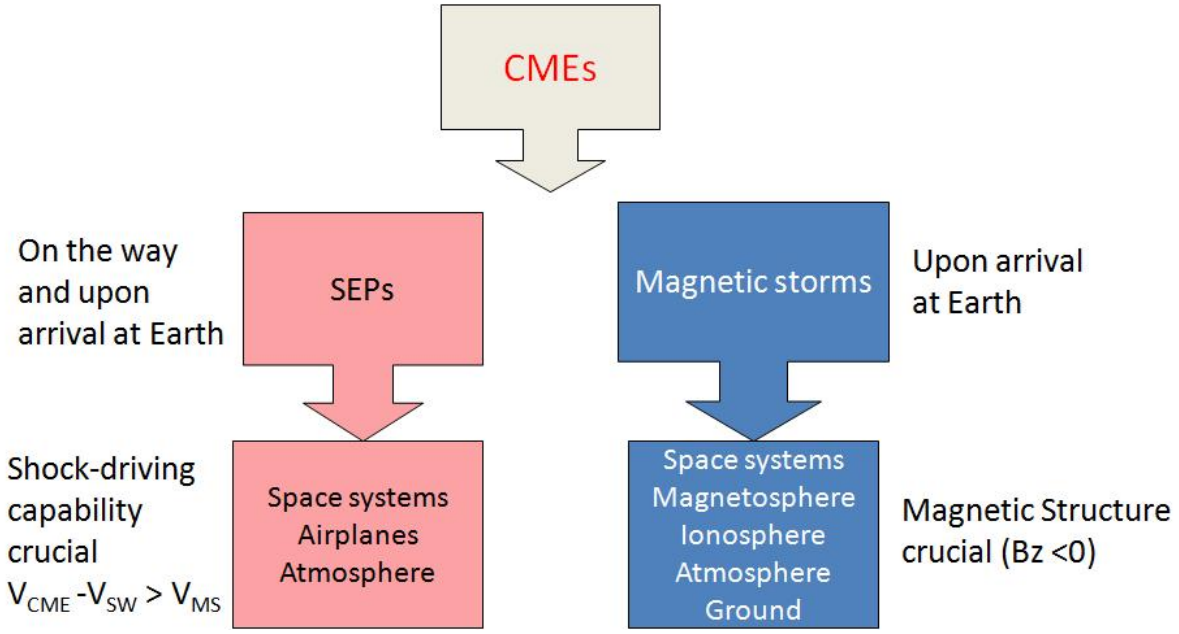

Figure 13. *The two space weather aspects of CMEs: SEPs and magnetic storms. SEPs are produced by CME-driven shocks on the way and upon arrival at Earth. CME speed (V_{CME}) must exceed sum of the solar wind speed (V_{SW}) and the ambient magnetosonic speed (V_{MS}) in order to drive shocks. The SEPs affect space systems (with or without humans), passengers in high-altitude airplanes, and Earth's atmosphere. Geomagnetic storms are produced only when CMEs arrive at Earth with the additional condition that they possess south-pointing magnetic fields (Bz < 0). Geomagnetic storms have consequences to space systems, the entire geospace and even to the ground.*

5.1. CMEs and Geomagnetic Storms

The primary CME link to the geomagnetic storms arises from the fact that they can introduce an out-of-the ecliptic component to the interplanetary magnetic field that arrives at Earth. Whenever the out-of-the-ecliptic component of the magnetic field in a solar wind structure points to the south, a geomagnetic storm ensues due to a series of physical processes elucidated by Dungey (1961). The intensity of a geomagnetic storm is expressed using a number of indices. Here we use the Dst (disturbance storm time) index, which represents the average change in the horizontal component of Earth's magnetic field (in units of nT) brought about by the geomagnetic storm at four low-latitude stations (see http://swdcwww.kugi.kyoto-

u.ac.jp/dstdir/dst2/onDstindex.html). A storm is indicated when Dst ≤ −50 nT (Loewe & Prolss 1997); Dst ≤ −100 nT indicates intense storms. Alfven waves in the solar wind, corotating interaction regions (CIRs) and coronal mass ejections (CMEs) are the sources of Bs in the IP magnetic field (IMF; Lindsay et al. 1995; Echer, et al. 2006; Xu et al. 2009). CMEs cause the most intense of the storms (see e.g., Zhang et al. 2007; Gopalswamy et al., 2007). The CME link to geomagnetic storms can be readily seen from the empirical relationship between the Dst index (nT) and the speed (V in km/s) and the magnitude of the out-of-the-ecliptic component of the IMF (Bs = −Bz in nT) of the solar wind structure: Dst = −0.01V Bz – 32. This empirical relation was obtained by Gopalswamy et al. (2008c) for MCs. For V = 1000 km/s and Bz = 60 nT, one gets Dst = −632 nT, which is roughly the maximum recorded value of the Dst index since solar cycle 19. For extreme CMEs, the 1 AU speed can reach more than 2000 km/s, in which case the magnitude of the Dst index can exceed 1000 nT. For the Halloween 2003 CMEs, indeed had such speeds, but the Bs values were not too large, so the storm intensity did not exceed ~400 nT (Gopalswamy et al. 2005b). The southward component of the magnetic field in a CME arises from their flux-rope structure and in the sheath region due to field line draping around the flux rope and compression. The flux rope originates from the source active region, whereas the sheath field is from the heliosphere. The CME speed depends on the active region free energy, modified by the interaction with the solar wind. Thus both the speed and magnetic field parameters are linked to the free energy and magnetic properties of the source active region.

When the ICME is a MC, then one can infer which section of the MC is geoeffective based on the magnetic structure of the MC (flux rope orientation with respect to the ecliptic plane and its sense of rotation. Although most of the large geomagnetic storms are caused by magnetic clouds, non-cloud ejecta can also be geoeffective. Depending on the magnetic structure in the sheath and cloud portions, the following situations are encountered: (1) sheath and MC are geoeffective, (2) Sheath alone is geoeffective, (3) MCs alone are geoeffective, and (4) None are geoeffective. The last situation arises when neither the sheath nor the MC contains south-

pointing magnetic field component. When both sheath and MC are geoeffective, the Dst profile can be complex depending on the location of the south-pointing field in the sheath and cloud portions.

5.2. CMEs and SEPs

SEPs are so-called because they are of solar origin as opposed to cosmic rays, which are energetic particles of galactic origin. The SEP kinetic energy is much higher than that of the solar wind particles. The SEP intensity is defined in terms of particle flux units (pfu, 1 pfu = 1 particle cm^{-2} s^{-1} sr^{-1}). SEPs of intensity exceeding 10 pfu in the >10 MeV energy channel are considered to be important for space weather. Occasionally the >10 MeV SEP intensity can exceed 10^4 pfu (see Gopalswamy et al., 2005b). Each SEP event can be uniquely associated with an energetic CME (fast and wide). The average sky-plane speed of SEP-associated CMEs is ~1623 km/s, much larger than the average speed (475 km/s) of all CMEs (see Fig. 8). There is a high concentration of halo or partial halo CMEs among the SEP-producing CMEs, which is an indicator of their higher energy. Figure 14 compares the speed distribution of SEP-associated CMEs with three other types of CMEs. It is clear that all the distributions are skewed, except for the speed distribution of SEP-associated CMEs (symmetric, approximate Gaussian). The average speed of the SEP-associated CMEs is also about 50% higher.

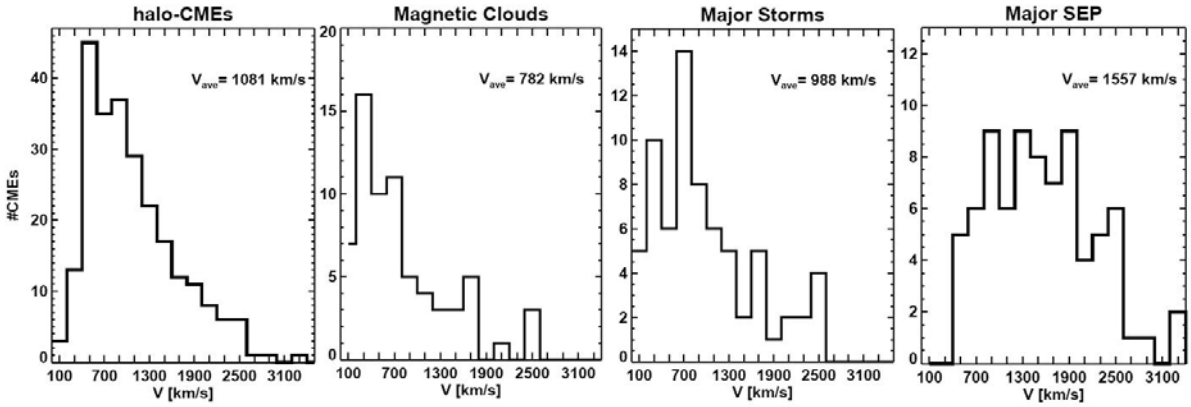

Figure 14. *Speed distributions of several CME populations (from left to right): halo CMEs, CMEs resulting in MCs, CMEs producing major geomagnetic storms, and SEP=producing CMEs. The average speeds of the first three are similar, while that of the SEP-producing CMEs is the highest.*

The close similarity among the first three distributions in Fig. 14 is expected because the concerned CMEs originate close to the disk center of the Sun. Therefore, they are subject to large projection effects. These three populations are highly likely to travel to Earth and impact the magnetosphere (halo CMEs need to be frontsided for this). On the other hand, the SEP associated CMEs originate from the western hemisphere with many events at the limb and even slightly behind the west limb, so they are subject to minimal projection effects (see Fig. 15). Apart from the projection effects, the SEP-producing CMEs may be faster because they have to drive strong shocks that accelerate the particles. The different source positions of CMEs resulting in large SEP events and major geomagnetic storms arise from the geometrical requirements for an observer along the Sun-Earth line. SEPs travel along the Parker spiral field lines of the IP medium, so only particles propagating along the field lines intercepted by Earth can be detected by an observer near Earth. Sources located on the western hemisphere of the Sun are “well-connected” to Earth. Since CME-driven shocks are of large extent, shock flanks of CMEs originating from outside the well-connected region can connect to the Sun-Earth field lines and cause weak SEP events. The geomagnetic storms are caused by direct plasma impact, so only those CMEs aimed directly at Earth have the highest probability in hitting Earth. This happens only for CMEs originating close to the central meridian on the Sun, as is clear from Fig. 15.

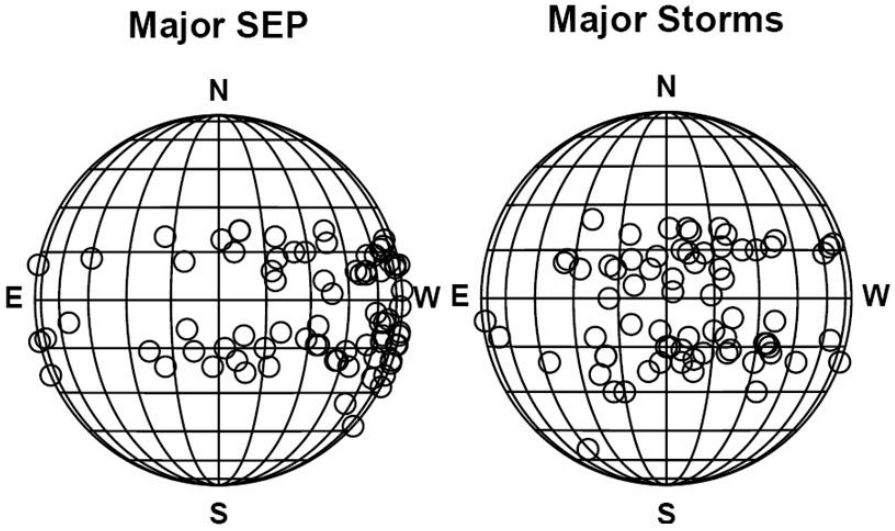

Figure 15. *Solar source locations of CMEs that produce large SEP events (left) and major (Dst ≤ -100nT) geomagnetic storms (right).*

The speed distribution of SEP-producing CMEs is virtually the same (Gopalswamy et al., 2005a) as that of CMEs associated with type II radio bursts that start near the Sun (meter wavelengths) and continue to 1 AU (kilometer wavelengths). These bursts are referred to m-km type IIs because the underlying CMEs are capable of driving strong shocks throughout the inner heliosphere. There is nearly one-to-one correspondence between the m-km type II bursts originating from the western hemispheric CMEs and the large SEP events (see Gopalswamy et al., 2008a) because the same shock accelerates electrons (observed as type II bursts) and SEPs (detected when they arrive at the detector).

Despite the close correspondence between CMEs and SEP events, several questions remain: CMEs as slow as 500 km/s can produce an SEP event, while a CME as fast as 1500 km/s may not produce an SEP event. There have been attempts to account for this variability using the variability in the Alfven speed of the ambient medium, the local shock geometry, and the availability of seed particles in the upstream medium. Flares are also known accelerators of SEPs and energetic CMEs are associated with major flares, so it is not easy to separate the contributions from the flare and CME in a given SEP event. Since the flare site has a very small

angular extent, the SEP events from poorly-connected CMEs are certainly due to shocks. The difficulty is when the CME is well connected to the observer, in which case one cannot tell whether the SEPs are from the flare site or from the nose of the shock, which is located radially above the flare site, but a few solar radii away (Gopalswamy, 2008a). In extremely rare cases, the early anisotropic peak in the intensity of SEP events with ground level enhancement (GLE) has been interpreted to be due to flare acceleration (McCracken et al., 2008).

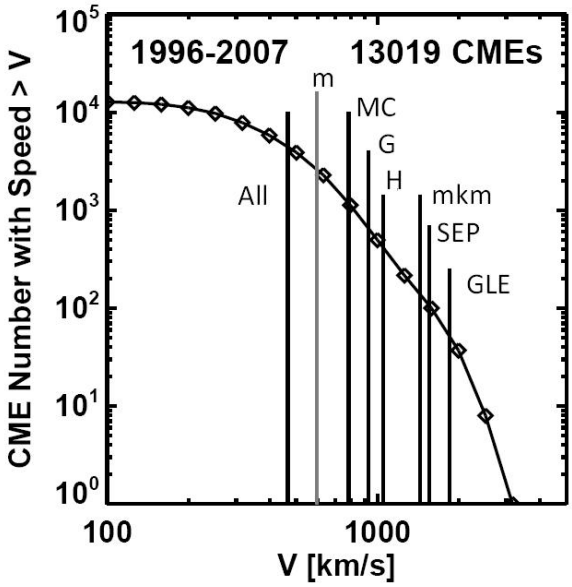

Figure 16. *The cumulative distribution of more than 13000 CMEs observed by SOHO/LASCO until the end of 2007. The average speeds of various energetic subsets are marked.*

6.0. Summary

In this article, we discussed on the two important aspects of solar eruptions, viz., solar flares and coronal mass ejections. The primary aspect of solar flares is the enhanced electromagnetic emission from minutes to hours that produce excess ionization in Earth's atmosphere. Flares also accelerate particles, which are responsible for most of the nonthermal emissions in radio, X-ray and gamma rays. CMEs, on the other hand, represent the mass emission aspect of solar eruptions. CMEs constitute the highest energy phenomenon in the heliosphere because of the amount of kinetic energy they carry. CMEs are also responsible for fast mode MHD shocks in the heliosphere that accelerate electrons and ions from the ambient medium.

The vast majority of CMEs are not detected above the background by the time they reach 1 AU. Only a small fraction of CMEs are responsible for significant consequences. Figure16 shows a cumulative distribution of CME speeds with the average speeds of several CME subsets marked. These speeds are all far higher than the average speed of the general population (466 km/s). The CME subsets are: (1) CMEs associated with metric type II radio bursts (m, 610 km/s), which drive shocks very close to the Sun (within 2 Ro). (2) CMEs associated with magnetic clouds (MCs, 782 km/s). These CMEs originate close to the disk center. (3) CMEs that cause major geomagnetic storms (G, 988 km/s). (4) Halo CMEs (H, 1081 km/s) are those which appear to surround the occulting disk of the coronagraph. (5) CMEs associated with type II bursts having emission components at all (from metric to kilometric) wavelengths (mkm, 1532 km/s). (6) CMEs that produce large SEP events (SEP, 1557 km/s). (7) CMEs associated with the ground level enhancement (GLE, 1916 km/s) events. Note that the three fastest populations (mkm, SEP, GLE) all drive shocks and accelerate particles. The three populations with intermediate speed (MC, G, and H) are important for plasma impact on Earth's magnetosphere. The m population also drives shocks, but very close to the Sun. The average speed of CMEs associated with metric type II bursts is only ~600 km/s, so they do not have enough energy to drive shocks far into the IP medium. Note that only ~3000 CMEs have significant consequences. If we exclude the m CMEs that drive shocks only near the Sun, we see that slightly more than ~1000 CMEs over the solar cycle that are responsible for the space weather effects (SEPs, geomagnetic storms). In other words, ~10% of the fastest CMEs make significant impact on the heliosphere.

References

Bale, S. D., Reiner, M. J., Bougeret, J.-L., Kaiser, M. L., Krucker, S., Larson, D. E., Lin, R. P., The source region of an interplanetary type II radio burst, Geophys. Res. Lett., 26, 1573, (1999).

Bothmer, V. and R. Schwenn, Eruptive prominences as sources of magnetic clouds in the solar wind, Space Sci. Rev., 70, 215, (1994).

Burlaga, L., E. Sittler, F. Mariani, and R. Schwenn, Magnetic loop behind an interplanetary shock—Voyager, Helios, and IMP 8 observations, J. Geophys. Res., 86, 6673, (1981)

Dungey, J. W., Interplanetary magnetic field and the auroral zones, Phys. Rev. Lett., 6, 47, (1961).

Echer, E., M. V. Alves, and W. D. Gonzalez, A statistical study of magnetic cloud parameters and geoeffectiveness, J. Atmos. Sol.-Terr. Phys., 67, 839, (2005).

Echer, E., Gonzalez, W. D., and Alves, M. V., Geoeffectiveness of interplanetary shocks during solar minimum (1995 1996) and solar maximum (2000), Space Weather 4, S06001, (2006).

Gold, T., Magnetic storms, Space Sci. Rev., 1, 100, (1962).

Gopalswamy, N., In: Poletto, G., Suess, S. (Eds.), The Sun the Heliosphere as an Integrated System. Springer, New York, p. 201, (2004).

Gopalswamy, N., Coronal mass ejections of solar cycle 23, J. Astrophys. Astron., 27, 243, (2006a).

Gopalswamy, N., Consequences of coronal mass ejections in the heliosphere, Sun and Geosphere, 1(2), 5, (2006b).

Gopalswamy, N., Properties of interplanetary coronal mass ejections, Space Sci. Rev., 124, 145, 2006c.

Gopalswamy, N. In: Kodai School on Solar physics, Eds: S. S. Hasan and D. Banerjee, AIP conference Proceedings 919, AIP, New York, p. 275, (2007).

Gopalswamy, N., Type II radio emission and solar energetic particle events, American Institute of Physics Conference Series, volume 1039, p. 196, (2008a).

Gopalswamy, N., J. Atm. Solar Terr. Phys., doi:10.1016/j.jastp.2008.06.010 (2008b).

Gopalswamy, N., Coronal mass ejections and space weather, In: Climate and Weather of the Sun-Earth System (CAWSES): Selected Papers from the 2007 Kyoto Symposium, Edited by T. Tsuda, R. Fujii, K. Shibata, and M. A. Geller, pp. 77–120, (2009).

Gopalswamy, N., A. Lara, R. P. Lepping, M. L. Kaiser, D. Berdichevsky, and O. C. St. Cyr, Interplanetary acceleration of coronal mass ejections, Geophys. Res. Lett., 27, 145, (2000).

Gopalswamy, N., Lara, A., Kaiser, M. L., and Bougeret, J.-L., J. Geophys. Res., 106, 25261, (2001).

Gopalswamy, N., Shimojo, M., Lu, W., Yashiro, S., Shibasaki, K., Howard, R. A., Astrophys. J., 586, 562, (2003).

Gopalswamy, N., Aguilar-Rodriguez, E., Yashiro, S., Nunes, S., Kaiser, M. L., Howard, R. J. Geophys. Res., A. 110, 12S07, (2005a).

Gopalswamy, N., S. Yashiro, Y. Liu et al., Coronal mass ejections and other extreme characteristics of the 2003 October-November solar eruptions, J. Geophys. Res., 110, A09S15, (2005b).

Gopalswamy, N., R. Mewaldt, J. Torsti, Editors, Geophysical Monograph Series, Volume 165, 385p, AGU, Washington DC (2006).

Gopalswamy, N., Yashiro, S., Akiyama, S., J. Geophys. Res. 112, A06112, (2007).

Gopalswamy, N., S. Yashiro, S. Akiyama, P. Mäkelä, H. Xie, M. L. Kaiser, R. A. Howard, and J.-L. Bougeret, Coronal mass ejections, type II radio bursts, and solar energetic particle events in the SOHO era, Ann. Geophys., 26, 1, (2008a).

Gopalswamy, N., Yashiro, S., Xie, H., Akiyama, S., Aguilar-Rodriguez, E.,

Kaiser, M.L., Howard, R.A., Bougeret, J.L., Astrophys. J., 674, 560 (2008b).

Gopalswamy, N., S. Akiyama, S. Yashiro, G. Michalek, and R. P. Lepping, Solar sources and geospace consequences of interplanetary magnetic clouds observed during solar cycle 23, J. Atmos. Sol.-Terr. Phys., 70, 245, (2008c).

Gopalswamy, N., Dal Lago, Yashiro, S., and Akiyama, S., The expansion and radial speeds of coronal mass ejections, Cent. Eur. Astrophys. Bull., 33, 115, (2009a).

Gopalswamy, N., Akiyama, S., and Yashiro, S., and Mäkelä, P., Coronal Mass Ejections from Sunspot and non-Sunspot Regions, arXiv:0903.1087v1, (2009b).

Gopalswamy, N., Akiyama, S., and Yashiro, S. , Major solar flares without coronal mass ejections, In: Universal Heliophysical Processes, Proceedings of the International Astronomical Union, IAU Symposium, Volume 257, p. 283-286, (2009c).

Gopalswamy, N., Xie, H., Mäkelä, P., Akiyama, S., Yashiro, S., Kaiser, M. L. Howard, R. A. and Bougeret, J.-L., Interplanetary shocks lacking type II radio bursts, arXiv:0912.4719, (2009d).

Gopalswamy, N., Mäkelä, P., Xie, H., Akiyama, S., and Yashiro, S., CME interactions with coronal holes and their interplanetary consequences, J. Geophys. Res. 114, A00A22, (2009e).

Gosling, J. T., Coronal mass ejections and magnetic flux ropes in interplanetary space, in Physics of Magnetic Flux Ropes, AGU Monograph 58, p. 343, (1990).

Howard, R. A., Michels, D. J., Sheeley, N. R., & Koomen, M. J., ApJ, 263, L101 (1982).

Howard, R. A., D. Michels, N. R. Sheeley, and M. J. Koomen, Coronal mass ejections—1979-1981, J. Geophys. Res., 90, 8173, (1985).

Hundhausen, A. J., Sizes and locations of coronal mass ejections—SMM observations from 1980 and 1984-1989, J. Geophys. Res., 98, 13177, (1993).

Hundhausen, A. J., An introduction, in Coronal Mass Ejections, AGU Monograph 99, p.1, (1997).

Kahler, S. W., in: Gopalswamy, N., R. Mewaldt, J. Torsti, Editors, Geophysical Monograph Series, Solar Eruptions and Energetic Particles, Volume 165, p.21 (2006).

Kay, H. R. M., Harra, L. K., Matthews, S. A., Culhane, J. L., and Green, L. M., The soft X-ray characteristics of solar flares, both with and without associated CMEs, Astron. Astrophys., 400, 779 (2003).

Koomen, M., R. Howard, R. Hansen, and S. Hansen, The coronal transient of 16 June 1972, Sol. Phys., 34, 447, (1974).

Lepping, R. P. and D. Berdichevski, Interplanetary magnetic clouds: Sources, properties, modeling, and geomagnetic relationship, Recent. Res. Geophys., 3, 77, (2000).

Lindsay, G. M., Russell, C. T., Luhmann, J. G., Coronal mass ejection and stream interaction region characteristics and their potential geomagnetic effectiveness, J. Geophys. Res., 100, 16999, (1995).

Loewe, C. A. and G. W. Prolss, Classification and mean behavior of magnetic storms, J. Geophys. Res., 102, 14209, (1997).

McCracken, K. G., Moraal, H. and Stoker, P. H., Investigation of the multiple-component structure of the 20 January 2005 cosmic ray ground level enhancement J. Geophys. Res. 113, A12101, (2008).

Neugebauer, M. and B. E. Goldstein, Particle and field signatures of coronal mass ejections in the solar wind, in Coronal Mass Ejections, AGU Monograph 99, 245, (1997).

Parker, E. N., The gross dynamics of a hydromagnetic gas cloud, Astrophys. J., S 3, 51, (1957).

Riley, P., C. Schatzman, H. V. Cane, I. G. Richardson, and N. Gopalswamy, On the rates of coronal mass ejections: Remote solar and in situ observations, Astrophys. J., 647, 648, (2006).

Sonnet, C. P., D. S. Colburn, L. Davis, E. J. Smith, and P. J. Coleman, Evidence for a collision-free magneto hydrodynamic shock in interplanetary space, Phys. Rev. Lett., 13, 153, (1964).

Tokumaru, M., M. Kojima, K. Fujiki, M. Yamashita, and B. V. Jackson, The source and propagation of the interplanetary disturbance associated with the full-halo coronal mass ejection on 28 October 2003,J. Geophys. Res., 112, A05106, (2007).

Wang, C., D. Du, and J. D. Richardson, Characteristics of the interplanetary coronal mass ejections in the heliosphere between 0.3 and 5.4 AU, J. Geophys. Res., 110, A10107, (2005).

Xu, D., Chen, T., Zhang, X.X. and Liu, Z., Statistical relationship between solar wind conditions and geomagnetic storms in 1998-2008, J. Atmos. Sol.-Terr. Phy. 57, 1500, (2009).

Yashiro, S., Michalek, G., Akiyama, S., Gopalswamy, N., Howard, R. A., Astrophys. J., 673, 1174, (2008).

Yashiro, S., and Gopalswamy, N., Statistical relationship between solar flares and coronal mass ejections, Universal Heliophysical Processes, Proceedings of the International Astronomical Union, IAU Symposium, Volume 257, p. 233-243, (2009).

Zhang, G. and Burlaga, L. F., Magnetic clouds, geomagnetic disturbances, and cosmic ray decreases, J. Geophys. Res. 93, 2511-2518, (1988).

Zhang, J., I. Richardson, D. F. Webb et al., Solar and interplanetary sources of major geomagnetic storms (Dst≤−100 nT) During 1996–2005, J. Geophys. Res., 112, A10102, (2007).

NIGERIAN JOURNAL OF SPACE RESEARCH **8**: 33-55, 2009 September 1

Energetic Particles in the Heliosphere

Pius N. OKEKE PhD. FAS
NASRDA Centre for Basic Space Science
Nsukka, Nigeria
E-mail: okekepius@yahoo.com
Cell Phone: +234 8036092300

Table of Contents

1. Introduction

Energetic particles include: mildly relativistic particles (with energy E $\geq$ 30 eV) and relativistic particles (with energy E $\geq$ 0.3MeV) .

The word ***Heliosphere*** refers to region 100 – 300 AU, where 1 AU = Earth-Sun mean distance = 10^{11} m. The Content of the Heliosphere includes:
(i) primary and secondary particles of Planetary, Galactic and extragalactic origin.
(ii) magnetic fields
(iii) ions and nuclei.

It is therefore obvious that fundamental '**Particle interactions'** as well as **'Reacceleration'** processes should be continuously taken place in such an environment.

Sources of the Heliospheric energetic particles include: High energy cosmic rays, solar winds, solar flares, Coronal Mass Ejection (CMEs), Particles accelerated by pulsars, accretion discs of massive black holes, and supernovae particles. However, the proportion of particles spewed into the heliosphere by each of these sources is not definite .

2. Physical constants, units, Elementary particles and e-m spectrum

2.1. Physical constants

Astronomical units (AU) = mean Earth-Sun distance = 1.5x10 ^{11}m
Parsec (pc) = 3x10^{16}m = 3.3LY = 6.3x10^{4}AU.

Angstron (A^o) = 10^{-10}m

Speed of light (c) = $3x10^8 ms^{-1}$

Gravitational constant (G) = $6.7x10^{-11}$m $3kg^{-1}s^{-2}$ = $6.7x10^{-16}ergsK^{-1}$

Plank's constant (h) = $6.63x10^{-34}$ J.S = $6.63x10^{-27}$ ergs

Mass of electron (me) = $9.1x10^{-31}$kg

Mass of proton or neutron or hydrogen, $m_p = m_n = m_H = 1.67x10^{-27}$kg

Rest masses of proton and neutron: $m_p = m_n$ = 207MeV

Rest mass of electron, m_e = 0.511 MeV

Ration m_p/m_e = 2000 (1836)

Electronic Charge = $1.6x10^{-19}$C

Ratio $e/m_e = 1.6x10^{-19}/ 9.1x10^{-31}$C/kg

Classical electron radius $r_o = e^2/mc^2 = 2.8x10^{-13}$cm

Thomson cross-section = $6.6x10^{-25}cm^2$; 1 barn = $10^{-25}cm^2$

1 solar mass ($M_{sun} = 1.989x10^{30}$kg): 1 solar radius ($R_{sun} = 6.96x10^8$m)

Luminosity of sun $L_{sun} = 3.9x10^{26}$W.

2.2. Units of Energy

Joule – J, erg, or eV

1J = 10^7 erg and 1 eV = $1.6x10^{-19}$ J = $1.6x10^{-12}$ erg = 1165.9 K = $2.4x10^{14}$ Hz ~ 12396.3 A^0

Energies play important role in high energy astrophysics. It is usually quoted in eV, with usual SI modifications for greater orders.

1 KeV = 10^3eV, 1MeV = 10^6eV, 1 GeV = 10^9eV, 1 TeV = 10^{12} eV

The following conversion factor will be found useful:

Proton rest mass energy (m_pc^2) = 938.3 MeV = 10^9 eV ~ 1 GeV

Electron rest mass energy (m_ec^2) = 0.511 MeV = $5x10^5$eV

Where frequency is in hertz and wavelength, λ is in microns, 10^{-6}m.

Although wavelength λ is usually measured in A^o some people use Microns (μ), micrometers (μm) and nanometers (nm). Recall 1 $A^0 = 0.1nm = 10^{-4}\mu m = 10^{-10}$ m

Very often we are interested in the radiation from hot bodies, then we use the conversion:

$E = KT = 1.38 \times 10^{-23}$ T; $J = 8.617 \times 10^{-5}$TeV

2.3. Flux

Flux is the amount of something, particles, radiation, energy passing through a surface per unit time.

Flux density = $S_v = Wm^{-2}Hz^{-1}$ (J_y)

1 $J_y = 10^{-26}$ $W/m^2/Hz$ or $ergs/cm^2/Hz$

Luminosity on the other hand is the energy per second. It is given in Js^{-1} or $ergs^{-1.}$

2.4. Elementary Particles

Historical Timelines:

1808: the atom was considered to be an elementary particle i.e. the smallest indivisible constituents of matter –

1897: Thomson discovered electron.

1913: Bohr theory of nuclear atom was propounded

1932: Discovery of neutrons *'n'* and Positrons *'e^{+}'*. Shortly after this, the muons, μ, pions, π and many particles were discovered, or predicted.

1950: Enormous amounts of money were invested into the construction of a number of particle accelerators of greater energies in the hopes of discovering particles predicted by theories. Consequently, some fundamental particles were discovered or detected..

2.4.1. Classification

There are four basic interactions found in nature:

i. The strong nuclear interaction (forces between nucleons – hadronic interaction).

ii. The electromagnetic interaction. (mediated by Photons)
iii. The weak (nuclear) interaction – mainly decays.
iv. The gravitational interactions (very important in the universe but negligible in particles physics).

Particles that interact via strong interaction are called Hadrons. There are two kinds of Hadrons: Baryons and mesons. Baryons have spin ½ (or 3/2, 5/2 and so on).
Mesons have spin 0 or integral. Baryons, which include nucleons, are mostly massive elementary particles. Mesons have intermediate mass between the mass of protons and electrons.

The existence of π-meson was discovered by Yukawa in 1947. Particles that decay via strong interaction have very short life times of ~ 10^{-23}s which is about the time it takes light to travel a distance equal to the diameter of a nucleus. Particles that decay via the weak interaction have a much longer lifetime of ~ 10^{-10}s.

It is now believed that all hadrons are composed of more fundamental entities called quarks, which are truly elementary particles. Table 1 lists the properties of some hadrons and their decay modes via strong interaction.

2.4.2. Properties

For every elementary particle there is an anti–particle. Elementary particles are particles that have well defined mass, charge and angular momentum, with their anti – particles included ($\overline{p}$). See Tables 2 and 3 for list of elementary particles and their anti-particles and some physical properties of elementary particles respectively. Strange particles are high energy particles formed by collision of fundamental particles. These particles decay fast.

Table 1. The Properties of Some Hadrons and their Decay Modes

Names	Symbol	Mass MeV/c^2	Spin H	Charge	Anti particles	Mean life Time, sec.
Baryons Nucleon	p n	938.3 939.6	½ ½	+1 0	p- n-	Infinite 930
Lambda	∧o	1116	½	0	∧o	2.5 x 10-10
Sigma	Σ^+	1189	½	+1	∑-	0.8 x 10-10
	Σ^-	1197	½	0	∑+	10-20
	∑0	1193	½	0	∑0	~10-10
Xi	$\cong^0$	1315	½	0	$\cong^0$	3.0x10-10
	$\cong^-$	1321		-1	$\cong^+$	1.7 x 10-10
Omega	Ω-	1672	3/2	-1	Ω^+	1.3x10-10
Mesons	π^+	139.6	0	+1	π^-	2.6x10-8
Pi	π^0	.135	0	0	π^0	0.8x10-16
	π^-	139.6	0	-1	π^+	2.6x10-8
	K^+	497	0	0	K^0	1.24x10-10
Kaon	K^0	497	0	0	K^0	0.8810-10
Eta	η^0	549	0	0		2.0x10-19

Table 2: Elementary Particles and their Anti-particles

Electrons (e)	Anti-particle	Positron e^+
Protons (p)	Anti-particle	Anti-proton ($\overline{p}$)
Neutrons $(n)'$	Anti-particle	Anti-neutron ($(\overline{n})$
Photon (γ)	Anti-particle	γ
Neutrino νe,νμ	Anti-particle	$\overline{\nu}_e, \overline{\nu}_\mu$
Pions $\pi^+\pi^-\pi^0$	Anti-particle	$\pi^-\pi^+\pi^0$
Muon $\mu^+\mu^-$	Anti-particle	$\mu^-\mu^+$

Table 3. Some Physical Properties of Elementary particles

Particles	Symbol	Spin	Rest mass (Mev)	Charge (C)	Mean life (s)
Electron	e-,e^+	½	0.511	4.8 x 10^{-10}	Infinite
Proton	P, $\overline{p}$	½	938.3	+4.8 x 10^{-10}	Infinite
Neutron	$n, \overline{n}$	½	939.6	0	103
Photon	γ	1	0	0	Infinite
Pions	π^+,π^-,π^0	0	139,135(π^0)	-	10-8
Muons	μ^-,μ^+	½	-	105.7	10^{-6}
Neutrino	ν_e, ν_μ	½	0	0	infinite
anti-ν	$\overline{\nu}_e, \overline{\nu}\mu$				

2.4.3. Decay modes of μ and π

$\pi+ \rightarrow \mu\pm + \nu\mu / \overline{\nu}\mu$

$\mu\pm \rightarrow \nu e / \overline{\nu}_e + \nu_\mu / \overline{\nu}_\mu + e^\pm + \gamma\gamma$; or $\mu^\pm \rightarrow e^\pm + \gamma$

$\pi^0 \rightarrow \gamma\gamma$; $\pi^0 \rightarrow \gamma\gamma\gamma$; $\pi^0 \rightarrow \gamma + e^+ + e^-$; $\eta^0 \rightarrow 2e+ +2e-$

Cross section for neutrino (ν_e) production ~ $10^{-44}cm^2$; very small.

Weak interaction involving electron and muon neutrinos (ν_e and ν_μ)

*2.4.4. **The Quark Model***

The quark model assumes that all hadrons are thought to consist of combination of two or three elementary particles called quarks. Table 4 presents approximate masses of fundamental quarks.

Table 4. Fundamental Quarks and their Approximate Masses:

Particle	Light	Medium	Heavy	Charge
Quarks	u(-400MeV/c2)	c(1.59eV/c2)	t(89eV/c2)	+2/3e
	d(~700MeV/c2)	s(-0.15eV/c2)	b(-4.7eV/c2)	-1/3e
Lepton	e(0.511MeV/c2)	μ(106MeV/c2)	τ(1.78GeV/c2)	-1e
	υ_e(≤16eV/c)	υ_μ(≤300keV/c2)	υ_τ(≤40MeV/c2)	0

Table 5. Bosons that mediate in basic interactions

Type	Bosons	Spin	Mass	charge
Strong	Gluon	1	0	0
Weak	$W^{\pm}$; Z0	1	79.8GeV/c2, 91GeV/c2	±1e
EM	γ	1	0	0
Gravitational	graviton$^+$	2	0	0

+not yet observed

2.5. Electromagnetic Spectrum

Table 6 shows the 7 bands of the electromagnetic *'em'* spectrum which however overlap. As shown above the wavelengths range from 0.1 Å to 1 m. The associated frequencies range from 10^{19} Hz to 10^6 Hz.

Table 6. Electromagnetic Spectrum

Component	γ –Ray	X-ray	UV	Visible	Infrared	mm Band	Radio
Wavelength	0.1Å	10Å	1000Å	1 μ	100μ	1000μ (mm)	1cm -1m
Frequency	~10^{19}Hz	10^{16}	10^{15}	10^{14}	10^{12}	10^{10}	10^{6}Hz

Table 6 shows the 7 bands of the electromagnetic *'em'* spectrum which however overlap. As shown above the wavelengths range from 0.1 Å to 1 m. The associated frequencies range from 10^{19} Hz to 10^{6} Hz.

1 micron, 1 μ = 10^{-6}m; 1Å = 10^{-10}m; 1nm = 10Å, 10^{3}Hz = 1MHz, 10^{6}Hz = 1GHz

Deduction from above:

γ – ray has the shortest wavelength ≤ 1 Å

X – ray lies between 1 Å and 100 Å

UV lies between 100 Å and 1000 Å

Violet ~400 Å or 400nm; orange ~600 Å; red light ~ 6500 Å; Human eye is sensitive to 4000 Å - 6600 Å

Infrared Astronomy lies between 6600 Å - 100 μ

mm Astronomy lies from 10mm – 0.1mm, i.e. 1000 μ - 100μ

Radio Astronomy lies 100 – 1cm

3.0. High Energy Processes in Astrophysical Sites.

This chapter considers high energy processes involving either particles or photons.

3.1 Creation of electron positron pairs

Creation of electron-position pairs (e^{-} + e^{+}) by γ ray absorption occurs in the presence of a Nucleus:

$$\gamma + Ze \rightarrow e- + e+ Ze \quad \text{----------3.1}$$

It can be shown that the cross-section for the pair production reaction is:

$$\sigma_{pair} \propto Z^2 r_o^2 \quad \text{----------3.2}$$

Where the classical radius of electron:

$$r_o = e^2/(mc^2) \sim 2.818 \times 10^{-13} cm \quad \text{----------3.3}$$

Creation of μ -meson pair by γ -rays in the presence of a Nucleus

$$\gamma + Ze \rightarrow \mu^+ + \mu^- + Z_e -- \quad \text{----------3.5}$$

This is similar to the process above. The cross – section will be given by the corresponding value for e^+e^- with m_μ replacing m_e.

3.2 Creation of Electron-Positron Pairs by Two-Photon Collision

$$\gamma + \gamma \rightarrow e^- + e^+ \quad \text{----------3.6}$$

An electron – positron pair may be produced in the collision of a photon of energy E1 with a photon of energy E_2, provided that $(E_1.E_2) > (mc^2)^2$; where $mc^2 = 0.511$ MeV is the rest mass energy electron.

The cross section σ is of the same order as the Thomson cross – section, σ_T. This reaction is important in high energy gamma-ray astrophysics. It is known that the absorption process $\gamma + \gamma \rightarrow e^- + e^+$ as it may be called takes place in the interstellar space by optical photons at very high energies E > 1018 eV where absorption of very high energy γ-ray by radio photons seriously occurs.

3.3 Pair annihilation or creation of photons by e+e- annihilation

$$e^+ + e^- \rightarrow \gamma + \gamma \quad \text{----------3.8}$$

A positron may collide with an electron e- to produce two gamma ray photons according to the reaction: $e^+ + e^- \rightarrow \gamma + \gamma$

This is an electromagnetic process. If the energy of the positron is given by γmc^2 where γ is Lorenz factor, the cross-section for the two photon annihilation with free electron at rest is given by

It is discovered recently that this occurs at the galactic centre as 0.5MeV γ ray line observations.

3.4 Creation of Recoil (knock – on) Electrons by charged particles.

$$e + p \text{ (Electron energy = Eo)} \rightarrow e + p \text{ (Electron energy=Wr> Eo)} \quad \text{---------3.12}$$

3.5 Collisional Bremstralung:

High Energy Photon Emission by the Bremstralung of a relativistic electron or muon

$$e + Ze \rightarrow Ze + \gamma \text{----------3.15}$$

3.6 Photon emission by synchrotron process (magnetic Bremstrahlung)

Other process of particle emission which is similar to collisional bremstrahlung is magnetic bremstrahlung in which an electron emits a photon radiation when it sees a magnetic field. In other words, when a relativistic electron of energy E is moving through a region of uniform magnetic field H, it emits high photons by synchrotron radiation.

3.7. Emission of High Energy Photon by the Inverse Compton Effect

e	+	γ	$\rightarrow$	e	+	γ	
$\downarrow$		$\downarrow$		$\downarrow$		$\downarrow$	
High energy electron,E		$h\upsilon$	Low energy	E_1	reduced energy	$h\upsilon_1$	higher energy photon ----------3.17

This is a process in which a free electron with energy , E= γmc^2 collides with a photon of energy hυ, to produce a new photon whose energy is enhanced $h\upsilon_1$.

The enhanced frequency υ_1 is given by:

$$\upsilon_1 = \gamma^2 \upsilon \text{ or } h\upsilon_1 = h\gamma^2 \upsilon \qquad \text{----------3.18}$$

3.8 High Energy electron loss Mechanisms

Ionization Losses

When ultra-relativistic electrons of free electron density Ne and energy γ, are incident upon matter, ionization occurs. The ionization rate is:

$$\frac{dE}{dx} = 2.54x10^{-19} N_e (\ln\gamma - \ln Ne + 73.4)\ eVcm^{-1} \qquad \text{----------3.20}$$

Loss by Bremstrahlung

When a relativistic electron of energy E, collides with a target nuclei of charge eZ and number density N (for special case of hydrogen atom Z =1)

$$-\frac{dE}{dx} = 2.6\ x10^{-26} N_e\ eVcm^{-1} \qquad \text{for } E \geq mc^2/\alpha \qquad \text{-----3.21}$$

Inverse Compton Loss

When a relativistic electron of energy $E = mc^2\gamma$ collide with photon of energy hυ, it produces a photon of energy $E\gamma = \gamma^2 h\upsilon$ and loses energy according to:

$$-\frac{dE}{dx} = \sigma TU^2 \qquad \text{(where } \sigma T = 6.65 \text{ x } 10^{-25} \text{ cm}^2\text{)} \qquad \text{--------3.22}$$

$U = h\upsilon N(h\upsilon)$.

Synchrotron Loss

When a relativistic electron of energy $E = \gamma mc^2$ moves with velocity v in a magnetic field of strength H, it looses energy according to:

$$-dE = 6.6 \text{ x } 10^{14} E^2H^2 \text{ erg cm}^{-1} \qquad \text{----------3.23}$$

where $\beta = v/c$, E is in ergs and H in Gauss. (For conversion 1 eV = 1.6021 x 10^{12} ergs).

Nuclear Interactions

The important reactions for the production of π-mesons are:

$$P + P \rightarrow P + P + n_1 (\pi^+ + \pi^-) + P2\pi^0$$
$$P + P \rightarrow P + n^+ \pi^+ + n3 (\pi^+ + \pi^-) + n4\pi^0$$
$$P + P \rightarrow n + n + 2\pi^+ + n5 (\pi^+ + \pi\text{-}) + n6\pi^0$$
$$P + P \rightarrow D + \pi^+ + n7 (\pi^+ + \pi^-) + n8\pi^0 \qquad \text{----------3.24}$$

Where P = protons, n = neutrons, D = deuterium, $n_1 - n_8$ are positive integers. Once π-mesons are produced, μ-mesons, electrons, positrons and neutrinos may also be produced through the decay reactions:

$$\pi^{\pm} \rightarrow \mu^{\pm} + \upsilon\mu/\overline{\nu}\,\mu\text{-}$$
$$\pi^0 \rightarrow \gamma\gamma$$
$$\mu^{\pm} \rightarrow e^{\pm} + \upsilon e/\overline{\nu}\, e + \upsilon\mu/\overline{\nu}\,\mu \qquad \text{----------3.25}$$

4.0. Cosmic Rays in the Heliosphere

Cosmic Rays can be defined as all particles (mostly protons) that arrives the surface of the earth from outer space. There are two categories of cosmic rays (CR): *Primary* and *secondary* cosmic rays.

4.1. Primary and Secondary CR

Primary CR are rays (or particles mainly proton) that arrive at the top of the atmosphere from outer space without interaction with the atmosphere. These are expected to very energetic protons of low flux density.

Secondary CR are rays produced as a result of interaction of primary cosmic rays with the nuclei of atmospheric gas molecules. In these high energy collisions mainly secondary particles are produced including high energy pions. A high energy charged pion decays into high energy muon.

$$\Pi^{\pm} \rightarrow \mu^{\pm} + e^{\pm} + \nu_{\bar{u}} \qquad \text{----------4.1}$$

4.2 Low, high and very highest energy cosmic rays

Low energy cosmic rays are made up of low energy protons and electrons. Most of them are produce by the sun as we know the solar wind consist mainly of low energy protons and electrons ejected from the solar corona and from solar flares. Only a small fraction are energetic particles. The rest have very low energy.

High energy cosmic rays constitute mainly protons that come from interstellar space and sometimes Galaxy. Some are also thought of coming from beyond our galaxy. These solar winds are continuous stream of plasma - protons and electrons. Their influence is felt in the region of space which we are currently discussing – the heliosphere, which extends far beyond the orbit of Pluto. Because the solar wind is plasma, it is electrically conducting and transmits a part of the sun's magnetic field. When CR approaches the sun, they encounter the Helioshere and the magnetic field within it. Because of the shape of the magnetic field, the CRs loose some of their energy, and the lower energy ones never reach the vicinity of the earth.

The cosmic rays we are interested in here are those with much higher energy than those from the sun. They typically have energies of several billion eV (GeV) – trillion eV, (TeV) $>10^{12}$ eV. They are mainly protons and come from outer space outside our galaxy. It is not precisely known where these come from and how these protons get their high energy. One probability is that they are accelerated in very high and extensive magnetic fields surrounding for example the remnants of supernova explosions.

The very highest energy cosmic rays are of particular interest for various reasons. They may provide a useful tool for finding the origin of cosmic rays because they are deflected very little by the galactic and interstellar magnetic fields that permeate space. Therefore the direction in which they are traveling when they arrive at Earth should point back to the area of space where they came from. There are many unanswered questions regarding their production:-

How are they produced?

Mechanisms to accelerate particles up to energies of 10^{15} eV have been proposed and generally consist of binary star systems (two stars in orbit around each other) or supernova remnants (the turbulent shell of gas left behind after a star has exploded). However the acceleration mechanisms involved in producing the highest energy cosmic rays are still unknown. There may even be new physics involved. One possibility is that they are generated by very massive particles produced at the beginning of time.

Where are they produced?

The places in the universe where cosmic rays of $>10^{18}$ eV are produced must either have very large magnetic fields or be of enormous size. Could it be from within our galaxy then the production sites would be expected to be relatively close to Earth because the galaxy cannot trap such energetic particles within its magnetic field (unlike lower energy cosmic rays)

5. Solar Wind in the Heliosphere

Solar wind is a stream of low energy (mildly relativistic) charged particles, protons, electrons and heavy ions ejected from the sun into space. The sun can spew clouds of charged particles into its surroundings both from the study of geomagnetic storms and cosmic rays (Okeke et al. 2004).

It was found that ions in the comet's plasma tails are always systematically accelerated in anti-solar direction and the plasma tails are always present in all heliographic latitudes. It was

shown that this outflow of particles from the sun is almost at uniform rate much like wind. Estimates show that the flow is super-sonic speed, that is, speed greater than that of sound waves. The ionic composition of solar wind plasma is about 95% and 5% helium nuclei (α particle). The solar wind plasma has very high temperature and is therefore very conductive. It carries with it magnetic field which is ultimately the source of the interplanetary magnetic field. At 1 AU, the interplanetary magnetic field ranges from 1 to 10^{-4}Gauss.

5.1 Distribution of Solar Wind

Solar wind and energetic particles represent major and minor population of particle distribution function $f_{i,e}$ (r,v,t) for ions and electrons in the heliosphere. There is no strict and well defined boundaries between both populations in the phase space (r,v). These particles are intermixed every time and everywhere in the heliosphere in the way that the solar wind can be associated with the main body of the ion distribution functions.

It is peaked around several hundred volts or Kev domains for typical and perturbed solar wind bulk velocities which are nearly the same for different kinds of ions. (Vesclovsky, 2006). The distribution function of electrons in the solar wind has approximately Maxwellian cores with energies of the order of ten eV.

Local Maxwellian distribution functions are often used as approximations allowing the calculations of first lower moments: density η, bulk velocity v, temperature T and heat flux q for each kind of particle in the solar wind (ions and electrons). As stated earlier, the main ion component of the solar wind are protons and α-particle more than 90% with proton more abundant in the solar wind everywhere and every time. Solar wind density varies roughly as the square of the heliocentric distance because of the super-magnetosonic radial plasma expansion.

The bulk velocity of electrons in the solar wind is poorly known because of difficulties with the measurements. The main part of energy, mass and momentum transferred by the solar wind is

attributed to proton radial motion away from the sun. Transportation by heat is of secondary importance. Demarcation between particle populations in the phase space is not physically meaningful. Solar energetic particles and heliospheric particles are difficult to distinguish or to be considered as separate population in any real situation where acceleration and propagation process accompany each other in the phase space and time.

Nevertheless, one can indicate clear acceleration and heating sites in solar flares, CN ejection and propagating shocks in the heliosphere. In the opinion of the author, there is no universal geometry or parameter of accelerators on the sun and heliosphere. At the same time magnetic field in the heliosphere plays an important role in the plasma and particle dynamics. The free magnetic energy of the heliospheric electric current is the key factor of the non-local electromagnetic solar terrestrial connection producing geomagnetic storms.

5.2 Some Astrophysical and Geophysical effects of the Solar Wind

Solar wind plays an important role in the heliosphere. It forms an outer plasma environment of the sun, the corona and the heliosphere. The free energy of the solar wind feeds dynamical plasma processes in a broad range of space-time scales from smallest kinetic structures up to largest bulk inhomogeneities and variations of many orders of magnitude. It drives the electric current and the magnetic fields here.

The solar wind plays an important role in shaping the outer solar corona seen as bright coronal streams and rays. The solar wind and heliospheric magnetic fields control the formation and dynamics of planetary magnetospheres and comet tails. The variability of the solar wind is one of the factors regulating the space weather conditions, geomagnetic perturbations and magnetic storms.

5.3 Energetic Particles: Terrestrial Impacts

Solar energetic particles penetrate the magnetosphere and influence on the upper atmosphere and the ionosphere in many ways. Energetic solar protons produce ionization in the D-region and corresponding black-outs in the short-wave radio communication. The same protons play their role in the chemistry of the upper atmosphere. They destroy ozone molecules, influence nitric oxide balance. Radiation damages of materials in space by solar energetic protons and ions are essential especially for semiconductors and dielectrics (solar panels, microelectronics, optical glasses). They can be a risk factor during man's flight in space and even for aircraft crew and passengers crossing polar region of the earth during storms in space weather. Relativistic electrons accelerated inside the geomagnetic storm appear sometime at the geostationary orbit with severe consequences for communication satellites.

6. Solar Flares and Coronal Mass Ejection

6.1 Solar Flares

Solar flares are complex energetic events, seen normally as sudden brightening near the solar surface, a legacy linked to solar magnetic activities. Flares occur within the magnetically active regions near sunspots. Solar flare is a violent explosive outburst of energy that sends particles and radiation into the interplanetary space. The energetic particles include protons and electrons with energies in kilo-electron-volts. The radiation produced in flares emits over the full electromagnetic spectrum from gamma-rays, X-rays and the long radio waves. The Japanese satellite Yohkoh launched into space in August 1991, for example, is partly devoted to studying solar flares.

Flare events last for a few minutes to hours, but the effect can be felt for days in the interplanetary space. The ejected particles may reach the Earth within a day or more and sometimes interact with the Earth's magnetic field. Flares can disrupt radio waves transmission, trigger auroras, and on occasions they can cause surges in high voltage transmission lines. Thus, the study of solar flare is both practically useful as well as intellectually challenging.

Although flares are believed to be associated with sudden release of magnetically stored energy but the way of conversion into particles energy is still an open question.

6.2 Coronal Mass Ejection

Coronal Mass Ejection or CME is a sudden expulsion of solar coronal material into space. The total mass and kinetic energy ejected by CME has been estimated to be 2 x 10^{14} to 2 x 10^{16}g and 2 x 10^{29} to 5 x 10^{31} ergs, respectively. Some CME events are associated with flares and those events may have speed of ejecta up to 1000kms-1 with energetic particles spewed into the Heliosphere. One example of a CME event is observed with the Solar and Heliospheric Observatory (SOHO), a satellite launched around 1996.

7. Supernovae, Neutron Stars and Pulsars

Supernovae could be a Source of heliospheric electrons. The radio properties of supernova remnants provide convincing evidence that they are sources of cosmic ray/heliospheric electrons. The energy liberated in the collapse of the central regions of the star is deposited in the outer layers which are heated to high temperature and ejected with a velocity of about 10^4 – 2 x 10^4 kms^{-1}. As the remnant continues to expand, the temperature in the region behind the shock front drops below 10^6K, the expansion eventually becomes subsonic (≤ 20kms-1) and the remnant loses its identity.

A pulsar is probably a neutron star whose magnetic field lines accelerate electrons along the magnetic axis, causing emission of a beam of radio waves rotating with the star and producing a pulse when the bean intercepts the line of sight of an observer. Since 1968, numerous other pulsars have been discovered and some of them have been found to emit not only in the radio wavelength but also at higher frequencies up to X-rays and γ-rays. All frequencies are modulated in the same way by the rotation of the star.

About 700 radio pulsars are known to-date. They are mostly situated in the galactic plane; with concentration within a few kilo-parsecs of the Sun. Obviously the most promising place to look for pulsars is in supernovae remnants (SNR). Current theories suggest that radiation emitted by pulsars is as a result of charged particles emitted by neutron stars that are accelerated along star's magnetic field lines as a consequence of rapid rotation. The Crab pulsar is also an optical variable and emits energy at an incredible rate; 3 x 1038 erg s-1 (1031W). Its period is equally incredible; only 0.33 s, one of the shortest periods known. Also, as it emits energy into space, the neutron star slowly cools and tries to approach thermal equilibrium with the universe like what the white dwarf does.

8. Black Holes and Accretion Discs

Double star systems in which one very compact component, which optically invisible, emits a considerable flux of X-rays. The detection of these binaries, made possible through satellites like the first X-ray satellite UHURU, and HEAO-1 and -2, is one of the major discoveries in recent years. On a much larger scale, the superactive galaxies such as seyferts, quasars and BL Lacertae objects (or BL Lac objects, or an elliptical galaxy with very bright nucleus) emit far greater amount of energy than a normal galaxy, at all wavelengths from the radio region through X-rays and gamma-rays. The important point is that all of those violent phenomena appear to be associated with the presence of very compact massive bodies; neutron stars or stellar black holes in the case of X-ray binaries, giant or supermassive black holes for active galactic nuclei (also referred to by astronomers as AGN).

A black hole is thus the most efficient device for converting the mass-energy of a body into electro-magnetic radiation. In the case of X-ray binary sources, the compact star swallows the atmosphere of its companion and falling gas produces the observed X-rays. However, the compact star could be either neutron star or black hole.

Another class of observed ultra-energetic phenomenon is that of the gamma-ray burst like that studied by the BeppoSax and the Compton Gamma-Ray Observatory satellites. The gamma-ray bursts are the supremely energetic events of our heaven, often sending photons of energies between 5 keV to GeV (more typical range is 100 KeV to 2MeV) in bursts between 100 milliseconds and 100 seconds to the Earth's detectors. Research on the origin of gamma-ray bursts is a rapidly expanding field. Gamma-ray bursts seem to be associated with the already known astronomical objects and phenomena like supernova, neutron star, and black hole nuclei of galaxies. Well, if so, where is the supermassive black hole?

9. Particle Acceleration from Solar System/Heliosphere

Several IAU symposia have been dedicated to the discussion of particle acceleration; for examples: IAU coloquim 142, 1993 and that of General Assembly IAU XXVI, 2006.

It is shown that all the high energy advances have been further enhanced by coordinated multi-wavelength observations especially in the radio. These have expanded our knowledge of particle acceleration in all cosmic scales including: Planetary and interplanetary particles, solar flare particles, stellar fast particles in colliding hot star winds, pulsar shell type supernovae, extragalactic jets, AGN, ultra-high energy cosmic rays.

Despite all the efforts put in both theoretical and observational investigation, particle acceleration process remains one of the greatest unsolved problems in Astrophysics. Melrose D.B 2006, discussed acceleration problems and progress. Robert P. Lin, 2006 discussed the solar system as a laboratory for the study of physics of particle acceleration. He stated that a remarkable variety of particle acceleration occurs in the solar system.

Electrons are accelerated to tens of MeV energy in planetary atmosphere and acceleration of auroral and radiation belt particles in planetary atmospheres. Shocks are driven by fast coronal

mass ejections and possibly at the heliosphere. Acceleration also takes place in the reconnection regions in solar flares and at the planetary magnetospause and magnetotail current sheets. These accelerations occur in conjunction with efficient energy release. Unlike the acceleration process outside the solar system, the accelerated particles and physical conditions can be studied through direct in situ measurements or through imaging spectroscopy.

Stephen W. Kahler 2006, discussed evidences for solar shock production of heliospheric near-relativistic and relativistic electron events. He reviewed properties of near-relativistic ($E \geq$ 30KeV) and relativistic $E \geq 0.3$MeV) electron events produced near the sun observed within 1 AU. He highlighted the recent very high energy γ-ray observation (VHE) which is the current and most direct probe of particle acceleration in the Galaxy up to energies of several hundreds of TeV.

10. Heliosphere and Space Weather

Space Weather in the heliosphere (solar wind, magnetosphere, ionosphere and thermosphere) can influence the performance and reliability of space-borne and ground-based technological systems and can endanger human life and health. This is as a result of violent transfer of Energy via energetic particles from sun to the earth.

Within our own solar system, space weather is greatly influenced by solar wind plasma. A variety of phenomena associated with Space Weather including geomagnetic storms and sub-storms, ionospheric disturbances, scintillation and magnetic induced current at earth's surface.
Solar energetic particles accelerated by coronal mass ejection or solar flare are important drivers of Space Weather as they can damage electronics on board spacecrafts and threaten the life of astronauts. An understanding of space environment is important in designing and shielding life support systems for manned spacecraft.

References

Longair. M, High Energy Astrophysics, Cambridge University Press, 1995

Melrose D.B, IAU General Assembly XXVI , 2006

Melrose D.B, IAU Coloquim 142, 2006.

Okeke. P.N, and W. Soon, Introduction to Astronomy: SAM- PRESS, 2003

Okeke. P.N, Lecture Notes in High Energy Astrophysics, 2002, Edited by A.O.Animalu

Robert P.Lin, IAU General Assembly, 2006.

Stephen W. Kahler, IAU General Assembly, 2006

Vesclovsky.S.I, Proceedings of IAU Symp. N0.23, 2006

NIGERIAN JOURNAL OF SPACE RESEARCH **8**: 56 – 86, 2009 September 1

Planetary Magnetospheres

A Babatunde RABIU PhD
Center for Space Research and Applications, Department of Physics,
Federal University of Technology, Akure, Nigeria.
Email: abrabiu@futa.edu.ng; tunderabiu@yahoo.com

Table of Contents

1.0. Introduction

Magnetosphere refers to the region of the upper atmosphere of an astronomical object which is dominated by its magnetic field. Different planets experience different degree of magnetic dominance. Six planets have significant internal magnetic fields and hence, substantial and active magnetospheres: Mercury, Earth, Jupiter, Saturn, Uranus, and Neptune (Bagenal, 1995). Mars is known to have patchy surface magnetization, while pulsars and some other celestial objects also have magnetosphere. The Earth's magnetosphere was discovered in 1958 by Explorer 1 during the International Geophysical Year. In 1959 Thomas Gold proposed the name magnetosphere and defined it as the region above the ionosphere in which the magnetic field of the earth has a dominant control over the motions of gas and fast charged particles is known to extend out to a distance of the order of 10 earth radii.

The magnetized plasmas of the solar corona, the solar wind, and the outer environments of the planets are all collisionless and highly electrically conducting. An electric field E = V x B is associated with a conductor moving through a magnetic field or with a moving magnetized conductor. Throughout most of the volume of the plasma in the solar system the electrical conductivity of the plasma is so high that this expression constitutes the Ohm's law of the plasma and as a consequence there are no significant electric fields parallel to the magnetic field in these regions. In such a situation it can be shown that the plasma and magnetic field threading it, a magnetic flux tube, move as a unit. The cross section of the tube, the density, and the velocity of the plasma may change but the same plasma elements remain connected by the same field lines at all times. Thus, one can approximate the interactions of such plasmas, by assuming they can press against one another but they will not interpenetrate. This principle greatly simplifies an exceedingly complex situation to a merely complex one.

Throughout most of the volume of the solar system plasma this guiding principle, called the frozen-in flux theorem, is obeyed and like plasmas are confined to elongated magnetic cells or flux tubes, along which they can communicate but across which they cannot, except to

equilibrate transverse pressure. However, in small but highly important regions where the frozen-in flux theorem is violated, parallel electric fields arise and magnetic field lines can slip from one plasma region to another. This slippage can occur due to collisions, as happens in planetary ionospheres, and due to resistive instabilities, as those that lead to the process known as reconnection, which process occurs in an otherwise collisionless medium.

Guided by the frozen-in flux theorem we can develop a zero-order guide to the solar wind interaction with the planets. The solar wind plasma expands supersonically from the solar corona, well past the planet Pluto, until it achieves a low enough pressure that it can he stopped by the plasma of the local interstellar medium or very local interstellar medium as the astronomers refer to it. There is no static solution for the plasma of the solar corona because any static solution has a pressure at infinity that dominates over the pressure of the local interstellar medium. The velocity relative to the planets, attained by the solar wind as it accelerates away from the Sun, surpasses that of the compressional waves in the plasma. Hence the solar wind flows supersonically with respect to the planets and any interaction with the planets will be accompanied by a shock wave standing in the flow. The obstacle which deflects the flow and results in the shock wave is the planetary ionosphere in the case of Venus and Mars. At highest ionospheric altitudes the ionospheres are collisionless although, when the momentum flux of the solar wind is large, the altitude to which the solar wind reaches decreases, collisions become important, and the physics of the interaction changes. At Earth, Mercury and the Jovian planets, the magnetized solar wind is deflected by the planetary magnetic field generated in the interior magnetic dynamo. While the interactions at each of the planets have certain similarities they also have critical differences in part because the evolution of the properties of the solar wind with distance from the Sun.

2.0. Earth's Magnetosphere

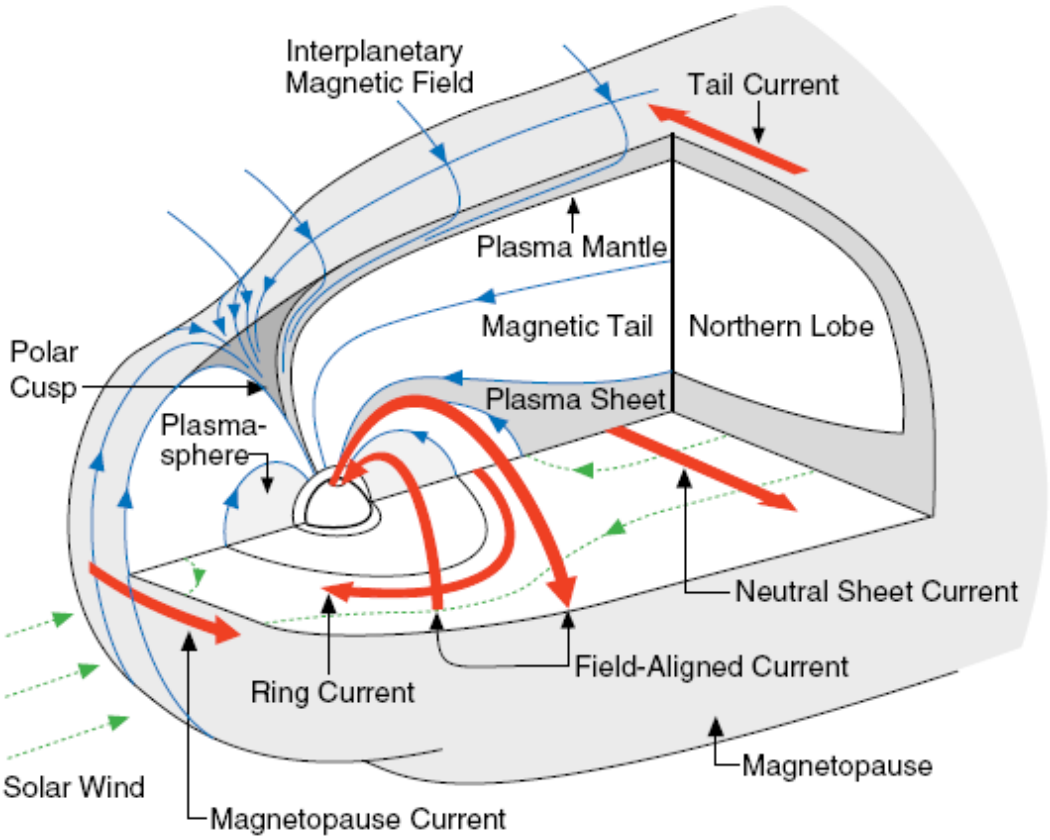

Figure 1. A cut away drawing of the Earth's magnetosphere (showing various different plasma regimes).

The magnetosphere of the Earth is of course the most widely studied magnetosphere. Because the properties of this magnetosphere generally lie in the middle of the range of properties found in the solar system we can regard the terrestrial magnetosphere as typical. Figure 1 shows a cut away drawing of the magnetosphere. The outer boundary of the magnetosphere is called the magnetopause, upon which flows the magnetopause current, a large current vortex which separates the magnetic field of the Earth and the solar wind. Behind the Earth are the two lobes of the magnetic tail, the top one pointing to the Earth and the bottom one pointing away. These magnetic field lines enter and leave the Earth in oval shaped regions known as the polar cusps. These polar cusps vary in size as solar wind conditions vary. This variation plays a very

important role in energy transfer into the magnetosphere and will be discussed in greater detail below. Between the two tail lobes flows the neutral sheet current which is simply part of the magnetopause current vortex and also the plasma sheet a hotter and denser plasma than in the surrounding regions. The production of this plasma sheet is one of the areas of most intense study at the present time.

Deeper in the magnetosphere is the plasmasphere, a region of dense cold plasma which is the upper extension of the ionosphere. The plasmasphere extends out to about 5 Earth radii. Within this distance magnetic flux tubes fill up with cold plasma from the ionosphere below. Outside this distance the filling time is long compared to the transport and loss time so the magnetic flux tubes do not fill up with cold plasma.

The closed, dipolar field lines in the magnetosphere provide efficient magnetic mirrors in which to trap energetic particles. Close to the Earth these radiation belts are very stable and can remain constant for hundreds of years but in the outer regions the belts are subject to frequent disturbances and change from day-to-day. Particles from the outer regions can cross the field lines by diffusion and convection. Diffusion is a slow process which relies on fluctuations of the magnetic and electric fields. Convection refers to the drifts induced by the large scale electric field in the magnetosphere. It is important only for low energy particles and only in the outer parts of the magnetosphere.

If one pushes or pulls on the outer parts of the magnetosphere, one would expect the stresses created by that action to affect the plasma in the Earth's ionosphere for the ionosphere is where the magnetosphere is coupled to the Earth. The magnetosphere communicates this stress through field-aligned currents. Figure 1 shows the paths of some of these currents.

3.0. General Structure of the Magnetosphere

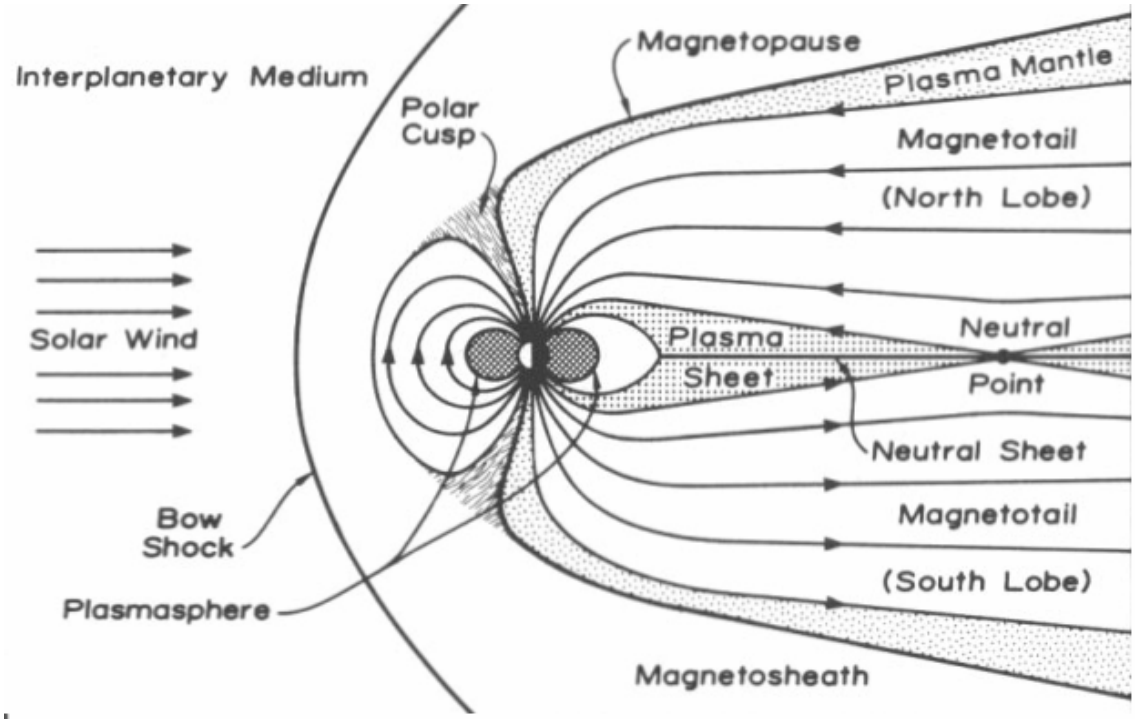

Figure 2. Noon-midnight slice of the interaction of the solar wind with the Earth's intrinsic magnetosphere, the solar wind flows from the left, crossing the Earth's bow shock where it is slowed, heated, and deflected about the magnetospheric cavity. This post-shock region is called the polar cusp. Behind the Earth are the two lobes of the magnetotail, one with field directed toward the Earth and one away from the Earth. The centre of the tail contains a sheet of plasma that carries the current that reverses the field in the two lobes of tail. The lines with arrows in the magnetosphere represent the magnetic field connected to the Earth.

The magnetosphere is a large plasma cavity generated by the Earth's magnetic field and the solar wind plasma. The streaming solar wind, as illustrated in Fig. 2, compresses the dayside portion of the Earth's field and generates a tail which is many hundreds of Earth radii long. The basic mechanism for the formation of the magnetosphere is extremely simple; it is a magnetic dipole exposed to a stream of charged particles. The entire magnetosphere is subject to only two boundary conditions, explicitly the boundary between the magnetosphere on the streaming

solar wind and the boundary of the plasma in the ionosphere. The basic elements of the magnetosphere are

3.1. The Bow Shock and the Magnetosheath

While not part of the magnetosphere proper the magnetosheath is an outer layer embedding the magnetosphere. The solar wind plasma travels usually at super-fast speeds relative to the magnetosphere. Therefore a standing shock wave forms around the magnetosphere just as in front of an aircraft traveling at supersonic speeds. The bow shock is the shock in front of the magnetosphere and the magnetosheath is the shocked solar wind plasma. Therefore it is not directly the solar wind plasma which constitutes the boundary of the magnetosphere but the strongly heated and compressed plasma behind the bow shock. The region is rich in various wave phenomena, boundaries and shocks are often treated as discontinuities.

3.2. The Magnetopause

The magnetopause is the actual boundary between the shocked solar wind and the magnetospheric plasma. However, the magnetosphere is not closed in terms of the magnetic field but there is considerable magnetic flux crossing the magnetopause. Thus it is not easy to define this boundary precisely. Also the boundary does permit a certain amount of solar wind plasma entry. This entry is easier along magnetic field lines. The magnetopause is an highly important region because the physical processes at this boundary control the entry of plasma, momentum, energy and the redistribution of geomagnetic flux. Essential instabilities are reconnection (tearing modes) and Kelvin Helmholtz modes in addition to various micro-instabilities.

3.3. Cusp and Mantle

The cusp and mantle regions are directly adjacent and inward of the magnetopause. The cusp is the region where dipolar field lines converge and in a two-dimensional case represents a field line which goes into a singularity with $B = 0$. The mantle region represents a boundary to the

magnetotail usually filled with solar wind plasma but with a stretched magnetospheric magnetic field. The role of the cusps is not fully understood but it is a region where highly energetic particle can be produced and it is very active in terms of turbulence and wave energy because the boundary field lines converge in the cusp and all waves which travel along the magnetic field are channeled into this region.

3.4. The Quiet Magnetotail

The magnetotail is the long tail-like extension of the magnetosphere on anti-sunward side of the magnetosphere. since the magnetic field points toward the Earth in the northern lobe and away in the southern lobe there is a current in the westward direction. Because of its structure there is considerable energy stored in the magnetic field in the magnetotail. During magnetically quiet times convection is typically low and energy in the plasma flow is only a tiny fraction of the overall energy density.

3.5. The inner Magnetosphere

The inner magnetosphere is different from most of the magnetosphere in that the magnetic field is mostly dipolar and perturbations of the field are small compared to the average dipole field. However, there can still be large amounts of energy stored in this region in particular during so-called storm times. During such times the ring current (current due to gradient curvature drifts of charged particles) intensifies strongly and is responsible for strong magnetic perturbations at low geomagnetic latitudes on the Earth.

3.6. Magnetosphere - Ionosphere Coupling

The ionosphere is the region where the atmosphere is partially ionized and plasma and neutrals strongly interact. This interaction exerts a drag on the plasma. The plasma density can be very high but also strongly variable such that the ionospheric conductance can vary by orders of magnitude. Magnetospheric plasma motion is transmitted into the ionosphere and forces ionospheric convection. This also implies the existence of strong currents along magnetic field

lines which close through the ionosphere. In particular at high latitudes these currents lead to magnetic perturbations during times of strong magnetospheric activity (fast convection and changes of the magnetospheric configuration).

4.0. Intrinsic and induced magnetospheres

All planets and comets explored to date have magnetospheres. The existence of these magnetospheres is independent of whether the planet has an internally generated or intrinsic magnetic field, but the nature of these magnetospheres is quite dependent on this fact. For the planets that have no internal magnetic dynamo the solar wind induces a magnetosphere through its interaction with the upper atmosphere and ionosphere. These two types of magnetospheres are referred to as intrinsic and induced magnetospheres according to the source of their magnetic fields and fully discussed by Russell (1991) as follows:

4.1. Induced Magnetospheres

The sun emits a constant stream of electrons and protons in all directions at speeds well above the speed of "sound". This supersonic ionized gas, or plasma, called the solar wind carries with it a magnetic field and a frame dependent electric field. The frame-dependence arises due to the high electrical conductivity of the plasma and its magnetic field. In the frame moving with the plasma the electric field under most circumstances is zero. There is no electric field parallel or perpendicular to the magnetic field. In a frame not moving with the plasma there is an electric field perpendicular to the magnetic field and to the velocity vector proportional to both the magnetic field and the component of velocity perpendicular to the magnetic field. This electric field is very important for the removal of a planetary atmosphere from an unmagnetized planet.

Solar extreme ultraviolet radiation ionizes the upper atmospheres of all planets to varying degrees. If the thermal pressure of this ionosphere exceeds the solar wind momentum flux or dynamic pressure, a quantity proportional to the density times the square of the velocity, then the ionosphere can stand off the solar wind and it remains unmagnetized. A magnetic lid or cap

forms on the ionosphere called the magnetic barrier and this barrier in turn deflects the solar wind. The solar wind as mentioned above is supersonic and thus this deflection must involve the formation of a detached bow shock. This bow shock, which interestingly forms without the aid of collisions in the gas, slows, heats and deflects the solar wind. Figure 3 shows a cross section of this interaction.

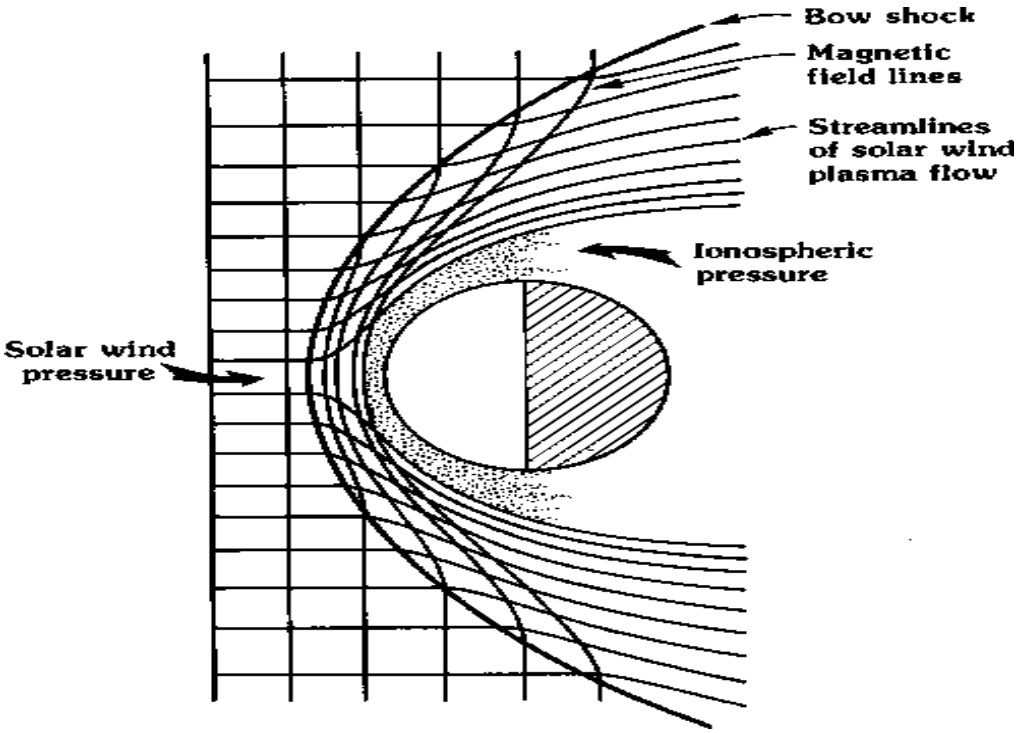

Figure 3. Schematic of the solar wind interaction with an unmagnetized planet. Horizontal lines which curve around the planet represent streamlines of the solar wind flow. Flow proceeds from left to right. Vertical lines represent the interplanetary magnetic field which is carried to the planet by the solar wind and draped over it. (Russel 1993)

The behavior of the ionosphere in such an interaction is quite unexpected. Although the thermal pressure of the ionosphere may be strong enough to hold off the solar wind, still small magnetic filaments or magnetic flux ropes sink from the magnetic barrier into the ionosphere, providing an opportunity to study, in- situ, a phenomenon otherwise seen only remotely on the solar surface. When the solar wind dynamic pressure is high and exceeds that of the thermal

ionosphere magnetic field and plasma is pushed downward into the ionosphere and it acquires a steady global magnetic field.

The induced magnetosphere has one more very important feature. The solar wind moves past the planet at supersonic speed carrying its magnetic field with it. Near the planet the flow is slowed. The magnetic field that connects the fast and slow regions must perforce be distorted as shown in Figure 3 leading to the generation of a magnetic tail. The interaction can pick up mass from the ionosphere, and through ionization from the atmosphere. This further slows the flow near the planet and increases the magnetic flux in the tail. The bend in the magnetic field and gradients in field strength act to accelerate the plasma in the antisolar direction. Much plasma can reach escape velocities by this mechanism.

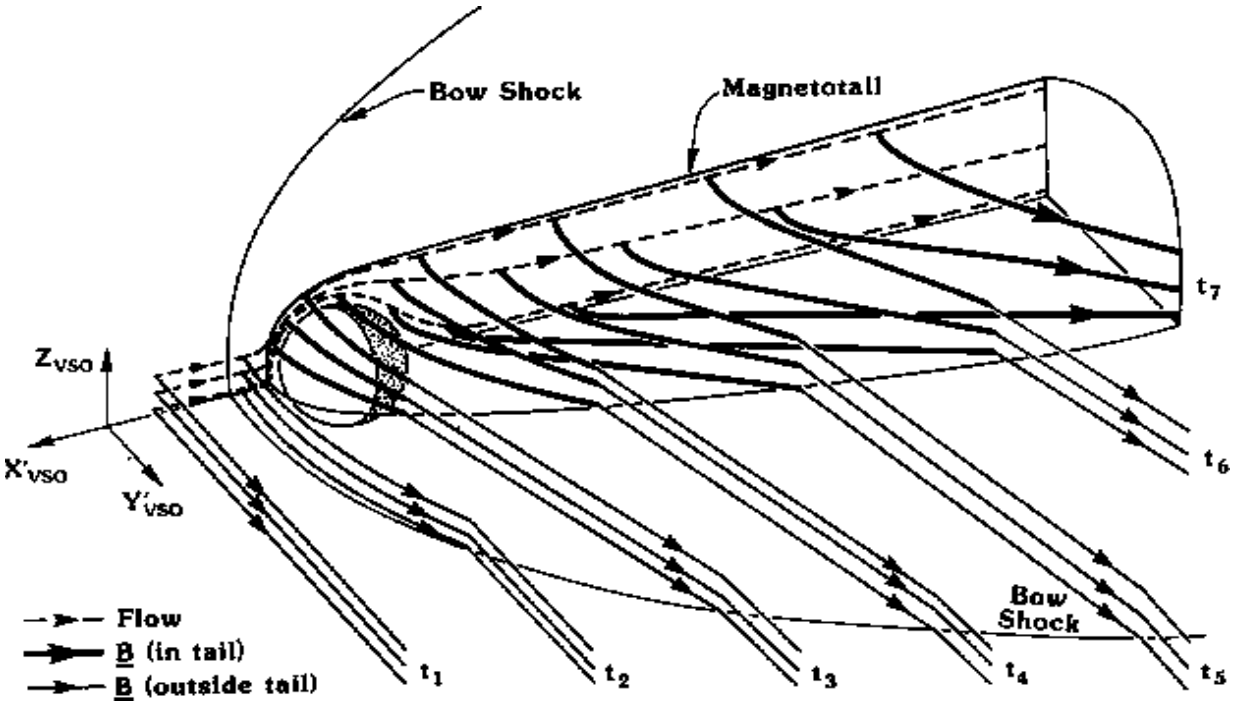

Figure 4. Schematic illustration of the formation of a magnetic tail in the interaction of the solar wind with an unmagnetized planet. Field lines from the solar wind which are convected closest to the planet move most slowly as they pass the planet and become stretched the most. (Saunders and Russell 1988)

Another route for atmospheric loss is the electric field of the solar wind. If particles are ionized in the magnetized flow, they will be quickly accelerated by the electric field and if the direction of the acceleration is correct they can spiral out into the solar wind as illustrated in Figure 4. The combined effect of the electric and magnetic fields of the solar wind acts to remove atmospheric gases from the unmagnetized planets only some of which is replenished by the absorption of the incoming solar wind. Magnetosphere of Venus, Mars and comets are formed this way.

4.2. Venus

The magnetic moment of Venus is less than one hundred thousandths of that of the Earth and plays no role in the solar wind interaction with the planet. Venus has been extensively explored in the Soviet and American programs with the Mariner 2, 5 and 10 flyby missions, the Venera 2, 4, 6, 8-14 landers; the Venera 9 and 10 orbiters and the Pioneer Venus atmospheric probes and orbiter. The orbiter missions especially have revealed much of the understanding outlined above. Nevertheless we still do not know how much atmosphere is being lost to the solar wind, nor do we understand many of the phenomena found to occur in the ionosphere such as the formation of magnetic flux ropes.

4.3. Mars

The precise size of the magnetic field of Mars is not known but its strength is probably much less than one ten thousandths of that of the Earth and like Venus the intrinsic magnetic field is not significant for the solar wind interaction. The Martian magnetosphere has been studied by the Mariner 4 flyby mission and the Mars 2, 3, 5 and Phobos orbiters. The ionosphere is thought to be magnetized because the solar wind dynamic pressure exceeds the thermal pressure of the ionosphere but no measurements have been made to confirm this hypothesis. Other features, such as the bow shock and magnetotail, are very similar to those of Venus. We have better measurements of the loss of the Martian ionosphere due to the solar wind interaction taken on the Phobos mission but at this writing these data are not yet fully reduced.

4.4. Comets

Comets are much smaller objects than planets if only their nuclei are considered. Their much smaller mass means that gravity is not a factor in the solar wind interaction. The size over which the cometary gas can spread in the solar wind is thus controlled by the speed of expansion of the cometary gas (about one km/s) and the ionization time (about a day at 1 AU from the Sun). Their product is about 10^5 km which is much larger than the size of the interaction regions at Venus and Mars. Not only does the interaction cover greater territory but it is much more gradual. Thus, for example, the bow shock is much weaker at a comet because much of the ionization forms ahead of the region where the bow shock forms so the solar wind is slowed prior to the shock. Measurements at and near comet Halley were made by five spacecrafts: Vega 1 and 2, Giotto, Sakigake and Suisei. Measurements from the smaller comet Giacobini- Zinner, were obtained from the ISEE-3 spacecraft. In no case were measurements made in the fully developed cometary tail. The data returned by these missions provided interesting insights into the physics of cometary magnetospheres but mainly whetted the appetites of cometary physicists. A mission that matches trajectories with a comet and can take long-term measurements is needed before the processes occurring at a comet are fully understood.

4.5. Intrinsic Magnetospheres

An intrinsic magnetosphere is created when the currents driven by convective motions within a planet are sufficiently strong to create a magnetic field whose pressure is sufficient to balance the incoming **solar** wind pressure. The size of the magnetosphere is determined by a balance between the dynamic pressure exerted by the solar wind and, to first order, the pressure exerted by the planetary magnetic field. For the magnetized planets, those with intrinsic magnetic fields, the obstacle to the solar wind is the planetary magnetic field and the size of the magnetosphere is governed by the relative strengths of the magnetic field and the solar wind at the planet. The strength of a planetary magnetic field is given by its dipole magnetic moment,

the equatorial surface field strength times the cube of the planetary radius. The dipole magnetic field falls off as the cube of the radius of the planet. Since the pressure balance is established between the magnetic pressure and the solar wind dynamic pressure at the subsolar point and since magnetic pressure is proportional to the square of the magnetic field strength, the sizes of planetary magnetospheres are proportional to the sixth root of the dynamic pressure. Table 1 lists the dipole magnetic moments for all of the planets, the average solar wind dynamic pressure for each planet which decreases as the square of the distance from the sun and the expected location of the pressure balance point along the subsolar direction. Only one planet, Jupiter, fails to follow this simple relation. At Jupiter part of the outward pressure is supplied by rapidly rotating plasma supplied by the volcanoes of Io. As the Table shows the magnetosphere of Mercury is clearly the smallest and that of Jupiter is by far the largest.

Table 1. Dipole magnetic moments and average solar wind dynamic pressure for each planet

Planet	Distance from sun (AU)	Magnetic moment (ME)	Solar wind pressure	Magnetopause distance
Mercury	0.4	4 x 10E-4	20 nPa	1.5 Rm
Earth	1.0	1.0	3.0 nPa	10 Re
Jupiter	5.2	1.8 x 10E4	0.1 nPa	70 Rj
Saturn	9.5	580	30 pPa	21 Rs
Uranus	19.2	50	8 pPa	27 Ru
Neptune	30.1	24	3 Ppa	26 Rn

4.6. Mercury

The magnetic moment of Mercury is about one 1/3000th of the terrestrial magnetic moment. The equatorial surface magnetic field strength is about 250 nT. Mercury has been explored by only one spacecraft Mariner 10 which passed by Mercury 3 times in 1974 and 1975. On two of these passes the spacecraft passed through the wake of the planet encountering a mini-magnetosphere much like that of the Earth. These two passes gave us only a brief glimpse of the nature of the Mercury magnetosphere. This glimpse was not enough to precisely determine the strength of the magnetic moment of the planet. It did however suggest that the

magnetosphere more efficiently extracts energy from the solar wind than does the Earth's magnetosphere.

4.7. Earth

The equatorial surface field of the Earth is about 31,000 nT. It is strong enough to activate rudimentary magnetic compasses and has been used as a navigational aid for at least 1000 years. The investigation of the earth's magnetic field began in about the 16th century but reached its zenith in the space age when it could be more fully explored with spacecraft. The spacecraft which have examined the Earth's magnetosphere are too numerous to name and have been launched by all the spacefaring nations. At present the most active area of research in magnetospheric physics is energy transfer from the solar wind to the magnetosphere.

4.8. Jupiter

The magnetic moment of Jupiter, as befitting the largest planet in the solar system, is also the largest of the planetary system over 10,000 times that of the earth. Its equatorial surface field is over 10 times that of the Earth. The strength of its magnetic field combined with the weakness of the solar wind at Jupiter produces a magnetosphere that is enormous. The sun could easily fit inside the magnetosphere. Its tail is thought to extend past Saturn, over 5 AU away. If Jupiter's magnetosphere could be seen from Earth it would appear to be larger than the Earth's moon.

Deep inside the Jovian magnetosphere orbit the Galilean satellites. One of these, Io, has a volcanically produced atmosphere that is constantly being bombarded by the intense radiation belts of Jupiter. This bombardment knocks atoms out of the atmosphere of Io into the magnetosphere of Jupiter where they become ionized. This process produces a torus, or doughnut, of hot ions circling Jupiter near Io's orbit. This torus together with the enormous electrical and magnetic forces in the Jovian magnetosphere leads to intense radiation belts and radio emissions. These emissions can be detected from Earth and were the first indication of Jupiter's enormous magnetic field well before the first interplanetary spacecraft were launched.

Jupiter has been visited four times by spacecraft: Pioneer 10 in 1973; Pioneer 11 in 1974; and Voyager 1 and 2 in 1979. Each of these spacecraft were on flyby trajectories.

4.9. Saturn

The magnetosphere of Saturn is quite benign compared to that of Jupiter. Since Saturn is a smaller planet, its conducting core in which the planetary magnetic field is generated is smaller, and so is the planetary magnetic field. The magnetic moment of Saturn is 580 times that of the Earth but its equatorial surface magnetic field strength is about equal that of the Earth. In stark contrast to the magnetic fields of all the other planets, the Saturnian dipole moment is not tilted with respect to the rotation axis of the planet. This observation was a great surprise to those studying planetary magnetic dynamos. Saturn's ring system absorbs radiation belt particles so that the radiation belts are weaker than at Jupiter and none of Saturn's moons exhibits volcanic activity similar to that of Io. As a consequence Saturn's radiation belt resemble more those of the Earth than those of Jupiter and few radio emissions are produced.

Saturn has been visited by 3 spacecraft Pioneer 11 in 1979, Voyager 1 in 1980 and Voyager 2 in 1981. Each of these were on flyby trajectories. NASA and ESA are working on an orbiter/probe mission called Cassini/Huygens which is scheduled to arrive at Saturn early in the 21st century.

4.10. Uranus and Neptune

The magnetic fields of Uranus and Neptune are quite unlike those of the other planets. The magnetic fields are quite irregular and cannot be well represented by a simple dipole field. When a dipole moment is fit to the flyby data available from Voyager 2 which flew by these planets in 1986 and 1989 respectively, a very large tilt angle between the rotation axis and the dipole axis is found, about 50^{o}. The magnetic fields are also much weaker than those found at Jupiter and Saturn. The magnetic moments are about 40 times that of Earth and their surface magnetic fields slightly less than the terrestrial field. The reason for this weakness and the irregularity may be that the magnetic field is generated, not in a deep molten core like the

Earth's, but in salty ice/water oceans closer to the surface. The radiation both of Uranus and Neptune are quite weak.

4.11. Comparison of Intrinsic and Induced Magnetospheres

The induced magnetosphere is created when the intrinsic magnetic field magnetic field, if any, is too weak to stand off the solar wind but the thermal pressure of the ionosphere exceeds the dynamic pressure of the solar wind. The scale size of the induced magnetosphere **is** usually similar to the radius of the planet since the ionosphere is usually gravitationally bound to the planet and has a relatively small scale height. Figure **5** shows a noon-midnight cross section of the Venus induced magnetosphere.

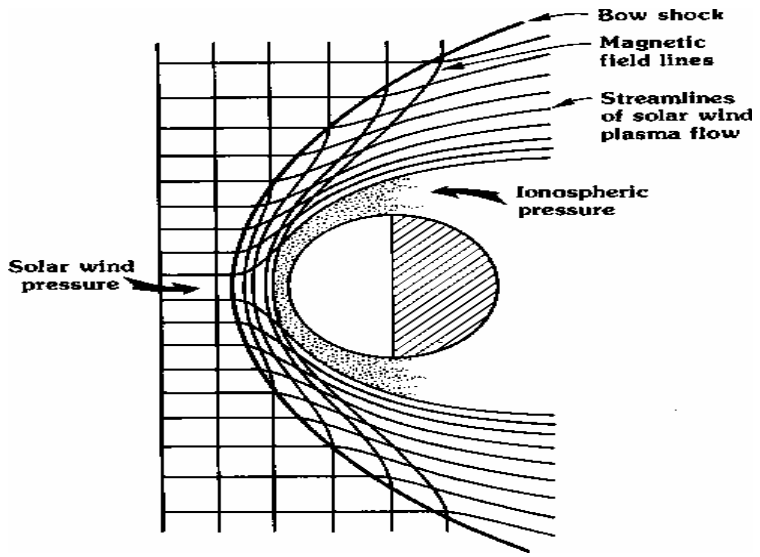

Figure 5. Noon-midnight cross section of the Venus induced magnetosphere. Slice of the interadon of the solar wind with the planet Venus in the plane containing the upstream magnetic field, the solar wind velocity and the centre of the planet. The solar wind, flowing from the left, carries magnetized plasma across the bow shock that slows, heats and deflects the flow around the planer The magnetic field draped across the ionosphere both builds up in pressure and loses its plasma so that it forms a magnetic barrier with a magnetic pressure that balances the dynamic pressure of the incoming Bow. (After Russel, 1991)

The induced and intrinsic magnetospheres have several common features. First, since the solar wind that these 'obstacles' deflect is supersonic relative to the velocity of compressional waves in the solar wind plasma, a standing bow shock wave forms in front of each. This non-linear bow wave heats, **slows** and deflects the solar wind at both types of obstacles. The forward or sunward parts of the magnetospheres are confined to a roughly elliptical region filled in the case of the intrinsic magnetosphere with a planetary magnetic field and in the case of an induced magnetosphere usually with a nearly magnetic field-free ionospheric plasma. The night side of each of the magnetospheres contains a region of elongated magnetic field called the magnetotail. The intrinsic magnetotail contains magnetic field lines which intersect the surface of the planet in two regions named the polar cusps.

The induced magnetotail consists of field lines which in general do not intersect the surface of the planet but rather close in the tail or in the solar wind. Figure 6 illustrates how an unmagnetized planet manages to stand off the solar wind Bow. As shown in the top two panels, the Sun ionizes the upper atmosphere with its EUV radiations. The solar wind might be absorbed by the ionosphere as in the lower right, but it carries magnetic flux tubes as shown in the lower left. Flux tubes are pushed against the planetary obstacle. Those coming closest to the planet are slowed the most. As they go by the planet they may also pick up more planetary ions than more distant magnetic field lines and slow down even more. The ends of these magnetic field lines, in the solar wind beyond the shock, are not slowed down and thus the tail is stretched into its familiar configuration shown in figures 1 and 2. The bent magnetic field then attempts to shorten itself by accelerating plasma away from the planet in the antisolar direction. Eventually far downstream the magnetic field will straighten itself.

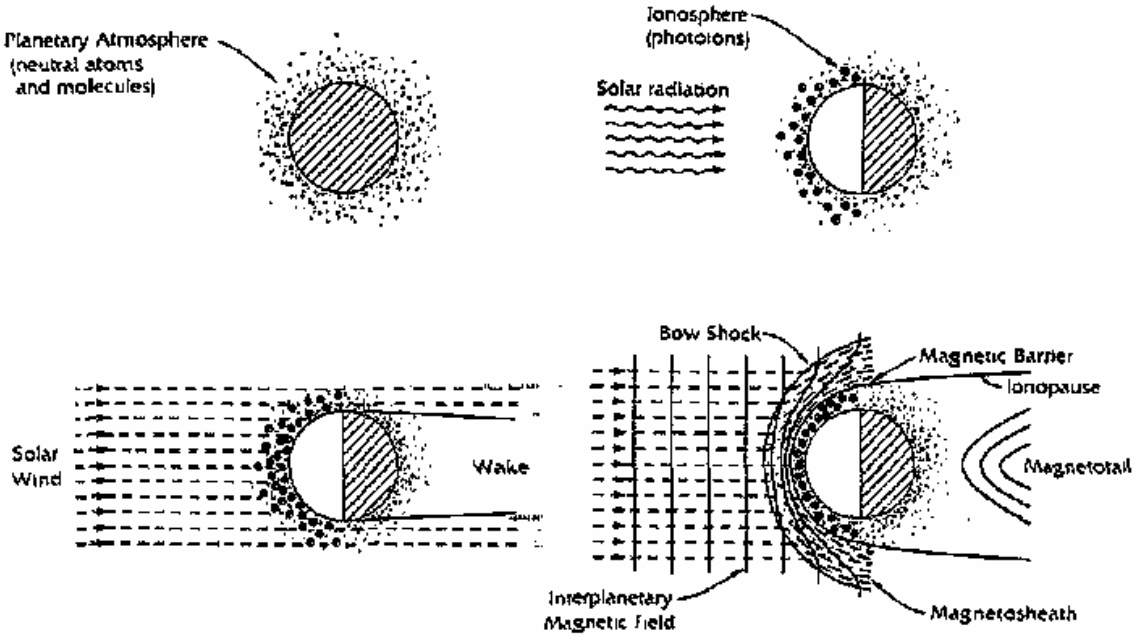

Figure 6. The formation of a planetary ionosphere and induced magnetosphere. The upper left panel shows the planetary atmosphere in the absence of other effects. In the upper right panel, the Sun shines on the atmosphere ionizing it with its extreme ultraviolet radiation (EUV). In the lower right an unmagnetized solar wind blows against the ionosphere. An unmagnetized solar wind would collide with the planetary atmosphere and be absorbed, but since it is magnetized, the magnetic field, which cannot penetrate the conducting ionosphere, piles up and creates a magnetic barrier that in turn deflects the solar wind around the ionosphere. (after Russel 1993)

The process that creates an intrinsic magnetotail is quite different. The intrinsic field is stretched in the antisolar direction by tangential stresses on the tail. These tangential stresses in turn are caused by phenomena such as viscosity and the reconnection process that we describe in more detail near the end of this review. Another important difference between induced and intrinsic magnetospheres is that intrinsic magnetospheres are generally much larger than induced magnetospheres.

5.0. Factors that affect structure and behavior of the magnetosphere

Two factors determine the structure and behavior of the magnetosphere: (1) The internal field of the Earth, and (2) The solar wind.

5.1. The internal field of the planet

The internal field of any planet (its "main field") appears to be generated in the planet's core. For example that of the Earth is generated at its core by a dynamo process, associated with the circulation of liquid metal in the core, driven by internal heat sources. Its major part resembles the field of a bar magnet ("dipole field") inclined by about 10° to the rotation axis of Earth, but more complex parts ("higher harmonics") also exist, as first shown by Carl Friedrich Gauss. The dipole field has an intensity of about $3 \times 10^4 - 6 \times 10^4$ nT at the Earth's surface, and its intensity diminishes like the inverse of the cube of the distance, i.e. at a distance of R Earth radii it only amounts to $1/R^3$ of the surface field in the same direction. Higher harmonics diminish faster, like higher powers of 1/R, making the dipole field the only important internal source in most of the magnetosphere.

5.2. The solar wind

The solar wind is a fast outflow of hot plasma from the sun in all directions. Above the sun's equator it typically attains 400 km/s; above the sun's poles, up to twice as much. The flow is powered by the million-degree temperature of the sun's corona, for which no generally accepted explanation exists as yet. Its composition resembles that of the Sun—about 95% of the ions are protons, about 4% helium nuclei, with 1% of heavier matter (C, N, O, Ne, Si, Mg... up to Fe) and enough electrons to keep charge neutrality. At Earth's orbit its typical density is 6 ions/cm3 (variable, as is the velocity), and it contains a variable interplanetary magnetic field (IMF) of (typically) 2–5 nT. The IMF is produced by stretched-out magnetic field lines originating on the Sun.

Schulz (1995) described the usual configuration of a planetary magnetosphere as a result of dayside compression and nightside extension of an intrinsic planetary magnetic field by the solar wind. In his words “The planetary magnetic field is thus confined (in first approximation) behind an elongated boundary known as the magnetopause, whose position is determined

largely by the requirement of kinetic pressure balance between the magnetic field and the solar wind.”

Physical reasons make it difficult for solar wind plasma with its embedded IMF to mix with terrestrial plasma whose magnetic field has a different source. The two plasmas end up separated by a boundary, the magnetopause, and the Earth's plasma is confined to a cavity inside the flowing solar wind, the magnetosphere. The isolation is not complete, thanks to secondary processes such as magnetic reconnection — otherwise it would be hard for the solar wind to transmit much energy to the magnetosphere — but it still determines the overall configuration.

An additional feature is a collision-free bow shock which forms in the solar wind ahead of Earth, typically at 13.5 RE on the sunward side. It forms because the solar velocity of the wind exceeds (typically 2–3 times) that of Alfvén waves, a family of characteristic waves with which disturbances propagate in a magnetized fluid. In the region behind the shock ("magnetosheath") the velocity drops briefly to the Alfvén velocity (and the temperature rises, absorbing lost kinetic energy), but the velocity soon rises back as plasma is dragged forward by the surrounding solar wind flow.

To understand the magnetosphere, one needs to visualize its magnetic field lines, that everywhere point in the direction of the magnetic field—e.g., diverging out near the magnetic north pole (or geographic southpole), and converging again around the magnetic south pole (or the geographic northpole), where they enter the Earth. They are discussed in MSPF, but for now they can be visualized like wires which tie the magnetosphere together—wires that also guide the motions of trapped particles, which slide along them like beads (though other motions may also occur).

The average position of a magnetopause, and therefore the size of a magnetosphere, can be calculated from the properties of the solar wind. Much of the solar wind is deflected round a magnetopause. Round a magnetosphere there is a shock wave, similar to the bow wave of a ship, where the magnetic field lines abruptly change direction. Some of the waves that can propagate in plasmas—ionized gases such as the solar wind—are similar to ordinary sound waves. The nature of the interaction of an obstacle, such as the Earth's magnetic field, with the solar wind depends on the ratio of the velocity of the medium to the sound velocity, the Mach number. If the Mach number is greater than 1, a shock wave develops ahead of the obstacle. Depending on solar wind conditions, the Mach number of a magnetosphere in the solar wind is between 5 and 10.

6.0. Advances in Planetary Magnetospheres

Reviews which gave excellent information on advances in magnetosphere include works of Kennel (1973), Akasofu (1983), Baker (1995), Bagenal (1995), Schulz (1995), Stern (1996) and Blanc et al (2005). Stern (1996) observed that space missions to other planets of the solar system have shown that most of them are magnetized. In particular, the giant planets are magnetized much more strongly than Earth (Bagenal, 1992) and their magnetospheres are all much larger than ours, in part because of the stronger dipole moments, in part because the solar wind becomes increasingly rarefied far from the Sun. Tiny Mercury has a magnetic moment only about 1/2000 that of Earth and a very small magnetosphere, Venus seems non-magnetic and Mars may or may not have a weak field. The magnitudes of the dipole moments of Mercury, Earth, Jupiter, Saturn, Uranus and Neptune, in units of 10^{25} Gauss cm^{-3}, are 0.004 (approx.), 7.9, 150,000, 4300, 420 and 200, respectively (Lepping, 1995).

Planetary magnetospheres have great diversity. Space missions that have been used to probe planetary magnetosphere include Pioneer 10 (Jupiter), Mariner 10 (Mercury), Pioneer 11 and Voyager 1 (Jupiter and Saturn), Voyager 2 (Jupiter, Saturn, Uranus and Neptune) and Ulysses

(Jupiter) (Stern, 1996). The Galileo spacecraft reached Jupiter in December 1995 and entered an orbit around the planet, after successfully launching a probe into Jupiter's atmosphere.

The strongest magnetic field and the most intense trapped radiation are found in the magnetosphere of Jupiter, which is also the largest (Dessler, 1983). This was furthermore the first planetary magnetosphere to be discovered: in 1955 strange radio noise was traced by Burke and Franklin to the planet Jupiter (Franklin, 1959, 1985), although it was only attributed to magnetically trapped plasma after the discovery of the Earth's radiation belt (Drake, 1985). Jupiter's magnetosphere is loaded with ions of sulfur and also of sodium, ejected from "volcanoes" on the satellite Io. Io also has an ionosphere with an interesting dynamo interaction with Jupiter (Ness et al., 1979). Jupiter's trapped plasma carries a dense ring current, and seems to co-rotate with the planet, perhaps up to the magnetopause. Its density profile contains dips due to absorption by Jupiter's moons and by the planet's thin ring, which resembles Saturn's ring but is much narrower; the existence of that ring was first suggested by an absorption feature in the belt (Acuna and Ness, 1976). Jupiter also has an aurora, observable from Earth, and radio emissions with complicated patterns, some of them correlated with the position of Io.

Saturn's magnetosphere similarly tends to rotate with the planet and contains absorption features. The planet seems to have an inner belt like the Earth's, believed to arise from albedo neutrons knocked out of the planet's rings by cosmic rays (Cooper and Simpson, 1980).

The Earth's magnetic axis is very close to its rotation axis. Similar proximity between the two axes was found for Jupiter, Saturn and Mercury (for Saturn the axes coincided within observational error), and this was therefore widely held to be a general feature of planetary magnetic fields. At the time of the encounter between Voyager 2 and Uranus, on 24 January 1986, the planet's axis pointed within a few degrees of the Sun. It was therefore expected that here was a "pole-on" magnetosphere, a previously unstudied configuration in which the axis of the planetary magnet pointed approximately into the solar wind (Stern, 1996).

But it was not to be. The magnetic axis of Uranus - and later also that of Neptune - was found to make an angle of about 60º with the planetary rotation axis, causing the field to swing widely with each rotation of the planet. As Uranus orbits the Sun, there will arise occasions when a "pole-on" magnetosphere is realized, but it did not happen during the Voyager 2 encounter.

Finally, Mercury's magnetosphere (Ness et al., 1979) seems to be too small for energetic particles to become trapped in it. However, as Mariner 10 went past the planet's night side, it encountered a burst of energetic particles, which could be the result of a substorm-type event in Mercury’s magnetic tail.

Interesting magnetic cavities are also formed around Venus, the Moon and comets (and probably, Mars), but if the obstacle is not a planetary magnetic field, the cavity produced is quite different from the ones described above. All this suggests a rather rich field for future research, involving configurations unlike the Earth's, on which many additional observations still remain to be made.

Table 2 presents the summary of the attributes of the magnetospheres of the planets, while Fig 7 illustrates the relative sizes of the planetary magnetospheres.

Table 2. Planetary Magnetic fields

Planet	Heliocentric distance (AU)	Radius (km)	Rotation period (days)	Magnetic moment (Tm^3)	Magnetic moment (M_E)	Tilt angle (deg.)	Equatorial surface field (nT)
Mercury	0.39	2 439	58.7	$\sim 4 \times 10^{12}$	$\sim 5 \times 10^{-4}$	?	~300
Venus	0.72	6 052	243.0	$\leq 1 \times 10^{14}$	$< 10^{-5}$	?	<0.5
Earth	1.0	6 371	1.00	7.8×10^{15}	1	10.8	30 200
Mars	1.5	3 394	1.03	$< 5 \times 10^{11}$	$< 6 \times 10^{-5}$	?	< 15
Jupiter	5.2	71 400	0.41	1.55×10^{20}	2.0×10^{4}	9.7	400 000
Saturn	9.5	60 330	0.43	4.6×10^{18}	590	<1	21 000
Uranus	19.2	25 559	0.75	3.8×10^{17}	49	59	23 000
Neptune	30.1	24 764	0.8	2.1×10^{17}	27	47	14 000

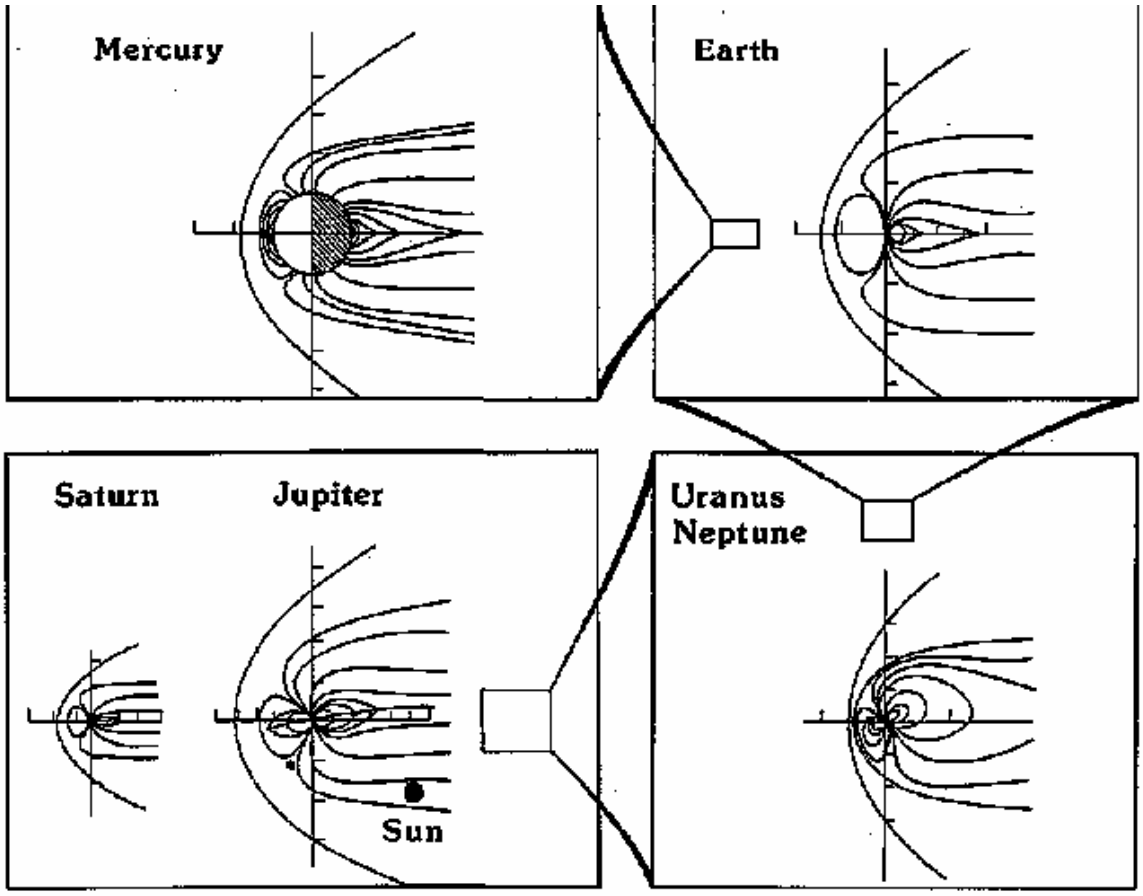

Fig, 7, The magnetosphere of the five magnetized planets. Boxes illustrate the relative sizes of the magnetospheres. The conical shape on the left of each planet represents the bow shock. The swept-back dipolar lines represent the planetary magnetic field. The size of the Sun is shown m the Jovian magnetosphere for scale. (After Russel 1993)

7.0. Comparative Planetary Magnetospheric Processes

The magnetospheres of the planets differ both in size and internal energy sources but also in the strength of the solar wind flow past their surfaces. Thus, the interaction of each of the magnetospheres with the solar wind differs in some degree from the others. Herein we examine how some of these processes vary from planet to planet.

7.1. The Bow Shock

The bow shock is a standing wave in front of a magnetosphere at which the supersonic solar wind is slowed, heated, and deflected around the planet. The strength of this shock depends on the flow velocity of the solar wind relative to the velocity of compressional waves in the plasma. This latter velocity decreases with increasing distance from the sun while the former remains quite constant. As a result, the strength or Mach number of the bow shock increases markedly from the inner solar system to the outer solar system. At Mercury the bow shock has a Mach number of about 4 but at Neptune it is about 20. At low Mach numbers the shock is found to be quite smoothly varying or laminar in appearance but at high Mach number the shock becomes very turbulent.

7.2. Upstream Waves

The bow shock represents an obstacle to some of the solar wind particles and they are reflected back upstream along the magnetic field. These counter-streaming particles cause waves to grow in the solar wind. These waves cannot propagate upstream against the solar wind and are blown back against the planetary shocks. The number of particles reflected by a planetary bow shock increases with the strength of the bow shock. Thus the strength and characteristics of the upstream waves change with heliocentric distance.

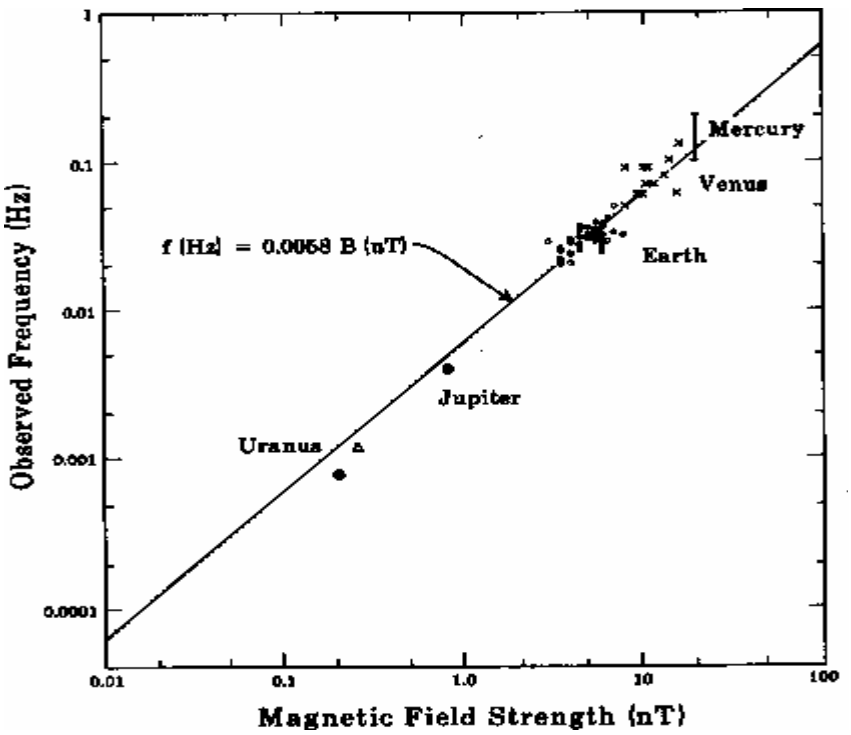

Fig 8. Upstream waves change with heliocentric distance (After Russel 1991)

Figure 8 shows one such property of the waves, their frequency. As one moves outward in the solar system the frequency of the waves change in proportion to the field strength as would be expected if the waves were associated with a gyro resonance with the reflected solar wind ions.

Another process that appears to be influenced by the Mach number is the reconnection. In this process magnetic field lines in the solar wind link up with those of the planetary magnetosphere, thereby increasing the tangential stress on the magnetosphere and adding magnetic energy to the magnetotail. Under solar wind conditions typical of those in the inner solar system this process is controlled principally by the direction of the solar wind magnetic field relative to the direction of the planetary magnetic field. When these directions are antiparallel, reconnection takes place readily and, when they are parallel, it does not take place at all. However, when solar wind conditions change to those typical of the outer solar system reconnection seems to cease. Reconnection is expected to be more important in the inner solar

system where the Mach number is typically 7 or less than in the outer solar system where it is often 10 or greater.

An associated phenomenon is that known as the Flux Transfer Event which appears to be the signature of temporally and spatially varying reconnection. These features have been observed at the magnetopauses of Mercury, Earth, and Jupiter. At Mercury these events are of short duration, about 1 s and occur frequently about every 30 s. At Earth these features last about 30 s and occur about every 5 minutes. At Jupiter the signature is similar to that at the Earth. This observation suggests that the small size of the Mercury magnetosphere affects the generation of Flux Transfer Events. However, at Earth and Jupiter the size of Flux Transfer Events may be controlled by some other property of the magnetosphere such as the thickness of the magnetopause which is the same at both planets.

8.0. Summary

- This article has outlined the general features of planetary magnetospheres. Some of these magnetospheres are induced and some intrinsic. Both types stand off the solar wind flow and cause planetary bow shocks.
- Magnetosphere refers to the region of the upper atmosphere of an astronomical object which is dominated by its magnetic field. Different planets experience different degree of magnetic dominance. Six planets have significant internal magnetic fields and hence, substantial and active magnetospheres: Mercury, Earth, Jupiter, Saturn, Uranus, and Neptune. Mars is known to have patchy surface magnetization, while pulsars and some other celestial objects also have magnetosphere.
- The Earth's magnetosphere was discovered in 1958 by Explorer 1 during the International Geophysical Year and is the most widely studied magnetosphere. The outer boundary of the magnetosphere is called the magnetopause, upon which flows the magnetopause current, a

large current vortex which separates the magnetic field of the Earth and the solar wind. Behind the Earth are the two lobes of the magnetic tail, the top one pointing to the Earth and the bottom one pointing away. These magnetic field lines enter and leave the Earth in oval shaped regions known as the polar cusps. Between the two tail lobes flows the neutral sheet current which is simply part of the magnetopause current vortex and also the plasma sheet a hotter and denser plasma than in the surrounding regions.

- Deeper in the magnetosphere is the plasmasphere, a region of dense cold plasma which is the upper extension of the ionosphere.
- The magnetosphere is a large plasma cavity generated by the Earth's magnetic field and the solar wind plasma. The basic elements of the magnetosphere are
    - *The Bow Shock and the Magnetosheath*
    - *The Magnetopause*
    - *Cusp and Mantle*
    - *The Quiet Magnetotail*
    - *The inner Magnetosphere*
- *Planetary magnetospheres are classified into two* according to the source of their magnetic fields*: Intrinsic and induced magnetospheres.*
- The induced magnetosphere is created when the intrinsic magnetic field magnetic field, if any, is too weak to stand off the solar wind but the thermal pressure of the ionosphere exceeds the dynamic pressure of the solar wind. Magnetospheres of Venus, Mars, Comets are induced.
- An intrinsic magnetosphere is created when the currents driven by convective motions within a planet are sufficiently strong to create a magnetic field whose pressure is sufficient to balance the incoming solar wind pressure. Magnetospheres of Mercury, Earth, Jupiter, Saturn, Uranus and Neptune are intrinsic.

- Two factors that determine the structure and behavior of the magnetosphere are the internal field of the Earth, and the solar wind. “The planetary magnetic field is thus confined behind an elongated boundary known as the magnetopause, whose position is determined largely by the requirement of kinetic pressure balance between the magnetic field and the solar wind.”

- The magnetospheres of the planets differ both in size and internal energy sources but also in the strength of the solar wind flow past their surfaces. Thus, the interaction of each of the magnetospheres with the solar wind differs in some degree from the others. Space missions that have been used to probe planetary magnetosphere include Pioneer 10, Mariner 10, Pioneer 11, Voyager 1, Voyager 2, Galileo, and Ulysses. The strongest magnetic field and the most intense trapped radiation are found in the magnetosphere of Jupiter. Mercury has the smallest and weakest magnetosphere.

References

Acuna, M. H. and N.F. Ness , 1976. Summary of the initial results from the GSFC fluxgate magnetometer on Pioneer 11, in *Jupiter*, pp. 830-847, edited by T. Gehrels, U. of Arizona Press

Akasofu, S.-I., 1983. Solar-Wind Disturbances And The Solar Wind-Magnetosphere Energy Coupling Function, *Space Science Reviews*, 34, 173-183.

Bagenal, F., 1995. Planetary Magnetospheres: 1991-1993. *Surveys in Geophysics* 16: 443-456, 1995.

Baker, D. N., 1995. The Inner Magnetosphere: A Review. *Surveys in Geophysics*, 16, 331-362,

Blanc, M., Kallenbach, R., and Erkaev, N.V., 2005. Solar system magnetospheres. Space Science Reviews, 116, 227–298. DOI: 10.1007/s11214-005-1958-y

Cooper, J. F. and J.A. Simpson , 1980. Sources of high-energy protons in Saturn's magnetosphere, *J. Geophys. Res., 85*, 5793-5802

Dessler, A. J. , 1983. *Physics of the Jovian Magnetosphere*. Cambridge Univ. Press., 544 pp.

Drake, Frank D., 1985. Discovery of the Jupiter Radiation Belts, in *Serendipitous Discoveries in Radio Astronomy*, K. Kellermann and B. Sheets, editors. National Radio Astronomy Observatory, Green Bank. p. 258-265.

Franklin, Kenneth L., 1959. An account of the discovery of Jupiter as a radio source, *Astron J., 64*, 37-39

Franklin, Kenneth L., 1985. The discovery of Jupiter Bursts, in *Serendipitous Discoveries in Radio Astronomy*, K. Kellermann and B. Sheets, editors, p. 252-257 National Radio Astronomy Observatory, Green Bank

Kennel, C. F., 1973. Magnetospheres of the Planets. *Space Science Reviews,* 14, 511-533.

Lepping, R. P., 1995. Characteristics of the magnetopauses of the magnetized planets, in *Physics of the Magnetopause*, B.U.O.Sonnerup and P. Song, editors, p. 61-70, Amer. Geophys. Union, Washington, D.C.

Ness, Norman F., M.H. Acuna, R.P. Lepping, L.F.Burlaga, K.W.Behannon and F.M.Neubauer, 1979. Magnetic field studies at Jupiter by Voyager 2: Preliminary results, *Science, 206*, 966-972

Russell, C. T., 1987. The Magnetosphere, In The Solar Wind and the Earth, edited by S. -I. Akasofu and Y. Kamide, pp 73-100. Copyright by Terra Scientific Publishing Company (TERRAPUB), Tokyo, 1987

Russell, C. T., 1991. Planetary Magnetospheres. Science Progress, 75, 93-105

Russell, C. T., 1993. Planetary magnetospheres. Rep. Prog. Phys., 56, 687-732.

Saunders M A and Russell C T., 1986 *J. Geophys. Res, 91* 5589-604

Schulz, M., 1995. Planetary Magnetospheres. *Earth, Moon, and Planets,* 67, 161-173

Stern, D. P., 1989. A brief history of magnetospheric physics before the spaceflight era, *Rev. Geophys., 27*, 103-114.

Stern, D. P., 1996. A brief history of magnetospheric physics during the space age. *Reviews of Geophysics, 34*, 1-31, 1996

NIGERIAN JOURNAL OF SPACE RESEARCH 8: 87-118, 2009 September 1

Earth's Currents and Energy System

Nikolai ØSTGAARD Ph.D.,
University of Bergen,
Allegt 55, N-5007, Norway
Email: Nikolai.Ostgaard@uib.no
Ph: +4755582794; Fax: +4755589440

Table of Content

1. Introduction

The purpose of this chapter is to give a brief description on how energy is transported and distributed in the solar wind-magnetosphere-ionosphere system. To give the necessary background information we begin by describing the main plasma regions and current systems in the Earth magnetosphere and ionosphere. Then we explain how the main current systems can be monitored using global magnetic disturbance indices. This will constitute the background for a further description of how the solar wind and its magnetic field can interact with the magnetosphere and how the solar wind energy can penetrate the magnetic shielding of the Earth. The energy transport within the magnetosphere-ionosphere system will be discussed and how it is distributed in three major energy sinks, that is, the energy injected into the ring current, the electron precipitation into the ionosphere and the Joule heating of the ionosphere. Finally, the total energy budget for the solar wind-magnetosphere-ionosphere system during substorms will be presented.

2. Plasma regions and currents in the Earth's magnetosphere

In this section we will give a brief description about the various plasma regions as well as explaining how the magnetosphere is shaped the way it is.

2.1. Overview of the plasma regions in the Earth's magnetosphere

2.1.1. The solar wind

In Figure 2.1.1-1 an illustration of the magnetosphere, its plasma regions and currents are shown. The Sun is to the left and the four white arrows indicate the solar wind flowing towards the magnetosphere. The magnetosphere is the region where the Earth's magnetic field dominates and this constitutes an obstacle for the solar wind flow. The solar wind contains plasma, that is, electrons and ions (mostly protons). Since the solar wind contains collisionless plasma the Sun's magnetic field, or the interplanetary field (IMF), can be considered to be 'frozen-in' the plasma and moves with the plasma. The most important characteristics of the solar wind and the IMF are given in
Table *2.1.1-1*.

Table 2.1.1-1 Solar wind characteristics (from G. Parks, 2004)

	Flow speed (km/sec)	**Flow direction**	**Particle number density (**cm^{-3})	**Average thermal energy**	**Intensity of B_{IMF}** (nT)
Range	300-800	Nearly parallel to the Earth Sun line	3-20	kTe < 100 eV kTp < 50 eV	1-30
Typical/ average	320		8	Te=10^5 K Tp=4 x 10^4 K	5

If we now consider these numbers in terms of different forms of energy we can estimate the kinetic energy as

$$E_{sw} = \frac{1}{2} N m_p v_{sw}^2 \qquad \text{.....1}$$

and by using the typical/average numbers from Table *2.1.1-1* and the proton mass, m_p=1.67 10^{-27} kg and the magnetic permeability, $\mu_0=4\pi 10^{-7}$ H/m, we can estimate how the other energy forms relate to the kinetic energy:

The magnetic energy:

$$E_B = \frac{B^2}{2\mu_0} = \frac{1}{70} E_{sw} \qquad \text{.....2}$$

The proton thermal energy

$$E_{Tp} = \frac{3}{2} N k T_p = \frac{1}{100} E_{sw} \qquad \text{.....3}$$

The electron thermal energy

$$E_{Te} = \frac{3}{2} N k T_e = \frac{1}{50} E_{sw} \qquad \text{.....4}$$

We see that for average solar wind conditions the kinetic energy dominates the other energy forms by about two orders of magnitude.

The parabolic bow shock that is formed upstream of the magnetopause is a result of the high-speed solar wind interacting with the magnetosphere obstacle. This is a region were the solar wind slows down and the temperature increases.

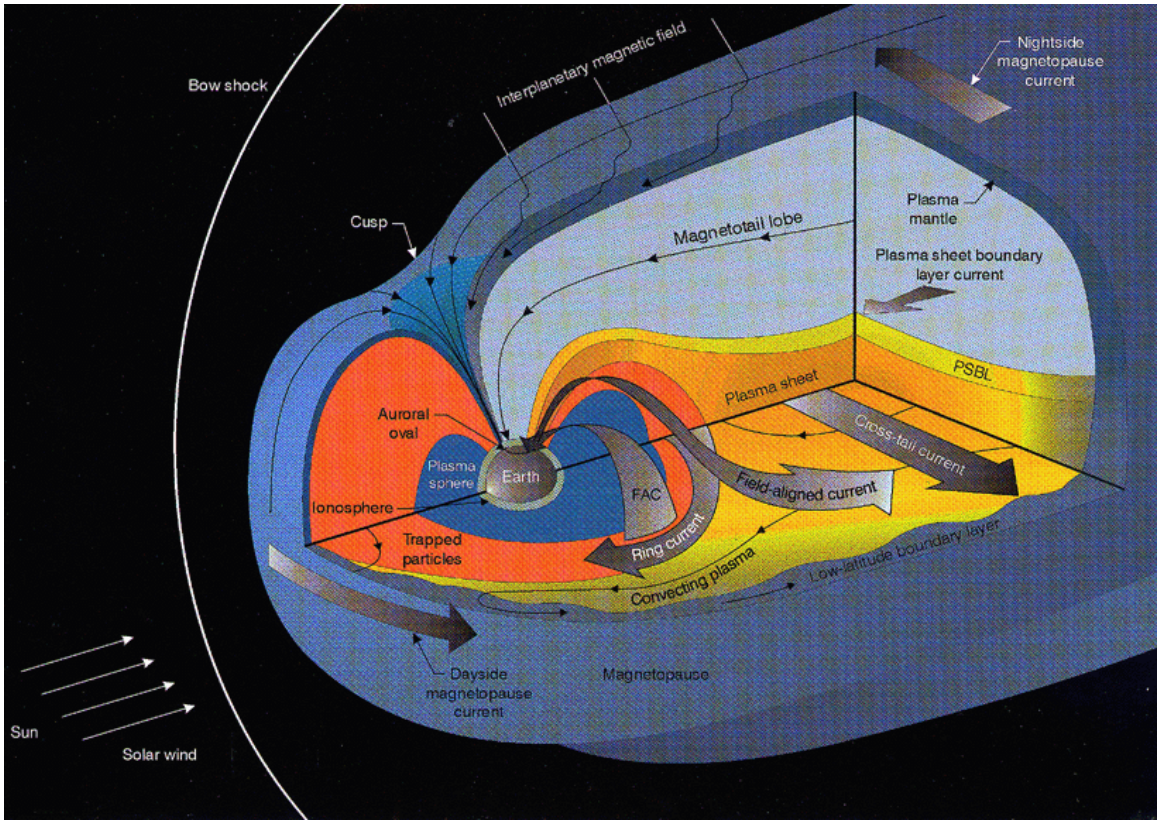

Figure 2.1.1-1 Currents and plasma regions in the Earths magnetosphere.

2.1.2. Magnetopause – magnetic shielding and pressure balance

The blue region is the magnetosphere and its surface is the magnetopause. The latter constitutes the boundary between the solar wind and the magnetosphere. A simple expression for the location of the magnetopause can be obtained by assuming pressure balance between the solar wind (*sw*) and the magnetosphere (*m*) (Mead and Beard, 1964)

$$(p_{sw} + \frac{B_{IMF}^{\ 2}}{2\mu_0}) = (p_m + \frac{B_m^{\ 2}}{2\mu_0}) \qquad \textbf{...5}$$

Before we proceed we will show how we arrive at this expression for pressure balance. Consider the equation of motion

$$m\frac{d\vec{v}}{dt} = \vec{F} \qquad \textbf{...6}$$

Letting the force be the Lorentz force we apply this equation on ions and electrons separately:

$$m_i n_i \frac{d\vec{v}_i}{dt} = q_i n_i (\vec{E} + \vec{v}_i \times \vec{B}) - \nabla p_i \qquad \textbf{…7}$$

$$m_e n_e \frac{d\vec{v}_e}{dt} = q_e n_e (\vec{E} + \vec{v}_e \times \vec{B}) - \nabla p_e \qquad \textbf{…8}$$

Adding the two equations and noticing that the charge, $q = q_i = -q_i$, the current, $J = nq(v_i - v_e)$ and the mass density is $\rho_m = m_i n_i + m_e n_e$,we can write

$$\rho_m \frac{d\vec{v}}{dt} = \vec{J} \times \vec{B} - \nabla p \qquad \textbf{…9}$$

Assuming equilibrium, $\rho_m \frac{d\vec{v}}{dt} = 0 = \vec{J} \times \vec{B} - \nabla p$ and using Amperes law $\vec{J} = \frac{\nabla \times \vec{B}}{\mu_0}$ to replace J one gets

$$\frac{(\nabla \times \vec{B}) \times \vec{B}}{\mu_0} = \nabla p \qquad \ldots 10$$

And finally by using vector identity under the assumption that we have a *straight* and *homogeneous* B we get

$$\nabla(p + \frac{B^2}{2\mu_0}) = 0 \qquad \textbf{….11}$$

This means that the total pressure is constant across a boundary, which is exactly what we wanted to show.

Now we can proceed. We make two fairly rough assumptions. 1) As the magnetic field outside the magnetopause (IMF) is only 1/10 – 1/20 of the field strength inside, the difference in magnetic pressure is 1/100 – 1/400 and we set the magnetic field outside to zero. 2) As the particle pressure inside the magnetosphere is only a small fraction of the solar wind bulk pressure we neglect the pressure inside. Of these two assumptions the second one may lead to a location too close to the Earth. We then get:

$$p_{sw} = \frac{B_m{}^2}{2\mu_0} \qquad \textbf{....12}$$

Particles reflected at the magnetopause (see sketch Figure 2.2.1-1) impose a pressure to the magnetopause given by

$$p_{sw} = 2Nm_p v^2 \qquad \textbf{....13}$$

where N is number density, m_p is proton mass and v is solar wind bulk speed

The dipole field strength is given by

$$B_d = \frac{\mu_0 M}{4\pi \cdot r^3} \qquad \textbf{..... 14}$$

where M is the Earth's magnetic moment

Taking into account the magnetopause currents (that will be explained in Section 2.2.1) the different contributions to the magnetic fields on both sides of the boundary is illustrated in Figure 2.1.2-1. The magnetopause current is decomposed into a planar and a curved component. *Bd* is the Earth's dipole magnetic field, *Bp* is the planar component and *Bc* is the curved component. Based on this sketch and disregarding the contribution from the curved current *Bc*, we can, according to Mead and Beard (1964), express the field strength just inside the magnetopause as being twice the dipole field strength

$$B_m = 2B_d \qquad \text{.....15}$$

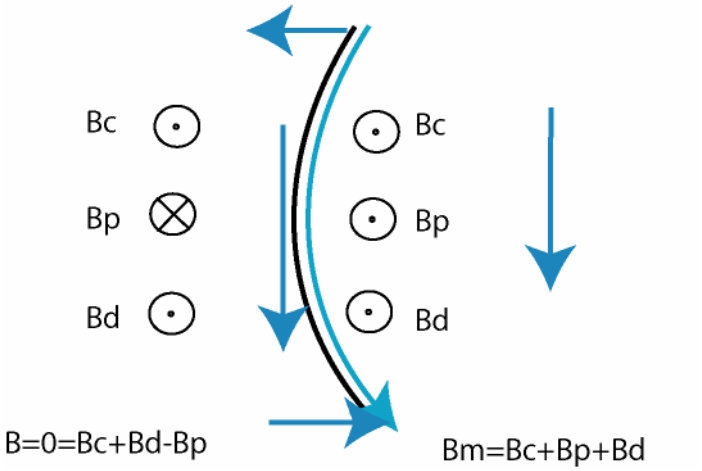

Figure 2.1.2-1 The various contributions to the magnetic field strength on both sides of the magnetopause.

Combining these equations one gets the following expression for the location of the magnetopause at the Sun-Earth line, also called the sub-solar point

$$r_0 = \sqrt[6]{\frac{\mu_0 M^2}{16\pi^2 N m_p v^2}} \qquad \text{....16}$$

where M is the Earth's magnetic moment of 8 10^{22} A m^2. With a typical solar wind parameters , N=10 10^6 m^{-3}, v=400 10^3 m/s and m_p=1.67 10^{-27} kg, you will get a sub-solar point at about 516000 km or about 8.1 R_e. As already pointed out, ignoring the IMF might be okay but ignoring the particle pressure inside the magnetopause may lead to a location closer to the Earth than the true location of the magnetopause. If the usual expression for dynamic pressure is used, i.e., without the factor 2, one will obtain r_0=9.1 Re, which is, as you will see below, closer to a more realistic location of the magnetopause. In the literature one will find that many uses the dynamic pressure, although that is not according to the approach by Mead and Beard (1964).

Let us now compare this result with what we would obtain if we use a more recent approach. Shue et al, (1997) developed an empiric model for the magnetopause using satellite passes through the magnetopause for different solar wind conditions. The expression for the magnetopause was chosen as

$$r = r_0(\frac{2}{1+\cos\theta})^{\alpha} \qquad \textbf{....17}$$

and for $\alpha = 0.5 : if\ \theta = 0\ then\ \ r\ = r_0, and\ if\ \ \theta \to 180\ then\ r \to \infty$,which gives the shape of the magnetopause as shown in Figure 2.1.2-2. Here r_0 is the sub-solar point, θ is the angle from the Sun-Earth line and α is the flaring angle. The Sun is to the right.

Based on more than 500 magnetopause satellite crossings the r_0 and α could be determined for northward ($B_z > 0$) and southward ($B_z < 0$) IMF separately.

$$r_0 = (11.4 + 0.013B_z)p_{sw}^{-\frac{1}{6.6}}, for B_z \geq 0 \qquad \textbf{....18}$$

$$r_0 = (11.4 + 0.14B_z)p_{sw}^{-\frac{1}{6.6}}, for B_z < 0 \qquad \textbf{....19}$$

$$\alpha = (0.58 - 0.010B_z)(1 + 0.010p) \qquad \textbf{.... 20}$$

where B_z is given in (nanoTesla) 10^{-9}T and p in (nanoPascal) 10^{-9}Pa. According to Shue et al., (1997) the solar wind dynamic pressure without the factor 2 for reflecting particles should be used:

$$p_{sw} = Nm_p v^2 \qquad \textbf{.... 21}$$

Using the same values for solar wind density and bulk velocity as above, the bulk pressure is 2.7 nPa . The magnetopause position at the Sun-Earth line (sub-solar point) for B_z=0 and -5 nT is then estimated to be r_0 = 9.8 Re and 9.2 Re, respectively. These results are probably closer to the true location than was obtained with the simplified pressure-balance concept (r_0 = 8.1 Re).

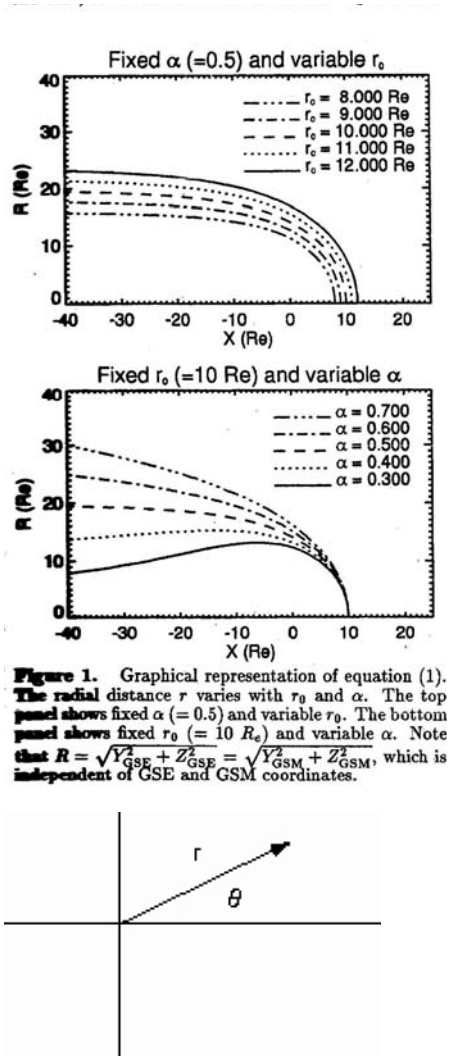

Figure 1. Graphical representation of equation (1). The radial distance r varies with r_0 and α. The top panel shows fixed α (= 0.5) and variable r_0. The bottom panel shows fixed r_0 (= 10 R_e) and variable α. Note that $R = \sqrt{Y_{GSE}^2 + Z_{GSE}^2} = \sqrt{Y_{GSM}^2 + Z_{GSM}^2}$, which is independent of GSE and GSM coordinates.

Figure 2.1.2-2 Modeled shape of the magnetopause by Shue et al., 1997 for two choices of r_0 and α. The coordinate system is explained in the bottom panel. The Sun is to the right

2.1.3. Plasma sheet and magnetotail

As the solar wind acts as a pressure force on the magnetosphere, the magnetosphere will be compressed on the dayside and due to tail currents in the plasma sheet it will be stretched out on the nightside. In the central part of the magnetotail the density of charged particles are larger than

in the lobes and this region is called the plasma sheet. The tail current, which is necessary to create the stretched configuration of the magnetosphere on the nightside, is flowing in the plasma sheet from morning to dusk, as seen in Figure 2.1.1-1). In the magnetic lobes the magnetic field strength is larger and the particle density is lower.

2.2. Overview of currents in the magnetosphere and ionosphere

2.2.1.Magnetopause currents

In Figure 2.2.1-1 we follow the trajectories of oppositely charged particles as they encounter a magnetic boundary like the magnetopause. Outside the boundary we assume the magnetic field strength to be zero and inside the magnetic field is pointing out of the plane, which corresponds to looking down on the magnetopause from north. As the particles enters the magnetosphere they are both affected by the magnetic force

$$\vec{F} = q\vec{v} \times \vec{B}_m \qquad \textbf{…. 22}$$

where q is the charge, v is the velocity and B is the magnetic field. Using this equation you can also obtain for the circular motion

$$m\frac{dv}{dt} = m\frac{v^2}{r} = qvB \qquad \textbf{…. 23}$$

and

$$r = \frac{mv}{qB} \qquad \text{…. 24}$$

that is the gyro radius, which is mass dependent and consequently much larger for protons than for electrons.

As the magnetic force is charge dependent the two particles with opposite electric charge will move in a circular but oppositely directed paths before they leave the magnetosphere as illustrated in Figure 2.2.1-1. The combined effect of this motion is that we get an electric current pointing along the boundary downward or eastward on the magnetopause, consistent with the magnetopause

current shown in Figure 2.1.1-1. The sketch also illustrates how the magnetosphere with its magnetopause acts as an efficient magnetic shield against charged particles. This makes it hard for solar wind particles to enter the magnetosphere, and creates a very important protection against all charged particles from the Heliosphere and the interstellar space.

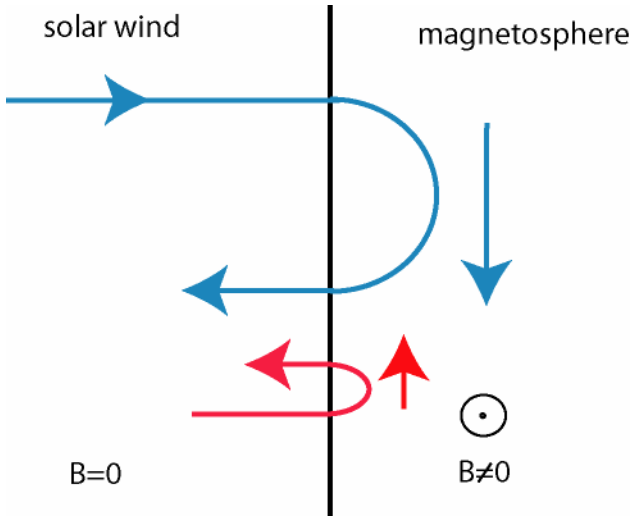

Figure 2.2.1-1 A positive charged particle (blue) and a negative charged particle (red) encountering the magnetosphere with the magnetic field pointing out of the plane

2.2.2. Ring current

Although charged particles gyrate around the magnetic field due to the magnetic force (see Figure 2.2.2-1), they also have a drift across the field lines as shown by the arrows; ions move westward and electron eastward.

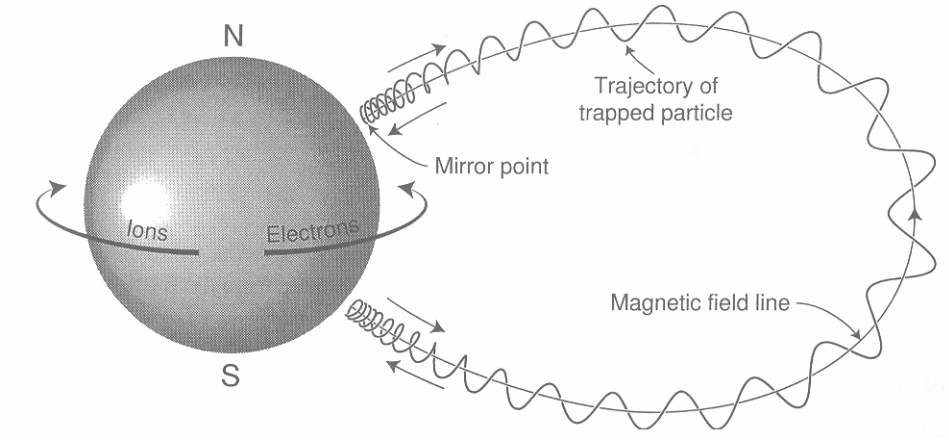

Figure 2.2.2-1 Trapped particle in the system

The general drift velocity perpendicular to the magnetic field of a charged particle moving in an electric field and an inhomogeneous magnetic field is given by

$$\vec{v}_d = \frac{\vec{E}\times\vec{B}}{B^2} + \frac{K}{qB^3}(1+\cos^2\alpha)\vec{B}\times\nabla B \qquad \textbf{.... 25}$$

where E is electric field, α is pitch angle (i.e., the angle between the magnetic field and the particle velocity vector) and K is kinetic energy of the particle. The first term on the right side is the electric drift which is energy and charge independent and gives the same direction for electrons and ions. This is illustrated in Figure 2.2.2-2 where an electron and a proton are shown gyrating in an electric field perpendicular to the magnetic field. The gyro motion is opposite for electrons and protons, but the acceleration due to the electric field is opposite, too. These two effects cancel resulting in drift motion in the same direction for both particles. The drift direction can be seen from the radius becoming smaller (larger) when the velocity gets smaller (larger).

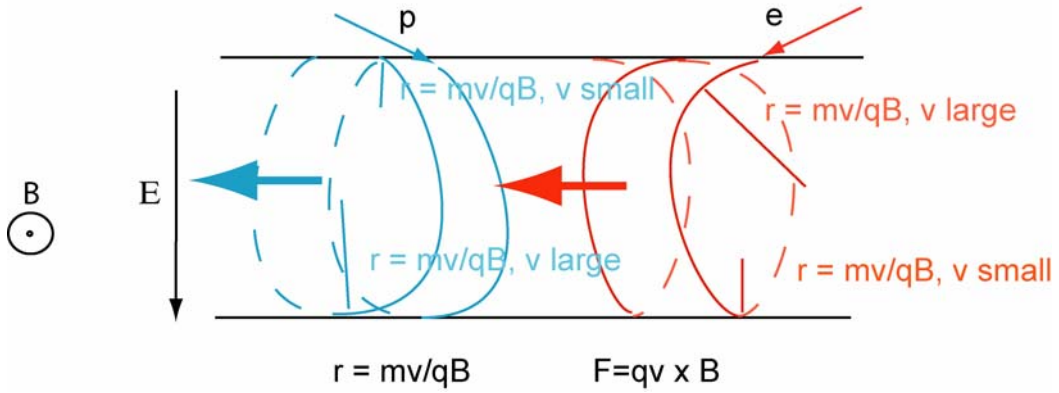

Figure 2.2.2-2 Illustration of the electric drift

The second term is the magnetic curvature and gradient drift and becomes important when the kinetic energy is large and there is a significant gradient in the magnetic field. This term is charge dependent and gives opposite direction for ions and electrons. This is illustrated in Figure 2.2.2-3. The drift direction can again be seen from the radius becoming smaller (larger) when the B is larger (smaller).

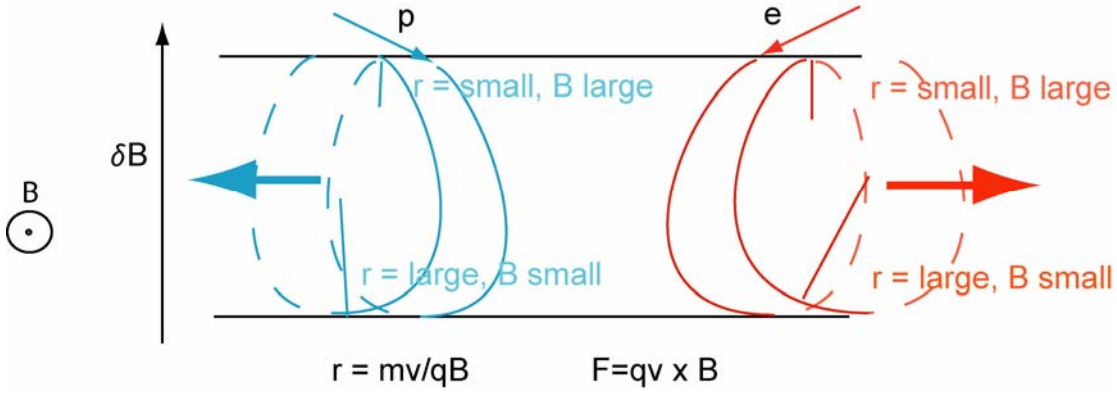

Figure 2.2.2-3 Illustration of the gradient drift

Energetic electrons and ions drifting towards the Earth from the magnetotail will first, as the magnetic gradient is small, drift together on approximately equi-potentials, i.e., according to first

term. We should emphasize the word 'approximately' because the magnetic gradient drift will still bring particles across equi-potentials resulting in energy gain for the particles, although this effect is very small in the tail. These drift trajectories (i.e. along equi-potentials), in the equatorial plane, are shown in Figure 2.2.2-4. Left panel shows the drift trajectories if only the convective electric field from dawn to dusk is considered. The middle panel shows drift trajectories when only the co-rotating electric field is considered and the right panel shows drift trajectories when the two fields are superposed.

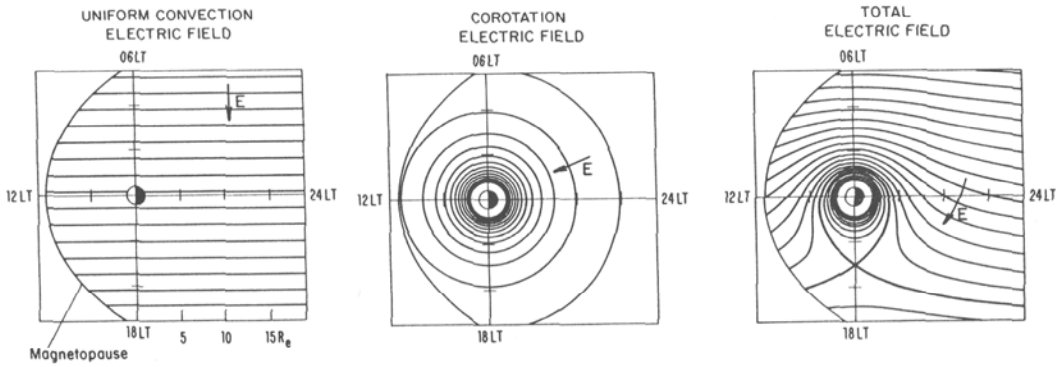

Figure 2.2.2-4 Drift trajectories for the electric drift in the equatorial plane. Sun is to the left. Left panel: The drift trajectories if only the convective electric field from dawn to dusk is considered. Middle panel: Drift trajectories when only the co-rotating electric field is considered. Right panel: The drift trajectories when the convective and co-rotating field are superposed. From Lyons and Williams (1983)

Closer to the Earth when the magnetic gradient becomes significant the particles will not drift along the equi-potentials but energetic ions will move westward and energetic electrons move eastward, creating the ring current as shown in Figure 2.1.1-1, Figure 2.2.2-1 and Figure 2.3.1-1. An injection of particles from the tail, associated with an increase in the solar wind electric field and more efficient energy transfer through the magnetic shield, will therefore lead to an increase of the ring current, and this is exactly what occurs during a magnetic storm.

2.2.3. Tail currents

Further down the tail, there is a current flowing in the plasma sheet from morning to dusk. Due to the Amperes law, $\vec{J} = \frac{1}{\mu_0} \nabla \times \vec{B}$, this current is consistent with the stretching of the magnetotail. The compression by the solar wind pressure on the dayside and the stretching on the nightside give the magnetosphere its characteristic shape.

2.2.4. Field aligned currents, Birkeland region 1 and 2

As the name indicates field-aligned currents are currents flowing along the magnetic field lines. These currents are also called Birkeland currents, due the first physicist, Kristian Birkeland, that suggested that the aurora was associated with field-aligned currents. In Figure 2.2.4-1 you can see the field aligned current pattern for two different geomagnetic disturbance levels (see definition about AL in Section 2.3.2). These are currents that couple the magnetosphere to the ionosphere and are very important for the dynamics of the system. Black is current into the ionosphere and white current is out of the ionosphere. We are looking down on the northern hemisphere in a magnetic coordinate system with the magnetic pole in the center, midnight to the bottom and the Sun towards the top. Dawn is to the right and dusk to the left. The inner ring, flowing into the ionosphere in the dawn and out at dusk is called the Region 1 current. These currents flow to the flanks of the magnetosphere as shown by the upper arrow marked 'Field aligned currents' in Figure 2.1.1-1. The outer ring, which is the Region 2 currents, has the opposite direction in the morning and evening from that of Region 1 currents. Region 2 currents maps to the inner plasma sheet as is shown by the lower arrow marked 'FAC' in Figure 2.1.1-1. North-south Pedersen currents will close region 1 and 2 currents in the ionosphere (see blue arrows in Figure 2.2.5-1).

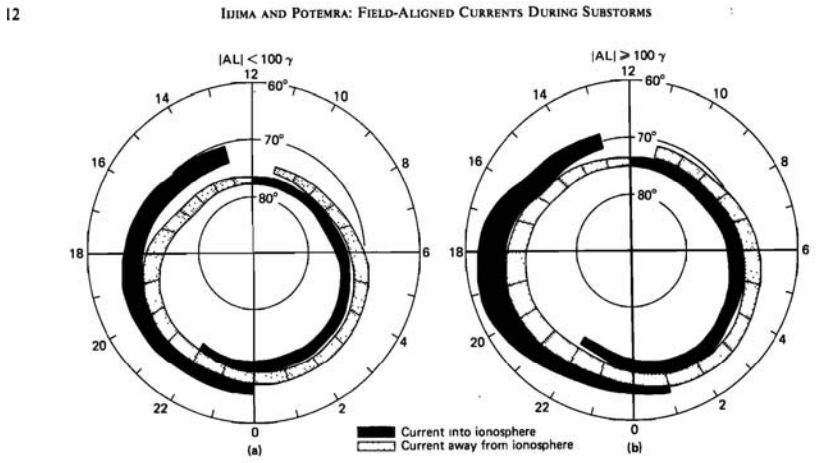

Fig. 13. A summary of the distribution and flow directions of large-scale field-aligned currents determined from (*a*) data obtained from 439 passes of Triad during weakly disturbed conditions ($|AL| < 100\ \gamma$) and (*b*) data obtained from 366 Triad passes during active periods ($|AL| \geq 100\ \gamma$).

Figure 2.2.4-1 Birkeland 1 and 2 currents as presented by Iijima and Potemra, (1978)

2.2.5. Ionospheric currents: Pedersen and Hall

Due to the differences in collision frequencies in the upper atmosphere there is a difference in conductivity properties that give rise to two different currents flowing in different directions. Hall currents are dominating below 130 km and are oriented in the direction of $-\vec{E}\times\vec{B}$. The Hall currents are east-west oriented in the auroral zone and is referred to as the Auroral electrojet as seen in Figure 2.2.5-1 as large open black arrows (labeled Jh). Here you see the eastward electrojet in the dusk sector and the westward electrojet at dawn and night. The Pedersen currents are dominating above 130 km. Pedersen currents are north-south oriented in the direction of the horizontal electric field in the ionosphere, shown by blue arrows and labeled Jp. Although both Hall and Pedersen currents are connected to the field-aligned currents, the Pedersen currents are usually the currents thought to close the region 1 and 2 Birkeland currents in the ionosphere (see Section 2.2.4)

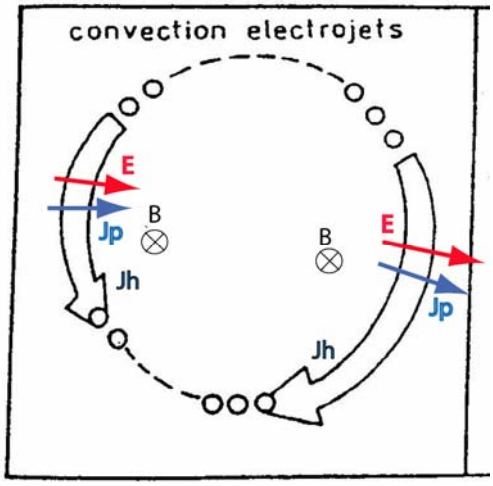

Figure 2.2.5-1 Black open arrows are the auroral electrojets, which are Hall currents (Jh) and blue arrows are Pedersen currents (Jp)

2.3. Magnetic indices and geomagnetic activity

There are several geomagnetic indices to monitor the disturbance level of the magnetosphere-ionosphere system. Here we will only describe two of these, the Dst and the AE . For information about other geomagnetic indices we refer to the Oulo textbook presentation (http://www.oulu.fi/~spaceweb/textbook/indices.html).

2.3.1. Dst, to monitor ring current during magnetic storms

Due to the Biot Savarts law,

$$\vec{B}(\vec{r}) = \frac{\mu_0}{4\pi}\int \frac{\vec{J}(\vec{r}-\vec{r}')\times(\vec{r}-\vec{r}')}{(\vec{r}-\vec{r}')^3} d^3r' \qquad \text{.... 26}$$

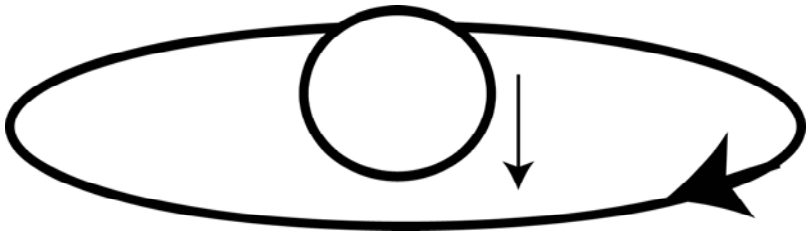

Figure 2.3.1-1 The ring current flowing westward around the Earth (thick arrow) and the magnetic disturbance at the Earth's equator shown by the arrow pointing toward the south.

any current (at **r'**) will have a magnetic signature that can be monitored remotely (at **r**). A simple sketch of the ring current is shown in Figure 2.3.1-1. As pointed out in Section 2.2.2 electrons will move eastward and ions westward when they get closer to the Earth where the gradient of the Earth's magnetic field will force them to move in opposite directions. This leads to the westward ring current.

At the Earth's surface at equator the effect of the ring current will be seen as a small perturbation (usually <1000 nT) on top of the much larger Earths magnetic field (32000nT). The stronger the ring current is the larger the perturbation is. A measure of the ring current strength is the hourly Dst index (Sugiura, 1964), which is obtained from magnetometer stations near the equator. At such latitudes the H (northward) component of the magnetic perturbation is dominated by the intensity of the magnetospheric ring current. As the Earth magnetic field is subtracted the Dst index is a direct measure of the hourly average of this perturbation. Large negative perturbations are indicative of an increase in the intensity of the ring current and typically appear on time scales of about an hour. The decrease in intensity may take much longer, on the order of several hours. The entire period is called a magnetic storm and an example is shown in Figure 2.1.1-1 . The increase seen in the beginning (shaded grey to the left) of the storm (21 April 16 UT) is due to enhanced eastward magnetopause currents on the dayside. The decrease (22 April 00–14 UT) which is the

main phase of the storm is when the ring current is increased. The slow recovery (shaded grey to the right) back to zero is called the recovery phase of the magnetic storm.

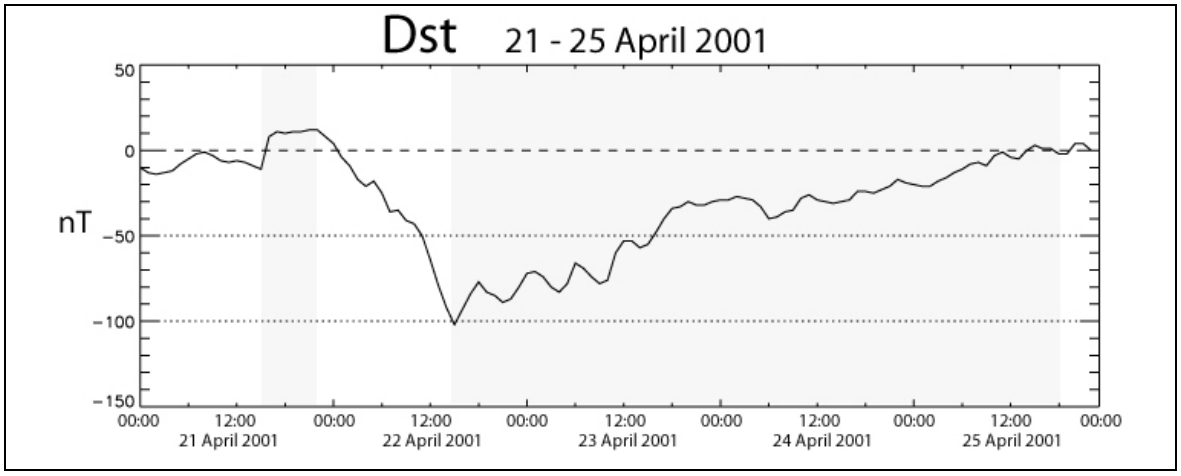

Figure 2.3.1-2 The Dst index during a typical geomagnetic storm

2.3.2. AE, to monitor ionospheric currents during substorms

AE index is an *auroral electrojet index* obtained from a number (usually greater than 10) of stations distributed in local time in the latitude region that is typical of the northern hemisphere auroral zone (Davis and Sugiura, 1966). For each of the stations the north-south magnetic perturbation H is recorded as a function of universal time.

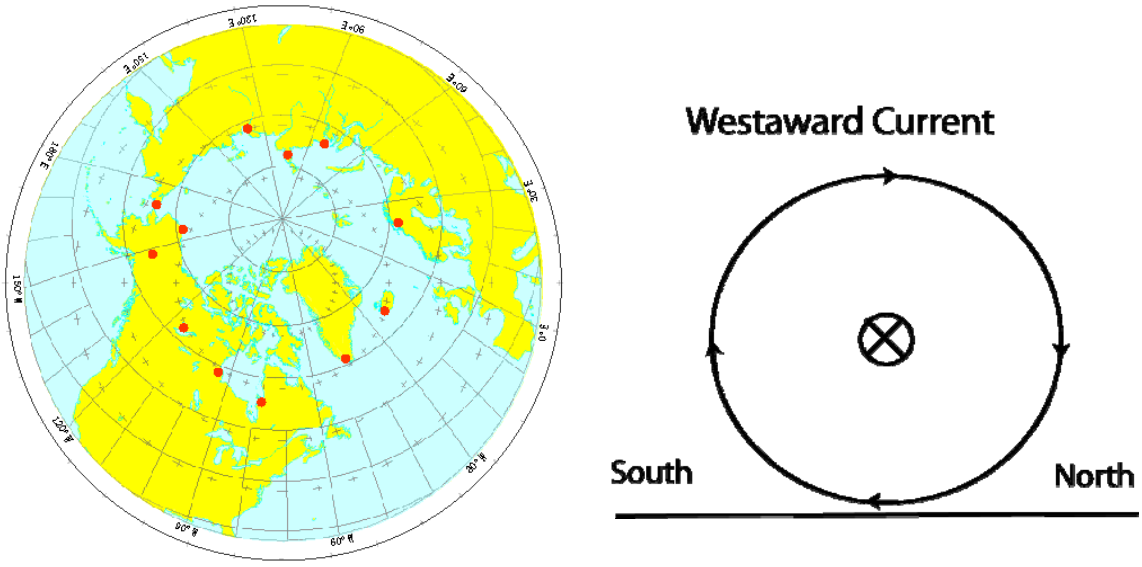

Figure 2.3.2-1 The twelve red dots on the map to the left show the position of the stations providing magnetic measurement to produce the AE, AL and AU indices. A sketch showing the magnetic disturbance seen on the ground from a current flowing westward (into the plane) above the observer

A superposition of these data from all the stations enables a lower bound or maximum negative excursion of the H component to be determined; this is called the AL index. Similarly, an upper bound or maximum positive excursion in H is determined; this is called the AU index. The difference between these two indices, AU-AL, is called the AE index. Notice that negative H perturbations occur when stations are under a westward-flowing current. Thus the indices AU and AL give some measure of the individual strengths of eastward and westward electrojets (shown in Figure 2.2.5-1), while AE provides a measure of the overall horizontal current strength. Excursions in the AE index from a nominal daily baseline are called magnetospheric substorms and may have durations of tens of minutes to several hours. In Figure 2.3.2-2 three subsequent substorms are shown. Upper panel shows AU (positive) and AL (negative) while lower panel shows the AE (positive). Notice that most of the signal is in the wesward electrojet (AL). For most of the day data from 10 stations were used to create the indices.

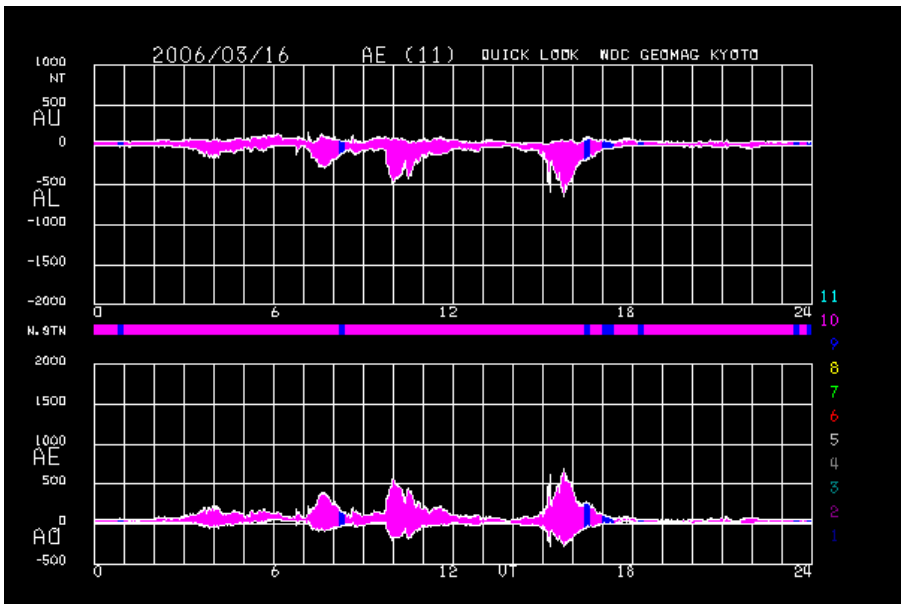

Figure 2.3.2-2 Signatures of three subsequent substorms seen in AU, AL and AE index.

3. The Energy system of the Earth's magnetosphere/ionosphere,

We will now discuss the energy flow of the solar wind – magnetosphere – ionosphere system.

- How much energy is available in the solar wind
- How can it penetrate the Earth's magnetic shield
- The three main energy sinks in the magnetosphere-ionosphere

3.1.1. Available energy in the solar wind

The kinetic energy flux of the solar wind available for the magnetosphere is given by

$$U_{sw} = \tfrac{1}{2}\rho v^3 A \qquad \text{…. 27}$$

where A is the area of the magnetosphere when assuming a cylindrical symmetric magnetosphere. The area for different solar wind conditions can be estimated by the formula given by Shue et al., (1997). There are three forms of energy in the solar wind, kinetic, magnetic and thermal, but the

kinetic energy is usually orders of magnitude larger than the two other forms (see Section 2.1.1) and we can therefore neglect the magnetic and thermal energy when we estimate the available energy in the solar wind.

3.1.2. Reconnection, the solar wind dynamo and the epsilon parameter

When the IMF has a southward component, there will be a region at the sub-solar point where the IMF and the Earth's magnetic field are anti-parallel. In such a configuration the two fields can merge in a process called magnetic reconnection. A simple sketch of the geometry and evolution of this process is shown in Figure 3.1.2-1.

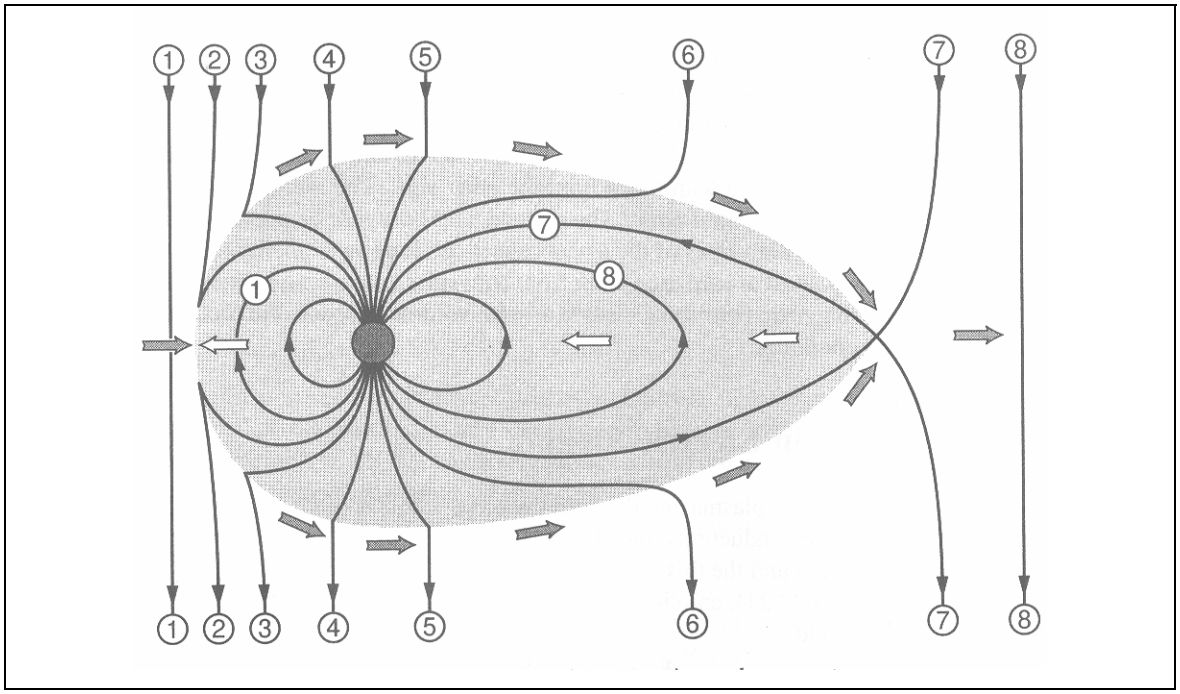

Figure 3.1.2-1 Sketch showing how a southward IMF interacts with the Earths magnetic field (Baumjohann and Treumann, 1997)

The numbers on the field lines indicate the temporal evolution of an interplanetary field line when it encounters the Earth's magnetic field (1) until it has returned to the interplanetary space (8).

Time step (2) indicates when the two field lines have been connected. Although we mentioned that solar wind particles could not penetrate the magnetic shield at the magnetopause, the reconnection process makes a small 'hole' in that shielding and solar wind particles can enter into the magnetosphere. Due to the curvature force acting on the field line, the plasma connected to the field will be accelerated from (2) to (4).

When the field line moves down the tail (5) to (7) the magnetic curvature will act as a braking force. In a reference frame at rest (in this case the Earth) the IMF moving with a speed, *v*, will give an electric field pointing out of the plane

$$\vec{E} = -\vec{v} \times \vec{B} \qquad \textbf{…. 28}$$

While the braking of the solar wind will give an electric current into the plane

$$\vec{J} = \frac{\vec{B} \times \rho \dfrac{d\vec{v}}{dt}}{B^2} \qquad \textbf{…. 29}$$

where ρ is the density of the solar wind. With *E* and *J* in opposite direction ($\vec{E} \cdot \vec{J} < 0$) this is the solar wind dynamo that drives field-aligned currents that we already discussed as Region 1 currents. This represents an energy transfer from the solar wind into the magnetosphere. One more comment before we continue with the energy transfer. The magnetic field line that is opened at step (2) is eventually closed again by reconnection at step (7). The plasma and the closed field lines will drift together towards the Earth by the electric drift motion described above, and will get back to step (1) and repeat the cycle. This cycle is called the Dungey cycle. The reconnection at step (7) can either occur at about 100 Re to create the far X-line or closer to Earth, i.e., at 15-25 Re, to create the Near-Earth Neutral Line.

There have been many efforts which have lead to more or less accurate estimates of the energy transfer from the solar wind to the magnetosphere. The most used (but not necessarily the most

accurate) parameter was developed by Perrault and Akasofu (1978) and is called the ε parameter and can be expressed in SI units as:

$$\varepsilon = 10^7 v B^2 \sin^4\left(\frac{\theta}{2}\right) l_0^2 \qquad \text{…. 30}$$

This is a semi-empirical parameter, based on the assumption that the Poynting flux can proxy the energy transfer. To take into account that reconnection is more efficient when the IMF is southward and opposite of the Earth's magnetic field orientation the parameter was given a clock-angle dependence, defined as

$$\theta = a\tan(B_y / B_z) \qquad \text{…. 31}$$

The energy will therefore be maximized for southward IMF and zero for northward IMF. The ε parameter also has an area variable, $l_{0,}$ which is set to 7 Re and is an estimate of the surface area (the little 'hole') on the magnetopause the energy transfer takes place. One can therefore say that the ε parameter seeks to mimic the reconnection process and the solar wind dynamo. Both the area variable, $l_{0,}$ and the trigonometric dependence on the clock angle were determined by comparing with data. Although the accuracy can be questioned, the ε parameter has been proven to be a useful estimate. Later we will refer to results testing how good it is.

3.1.3. The energy sinks in the system

Now we turn to the three main energy sinks in the system, the ring current increase, the particle precipitation and the Joule heating of the ionosphere. There are some other sinks in the system, but they are either very difficult to estimate, or they are not very important.

In the first category is the plasmoids which is a vast plasma bubble that is detached from the magnetosphere when the Near-Earth Neutral Line is formed. Another one is the plasma sheet heating which is thought to be very small (reference in Østgaard et al., 2002).

3.1.3.1. Energy injected to the Ring current (U_R)

As already explained the ring current is dependent on the energy of all the particles producing the ring current (see equation for drift velocity, …. 25, in Section 2.2.2). We can express the change of energy, *K*, in the ring current as:

$$\frac{\partial K}{\partial t} = U_R - \frac{K}{\tau} \qquad \textbf{…. 32}$$

Where U_R is in the energy injected to the ring current and the second term expresses the loss of ring current particles with a characteristic life-time, τ.

Remember that the ring current gives a magnetic perturbation that can be measured near equator. Due to Biot Savarts law (…. 26), the magnetic disturbance is dependent on the current density and the current density is proportional to the kinetic energy,

$J = Nqv_d \propto K$. We can therefore substitute *K* with *Dst** multiplied with a constant and it can be shown that the energy injected into the ring current, U_R, given in GW, is related to changes in the *Dst** index (in nT) in the following way:

$$U_R = 4 \cdot 10^4 \left(\frac{\partial Dst^*}{\partial t} + \frac{Dst^*}{\tau} \right) \qquad \textbf{…. 33}$$

The newly injected energy into the ring current, U_R, is therefore the sum of the total energy change of the ring current (i.e., the first term on the right side) and the loss term (i.e., the second term). Notice that the loss term is dependent on a characteristic life time, τ. This characteristic life time may not be constant and many studies (e.g., Østgaard et al, 2002) has let τ vary with the strength of Dst*. Notice that we use Dst* which is a pressure corrected Dst. This is because we are only interested in the magnetic disturbance that is due to the ring current and not other currents. As can be seen in Figure 2.3.1-2 there is an increase in the beginning of a storm that is due to magnetopause currents. As the magnetopause current has been found to be related to the pressure

in the solar wind, the Dst is pressure corrected to remove the magnetic perturbation from the magnetopause current (ΔH(p)).

$$Dst^* = Dst - \Delta H(p) \qquad \textbf{…. 34}$$

3.1.3.2. Particle precipitation (U_A)

Charge particles in the magnetosphere are bound to gyrate around the magnetic field. The Earth's magnetic field is also like a magnetic bottle. This means that when a particle follows a field line, the field strength becomes larger when you get closer to the Earth. Particles that gyrate on a field line can therefore bounce back and forth between the two hemispheres. If the pitch angle, i.e. the angle between particle velocity vector and the magnetic field line, is very small when crossing the equatorial plane at the most distant location (to the right in Figure 2.2.2-1) the particle will get close to the Earth before they bounce in its mirror point. If the mirror point is below 100 km, it is very likely, due to the increasing density of neutral particles that the incoming charged particle will collide with a neutral particle. Then the incoming or precipitating particles will deposit their energy through ionization, aurora and heating.

By global imaging of the aurora in different wavelengths, like ultraviolet (UV) and X-rays one can get a map of the precipitation by electrons. This is shown in

Figure ***3.1.3.2-1***. Most of the energy deposited by particles into the ionosphere is provided by electrons. As it is possible through forward modeling to obtain estimates about how much UV emissions and X-rays that are produces from a given distribution of electrons, one can also go the other way, and use the UV and X-ray signals to obtain information about the energy of the particle precipitation. This is what is done in the six images shown to the right in

Figure ***3.1.3.2-1*** (Østgaard et al., 2001). For two 5-minute intervals (0300-0305 UT and 0315-0320 UT) the total energy for 0.1-100 keV electrons are shown in the upper panel, 0.1-10 keV electrons in the middle and 10-100 keV electrons in the lower panel. By integrating over the entire

hemisphere one can get the global energy input by electron precipitation in that hemisphere. Unless imaging data are available from both hemispheres, one can simply multiply by two to get an estimate of both hemispheres.

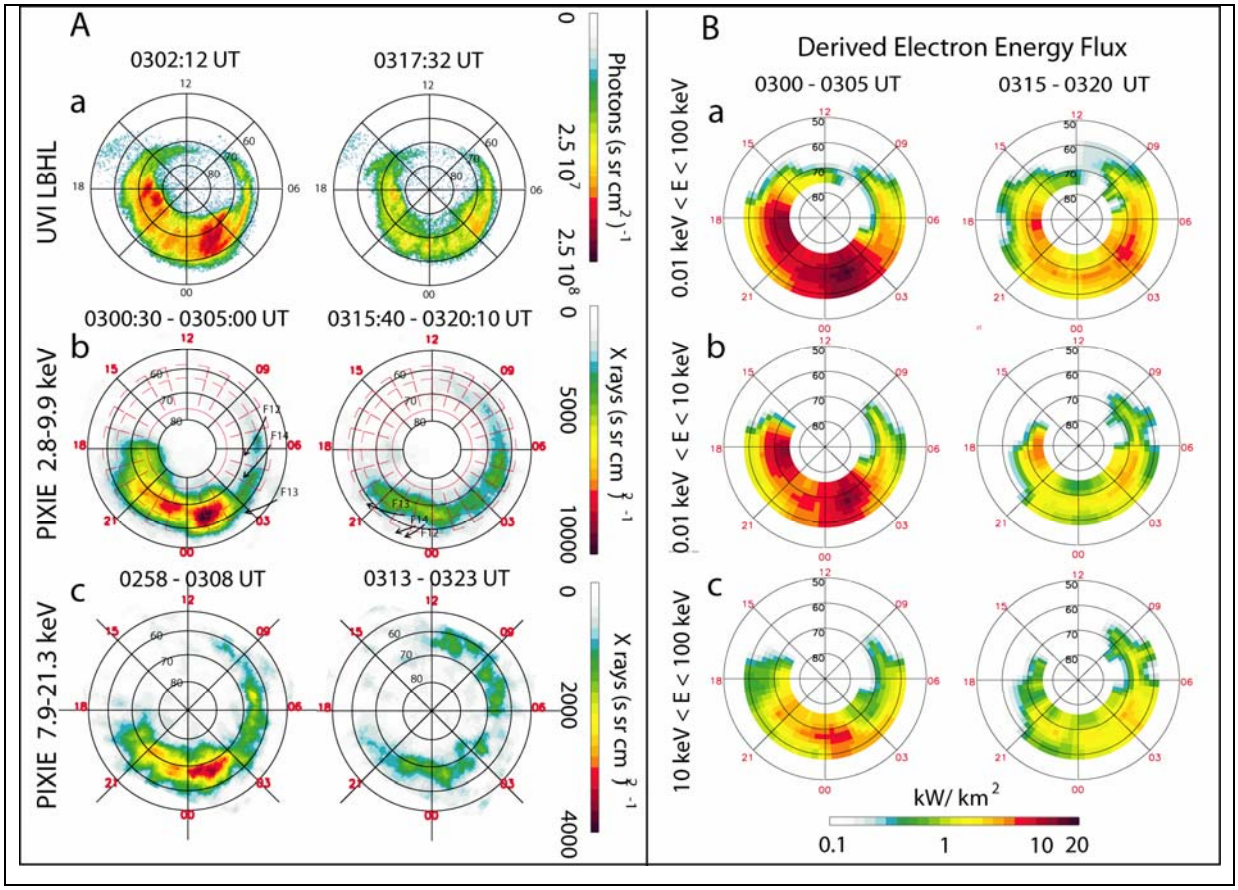

Figure 3.1.3.2-1 The six images to the left: Global images of the aurora on July 31, 1997 in UV (upper) in soft X-rays (middle) and harder X-rays (bottom). The six images to the right: Derived energy flux of precipitating electrons in three different energy intervals.

3.1.3.3. Joule heating of the ionosphere (U_J)

The last energy sink, but not the least, is the Joule heating of the ionosphere. The Joule heating is caused by the ionospheric current acting as a load and is given by

$$U_J = \vec{E} \cdot \vec{J} > 0 \qquad \text{…. 35}$$

It is therefore not surprising that the Joule heating can be estimated from the *AE* index, which is a response to the total electric currents in the ionosphere. However, one should be aware that it is the Pedersen currents that determines the Joule heating, while AE is an effect of the Hall current. This means that one has to make an important assumption, and that is that the Pedersen currents are proportional to the Hall currents. With this assumption many studies have tried to determine a linear relation between U_J and *AE*

$$U_J = aAE + b \qquad \text{…. 36}$$

U_J is given in GW and *AE* in nT. To estimate the Joule heating in both hemispheres Østgaard et al. (2002), combined the results from Ahn et al.(1989) and Richmond (1990) to obtain

$$U_J = 0.54AE + 1.8 \qquad \text{…. 37}$$

To learn more about how Joule heating can be estimated we refer to references given in Table 2 in Østgaard et al. (2002)

3.2. Analysis of energy budget during substorms

Finally, we will show some results using the expressions and methods we have explained so far for estimating the various energy input and sinks. In the study by Østgaard et al., 2002, nine susbstorms during 4 different days were analyzed and the results from one of the substorms are shown in Figure 3.2-1. To the left we show the different parameters that are uses to calculate the ε parameter, as well as U_A in one hemisphere and the *AE*.

To the right you can see the time evolution of the available energy, ε and the three energy sinks. Notice that U_J and U_A are including both hemisphere. The integrated energy from time 1 to time 2

($W(U_X)$, where subscript X can be R, A or J), during the substorm are shown by numbers in the various panels. The time intervals used for integrating the various energies during the substorms were defined as follows: Start time was determined from the lowest value of AE before the substorm and the end time was when there was no more imaging data for the event. Østgaard et al. (2002) examined nine substorms following this procedure and found the following:

Date	Subst	$W(U_R)$ [10^{14} J]	$W(U_J)$ [10^{14} J]	$W(U_A)$ [10^{14} J]	$W(U_T)$ [10^{14} J]	$W(\varepsilon)$ [10^{14} J]	$W(U_{SW})$ [10^{14} J]	CE [%]
Jul 09, 97	2	3.8(6%)	42.2(69%)	15.1(25%)	61.1	47	7850	0.8
Jul 24, 97	2	7.4(15%)	26.0(53%)	15.3(32%)	**48.7**	**24.2**	16100	0.3
Jul 31, 97	1	4.6(11%)	23.2(56%)	13.5(33%)	41.3	83.3	7880	0.5
Aug 28, 97	2	36.8(26%)	61.4(44%)	41.0(30%)	139.2	135.0	15200	0.9
Av.	7	15%	56%	29%				0.3-0.9

The results from the table can be summarized as:

1) The total energy deposition ($W(U_R)+ W(U_J)+ W(U_A)$) is distributed on average as; $W(U_R)$: 15%, $W(U_J)$: 56% and $W(U_A)$: 29%.
2) The coupling efficiency based on available energy and total energy deposited is less than 1%. This means that the Earth's magnetic shielding is in fact very efficient.
3) For some of the events the epsilon parameter did not provide enough energy transfer to balance the energy deposition in the system (marked with bold). An additional energy transfer mechanism that could be the viscous interaction between the solar wind and the

magnetosphere would need to transfer about 0.17% of U_{SW} into the magnetosphere to balance the total energy deposition.

It should be emphasized that these results are very different from what were suggested by Akasofu (1981). He thought that most of the energy would be deposited into the ring current (60%). Furthermore these results are consistent with what has been reported by Lu et al. (1998), Knipp et al. (1998) and Tanskanen et al (2002). We therefore believe our results give a more precise estimate of the various energy sinks and the coupling efficiency.

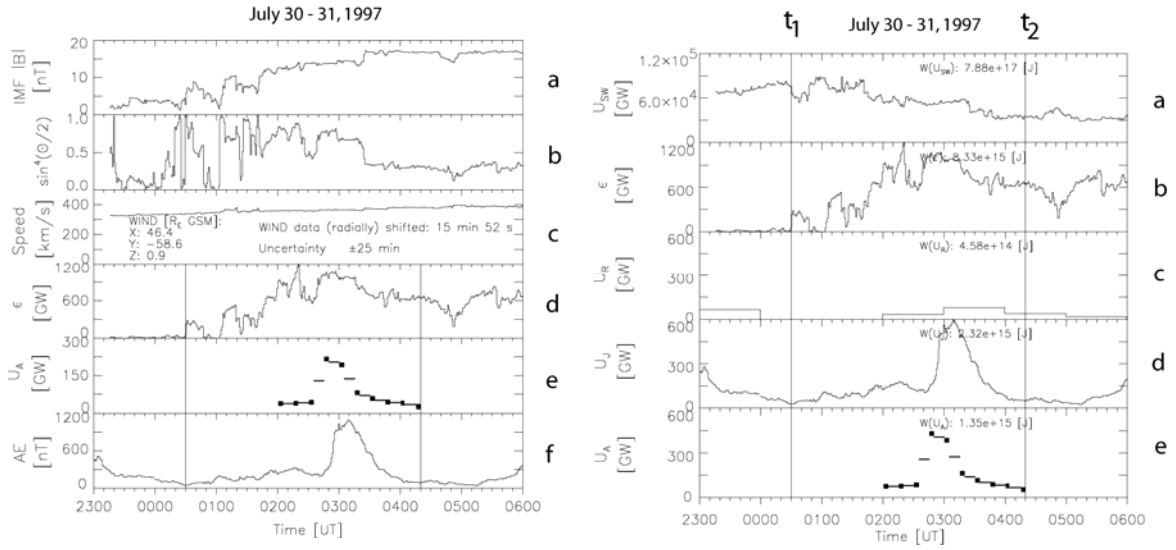

Figure 3.2-1 To the left: July 31, 1997, (a) the total magnetic field strength in the IMF, (b) the trigonometric expression for the clock-angle dependence of epsilon, (c) solar wind speed, (e) the integrated global energy from precipitation in one hemisphere and (f) the AE index. To the right: (a) available energy in the solar wind, (b) the epsilon paranmeter, (c) the energy injected into the ring current (d) the Joule heating both hemispheres (e) the Auroral precipitation energy in both hemispheres.

4. Summary

In this chapter we have given a brief description on how energy is transported and distributed in the solar wind-magnetospehere-ionosphere system. An overview of the main plasma regions and current systems of the Earth magnetosphere and ionosphere were presented. Some simple expressions to determine the magnetopause were given. As all currents are associated with magnetic perturbations geomagnetic activity can be monitored by global magnetic indices. Increases in the ring current during magnetic storms can be described by the Dst and variations in auroral electrojets during substorms and magnetic storms can be described by the AE index.

The second part of the chapter used these indices as well as measurements of the solar wind, to describe how we can estimate the available energy in the solar wind, how much we think penetrate the magnetic shield of the Earth and finally how the energy is distributed in the magnetosphere and ionosphere during substorms.

5. References

Akasofu, S. –I, Energy coupling between the solar wind and the magnetosphere, *Space Sci. Rev., 28*, 121-190,1981

Ahn B. H., H. W. Kroehl, Y. Kamide and D. J. Gorney. Estimation of ionospheric electrodynamic parameters using ionospheric conductance deduced from Breamstrahlung imaging data., J. Geophys Res., 94, 2565-2586, 1989.

Baumjohann W and R. Treumann, Basic Plasma Physics, Imperial College Press, 1997.

Davis, T. N., and M. Sugiura, Auroral electrojet activity index AE and its universal time variations, *J. Geophys. Res.*, **71**, 785-, 1966

Iijima and Potemra, J. Geophys. Res. Vol 83, A2, 599- 615, 1978

Knipp, D. J., et al., An overview of the early November 1993 geomagnetic storm, *J. Geophys. Res., 103, 26197-26220*, 1998.

Lu, G.et al., Global energty deposition during the January 1997 magnetic cloud event, *J. Geophys. Res., 103,* 11685-11694, 1998.

Lyons L. R. and D. J. Williams, Quantitative aspects of magnetospheric physics, D. Reidel publishing company, 1983.

Mead and Beard, J. Geophys. Res, 69, 1169, 1964
Østgaard N, J. Stadsnes, J. Bjordal, G. Germany, R. R. Vondrak, G. K. Parks, S. A. Cummer, D. L. Chenette, and J. G. Pronko. Auroral electron distributions derived from combined UV and X-ray emissions, J. Geophys. Res., Vol 106, A11, 26081-26089, 2001

Østgaard N, G. Germany, J. Stadsnes and R. R. Vondrak, Energy analysis of substorms based on remote sensing techniques, solar wind measurements, and geomagnetic indices, J. Geophys. Res., Vol 107, A9, doi:10.1029/2001JA002002, 2002

Parks G., Physics of Space Plasma, An Introduction, Second edition, Westview Press, Boulder, Colorado 80301, USA, 2004.

Perrault P.and S. I. Akasofu, A study of magnetic storms, Geophys. J. R. Astron. Soc., 54, 547, 1978.

Richmond A. D., Global measures of ionospheric electrodynamic activity inferred from combined incoherent scatter radar and ground magnetometer observations., J. Geophys. Res., 95, 1061-1071, 1990.

Shue J-H, J. K. Chao, H. C. Fu, C. T. Russell, P. Song, K.K. Khurana, H. J. Singer, J. Geophys. Res. Vol 102, A5, 9497-9511, 1997

Sugiura, M., Hourly values of equatorial Dst for IGY, pp. 945-948, in *Annals of the International Geophysical Year*, vol. 35, Pergamon Press, Oxford, 1964.

Tanskanen, E. T. I. Pulkkinen, H. E. J. Koskinen and J. A. Slavin. Substorm energy budget during low and high solar activity: 1997 and 1999 compared, *J. Geophys. Res.,* 107, 2002.

NIGERIAN JOURNAL OF SPACE RESEARCH **8**: 119 – 143, 2009 September 1

Heliospheric Physics: The heliosphere and galactic cosmic rays, the tiny messengers from outer space

Marius S. POTGIETER Ph.D and R. du Toit STRAUSS Ph.D.
Unit for Space Physics
North-West University
2520 Potchefstroom
South Africa
Email: fskmsp@puk.ac.za

Table of Contents

1. Introduction

Cosmic rays (CRs) are charged particles (not rays) that propagate through galactic space, interstellar space and heliospace to eventually reach the Earth. For this part, the focus is on the

propagation of galactic CRs through the heliosphere. Solar modulation studies examine the spatial, energy and time dependence of CR intensities throughout the heliosphere.

Cosmic rays can roughly be classified as follows:

- Galactic cosmic rays (GCRs) coming from outside the solar system, probably accelerated by supernova explosions to very high energies, from a about 1 MeV to as high as $\sim 10^{21}$ eV.
- Anomalous cosmic rays (ACRs) accelerated at the solar wind termination shock (TS). Data from the Voyager 1 spacecraft crossing of the TS shock suggest another type, dubbed termination shock particles also form directly at the TS (Stone et al., 2005).
- Solar energetic particles produced on the Sun by e.g. solar flares. Coronal mass ejections and shocks in the interplanetary medium can also produce these energetic particles. They have energies up to several hundred MeV, even a few GeV, but are observed at Earth for only a few hours.
- Jovian electrons that originate in the magnetosphere of Jupiter.

Cosmic rays were discovered during the period 1911-13 by the Austrian scientist Victor Hess. Before his discovery, scientists had been puzzled by the fact that the air in electroscopes became ionized irrespectively of how well the containers were insulated. They thought that radioactivity from the ground was responsible. In 1910, Theodore Wulf measured ionization at the bottom and top of the Eiffel Tower (~300 m apart), and found that considerably more ionization existed at the top than could be expected if it were caused by ground radiation, but his results were not generally accepted. Before making his historic balloon flights, Hess calculated the height at which ground radiation would stop producing ionization (~500 m) and designed instruments that would not be damaged by large changes in temperature and pressure. He then made ten historic balloon ascents, two in 1911, seven in 1912, and one in 1913, five at night, and found that ionization increased rapidly, so he concluded that a radiation of very high penetrating power enters the Earth's atmosphere from above. After making a flight during an almost total eclipse of the Sun on April 12, 1912, he further concluded that since ionization did

not decrease during the eclipse, the Sun could not itself be the main source of this radiation. His theory about 'rays from space' did not receive general acceptance at the time but increased research after World War I supported and confirmed it. The newly discovered radiation was dubbed "cosmic" by Robert Millikan in 1925. Victor Hess received the Nobel Price for this accomplishment in 1936 (with Carl Anderson who discovered positrons).
This and more biographical information about him can be found at

www.mpi-hd.mpg.de/hfm/HESS/public/hessbio.html, and
nobelprize.org/nobel_prizes/physics/laureates/1936/hess-bio.html.

The properties of these energetic particles are very important because they represent considerable hazard to both human and radiation sensitive systems in space where there high fluxes and energy can cause permanent effects in biological materials or miniature electronic circuits. They also carry information about the large scale properties of the heliosphere and the galaxy. Knowing the basic properties of these high energy particles, including their elemental composition, energy spectra and temporal variations is important for understanding more about our space environment, from ground level up to distant galaxies.

2. Galactic cosmic rays: spectrum and composition

Galactic CRs are observed at Earth as fully ionized particles with energies from about 1 MeV to as high as $\sim 10^{21}$ eV. Excluding low energy CRs, the 'all-particle' differential intensity spectrum, shown in Figure 1 is in the form of a power law with a spectral index of -2.7, but steepening to $\propto E^{-3.0}$ at the 'knee' region at about $\sim 10^{15}$ eV. A second smaller spectral break occurs at $\sim 10^{19}$ eV, called the 'ankle' region. It is generally believed that galactic CRs below the knee region are created inside our Galaxy and contained in the galactic magnetic field for up to $\sim 1.5 \times 10^{7}$ yrs (Ave et al., 2008 and reference therein). For energies above the knee region, the gyro-radii of the particles become large enough to escape the confines of the Galaxy, and it is believed that these particles have an extra-galactic origin. The generally accepted paradigm of galactic CR creation inside our Galaxy is through the process of diffusive

shock acceleration occurring at the shock front of supernovae. Note that the intensities decrease by about 30 orders of magnitude on the logarithmic scaling. At energies less than 10 GeV, significant modulation can take place when CRs enter the heliosphere.

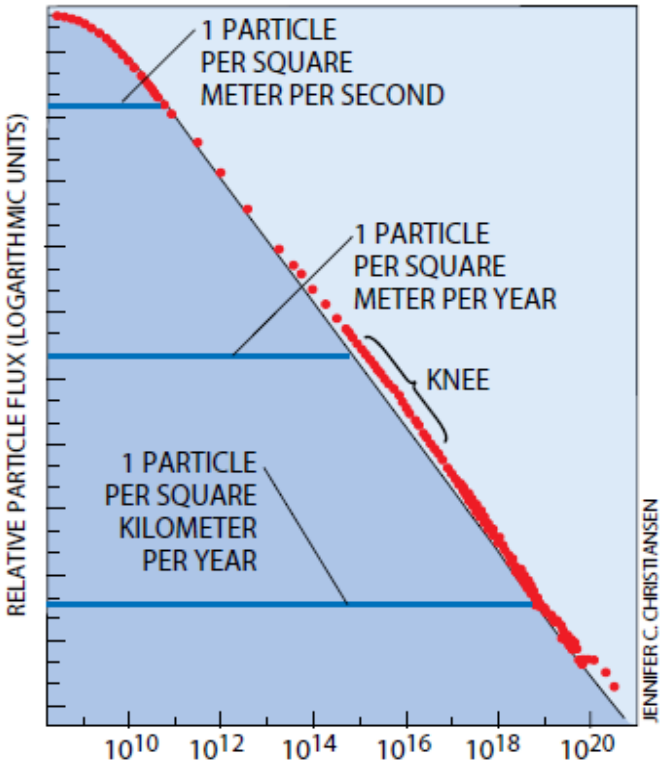

Figure 1. *The 'all-particle' energy spectrum of cosmic rays measured at the Earth. Note the power-law shape, with two spectral brakes, nicknamed 'knee' and 'ankle'. (http://www.telescopearray.org/images; Cronin et al., 1998).*

Figure 2 shows the measured composition of galactic CRs at an intermediate energy of ~1 GeV/nucleon. The relative abundances decrease with increasing charge number. At this energy range, galactic CRs are composed almost entirely of protons and helium with much smaller amounts of heavier nuclei (~1%), Hörandel (2008). Electrons account for ~1 % of the CRs. Two groups of elements Li, Be, B and Sc, Ti, V, Cr, Mn are many orders of magnitude over-

abundant in CRs than in the solar system. These exceptions yield important information about the galactic matter traversed by CRs. The isotopic composition provides key information about the origin, acceleration and transport mechanisms of CRs in our galaxy.

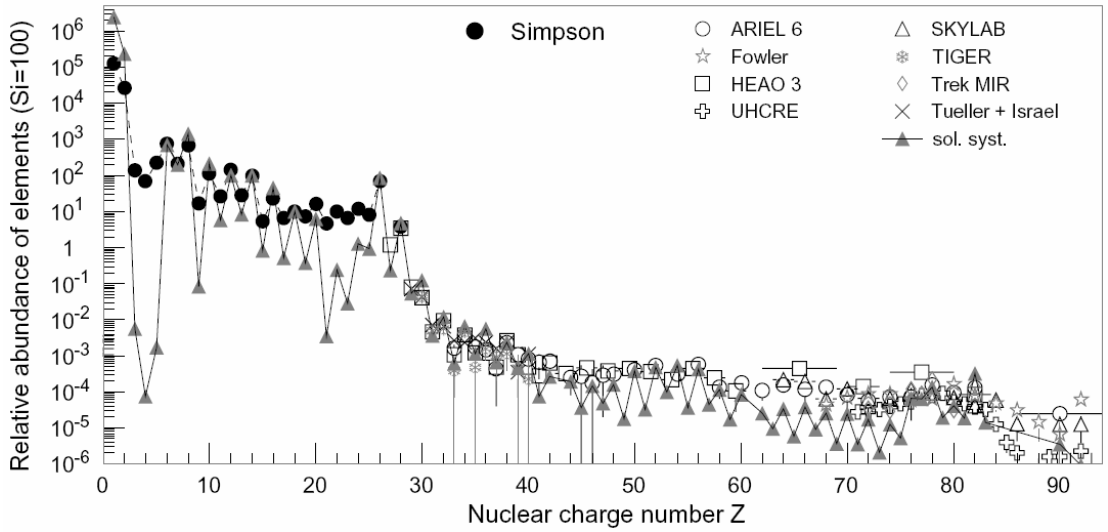

Figure 2. *The relative abundances of different galactic CR elements as a function of charge number as observed by different experiments, scaled to Si; from Hörandel (2008). Also see the appendix.*

3. Solar modulation of galactic cosmic rays

The Sun is constantly blowing its plasmatic atmosphere from its surface, producing the solar wind which transports the Sun's magnetic field into heliospace. This magnetic field determines the passage of CRs from the interstellar medium to Earth as a function of time, energy and position in the heliosphere. This process is known as the solar (or heliospheric) modulation of CRs. When CRs enter the heliosphere, they experience four major modulation processes: (1) Convection with the solar wind. (2) Adiabatic energy changes. (3) Diffusive random walk along and across the heliospheric magnetic field (HMF). (4) Drift motions caused by gradients and curvatures in the HMF or any abrupt changes in the field direction such as the heliospheric current sheet. These four major processes are described in full by Parker's transport equation (1958, 1965) that will be discussed below.

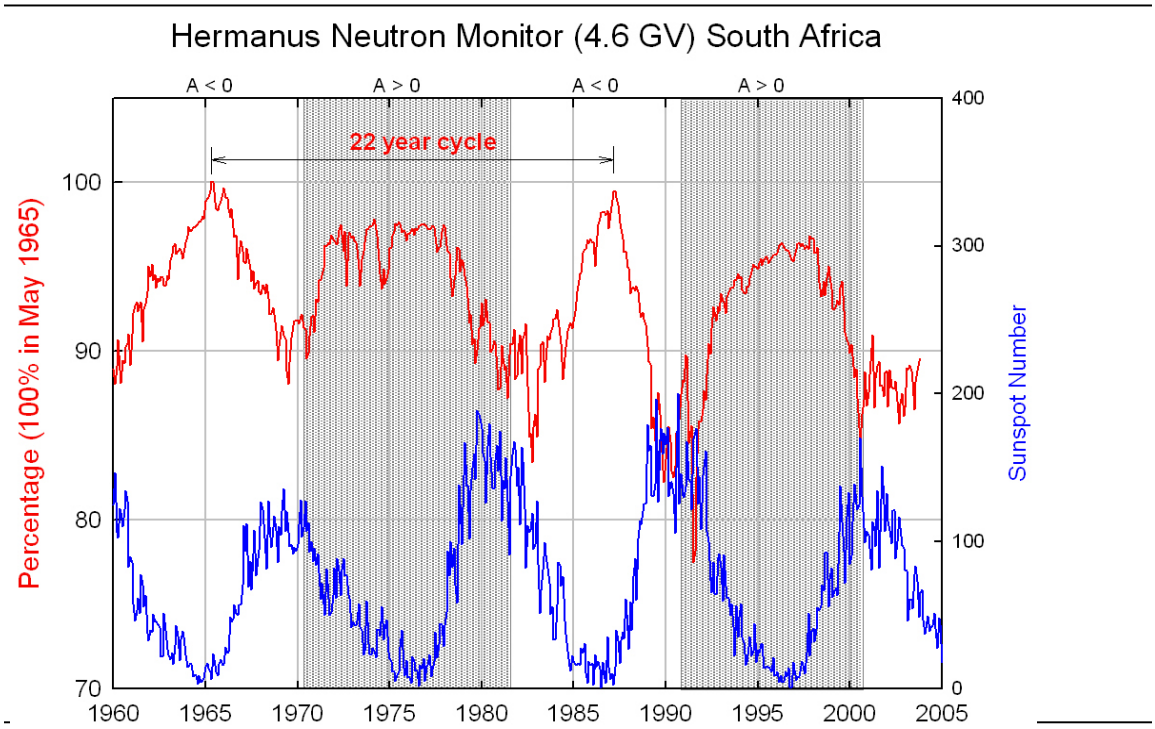

Figure 3. The 11-year modulation of galactic CRs as recorded by the Hermanus cosmic ray detector (neutron monitor) in South Africa with cut-off rigidity of 4.6 GV in comparison with sunspot numbers, showing the anti-correlation between solar activity and CR intensity. (Graph created by Rex Manuel). (sunspot data, http://www.ngdc.noaa.gov/stp/SOLAR/ftpsunspotnumber.html#international and Hermanus neutron monitor data, Unit for Space Physics, NWU).

Long term CR observations at ground level are made by so-called neutron monitors (NMs). Figure 3 shows the monthly average Hermanus NM count rate from 1960 onwards in comparison with solar activity as inferred from the international sunspot number. Note the anti-correlation between the NM counts and solar activity levels through the ~11 year solar activity cycle. During solar maximum conditions CRs are modulated more efficiently through an increase in the HMF strength and by increased turbulence. This leads to a decrease in the CR flux as observed at Earth in anti-correlation with solar activity. During solar minimum conditions, the CR flux at Earth becomes a maximum, decreasing to a minimum when solar activity reaches a maximum, giving rise to the 11-year cycle. Also evident from Figure 3 is the 22-year cycle in CR modulation caused by drifts and the reversal of the solar magnetic field

about every 11 years. Because CRs are charged particles, their drift motions in the background HMF are highly dependent on the geometry of the HMF, causing different drift patterns (and intensities) during different HMF polarity configurations known as $A > 0$ and $A < 0$ polarity periods (see Figure 5): $A > 0$ polarity cycle is when positively charged particles drift inwards to the Sun mainly through the polar regions of the heliosphere while during the $A < 0$ cycle protons drift inwards mainly through the equatorial regions of the heliosphere with consequences as shown in Figure 3. Negatively charged particles will drift in the opposite direction causing charged-sign-dependent modulation. See reviews by Heber and Potgieter (2006, 2007).

There are additional short periodicities evident in NM and other cosmic ray data, e.g., the 25-27-day variation owing to the rotational Sun, and the daily variation owing to the Earth's rotation. These variations seldom have magnitudes of more than 1% with respect to the previous quite time fluxes. Corotating interaction regions (CIRs) usually merge as they propagate outwards to form various types of interaction regions, the largest ones are known as global merged interaction regions (GMIRs). They are related to coronal mass ejections (CMEs) that are prominent with increased solar activity but dissipating during solar minimum. Although CIRs may be spread over a large region in azimuthal angle, they cannot cause long-term CR periodicities on the scale (amplitude) of the 11 year cycle. An isolated GMIR may cause a decrease similar in magnitude than the 11 year cycle but it usually lasts only several months. A series of GMIRs, on the other hand, may contribute significantly to long-term CR modulation during periods of increased solar activity, in the form of large discrete steps, increasing the overall amplitude of the 11 year cycle. These variations are causing the step-like changes in the CR intensity seen in Figure 4. See also the reviews by Potgieter (2008a,b).

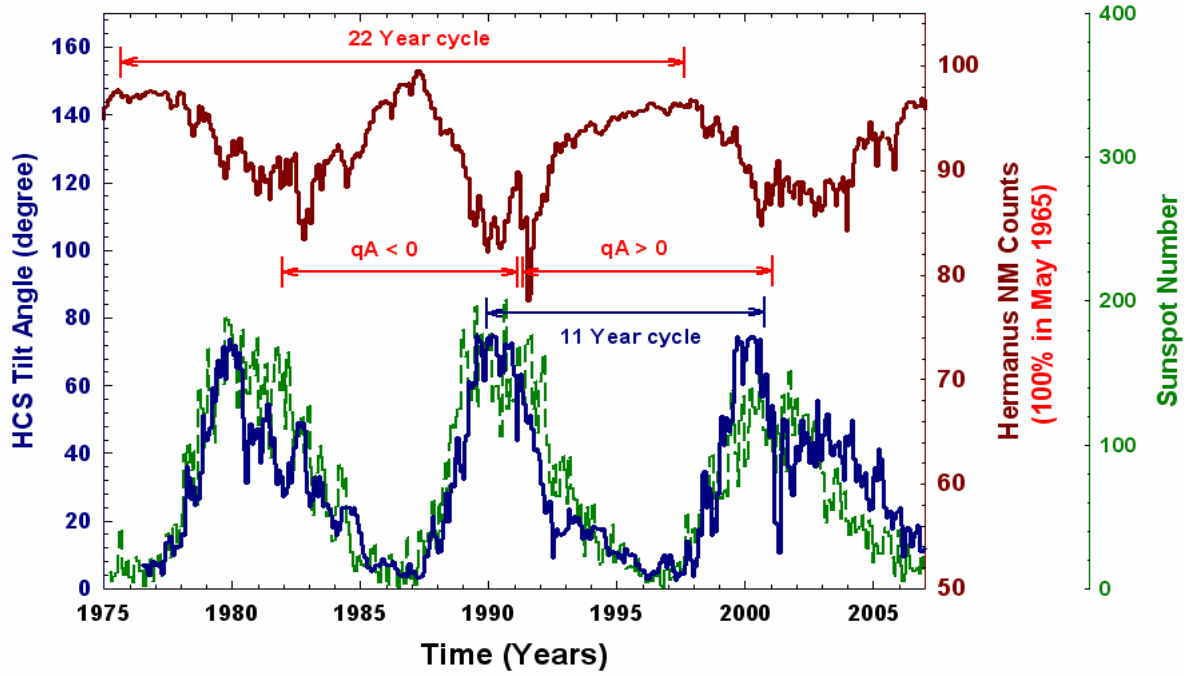

Figure 4. *The figure shows the monthly averaged NM count rates as registered by the Hermanus NM (solid red line). Also shown is the solar activity as inferred from the international sunspot number and the heliospheric current sheet tilt angle (Graph created by Du Toit Strauss).*

A major corotating structure in the heliosphere is the current sheet (HCS) which divides the solar magnetic field into hemispheres of opposite polarity, changing sign across this current sheet. Every ~11 years this field reverses polarity. The periods when the field is directed outwards in the northern hemisphere has become known as A > 0 epochs e.g., during the 1970's and 1990's, while the 1980's and the present epoch (2000~2010) are known as A < 0 cycles. The consequent 11-year and 22-year solar cycles and their effects on CRs are discussed below. The HCS has a wavy structure and is well correlated to solar activity. The waviness originates because the magnetic axis of the Sun is tilted relative to the rotational axis, approximated by using its tilt angle α close to the Sun (see lower panel of Figure 4). During high levels of activity, the observed $\alpha \rightarrow 75°$, becoming undetermined during times of extreme solar activity. During low solar activity the axis of the magnetic equator and the heliographic equator become nearly aligned, causing a relative small waviness with $\alpha = 5°\text{-}10°$. The tilt angles from 1976 onwards can be obtained from the Wilcox Solar Observatory at http://wso.stanford.edu/. The

waviness of the HCS plays an important role in CR modulation as were pointed out originally by Thomas and Smith (1981). It is still the best proxy for solar activity from a CR point of view. It is widely used in numerical modeling and some aspects are discussed below. A disadvantage is that it is not well-known how the waviness is preserved as it moves into the outer heliosphere and up to the TS. For a review on this subject, see Smith (2001).

The 11 and 22 year cycles together with the step-like modulation evident in Figure 4, in comparison with the heliospheric current sheet tilt angle, are good examples of the interplay of the main modulation mechanisms; global gradient, curvature and HCS drifts playing a dominant role during periods of minimum solar activity in conjunction with convection, diffusion and adiabatic energy losses.

Apart from the obvious 11-year and 22-year cycles, there are also indications of CR periods of 50-65 years and 90-130 years, also for a periodicity of about 220 and 600 years (e.g., McCracken et al., 2004). It is not yet clear whether these variabilities should be considered 'perturbations' or truly time-structured to be figured as superpositions of several periodic processes. Cases of strong 'perturbations' of the consecutive 11 year cycles are the 'grand minima' in solar activity, with the prime example the Maunder minimum (1640-1710) when sunspots almost completely disappeared. Assuming the HMF to have vanished as well or without any reversals during the Maunder minimum would be an oversimplification. The heliospheric modulation of CRs could have continued during this period but much less pronounced (with a small amplitude). It is reasonable to infer that less CMEs, for example, occurred so that the total flux of CRs at Earth then should have been higher than afterwards. See also the notes on Space Climate.

The galactic CR flux is not expected to be constant along the trajectory of the solar system in the galaxy. Interstellar conditions should differ significantly over very long time-scales, for example, when the Sun moves in and out of the galactic spiral arm (Shaviv, 2003). It is accepted that the concentration of ^{10}Be nuclei in polar ice exhibits temporal variations in response to changes in the flux of the primary CRs (Masarik and Beer, 1999, and references

therein). Exploring CR modulation over timescales of hundreds of years and during times when the heliosphere was significantly different from the present epoch is a very interesting development. The above mentioned topic has become known as space climate.

A proper understanding of the modulation cycles of galactic cosmic rays in the heliosphere up to energies of ~20 GeV requires knowledge of the galactic spectra for the various cosmic rays species. Reliable galactic spectra have been calculated by e.g., Moskalenko et al. (2002) and are widely in use. These spectra do not take into account contributions from the local interstellar medium, in fact, the very local interstellar spectra (LIS) below ~10 GeV required for detail modulation studies are difficult to determine. In Figure 5, the present available computed spectra for cosmic ray protons, anti-protons, electrons, anti-electrons, Helium, Boron and Carbon are compiled and illustrated.

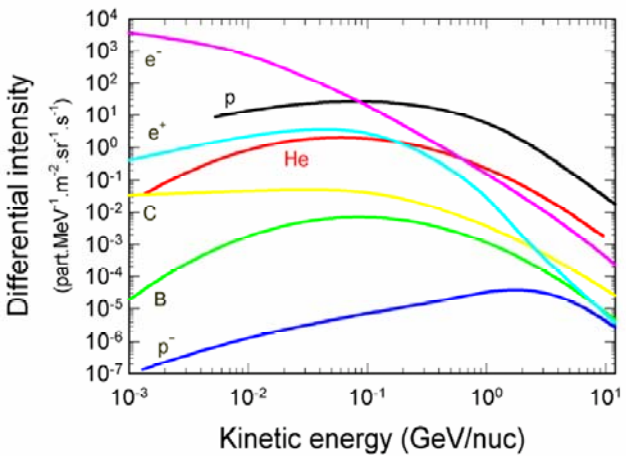

Figure 5. *A compilation of computed galactic spectra for cosmic ray protons, anti-protons, electrons, anti-electrons, Helium, Boron and Carbon (see also Moskalenko et al., 2002).*

4. Theoretical background and numerical models

Models for the global and long-term modulation of CRs in the heliosphere are based on numerical solutions of Parker's (1961, 1965) time-dependent transport equation (TPE):

$$\frac{\partial f}{\partial t} = -(\mathbf{V} + \langle \mathbf{v_D} \rangle) \cdot \nabla f + \nabla \cdot (\mathbf{K}_s \cdot \nabla f) + \frac{p}{3} (\nabla \cdot \mathbf{V}) \frac{\partial f}{\partial p} + J_{source}, \quad (1)$$

where $f(\mathbf{r},p,t)$ is the CR distribution function; p is momentum, $\mathbf{r}$ is position, $\mathbf{V}$ is the solar wind velocity and t is time. $\mathbf{V}$ is the solar wind velocity and $\mathbf{K}$ is the diffusion tensor. Terms on the right-hand side represent respectively convection, gradient, and curvature drifts, diffusion, adiabatic energy changes, and a source function e.g., for the anomalous CR component. The tensor $\boldsymbol{K_s}$ consists of a parallel diffusion coefficient ($K_{||}$) and two perpendicular diffusion coefficients, one in the radial direction ($K_{\perp r}$) and one in the polar direction ($K_{\perp\theta}$). The pitch angle averaged guiding center drift velocity for a near isotropic CR distribution is given by $\langle \mathbf{v}_D \rangle = \nabla \times (K_A \mathbf{e}_B)$, with $\mathbf{e}_B = \boldsymbol{B}/B_m$ and B_m the magnitude of the modified background HMF, with K_A the off-diagonal element of the full diffusion tensor. The rigidity is defined as the momentum per charge for a given species of particles. For clarity on the role of diffusion, drifts, convection, and adiabatic energy loss, the TPE is written as follows:

$$\frac{\partial f}{\partial t} = \overbrace{\left[\frac{1}{r^2}\frac{\partial}{\partial r}\left(r^2 K_{rr}\right) + \frac{1}{r\sin\theta}\frac{\partial K_{\phi r}}{\partial \phi}\right]\frac{\partial f}{\partial r} + \left[\frac{1}{r^2\sin\theta}\frac{\partial}{\partial\theta}\left(K_{\theta\theta}\sin\theta\right)\right]\frac{\partial f}{\partial\theta}}^{diffusion}$$

$$+ \overbrace{\left[\frac{1}{r^2\sin\theta}\frac{\partial}{\partial r}\left(rK_{r\phi}\right) + \frac{1}{r^2\sin^2\theta}\frac{\partial K_{\phi\phi}}{\partial\phi} + \Omega\right]\frac{\partial f}{\partial\phi}}^{diffusion}$$

$$+ \overbrace{\left[K_{rr}\frac{\partial^2 f}{\partial r^2} + \frac{K_{\theta\theta}}{r^2}\frac{\partial^2 f}{\partial\theta^2} + \frac{K_{\phi\phi}}{r^2\sin^2\theta}\frac{\partial^2 f}{\partial\phi^2} + \frac{2K_{r\phi}}{r\sin\theta}\frac{\partial^2 f}{\partial r\partial\phi}\right]}^{diffusion}$$

$$+ \overbrace{\left[\left[-\left\langle \mathrm{v}_d \right\rangle_r\right]\frac{\partial f}{\partial r} + \left[-\frac{1}{r}\left\langle \mathrm{v}_d \right\rangle_\theta\right]\frac{\partial f}{\partial\theta} + \left[-\frac{1}{r\sin\theta}\left\langle \mathrm{v}_d \right\rangle_\phi\right]\frac{\partial f}{\partial\phi}\right]}^{drift}$$

$$\overbrace{-V\frac{\partial f}{\partial r}}^{convection} + \overbrace{\frac{1}{3r^2}\frac{\partial(r^2V)}{\partial r}\frac{\partial f}{\partial lnP}}^{adiabatic\ energy\ changes} + \overbrace{Q_{source}}^{sources}. \qquad (2)$$

The components of the drift velocity in three dimensions are:

$$\left\langle \mathrm{v}_d \right\rangle_r = -\frac{A}{r\sin\theta}\frac{\partial}{\partial\theta}(\sin\theta K_{\theta r}), \qquad (3)$$

$$\langle \mathrm{v}_d \rangle_\theta = -\frac{A}{r}\left[\frac{1}{\sin\theta}\frac{\partial}{\partial\phi}(K_{\phi\theta}) + \frac{\partial}{\partial r}(rK_{r\theta})\right],$$

$$\langle \mathrm{v}_d \rangle_\phi = -\frac{A}{r}\frac{\partial}{\partial\theta}(K_{\theta\phi}),$$

or alternatively

$\langle \mathrm{v}_d \rangle_\phi = \nabla \times K_A \mathbf{e}_B$; $\mathbf{e}_B = \mathbf{B}_m / B$, and K_A the "drift" coefficient,

here $A = sign(Bq)$ determines the drifts direction of the charged particles in the heliosphere. For the A > 0 polarity cycle, positively charged particles drift from the polar region of the heliosphere down to the equatorial regions and they are largely insensitive to the conditions in the equatorial region, e.g. changes in HCS. For A < 0 polarity cycle, positively charged particles drift primarily in along the HCS and out over the polar regions and are sensitive to changes in the tilt angle of the HCS. These drift directions are shown in Figure 6 for protons. For negatively charged particles the drift is in the opposite direction.

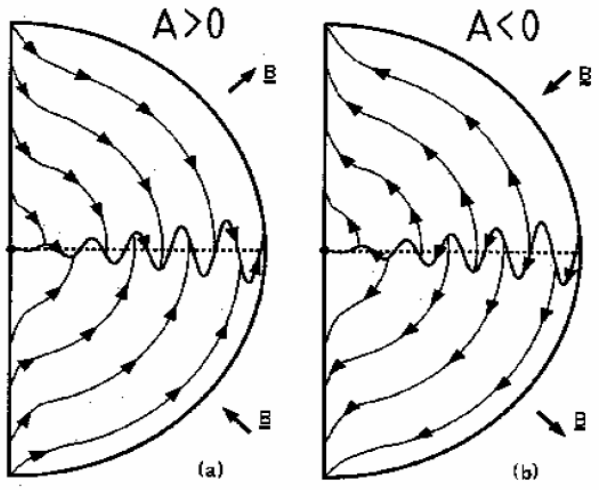

Figure 6. *The drift direction of protons caused by gradients, curvature and the current sheet of the HMF for (a) the A > 0 HMF, and (b) the A < 0 HMF polarity. The electron drift directions are opposite of the proton drift directions (Jokipii and Thomas, 1981).*

The transport of charged particles in the heliosphere is determined by a heliospheric diffusion tensor. This diffusion tensor **K** as introduced in the TPE above is given by the following

$$\mathbf{K} = \begin{bmatrix} K_{\parallel} & 0 & 0 \\ 0 & K_{\perp\theta} & K_A \\ 0 & -K_A & K_{\perp r} \end{bmatrix}, \tag{4}$$

where $K_{\parallel}$ is the diffusion coefficient parallel to the mean HMF, $K_{\perp\theta}$ and $K_{\perp r}$ denote the diffusion coefficients perpendicular to the mean HMF in the polar and radial direction respectively and the anti-symmetric K_A, describes particle drifts which include gradient, curvature and heliospheric current sheet drift in the large scale HMF as described above. The elements of the diffusion tensor with respect to heliocentric spherical coordinates are obtained by using the transformation matrix

$$\mathbf{T} = \begin{bmatrix} \cos\psi & 0 & \sin\psi \\ 0 & 1 & 0 \\ -\sin\psi & 0 & \cos\psi \end{bmatrix},$$

where ψ is the spiral angle of the HMF. That is:

$$\begin{bmatrix} K_{rr} & K_{r\theta} & K_{r\phi} \\ K_{\theta r} & K_{\theta\theta} & K_{\theta\phi} \\ K_{\phi r} & K_{\phi\theta} & K_{\phi\phi} \end{bmatrix} = \mathbf{TKT}^T,$$

$$= \begin{bmatrix} \cos\psi & 0 & \sin\psi \\ 0 & 1 & 0 \\ -\sin\psi & 0 & \cos\psi \end{bmatrix} \begin{bmatrix} K_{\parallel} & 0 & 0 \\ 0 & K_{\perp\theta} & K_A \\ 0 & -K_A & K_{\perp r} \end{bmatrix} \begin{bmatrix} \cos\psi & 0 & -\sin\psi \\ 0 & 1 & 0 \\ \sin\psi & 0 & \cos\psi \end{bmatrix},$$

$$= \begin{bmatrix} K_{\parallel}\cos^2\psi + K_{\perp r}\sin^2\psi & -K_A\sin\psi & (K_{\perp r} - K_{\parallel})\cos\psi\sin\psi \\ K_A\sin\psi & K_{\perp\theta} & K_A\cos\psi \\ (K_{\perp r} - K_{\parallel})\sin\psi\cos\psi & -K_A\cos\psi & K_{\perp r}\cos^2\psi + K_{\parallel}\sin^2\psi \end{bmatrix}, \tag{5}$$

where the superscript T denotes the transpose. A theoretical challenge in modulation is to determine the elements $K_{\parallel}$, $K_{\perp r}$, $K_{\perp\theta}$ and K_A as a function of rigidity (energy), position and time.

The present understanding of the mechanisms of global modulation in the heliosphere, as described above, is considered essentially correct. However, the main obstacle in solving Eq.

(1) is insufficient knowledge of the spatial, rigidity and especially the temporal dependence of the diffusion coefficients including the underlying features of the magnetic field turbulence, the size and geometry of heliosphere.

Figure 7 shows contour plots of the computed normalized differential intensity of 200 MeV galactic CR protons in the meridional plane of the heliosphere for the A < 0 polarity cycle (left panel) and the A > 0 cycle (right panel). This illustrates how the drift patterns in the heliosphere differ for protons during two successive 11-years cycles, essentially creating a clear 22-year cycles in galactic CR modulation.

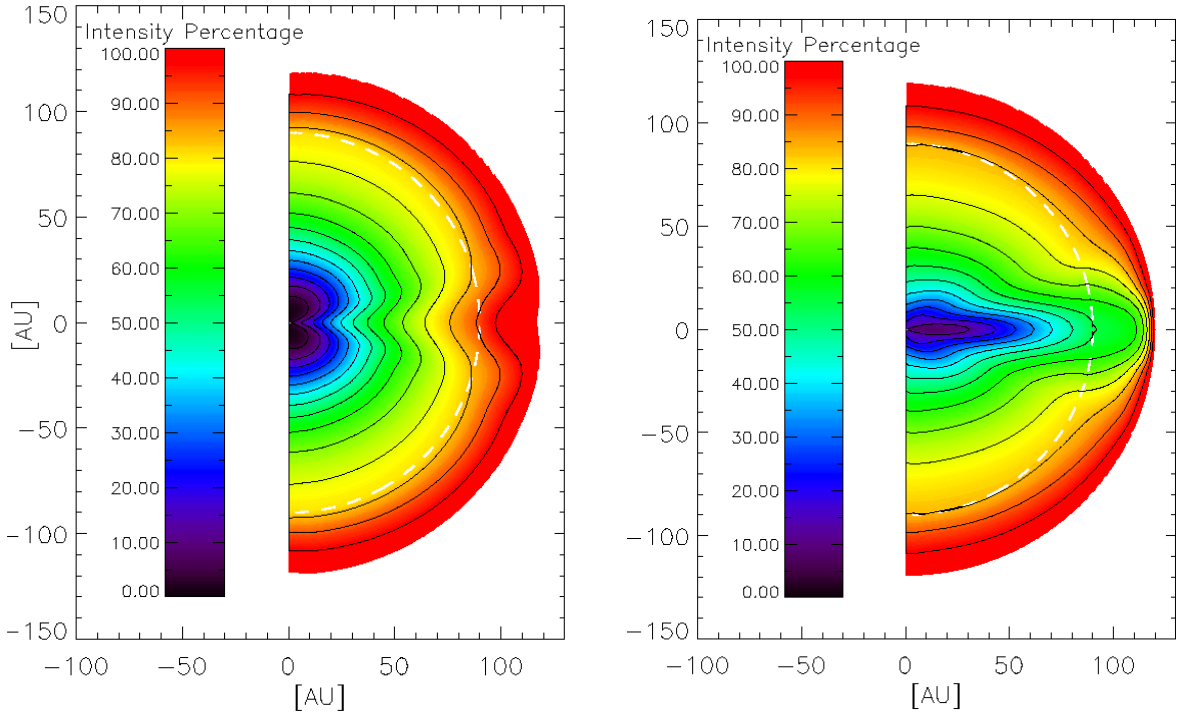

Figure 7. *Contour plots showing the normalized differential intensity of 200 MeV galactic CR protons in the meridional plane of the heliosphere for the A < 0 polarity cycle (left panel) and the A > 0 cycle (right panel). Note the different drift patterns in the figures, owing to the HMF polarity reversal. Red is high intensities, dark blue is for the lowest intensities. (Graphs created by Du Toit Strauss).*

The spatial and rigidity dependence of the elements of the diffusion tensor are not well-known but serious efforts are being made to improve the situation to come to an 'ab initio' formulation

(Bieber, 2003) of CR modulation in which the diffusion coefficients are calculated from basic diffusion (scattering) theories and from the underlying fluctuating parameters based on plasma and turbulence theories using known features of the solar wind and the HMF. These approaches must eventually be tested against CR observations at Earth, from Ulysses, the two Voyager and other spacecraft. Diffusion theory involves several turbulence parameters so that one needs to understand how solar wind turbulence evolves throughout the heliosphere, also at high heliolatitudes, and now also in the heliosheath. While in-situ observations at and inside ~1 AU from the Sun can be used as boundary conditions understand the process throughout the heliosphere is required. All CR transport models require knowledge of the global structure and geometry of heliosphere, the HMF, the HCS and the solar wind velocity. Observations by the Pioneer, Voyager, Ulysses and other spacecraft have contributed significantly to understand the spatial dependence and time evolution of these features.

5. Global causes of the 11-year and 22-year cycles

Significant progress has been made in solving Eq.(1) numerically with increasing sophistication and complexity, also time-dependently for both the $A > 0$ and $A < 0$ magnetic polarity cycles, using as main input parameters the time varying HCS tilt angles and the time varying measured HMF values at Earth (NSSDC COHOWeb: http://nssdc.gfc.nasa.gov/cohoweb). A basic departure point for the time-dependence of global, 11-year modulation is that propagating barriers (solar wind and magnetic field structures inhibiting the easy access of CRs) are formed and later dissipated in the heliosphere following the solar activity cycle. These propagating barriers are especially applicable to the phase of the solar activity cycle before and after solar maximum conditions when large steps in the particle intensities have been observed. A wide range of interaction regions occur in the heliosphere, with GMIRs the largest, introduced by Burlaga et al. (1993). They observed that a clear relation exists between CR decreases (recoveries) and the time dependent decline (recovery) of the HMF magnitude, and extent, local to the observation point. The paradigm on which this modulation 'barrier' is based is that interaction (and rarefaction) regions form with increasing radial distance from the Sun. This happens when two different solar wind speed regions become radially aligned to form an

interaction region when the fast one runs into the slower one, resulting in compression fronts with forward and backward shocks. When these narrow interaction regions propagate outwards and expand, they may wrap almost around the Sun to become CIRs. When they merge and interact, merged interaction regions and finally GMIRs are formed beyond 5-10 AU. See Intriligator et al. (2005) for an illustration of how these 'barriers' developed with distance and time in the heliosphere. The effects have been successfully modelled by Ferreira and Potgieter (2004) with a compound model.

The affects of GMIRs on 11-year modulation depend on their rate of occurrence, the speed with which they propagate, their spatial extent and amplitude, especially their latitudinal extent (to disturb global drifts), and the background modulation conditions they encounter and importantly on the radius of the heliosphere (i.e., how long they stay inside the modulation volume). Drifts, on the other hand, dominate the solar minimum modulation periods up to four years so that during an 11-year cycle a transition must occur (depending how solar activity develops and declines) from a period dominated by drifts to a period dominated by these propagating structures. The largest of the step decreases and recoveries shown in Figures 3 and 4 are caused by these GMIRs. The 11-year and 22-year cycles together with the step-like modulation, evident in Figures 3 and 4, are good examples of the interplay of the main modulation mechanisms; global gradient and curvature drifts playing a dominant role during periods of minimum solar activity in conjunction with convection, diffusion and adiabatic energy losses.

6. Charge-sign dependent modulation

Charge-sign dependent modulation is one of the important features of CR modulation because it is a direct indication of gradient, curvature, and HCS drifts. For a review, see Heber and Potgieter (2006, 2007). An important accomplishment of this compound approach is that it also produces the observed charge-sign dependent CR modulation from minimum to maximum solar activity.

7. Modulation in the heliosheath

Considering the modulation shown in Figure 4, the question that is relevant within the context of present Voyager 1 and 2 observations is how much modulation occurs inside the heliosheath and where does the CR modulation actually start? Can the heliosheath consider to be a modulation 'barrier'? The process is of course highly energy dependent so that the answer must depend on the energy range of CRs. An illustrative example of the amount of modulation that galactic CR protons may experience in the heliosheath in the nose direction is shown in Figure 8.

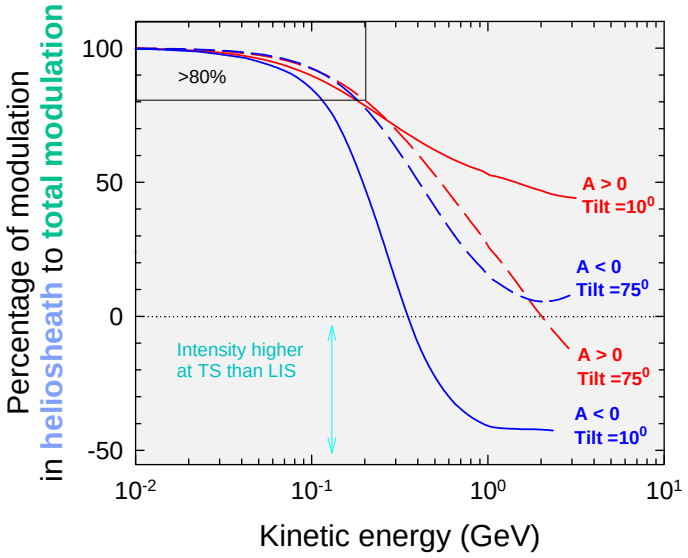

Figure 8. *Computed percentage of CR modulation in the heliosheath with respect to the total modulation (between 120 and 1 AU) as a function of kinetic energy for the two magnetic polarity cycles (A > 0 and A < 0), for solar minimum (α = 10°) and for moderate maximum (α = 75°) conditions, in the equatorial plane in the nose direction of the heliosphere. Negative percentages mean that the CRs can be reaccelerated at the TS.*

The percentage of modulation in the equatorial plane in the heliosheath is given with respect to the total modulation (between 120 AU and 1 AU) as a function of kinetic energy for both polarity cycles (A > 0 and A < 0), for solar minimum ($\alpha = 10°$) and moderate maximum ($\alpha = 75°$) conditions. Evidently, at E < ~0.02 GeV modulation of > 80% may occur in the heliosheath for both polarity cycles. For all four the conditions, the heliosheath modulation will

eventually reach 0% (not shown) but at different energies, indicating that it differs significantly with energy as well as with drift cycles. How much gradient and curvature drifts actually occur in the heliosheath is still unanswered. The negative percentages indicate that the intensity is actually increasing in the heliosheath as one moves inward from the outer boundary toward the TS because of the re-acceleration of CRs at the TS. This depends on many aspects, in particular the TS compression ratio.

In Figure 9 examples are shown of the modulation results of a numerical model containing a TS at 90 AU. The differential intensity is shown as a function of radial distance in AU in the left panel for three different energies. In the right hand panel the corresponding spectra are shown at various radial distances in the heliospheric equatorial plane, all for the A > 0 polarity cycle.

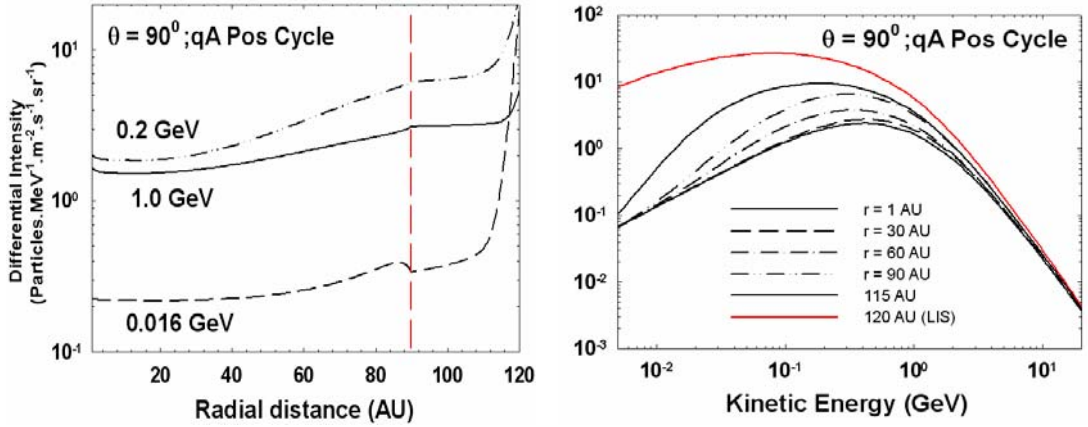

Figure 9. *The differential intensity of galactic CR protons as a function of radial distance (left panel) and as a function of energy (right panel). The position of the TS is indicated by the dashed red line, and the HP (LIS) by the solid red line. All other graphs shown later in the text were obtained for the qA > 0 polarity cycle during solar minimum conditions, in the equatorial plane (DuT Strauss).*

8. Cosmic rays in geospace

We are protected again CRs by three well-known space 'frontiers', the first one arguably the less appreciated of the three: (1) The solar wind and the accompanying relatively turbulent heliospheric magnetic field extending to distances of more than 500 AU in the equatorial plane and to more than 250 AU in the polar plane. The heliospheric volume may oscillate significantly with time depending on solar activity, and where the solar system is located in the

galaxy (Scherer et al., 2006). (2) The Earth's magnetic field, which is not at all uniform, e.g., large changes in the Earth's magnetic field are presently occurring over southern Africa. This means that significant changes in the cut-off rigidity at a given position occur. These changes seem sufficiently large over the past 400 years that the change in CR flux impacting the Earth may approximate the relative change in flux over a solar cycle (Shea and Smart, 2004). The magnetosphere also withstands all the space weather changes that the Sun produces, and can reverse its magnetic polarity on the long-term. (3) The atmosphere with all its complex physics and chemistry. The cosmic ray intensity decreases exponentially with increasing atmospheric pressure. The Sun contributes significantly to atmospheric changes through, e.g., variations in solar irradiance, and variations in the Earth's orbit.

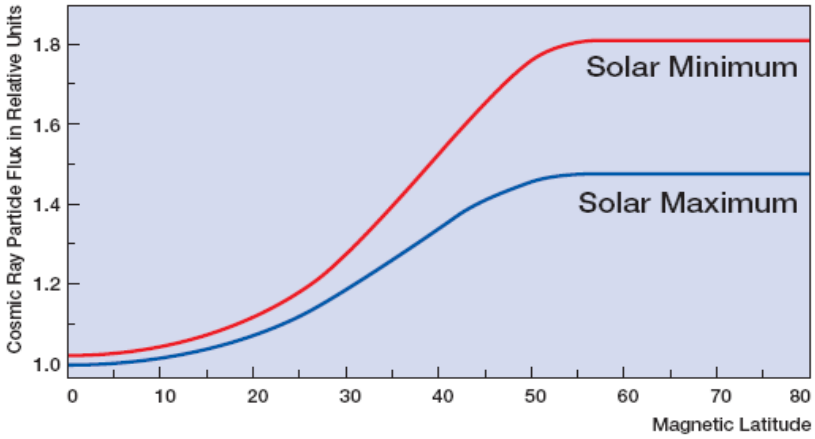

Figure 10. *Illustration of the cosmic ray latitude curve, the minimum value occur at the equator and the maximum values at polar latitudes. The values are relative since the numbers vary with altitude and solar activity. At high latitudes the cosmic ray flux levels off, since the shielding effect of the Earth's atmosphere becomes larger than the cosmic ray cut-off by the magnetic field (Schlaipfer, 2003).*

The magnetic field and the atmosphere form two powerful protective layers against the cosmic radiation on the Earth's surface. The magnetic field acts both as a shield and as a giant natural spectrometer for cosmic ray particles. If the particles possess energy, which is greater than the magnetic cut-off energy, they will cross through the magnetosphere and reach the upper layers of the atmosphere. But if their energy is insufficient, they will have a tendency to follow the

magnetic lines of force, with which they move easily, due to their lack of energy, and succeed in reaching the poles. It is the reason why the areas located near the poles receive radiation in higher quantities than near the equator, which is better protected by the Earth's magnetic field as shown in Figure 10. The second protective layer is the Earth's atmosphere. Upon arriving in the upper parts of the atmosphere, the cosmic ray particles interact with the atoms which they encounter as shown in Figure 11; these collisions create new cascades of particles that produce further successively lower energy nuclear disintegrations. This nucleonic cascade process caused by primary cosmic particles can be detected at the surface of the Earth.

9. Summary

Heliospace physics forms part of the universal physical processes that can be used to gain better understand of the features and characteristics of geospace and galactic space. The heliosphere is a typical small astrosphere. Cosmic ray variability contributes to the understanding of the importance of the complex field of space weather. Only recently has the dynamics of the heliosphere been studied and appreciated, in particular its role in cosmic ray variability and ultimately its role in space climate.

Heliospheric physics, and in particular, the outer heliosphere with the solar wind TS and heliosheath, has become most relevant and is being activity studied. The recent crossings of the TS by the two Voyager spacecraft have been a major accomplishment that has renewed the interest in CR modulation and the physics of the heliosheath. Observations of galactic and anomalous CRs in the outer heliosphere, together with the solar wind and magnetic field, have also caused new controversies and scientific issues. The acceleration of the anomalous CRs at the TS was thought to be caused mainly by diffusive shock acceleration but new information and modeling show that neglected mechanisms such as stochastic acceleration and solar wind adiabatic heating may be equally important.

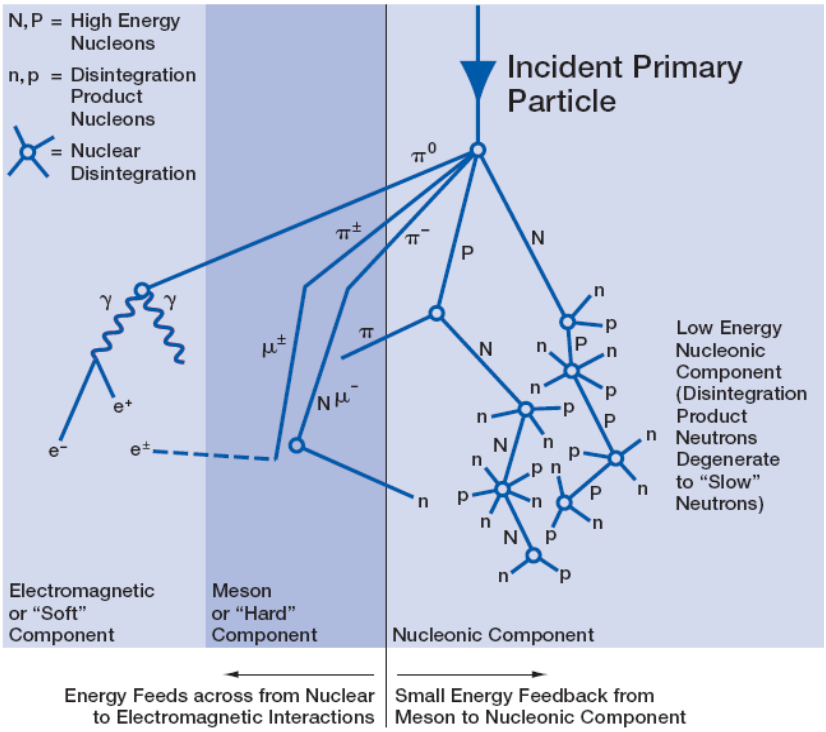

Figure 11. *A schematic diagram of a cosmic ray shower, an incident cosmic ray particle interacts with the atoms at the top of the atmosphere. Due to its high energy it disintegrates the atoms producing a cascade of electromagnetic radiation, of muons and nucleons, of which the neutrons are detected by the neutron monitors (Schlaipfer, 2003).*

Several challenges need to be studied: What is the global strength and structure of the TS? How are energetic particles accelerated at and beyond the TS? What are the global properties of the plasmatic flow beyond the TS and in the heliotail? How does the interstellar flow interact with the heliosphere beyond the HP? Understanding this physics will give the theoretical and modeling tools to study broader issues in both heliophysics and astrophysics.

The study of the heliosheath, the heliopause and the heliospheric interface with the local interstellar medium and how galactic and anomalous cosmic rays respond to the global dynamics thereof, will be one of the prominent heliospace research topics for the coming years.

References

Ave, M. et al. Composition of cosmic-ray nuclei at high energies. Astrophys. J. 678, 262, 2008.

Bieber, J.W., 2003. Transport of charged particles in the heliosphere: Theory. Adv. Space Res. 32, 549-560.

Burlaga, L. F. and McDonald, F. B. and Ness, N. F., Cosmic ray modulation and the distant heliospheric magnetic field - Voyager 1 and 2 observations from 1986 to 1989, J. Geophys. Res., 98, 1, 1993.

Cronin, J. W. Gaisser, T. K. and Swordy, S. P. Cosmic rays at the energy frontier, Scientific American, 62-67, 1998.

Ferreira, S. E. S. and Potgieter, M. S., Long-term cosmic-ray modulation in the heliosphere, Astrophys. J, 603, 744-752, 2004.

Heber, B., Potgieter, M. S. Cosmic rays at high heliolatitudes, Space Sci. Rev. 127, 117-194, 2006.

Heber, B. and Potgieter, M.S. Galactic and anomalous cosmic rays through the solar cycle: New insights from Ulysses', The heliosphere through the solar activity cycle, (A. Balogh and L. J. Lanzerotti, eds.) Springer, 2007.

Hörandel, J. R. Cosmic-ray composition and its relation to shock acceleration by supernova remnants. Adv. Space Res., 41, 442, 2008.

Intriligator, D. S., Sun, W., Dryer, M., Fry, C. D., Deehr, C., Intriligator, J. From the Sun to the outer heliosphere: Modeling and analyses of the interplanetary propagation of the October/November (Halloween) 2003 solar events, J. Geophys. Res., 110, 9, 2005.

Jokipii, J. R., and B. Thomas, Effects of drifts on the transport of cosmic rays. IV – Modulation by a wavy interplanetary current sheet, Astrophys. J., 243, 1115, 1981.

McCracken, K. G., McDonald, F. B., Beer, J,. Raisbeck, G. and Yiou, F. A., Phenomenological study of the long-term cosmic ray modulation, 850–1958 AD, J. Geophys. Res., 109, A12103, 2004.

Masarik, J., Beer, J., Simulation of particle fluxes and cosmogenic nuclide production in the Earth's atmosphere, J. Geophys. Res. 104, 12099, 1999.

Moskalenko, I. V., Strong, A. W., Ormes, J. F., Potgieter, M. S. Secondary antiprotons and propagation of cosmic rays in the galaxy and heliosphere. Astrophys. J. 565, 280, 2002.

Parker, E. N., Cosmic ray modulation by the solar wind. Physical Reviews, 110, 1445, 1958.

Parker, E. N., The Stellar-Wind Regions. Astrophys. J., 134, 20, 1961.

Parker, E. N. The passage of energetic charged particles through interplanetary space. Planet. Space Sci. 13, 9–49, 1965.

Potgieter M. S. Solar cycle variations and cosmic rays. J. Atmosp. & Solar-Terres. Phys. 70, 207-218, 2008a.

Potgieter M. S. Challenges to cosmic ray modeling: From beyond the solar wind termination shock. Adv. Space Res. 41, 245–258, 2008b.

Schlaipfer, H. Cosmic rays, Spatium, Association Pro International Space Science Institute, 2003.

Scherer, K., Fichtner, H., Borrmann, T., Beer, J., Desorgher, L., Flückiger, E., Fahr, H.-J., Ferreira, S.E.S., Langner, U.W., Potgieter, M.S., Heber, B., Masarik, J., Shaviv, N., Veizer, J. Interstellar-terrestrial relations: variable cosmic environments, the dynamic heliosphere and their imprints on terrestrial archive and climate. Space Sci. Rev. 127, 327–465, 2006.

Shaviv, N.J. The spiral structure of the Milky Way, cosmic rays, and ice age epochs on Earth. New Astron. 8, 39-77, 2003.

Smith, E. J. The heliospheric current sheet. J. Geophys. Res. 106, 15819-15832, 2001.

Stone E. C., Cummings, A. C., McDonald F. B., Heikkila B. C., Lal N., Webber W. R. Voyager 1 explores the termination shock region and the heliosheath beyond. Science, 309, 2017, 2005.

Thomas, B. T., Smith, E. J. The structure and dynamics of the heliospheric current sheet. J. Geophys. Res. 86, 11105, 1981.

Appendix

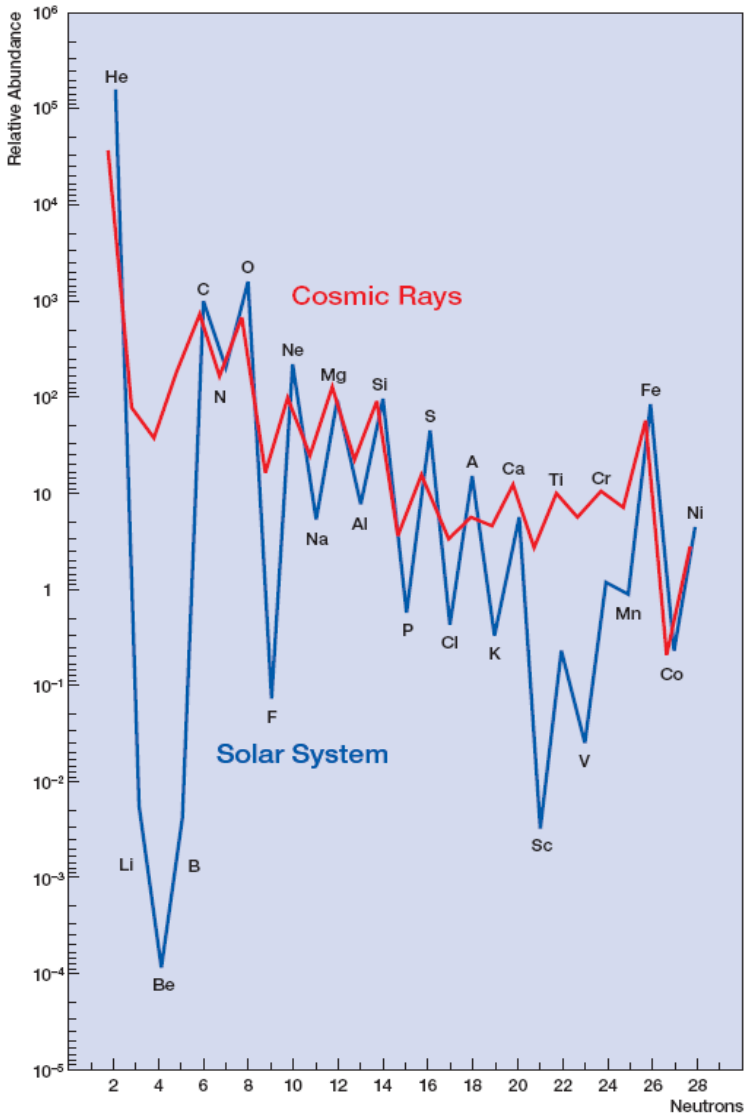

Relative abundance of He to Ni in cosmic rays (red line) and in the solar system (blue line) (Schlaipfer, 2003).

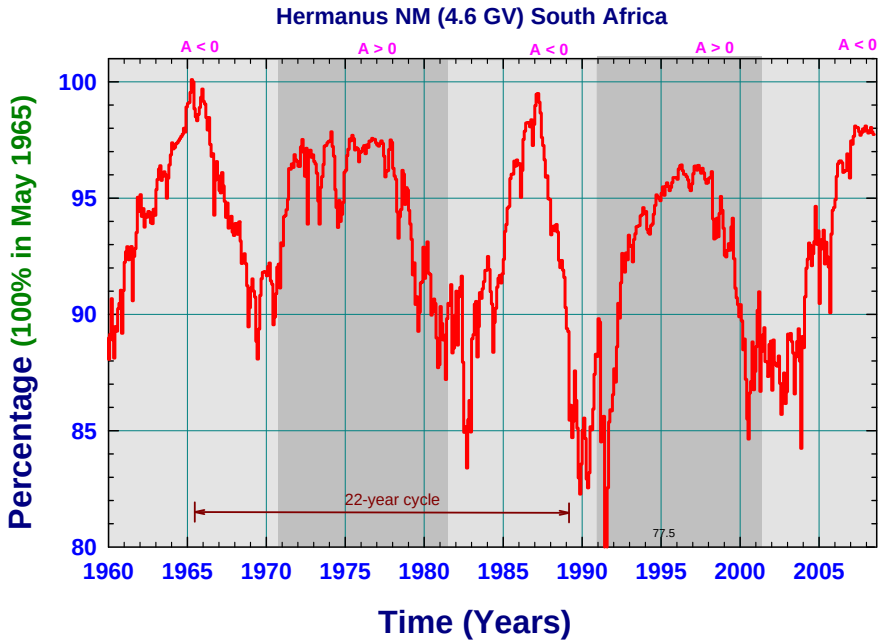

The Hermanus Cosmic Ray Monitor in South Africa, illustrating the 11-year and 22-year cycles and the large step-like decreases and recoveries of galactic cosmic ray intensities at Earth.

NIGERIAN JOURNAL OF SPACE RESEARCH **8**: 144-160, 2009 September 1

Heliospheric Physics: Shock Acceleration in the Heliosphere & Anomalous Cosmic Rays

Marius S. POTGIETER Ph.D and R. du Toit STRAUSS Ph.D
Unit for Space Physics
North-West University
2520 Potchefstroom
South Africa
Email: fskmsp@puk.ac.za

Table of Contents

1. Introduction

The first part describes the basic physics of shocks in space in general and then in the heliosphere. This is followed by a discussion of examples of shocks in space and their effect on charged particles.

2. Physics behind shock waves: Shock geometries, shock modes and Mach numbers

First a few basic definitions. A shock in a fluid (or medium, e.g. a plasma) can be defined as the abrupt change in some physical quantities associated with the fluid, e.g. the velocity **v**, and the mass density ρ. The shock can thus be seen as a discontinuity in the fluid, where the properties of the fluid changes considerable when crossing the shock. These types of discontinuities are usually associated with the compression of the fluid (e.g. an increase in density) and as such necessarily only applies to compressible fluids. Mathematically, a compressible fluid can be defined as

$$\nabla . v \neq 0 \ , \tag{1}$$

which implies a variable density and pressure *p*, throughout the medium. It holds for the solar wind, also in the heliosheath, unless $v_r \propto r^{-2}$ in this region. If we thus have a compressible medium, pressure and density waves may propagate through the medium. The sound speed of a medium is defined as

$$c_s \equiv \sqrt{\frac{\gamma p}{\rho}}, \tag{2}$$

with p the pressure and $\gamma \equiv C_p / C_v$, is the ratio of specific heats of the medium at constant pressure and volume. This is the speed at which sound waves (also called acoustic, ion or longitudinal pressure waves) propagate through the medium.

The physics of a collisionless shock is strongly dependent on the angle θ_{Bn} between the magnetic field and the shock normal. The following are used for θ_{Bn}: Perpendicular shocks: $\theta_{Bn} = 90^\circ$, Parallel shocks: $\theta_{Bn} = 0^\circ$, Oblique shocks: $0^\circ < \theta_{Bn} < 90^\circ$, which can be subdivided into quasi-parallel shocks: $90^\circ < \theta_{Bn} < 45^\circ$, and quasi-perpendicular shocks: $45^\circ < \theta_{Bn} < 90^\circ$. The normal vector is define so that the it points into the unshocked medium. In the shock rest frame, this normal points upstream. The downstream regime is defined accordingly. The magnetic field changes differently for the fast and slow shocks, thus the magnetic field increase

in fast shock but decrease in slow shock. Furthermore the plasma density correlates with the magnetic field amplitude in fast shock whereas it does not in slow shock. Another factor that characterise a shock is the Mach number.

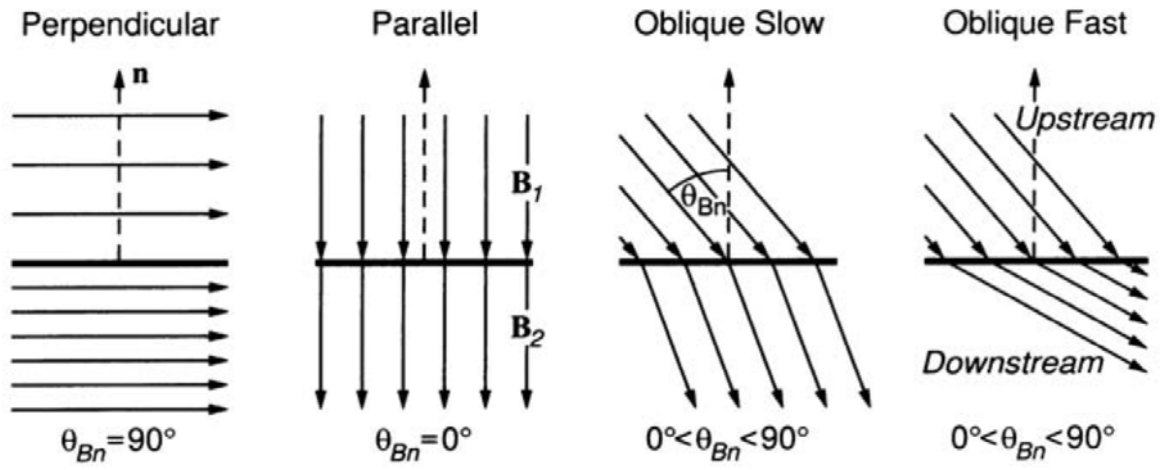

Figure 1. Possible geometry for the shock normal and magnetic field (Behlke, 2005).

The Mach number is defined as the ratio between the shock speed in the upstream medium and the sound speed. It is always determined in the rest frame of the shock. In the upstream medium $M > 1$, whereas in the downstream medium it is smaller. This implies that in the downward stream medium the plasma leave the shock with a speed less than the sound speed. Thus any disturbance in the downstream medium can propagate away from the shock.

The compression ratio of the shock is defined as the density ratio across the shock

$$s \equiv \frac{\rho_2}{\rho_1} \tag{3}$$

also written as $$s = \frac{v_1}{v_2}. \tag{4}$$

The compression ration can be re-written in terms of the supersonic Mach number M_1,

$$s \equiv \frac{(\gamma+1)M_1^2}{(\gamma-1)M_1^2+2}, \tag{5}$$

which is quite useful as the subsonic speed of the shock might not be known. For a strong shock ($M \to \infty$), the previous expression reduces to

$$s = \frac{\gamma+1}{\gamma-1}. \tag{6}$$

For a monatomic gas (such as the solar wind) we have $\gamma = 5/3$, and the maximum compression ration is $s = 4$. If the gas is relativistic $\gamma = 4/3$, and the maximum compression ratio is **s** = 7.

3. Examples of shocks in space

3.1. Bow shocks

A bow shock is an interface that forms between a supersonic fluid and an obstacle such as a denser medium. Bow shock, such as the magnetospheric bow shock, forms at the outermost part of a planetary magnetosphere where the high speed flow of the solar wind is suddenly slowed to subsonic speed by the planetary magnetic field. Bow shocks also form around hot young stars where vigorous stellar winds slam into stellar medium**.** The Earth's bow shock is shown in Figure 2; note where it is defined as a parallel and as a perpendicular shock, respectively.

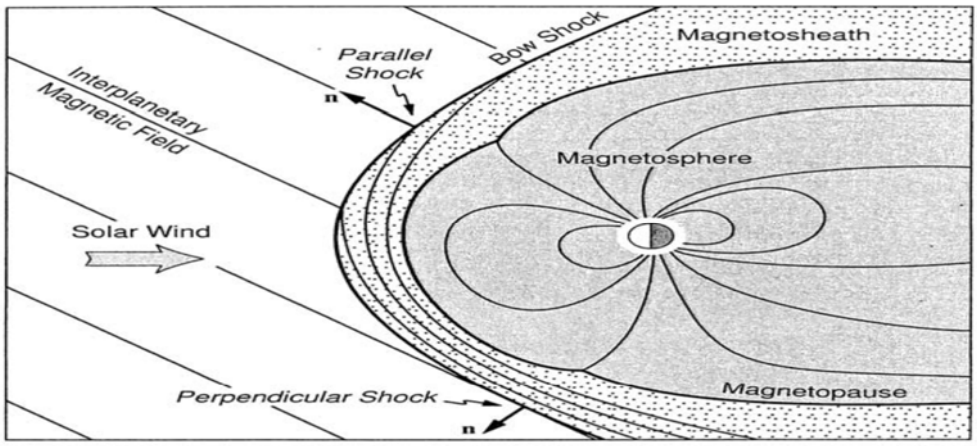

Figure 2. Overview of the Earth's magnetosphere showing the location of the quasi-perpendicular and quasi-parallel regions of the Earth's bow shock for average solar wind conditions (Behlke, 2005).

3.2. Cometary shocks

Cometary shocks have been observed by spacecraft, showing evidence for particle acceleration at the plasma shock formed when outgassed material is ionized in the solar wind.

3.3. Interplanetary shocks

An interplanetary shock is a disturbance that propagates into the expanding solar wind. Interplanetary shocks are identified by characteristic changes in the plasma and field parameters, in particular a sudden increase in plasma density, speed and temperature and a jump in the magnetic field strength. The shock develops because it expands relatively to the ambient medium that expands differently from the shock itself. The expansion of the shock leads to a decrease in the plasma and magnetic flux densities. Interplanetary shocks play an important role in particle acceleration and geomagnetic activity.

The two well-known sources of interplanetary shocks are coronal mass ejections (CMEs) and fast and slow solar wind streams interaction. CMEs are defined as the transient change in the coronagraphs as expanding ejected loops of material of enhanced density. CMEs drive the interplanetary shocks if they move or expand at a super-magnetosonic velocities with respect to

the ambient solar wind. There is close correlation between the rate at which fast coronal mass ejection are emitted from the lower corona and the rate of the occurrence of interplanetary shocks observed within 1 AU of the Sun. Transient interplanetary shock without a following CMEs body are also detected but these case are rare.

3.4. Shocks at corotating interaction regions

Corotating interaction regions (CIRs), as sketched in Figure 3, develop beyond 1 AU and observed as clearly defined enhancements in pressure, magnetic field strength and the general level of fluctuation. As the solar wind streams move outward, the pressure fronts steepen to form corotating shocks at the boundaries of the interaction region. They are usually consists of an outward propagation forward shock and an inward propagating reverse shock. CIRs usually start at the forward shock and end at the reverse shock. CIR shocks are weak or absent near 1 AU. Outside several AU, the shocks become quite strong, and a very large variation in pressure are associated with the interaction regions.

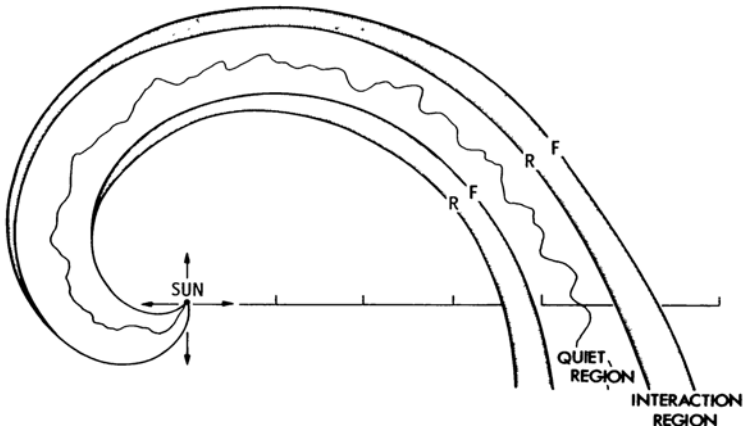

Figure 3. *Two CIR and intervening quiet regions are shown. F and R indicate forward and reverse shock, respectively. An interplanetary magnetic field line is shown within the quiet region.*

Figure 4 shows an example of CIR as observed by Voyager 2 in May 1979 at 5.1 AU. The signature of a forward fast shock is an increase in bulk speed and simultaneous increase in proton density, pressure and magnetic field strength. The signature of the reverse fast shock is

an increase in bulk speed, and simultaneous decreases in proton density, pressure and magnetic field strength. The pressure inside the interaction region is greater than that of the ambient solar wind by a factor of 100. Voyager 2 was immersed in the CIR for 4.7 days.

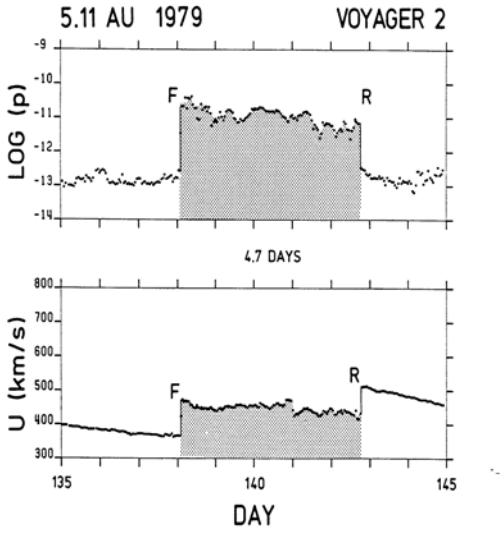

Figure 4. A CIR observed from Voyager 2 at 5.11 AU bounded by a well-developed shock pair.

3.5. Solar wind termination shock

Solar wind termination shock (TS) formed when the ram pressure of the supersonic solar wind drops to the value of the interstellar thermal pressure. When the pressure balance occurs the highly supersonic solar wind will be decelerated in a strong shock. The solar wind is weak compared to the wind of the massive hot star which may contribute to the production of the galactic CRs or at least serve as the injectors providing energetic seed particles which are later accelerated to cosmic ray energies. The solar wind TS is responsible for accelerating the anomalous component of cosmic rays. These particles are believed to originate as neutral interstellar atoms which enter the heliosphere and are subsequently ionized and accelerated at the nearly perpendicular shock.

3.6. Blast waves of a supernova (SN)

A SN is the violent end of a massive star. This process is marked with a blast wave, expelling stellar material at up to 10% of the speed of light. If the interstellar medium is isotropic, the

resulting blast wave will naturally propagate spherically away from the SN. At the front of the blast wave, a shock front will develop, moving radially away from the SN.

4. Diffusive Shock Acceleration

A collisionless plasma is a plasma where interactions between particles through collisions are negligible compared to charged particle–magnetic field interactions. These are normally long range interactions through electrodynamic forces and may propagate through the plasma due to its collective behaviour. Similarly, at a collisionless shock, collisions between particles are negligible. The collisions, and collision processes (e.g. diffusion) are simulated through the interaction between charged particles and magnetic fields. Diffusion is simulated by scattering of particles by irregularities in the magnetic field, called scattering points.

Following Choudhuri (1998), the process of diffusive shock acceleration is as follows: A MHD shock contains moving magnetic fields, which may act as magnetic mirrors, trapping charged particles through multiple 'collisions'. As in the normal Newtonian case, charged particles that collide 'head-on' with the moving magnetic field will gain energy, while a 'trailing' collision reduces the particle's energy. On average, particles will gain energy through these collisions. The particles are thus being accelerated by the moving magnetic field. This type of acceleration is called diffusive shock acceleration or first-order Fermi (Fermi I) acceleration. The existence of this process was doubted, until the discovery of accelerated particles in the Earth's bow shock. For Fermi I acceleration to occur at a shock, a necessary requirement is that there exists enough scattering points on both sides of the shock, in order for particles to suffer multiple collisions, gaining energy with each collision. In the following, a brief derivation is given of the accelerated spectrum of particles undergoing Fermi I acceleration over a shock.

The omni-directional particle distribution function is

$$f(\mathbf{r}, p_m, t) \equiv \frac{U_p(\mathbf{r}, p_m, t)}{4\pi p_m^2}, \tag{7}$$

with **r** the position, p_m the momentum and U_p the differential number density of particles. Consider the continuity properties of the shock. Since particles have mobility across the shock, the distribution function must be continuous, i.e.

$$f^- = f^+, \tag{8}$$

where (-) indicates the un-shocked (supersonic) medium and (+) the shocked (subsonic) medium.

Also the streaming of particles across the shock must satisfy the relation

$$\nabla . S_p = Q, \tag{9}$$

where $\mathbf{S}_p$ is the differential particle current density (streaming), and Q is a source of particles. Equation (19) states that the flux diverging from the shock must have its source at the shock (the so-called seed particles). For a one-dimensional shock, Equation (9) simply reduces to

$$S^+ - S^- = \lim_{\varepsilon \to 0} \int_{r_s - \varepsilon}^{r_s + \varepsilon} Q dr, \tag{10}$$

if r_s is the radial position of the shock. For the rest of the derivation, we must assume some sort of seed population at the shock. In case of the anomalous source of CRs, this will be a mono-energetic function, dependent on the number of seed particles N_0, and the momentum of these particles $p_{m,0}$.

The accelerated spectrum will be in the form:

$$f(0, p_m) = \frac{N_0}{4\pi p_{m,0}^2} q \left[\frac{p_m}{p_{m,0}} \right]^{-q}. \tag{11}$$

Equation (21) is in the form of a power-law with the spectral index given by

$$q \equiv \frac{3s}{s-1}, \tag{12}$$

only dependent on the compression ratio of the shock. The power-law accelerated spectrum is characteristic of Fermi I acceleration for an infinite planar shock. It should also be noted the power law obtained can only be achieved after sufficient time has elapsed for particles to reach the momentum. The characteristic time is

$$\tau = \frac{3}{V_1 - V_2} \int_{p_{m,0}}^{p_m} \left(\frac{\kappa_1}{V_1} + \frac{\kappa_2}{V_2} \right) \frac{dp_m'}{p_m'}, \tag{13}$$

where V is the speed and κ the diffusion coefficient; the subscripts 1 and 2 refer to up- and down stream velocities w.r.t. the shock; τ is thus the time it takes the particles to be accelerated from momentum $p_{m,0}$ to p_m. If we examine a curved shock (e.g. the TS), a curvature cut-off in the spectrum is found when the scale length κ/V becomes larger than the shock radius r_s.

5. Particle acceleration at shocks

Following mechanisms plays a major role for the particle acceleration at collisionless shocks:

- Shock drift acceleration (SDA) in the electric induction field in the shock front,
- Diffusive shock acceleration (DSA) due to repeated reflections in the plasma converging at the shock front (1^{st} order Fermi acceleration),
- Stochastic acceleration in the turbulence behind the shock front (2^{nd} order Fermi acceleration).

The effectiveness of these mechanisms depends on the properties of the shock. Shock drift acceleration is significant at perpendicular shocks, since the electric induction field is maximal but vanishes for parallel shocks. Diffusive shock acceleration is only efficient in the case of sufficient scattering both upstream and downstream of the shock and is thus effective at quasi-parallel shocks. Shochastic acceleration requires a strong enhancement in downstream turbulence.

In the case of SDA particles are accelerated in the electric induction field in the shock front. A charged particle drifts in the electric induction field, which in the shock rest frame is,

$$\mathbf{E} = -\mathbf{v}_1 \times \mathbf{B}_1 = -\mathbf{v}_2 \times \mathbf{B}_2 \tag{14}$$

This field is along the shock front and perpendicular to both magnetic field and bulk flow. It maximises at perpendicular shocks and vanishes at parallel shocks. The shock is a magnetic field discontinuity and thus a particle can drift along the shock front. The drift direction

depends on the charge of the particle and is always such that the particle gains energy (for fast mode shocks). It can be noted that the energy gain of the particle depends on how long the particle can interact with the shock front, which in its turn depends on the particle's speed perpendicular to the shock. If it is small, the particle sticks to the shock. If it is large, the particle escapes before it has gained a large amount of energy. SDA at the Earth's bow shock up to some tens of keV can be observed.

DSA is dominant at quasi-parallel shocks, where shock drift acceleration is negligible due to the vanishing electric induction field. In DSA, the particle scattering both upstream and downstream of the shock is essential. For this type of acceleration, two mirrors continually approach each other head on, and so the particles bounce off these mirrors many times and gain energy at each reflection (Kallenrode, 2004). For stochastic acceleration, the energy gain of the particles is achieved by reflections off mirrors moving random directions. This type of acceleration is less efficient than diffusive acceleration.

It is believed that galactic CRs are accelerated to very high energies (up to $\sim 10^{21}\text{eV}$) through Fermi I acceleration in SN blast waves. The observed galactic CR spectrum is shown in Figure 5, with a clear power-law form.

6. Anomalous Cosmic Rays

Anomalous cosmic rays (ACRs) were first observed as an increased flux of low energy CRs by Garcia-Munoz et al. (1973). Latest results are shown in Figure 6, from the Voyager 1 crossing of the TS in December 2004 (Stone et al., 2005). For helium and oxygen nuclei can clearly be distinguished between the GCR and the ACR components. It is generally accepted that ACRs are formed by the acceleration of low energy pick-up ions (PUIs) at the TS.

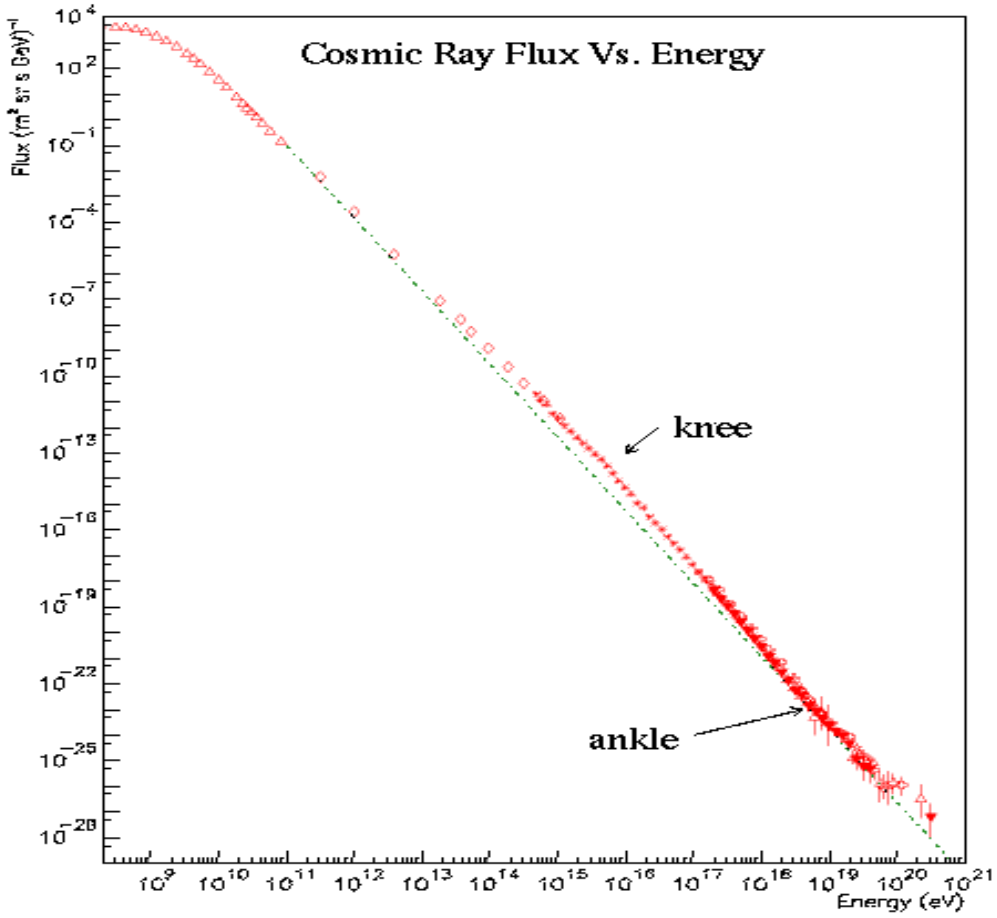

Figure 5. The left panel shows the GCR spectrum, from www.telescopearray.org.

The accepted norm, first proposed by Fisk et al. (1974), is that PUIs serve as the seed population for ACRs. It is generally believed that the local interstellar medium is a partly ionized medium consisting mainly of neutral components. As the neutral components are not electrically charged, neutral particles may enter the heliosphere without being affected by the HMF. It is believed that these particles may become singly ionized mainly through photo-ionization close to the Sun and through charge exchange with solar wind ions in the inner heliosheath. Once ionized, these particles are convected outwards by the solar wind and they are aptly named PUIs.

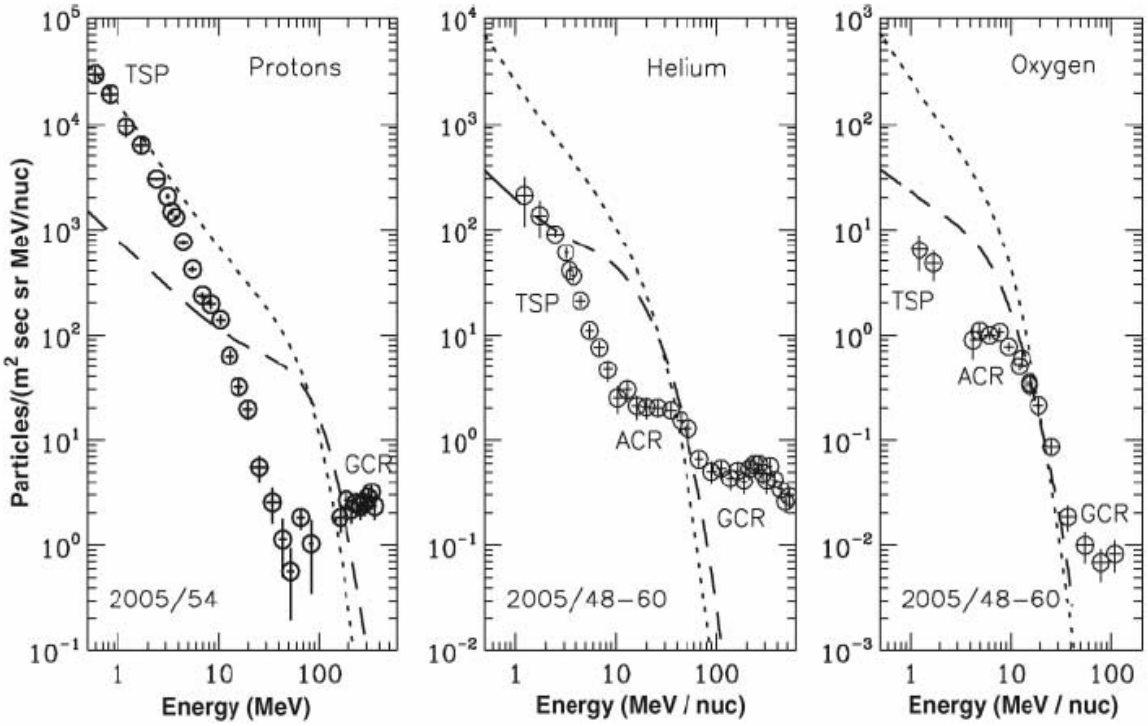

Figure 6. CR data obtained from the Voyager 1 crossing of the TS, clearly distinguishing the GCR and ACR populations of helium and oxygen. Note also the possible fifth CR population, the so-called TSPs. (Stone, et al., 2005).

The first observational evidence of PUIs was made by Möbius et al. (1985), by detecting pick-up helium. Figure 7 shows the computed PUI density in the meridional plane of the heliosphere for solar minimum and maximum conditions. The figure was obtained using a 5-fluid hydrodynamic (HD) model by Scherer and Ferreira (2005). From this figure we may distinguish the different regions in the heliosphere where PUI forming is dominant, namely the region near the Sun and in the inner heliosheath, where PUI densities are the highest.

Once PUIs are convected outwards, and reach the TS, they are injected into the shock, where they are accelerated via diffusive shock acceleration to ACR energies up to ~ 100 MeV/nuc. The precise mechanism of PUI injection at the TS is still unclear. PUI injection into the shock can be quantified by the so-called injection efficiency (or injection rate) which gives the fraction of PUIs reaching the TS that are accelerated to become ACRs. Recently, since the

Voyager 1 TS crossing, some authors have suggested that the TS may not be the 'source' of ACRs as no distinct source spectrum was observed during the crossing. This controversial subject still needs to be resolved.

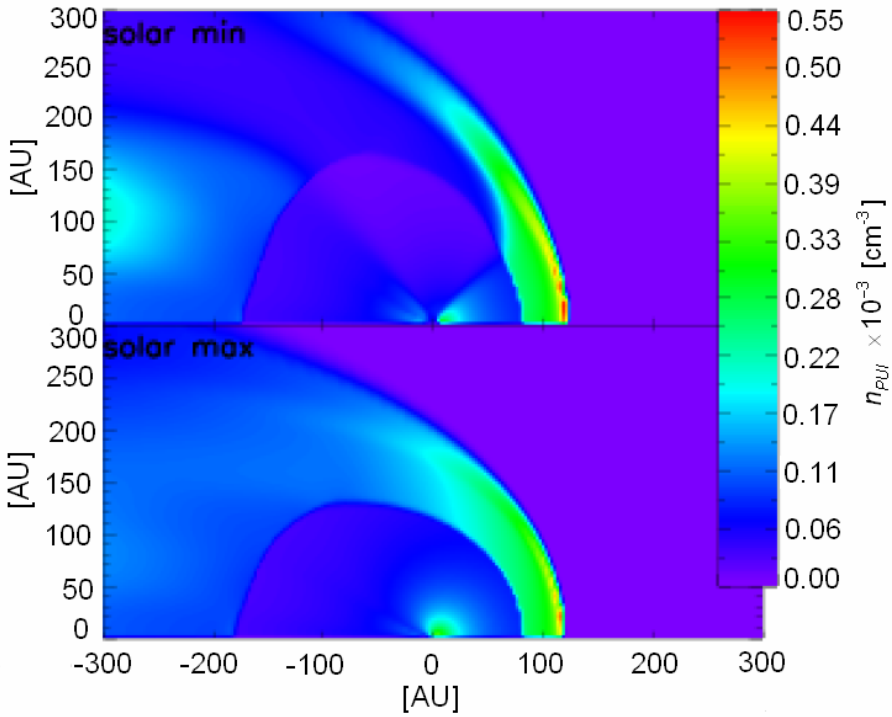

Figure 7. The distribution of PUIs in the meridional plane of the heliosphere for solar minimum (top panel) and solar minimum (bottom panel) conditions, computed using a 5-fluid HD model. Scherer and Ferreira (2005).

Figure 8 shows diffusive shock spectra for anomalous oxygen (lower panel) with modulated spectra at different radial distances in the equatorial plane of the heliopshere. In the upper panel the radial dependence is shown for different energies. The position of the TS in indicated by the dashed red line, at radial distance of 90 AU. The polarity cycles is A >0, with the current sheet tilt angle 100, indicating solar minimum activity.

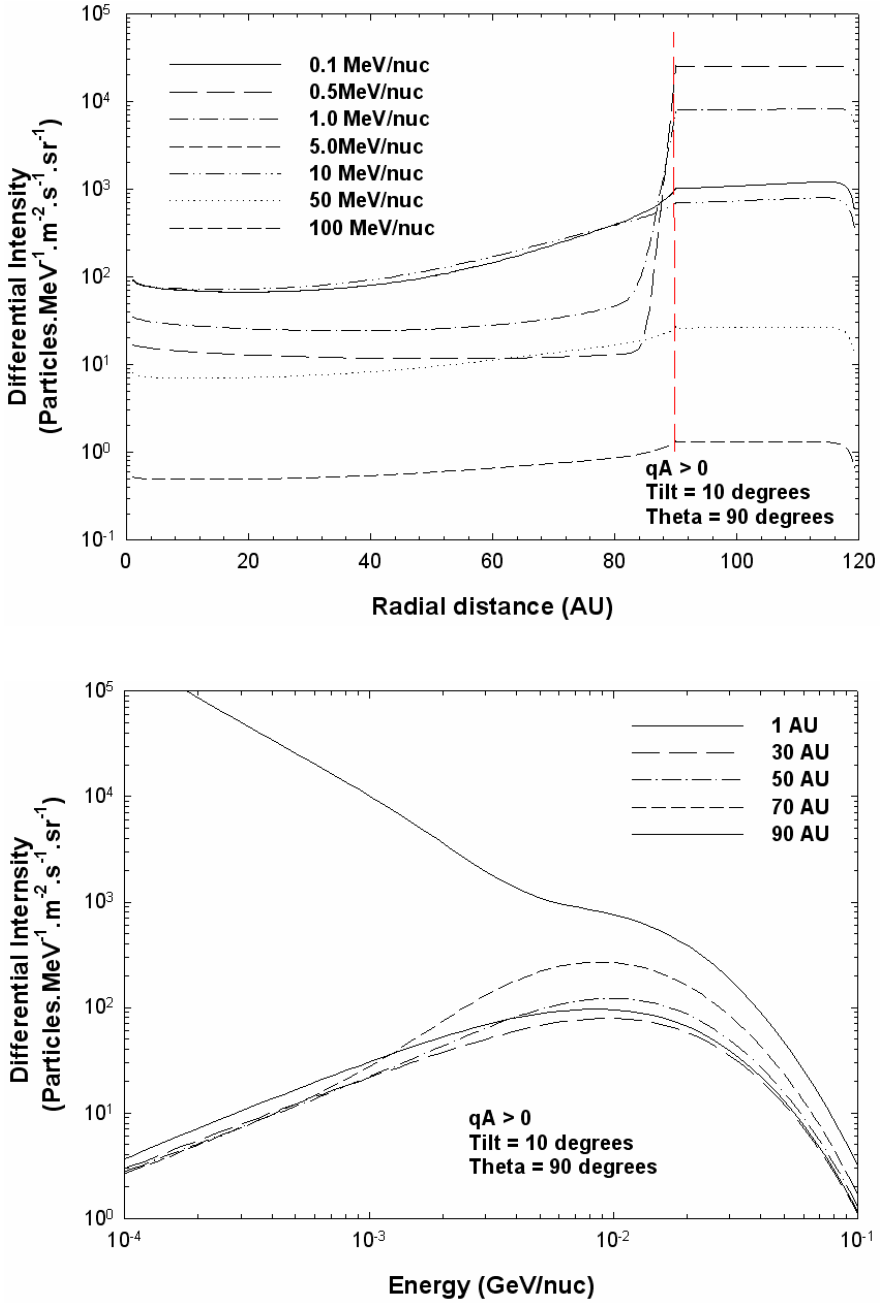

Figure 8. Diffusive shock accelerated spectrum for anomalous oxygen (lower panel) with modulated spectra at different radial distances in the equatorial plane of the heliopshere. In the upper panel the radial dependence is shown for different energies. The position of the TS in indicated by the dashed red line, at radial distance of 90 AU. The polarity cycles is A >0, with the current sheet tilt angle 100, indicating solar minimum activity.

References

Ave, M. et al. Composition of cosmic-ray nuclei at high energies. Astrophys. J. 678, 262, 2008.

Behlke, R., Dissipation at the Earth's quasi parallel bow shock, Ph.D. Thesis Uppsala University, Sweden. 2005

Burlaga, L. F. and McDonald, F. B. and Ness, N. F., Cosmic ray modulation and the distant heliospheric magnetic field - Voyager 1 and 2 observations from 1986 to 1989, J. Geophys. Res., 98, 1, 1993.

Choudhuri, A. R. The Physics of Fluids and Plasmas, Cambridge University Press, 1998.

Cronin, J. W. Gaisser, T. K. and Swordy, S. P. Cosmic rays at the energy frontier, Scientific American, 62-67, 1998.

Ferreira, S. E. S. and Potgieter, M. S., Long-term cosmic-ray modulation in the heliosphere, Astrophys. J, 603, 744, 2004.

Fisk, L. A. et al. An interpretation of the observed oxygen and nitrogen enhancements in low-energy cosmic rays. Astrophys. J., 190, L35, 1974

Heber, B., Potgieter, M. S. Cosmic rays at high heliolatitudes, Space Sci. Rev. 127, 117-194, 2006.

Heber, B. and Potgieter, M.S. Galactic and anomalous cosmic rays through the solar cycle: New insights from Ulysses', The heliosphere through the solar activity cycle, (A. Balogh and L. J. Lanzerotti, eds.) Springer, 2007.

Hörandel, J. R. Cosmic-ray composition and its relation to shock acceleration by supernova remnants. Adv. Space Res., 41, 442, 2008.

Intriligator, D. S., Sun, W., Dryer, M., Fry, C. D., Deehr, C., Intriligator, J. From the Sun to the outer heliosphere: Modeling and analyses of the interplanetary propagation of the October/November (Halloween) 2003 solar events, J. Geophys. Res., 110, 9, 2005.

Jokipii, J. R., and B. Thomas, Effects of drifts on the transport of cosmic rays. IV – Modulation by a wavy interplanetary current sheet, Astrophys. J., 243, 1115, 1981.

Kallenrode, M-B. Space Physics : An introduction to plasmas and particles in the heliosphere and magnetosphere, Springer, 2004.

McCracken, K. G., McDonald, F. B., Beer, J,. Raisbeck, G. and Yiou, F. A., Phenomenological study of the long-term cosmic ray modulation, 850–1958 AD, J. Geophys. Res., 109, A12103, 2004.

Masarik, J., Beer, J., Simulation of particle fluxes and cosmogenic nuclide production in the Earth's atmosphere, J. Geophys. Res. 104, 12099, 1999.

Moskalenko, I. V., Strong, A. W., Ormes, J. F., Potgieter, M. S. Secondary antiprotons and propagation of cosmic rays in the galaxy and heliosphere. Astrophys. J. 565, 280, 2002.

Möbius, E., et al. Direct observations of He^{+} pick-up ions of interstellar origin in the solar wind. Nature 318, 426, 1985.

Parker, E. N., Cosmic ray modulation by the solar wind. Physical Reviews, 110, 1445, 1958.

Parker, E. N., The Stellar-Wind Regions. Astrophys. J. 134**,** 20, 1961.

Parker, E. N. The passage of energetic charged particles through interplanetary space. Planet. Space Sci. 13, 9, 1965.

Potgieter M. S. Solar cycle variations and cosmic rays. J. Atmosp. & Solar-Terres. Phys. 70, 207, 2008a.

Potgieter M. S. Challenges to cosmic ray modeling: From beyond the solar wind termination shock. Adv. Space Res. 41, 245, 2008b.

Schlaipfer, H. Cosmic rays, Spatium, Association Pro International Space Science Institute, 2003.

Scherer, K., Fichtner, H., Borrmann, T., Beer, J., Desorgher, L., Flückiger, E., Fahr, H.-J., Ferreira, S.E.S., Langner, U.W., Potgieter, M.S., Heber, B., Masarik, J., Shaviv, N., Veizer, J. Interstellar-terrestrial relations: variable cosmic environments, the dynamic heliosphere and their imprints on terrestrial archive and climate. Space Sci. Rev. 127, 327–465, 2006.

Shaviv, N.J. The spiral structure of the Milky Way, cosmic rays, and ice age epochs on Earth. New Astron. 8, 39-77, 2003.

Smith, E. J. The heliospheric current sheet. J. Geophys. Res. 106, 15819, 2001.

Stone E. C., Cummings, A. C., McDonald F. B., Heikkila B. C., Lal N., Webber W. R. Voyager 1 explores the termination shock region and the heliosheath beyond. Science 309, 2017, 2005.

NIGERIAN JOURNAL OF SPACE RESEARCH **8**: 161– 177, 2009 September 1

Heliospheric Physics: The Dynamic Heliosphere

Marius S. POTGIETER Ph.D
Unit for Space Physics
North-West University
2520 Potchefstroom
South Africa
Email: fskmsp@puk.ac.za

Table of Contents

1. Our galactic neighbourhood

The Sun is the source of the solar wind and the heliospheric magnetic field. The heliospheric boundary lies far beyond the planetary system. The solar system refers to objects which are gravitationally bound to the Sun such as the planets and moons, Kuiper belt objects, asteroids and comets. Small objects in Keplerian orbits between Mars and Jupiter are called asteroids. Comets, usually with orbits that are highly eccentric, may cross planetary orbits. Some comets come from far beyond the boundary of the heliosphere. The reservoir of these long-periodic

comets is the called Oort cloud at a distance of about 20 000 to 50 000 AU as shown in Figure 1. At these distances the small perturbations of nearby stars can strongly influence the orbits of comets, from which some then migrate closer to the Sun where they are observed. At the outer rim of the Oort cloud the gravitational influence of the Sun vanishes. The Kuiper Belt is a disk-shaped region of icy bodies and debris (KBOs), 30 to 50 AU from the Sun. Its existence was confirmed only a decade ago. Pluto and Eris are now called dwarf planets.

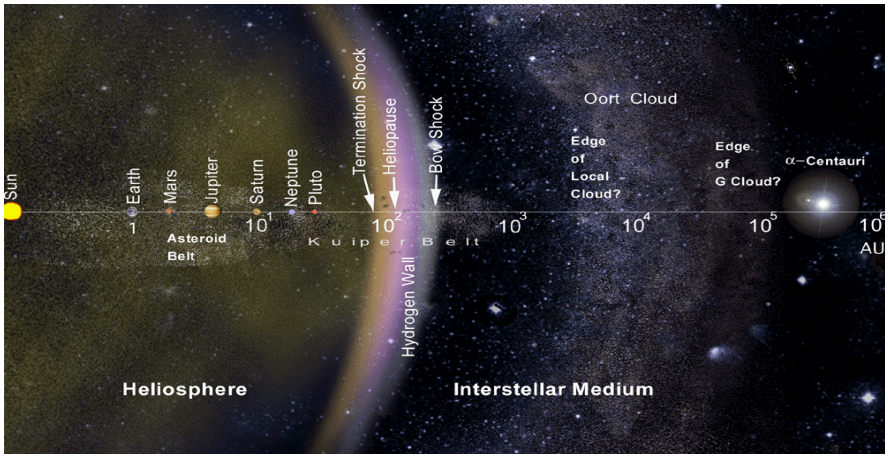

Figure 1. *The solar system and its nearby Galactic neighbourhood are illustrated here on a logarithmic scale extending from the Sun 1 to 10^6 AU. Note the relative position of the Sun, planets, Kuiper belt objects and the edge of the heliosphere, and the next nearest star. See also www.thaispaceweather.com/IHY/Heliosphere/images/theory02.bmp.*

In Figure 2 the heliosphere and its galactic neighbourhood is shown with the direction of motion of each region, with respect to the spiral arm of the Milk Way Galaxy. See e.g. http://www.solarviews.com/eng.

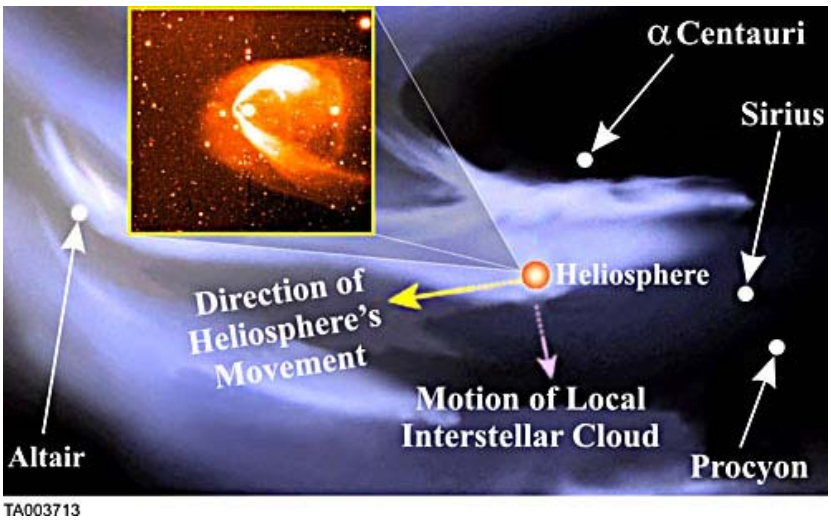

Figure 2: *The direction of motion of the heliosphere with respect to its galactic neighbourhood (http://ibex.swri.edu/multimedia/img/astro_research.jpg). See also Frisch and Slavin (2006*).

2. The heliosphere in interstellar Space Centre

The space between the Sun and nearby stars is filled with plasmas, magnetic fields, neutral and charged particles. The Sun moves through this interstellar medium (ISM) with a velocity of ~26 km.s-1 so that a heliospheric interface with the ISM is formed. The solar wind prevents this medium from flowing into the large volume dominated by the Sun, called the heliosphere. The solar wind 'blowing' away from the Sun thus creates the heliosphere which can be considered the 'influence sphere' of the Sun. The heliosphere is considered to be a small but typical astrosphere. The extent of an astrosphere depends on the ram pressure of the stellar wind compared to the total pressure of the ISM. Because it is moving through the ISM, the heliosphere is asymmetrical with respect to the Sun, with the tail region much more extended than the nose region, the direction in which it is moving. It extends over at least 500 AU in its equatorial regions and at least 250 AU in the polar plane. A schematic representation of the heliosphere is shown in Figure 3. It depicts the heliosphere in the rest frame of the Sun.

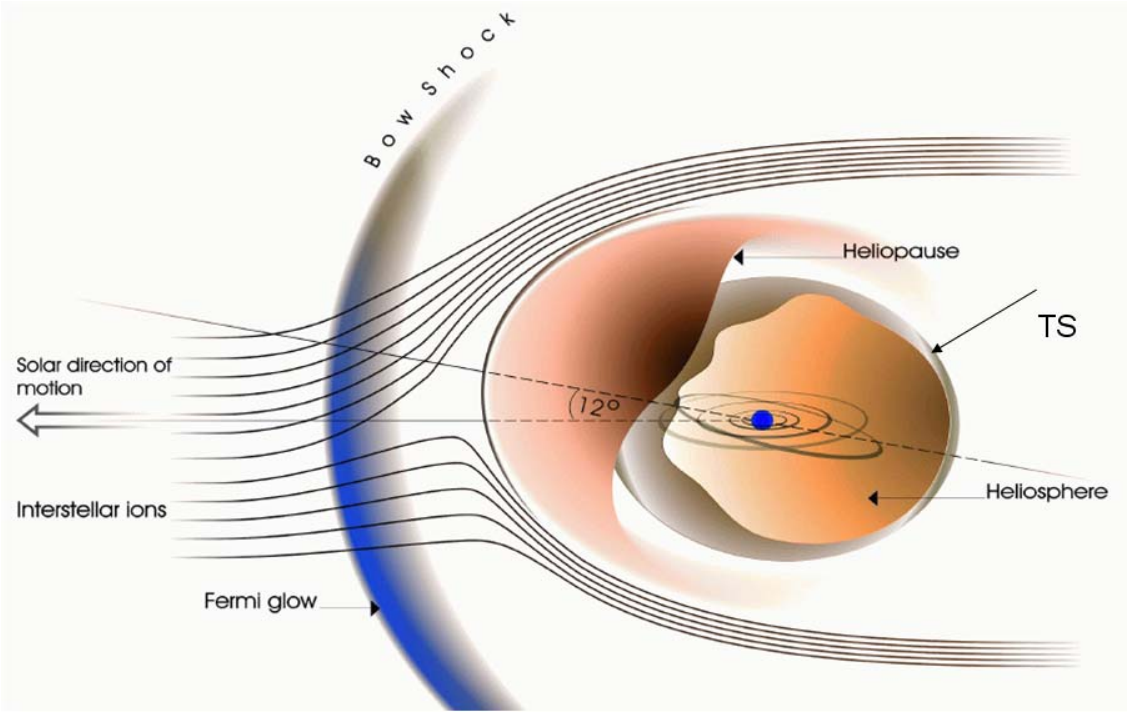

Figure 3: *A schematic representation of the heliosphere taken in the rest frame of the Sun. Note the solar wind termination shock (TS), the heliopause (HP) and the bow shock (BS). (See http://www.oal.ul.pt/oobservatorio/vol6/n5). The Fermi-glow relates to the hydrogen build-up.*

The main features of the heliosphere are the solar wind termination shock (TS), the heliopause (HP) and a bow shock (BS). The region between the TS and the HP defined as the inner heliosheath, with the outer heliosheath located between the HP and the BS. The latter is expected to be rather weak. The HP separates the solar wind and ISM so that it may be considered the outer boundary of the heliosphere. (For reviews, see Zank, 1999; Fichtner and Scherer, 2000; Fahr, 2004; Fichtner, 2005; Pogorelov et al., 2008 and reference therein).

3. The termination shock, heliopause and bow shock

A prediction of HD modeling is that the solar wind creates a TS where it goes from supersonic (400−800 km.s^{-1}) to subsonic speeds between ~85 and ~105 AU, as shown in Figure 4. It is predicted that the TS is dynamically asymmetric, yielding a ratio for the upwind-to-downwind TS distance of ~1:2. However, in the nose direction the TS movement is relatively limited. The

TS is elongated in its polar directions because of the latitudinal variation of the solar wind momentum flux. This asymmetry becomes more pronounced during solar minimum conditions.

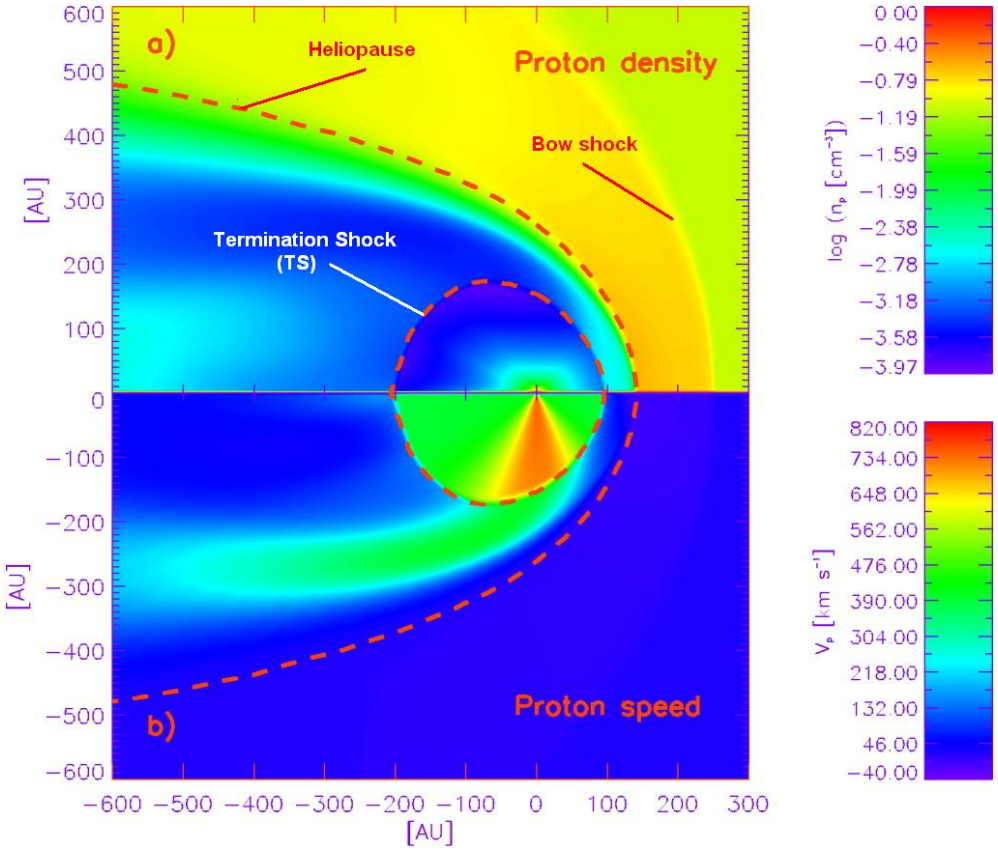

Figure 4: *The HD computed solar wind speed and proton density in the meridional plane of the heliosphere, shown as contour plots, indicating the TS, HP and BS. The ISM moves from right to left in the figure. The lower panel shows the fast solar wind, in terms of the proton speed, in the polar regions of the heliosphere for solar minimum activity conditions (Ferreira and Scherer, 2004; Smith and Wolfe, 1977).*

The TS position oscillates with solar activity, by as much as 3 AU in the upwind direction as it is driven outwards and by 5 AU backwards as it tries to recovery; in the tail direction this will be larger. The TS speed modifies the shock strength (indicated by e.g., the compression ratio) by as much as 20% . The shape of the HP is highly asymmetrical as shown in Figure 4; it is well defined in the nose direction, predicted to be at about 30-50 AU beyond the TS, but ill defined in the tail direction so that more modeling is required to understand these features. The

HP is a contact discontinuity, separating solar and the ISM. (A contact discontinuity is a surface separating two fluids with different densities and temperatures, with no mass exchange between the fluids. This implies no mobility of fluid particles across the surface, resulting in a zero perpendicular with respect to the contact surface flow speed between the fluids – more on this in the lecture on Shocks in Space).

The HP forms where the solar wind and ISM pressures (the thermal pressure, not to be confused with the ram pressure) are in equilibrium. Although the perpendicular component of the flow speed at the HP is zero, the flow may become tangential at the contact surface. It is thus believed that the solar wind becomes increasingly tangential when nearing the HP. Estimates of the HP position, through HD modelling, suggest that is varies from 140 AU in the equatorial plane in the nose region to 240 AU in the polar region during solar minimum conditions. HD models predicts the HP to form an open structure in the tail region of the heliosphere (e.g., Zank and Muller, 2003; Ferreira and Scherer, 2004).

The BS forms in analogy to the TS. The supersonic interstellar flow must decrease to subsonic speed in order to merge with the solar wind at the HP. This resulting shock is called the BS. HD modelling indicates that the BS may be located at a radial distance of ~250 AU in the equatorial plane of the nose region but this depends on the composition of the ISM.

Figure 5 highlights the dynamic nature of the heliospheric boundaries. These results were computed with a 3D HD model by Langner et al. (2006). Table 1 gives a summary of the boundary locations.

Table 1: *Average heliocentric distances to the termination shock (TS), the heliopause (HP) and the bow shock (BS) as generally modelled in the three main heliospheric directions. The relevant spatial regions of the heliosphere (the CR modulation domain or volume) are: (1) The region confined by the heliospheric TS. (2) The inner heliosheath between the TS and the HP. (3) The HP and the outer heliosheath. (4) The BS, and (5) the local interstellar medium (ISM).*

Nose direction	Poles	Tail direction
TS: (95 ± 5) AU	TS: (130 ± 10) AU	TS: (200 ± 15) AU
HP: (140 ± 10) AU	HP: (200 ± 30) AU	HP: > 500 AU
BS: ~ 250 AU	BS: > ~ 500 AU	na

4. Observations of the TS and the heliosheath

The spacecraft Voyager 1 encountered the TS in December 2004 at a distance of ~94 AU from the Sun, at a polar angle of ~60º. Its twin Voyager 2 crossed the TS in August 2007 at 83.7 AU in the southern hemisphere, at ~120º and ~10 AU closer to the Sun than found by Voyager 1;

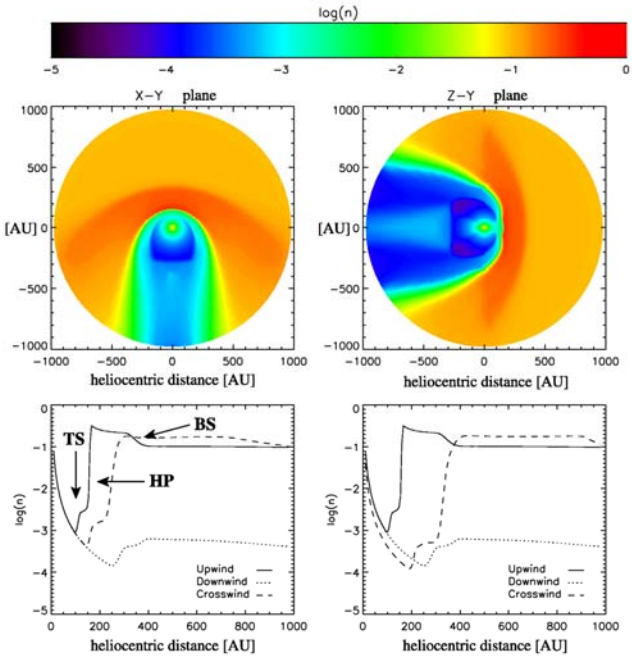

Figure 5: *Illustration of the heliospheric geometry, structure and boundaries using contour plots of the proton number density in the X-Y and Y-Z planes, obtained with a 3-dimensional HD model with the associated number density profiles in the heliospheric upwind, downwind, crosswind and polar directions in the lower panels (Langner et al., 2006).*

this is illustrated in Figure 6. This asymmetry could indicate an asymmetric pressure from an interstellar magnetic field, from transient-induced shock motion, or from the solar wind dynamic pressure. Stone et al. (2008) reported that the intensity of 4-5 MeV protons accelerated by the TS near Voyager 2 was three times that observed concurrently by Voyager 1, indicating differences in the TS at the two locations. Companion papers in Nature (July 2008) reported on the plasma, magnetic field, plasma-wave and lower energy particle observations at the TS.

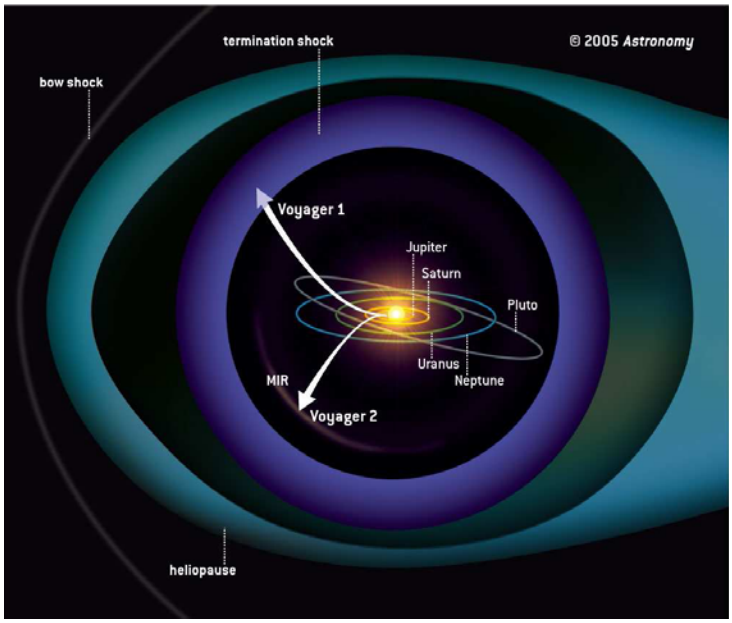

Figure 6: The trajectories of the two Voyager spacecraft with respect to the Sun in the middle of the sketch, the planets, the TS and the HP. (http://voyager.jpl.nasa.gov).

Unfortunately, the plasma experiment on board Voyager 1 malfunctioned long ago so that direct measurements of the solar wind speed and density are not available from this crossing. The plasma experiment on board Voyager 2 is operational (http://voyager.jpl.nasa.gov); Figure 7 depicts solar wind data from Voyager 2's TS crossing; note the drop in the solar wind speed in the top panel and the rise in temperature in the bottom panel.

The strength of the TS is measured by the compression ratio which gives the ratio of the supersonic to subsonic flow speeds. The maximum compression ratio for a planar shock is $s = 4$.

A compression ratio of $s = 4.0$ implies that the solar wind speed decreases from $V_1 = 400$ km.s^{-1} to $V_2 = 100$ km.s^{-1} across the TS. HD modelling shows that s may also have a significant latitudinal dependence.

Observations form Voyager 1 and 2 indicate that the compression ratio varies with time and the position of the TS between values of 2.3 and 1.8. This means that the TS is not a strong shock. Cosmic rays data from Voyager 1 (Decker et al., 2005) confirm the existence of a 'foreshock' (the initial continuous decrease). In fact, Voyager 2 made several crossings of the TS in August 2007. The HMF magnitude increases across the TS and its direction becomes steady as shown for Voyager 1 in Figure 8 and for Voyager 2 in Figure 9 (Burlaga et al., 2005, 2008). These observations are of major importance and quite an accomplishment for this 30 year long mission. (http://cohoweb.gsfc.nasa.gov/helios).

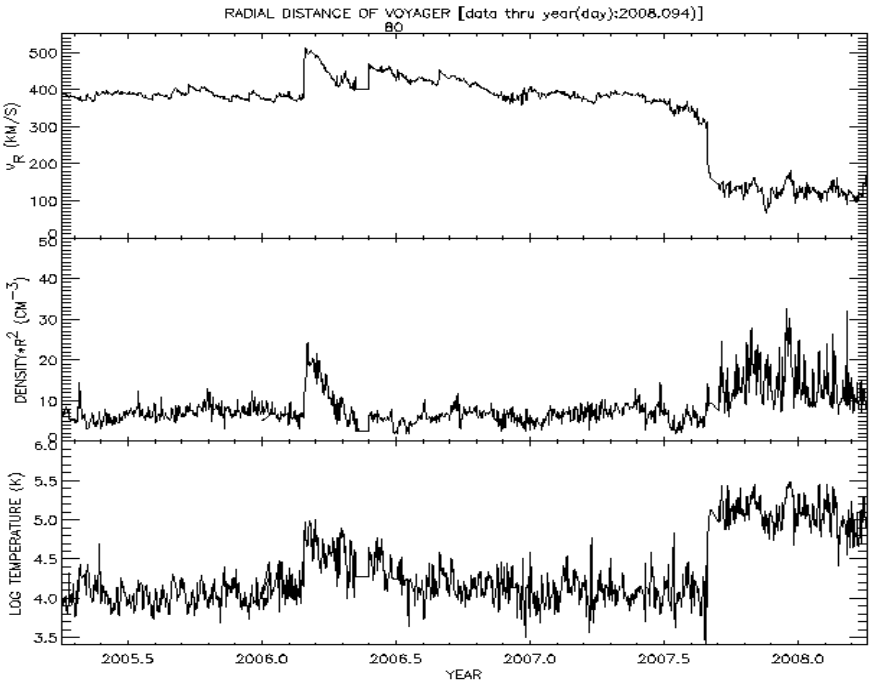

Figure 7: *Solar wind observations from the Voyager 2 crossing of the TS in August 2007 (http://voyager.jpl.nasa.gov.). Top panel shows the solar wind speed, middle panel the density and lower panel the temperature across the TS.*

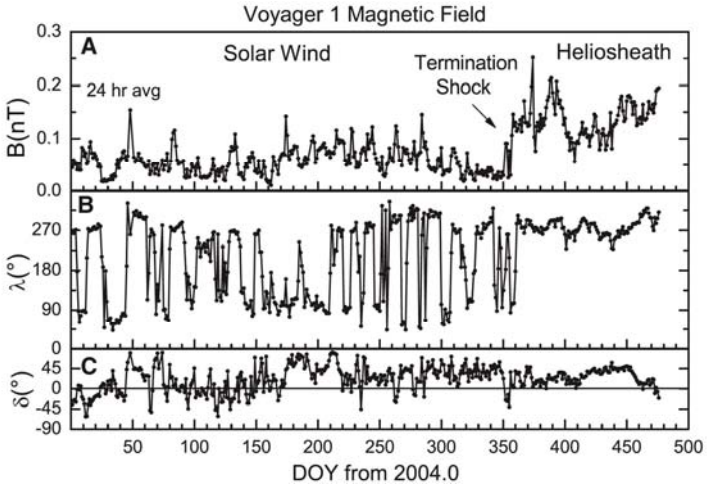

Figure 8: Daily averages of magnetic field strength B (A), azimuthal angle λ (B), and elevation angle δ (C) as a function of time measured in days from the beginning of 2004. The angles are in heliographic coordinates. DOY, day of year. (http://ibex.swri.edu/multimedia/img/misbot.jpg).

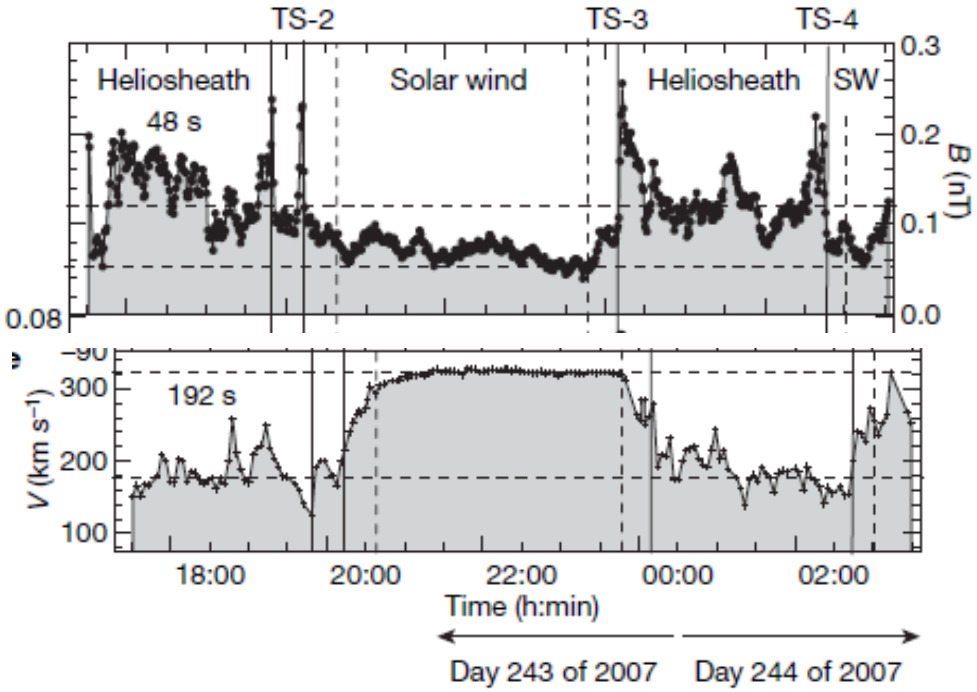

Figure 9: The changes in the solar wind speed and accompanying HMF magnitude variations from three TS crossings by Voyager 2 (Burlaga et al., 2008).

5. The physics of HD modeling

The heliosphere can be modelled as several fluids obeying the following set of Euler equations:

$$\frac{\partial}{\partial t}\rho_i + \nabla..(\rho_i u_i) = Q_{p,i} \qquad (1) \qquad (1)$$

$$\frac{\partial}{\partial t}(\rho_i u_i) + \nabla.(\rho_i u_i u_i + P_i I) = Q_{m,i}, \qquad (2)$$

$$\frac{\partial}{\partial t}\left(\frac{\rho_i}{2}u_i^2 + \frac{P_i}{\gamma_i - 1}\right) + \nabla.\left(\frac{\rho_i}{2}u_i u_i^2 + \frac{\gamma_i u_i P_i}{\gamma_i - 1}\right) = Q_{e,i}, \qquad (3)$$

which describes the conservation of mass, momentum and energy respectively. Here, ρ_i denotes the density, P_i the pressure, $\mathbf{u}_i$ the flow velocity, $\mathbf{I}$ is the unity tensor and γ_i is the adiabatic indices of the thermal components. Q_i indicates any sources related to interactions between various species, and *t* denotes the time. Equations (1) to (3) are solved simultaneously for solar wind and interstellar protons ($i = p$) and neutral hydrogen ($i = H$) in the so-called two fluid HD approach as discussed by Scherer and Ferreira (2005) and Ferreira et al. (2007).

For a list of models for heliospace physics, see http://ccmc.gsfc.nasa.gov/modelweb.

6. The solar wind in the heliosheath

An important subject is the solar wind speed profile in the heliosheath which obtains a large latitudinal component when the HP is approach, deviating from decreasing for example from $V \propto r^{-2}$. The radial dependence of the speed decreases from $V \propto r^{-2}$ directly beyond the TS to $V \propto r^{-6}$ near the HP, as illustrated in Figure 10. This behaviour has implications for cosmic ray modulation in the heliosheath and has to be studied in detail.

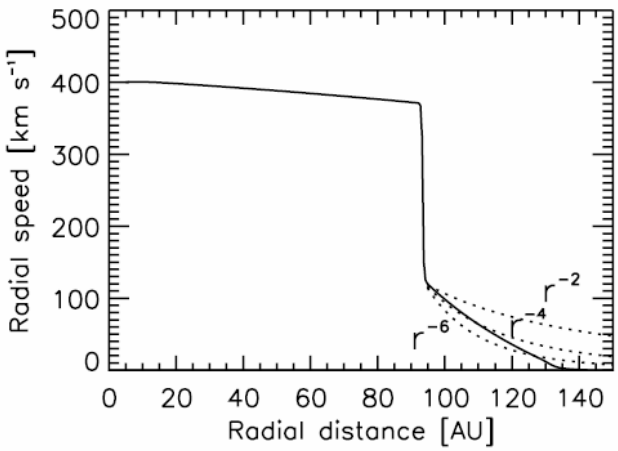

Figure 10: The solar wind speed profile as computed by a HD model, with several scenarios in the heliosheath. On this case the TS is located at ~95 AU (Ferreira et al. 2007).

7. Implications for cosmic rays

To model the modulation of CRs throughout the heliosphere, the heliospheric geometry must be specified as input to a CR model. The TS and especially the HP have significant physical importance as to how CRs are affected. The heliosheath contributes significantly to the modulation and general decrease in CRs in the outer heliosphere as shown in Figure 11 for 6 MeV Jovian and Galactic electrons from near the Earth to 140 AU where the HP is assumed. The local interstellar spectrum for electrons is specified at the HP where the modulation of CRs is assumed to start. It is generally accepted that the TS is the 'source' of the anomalous component through diffusive shock and other types of acceleration. This is discussed in a third lecture.

The latest observations of 6-14 MeV electrons on board Voyager 1 and 2 are shown in Figure 12 as a function of radial distance with the time of observation indicated by vertical lines. Note that differential intensity is usually expressed in units of particles.m^{-2}.s^{-1}.sr^{-1}.MeV^{-1}.

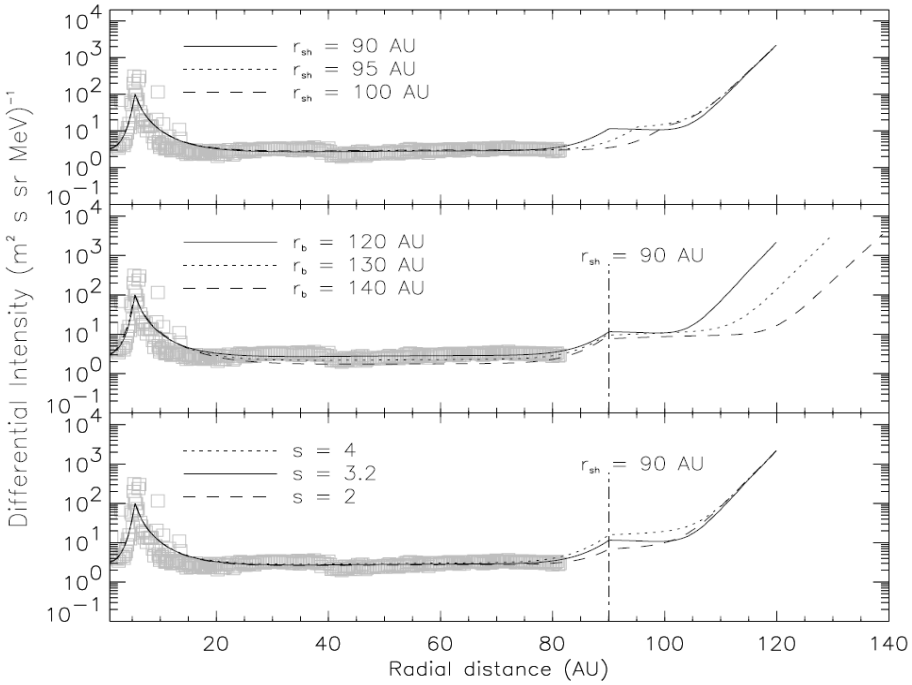

Figure 11. Computed 6 MeV Jovian and galactic electron intensities as a function of radial distance. The computed scenarios are shown with different values for the shock radius r_{sh} (top panel), modulation boundary r_b (middle panel) and compression ratio s (bottom panel). Shown in comparison are the observed 4-10 MeV electrons by Voyager 1. Note the dominance of the Jovian electron source in the inner heliosphere (Ferreira et al., 2004).

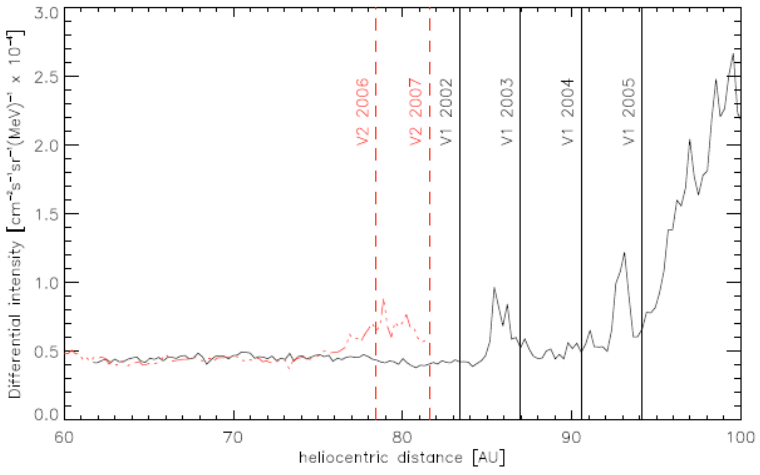

Figure 12. The flux of 10 MeV cosmic ray electrons observed in the outer heliosphere by Voyager 1 & 2 (Webber, 2008, private communication; Snyman, 2007).

8. Space climate

Space weather is a chain of processes originating at the Sun, propagated through interplanetary space, interacting with the Earth's magnetic field and eventually generating a number of phenomena in the Earth's magnetosphere, ionosphere and atmosphere. The Sun is the main driver of space weather. Sudden ejections of plasma and magnetic field structures from the Sun such as coronal mass ejections (CMEs) together with sudden bursts of radiation (solar particles), termed solar flares, all contribute to space weather effects at Earth. In addition, non-solar sources, such as galactic CRs, also contribute to altering space weather conditions at the Earth. While it is well-known that solar variability influences the near-Earth space environment at short timescales of several days, a more subtle influence of solar and heliospheric variability at longer timescales is also present and this topic is just beginning to be appreciated.

Long-term (> 22 years) solar forcing and changes to the heliosphere from outside the solar system is known as *Space Climate,* which has important consequences for the formation and evolution of planetary atmospheres, the evolution of life and global long term climate (over thousands of years) on Earth. Understanding the Sun's variability and global heliospheric changes, from the 11-year cycle to stellar and planetary evolutionary timescales, is of fundamental importance. However, our knowledge is limited by direct observations which exist only since the early 17th century so that numerical models are used extensively to study these effects. A documented phase of reduced solar activity between 1645 and 1715 A.D. known as the Maunder minimum coincided with a period of long winters and global cooling on Earth.

Studies also link solar activity and CRs to cloud cover and variations in rainfall. Solar ultraviolet radiation also causes destructively affects to the ozone layer in the upper atmosphere. This layer is widely believed to play a role in global climate. More and more such relationships between solar activity and terrestrial climate indicators are emerging from diverse interdisciplinary studies, revealing a profound link between the galaxy, the heliosphere, the Sun and Climate. Modeling predicts that the interstellar environment of the heliosphere influences its shape and structure and that the flux of CRs in the heliosphere is affected by changes of the

heliospheric geometry. The galactic CR flux is not only varying due to the solar activity-induced changes of the solar wind and heliospheric magnetic field (HMF) but also in response to the changing state of the ISM surrounding the heliosphere. For detail, the reader is referred to the comprehensive review by Scherer at al. (2006) and references therein.

The overall concept of Space Climate includes topics such as:

- How does long-term solar activity modify the near-Earth space environment (magnetosphere, ionosphere) and geomagnetic storms?
- What do we know of long-term solar change from different proxies like CRs, cosmogenic isotopes, geomagnetic activity etc.?
- How do different aspects of solar activity (sunspots, irradiance, global magnetic field, solar energetic particles etc..) evolve in time?
- What can be learned about the long-term evolution of the Sun from other stars?
- How can we understand long-term changes in the solar dynamo?
- How do the solar wind and the heliospheric magnetic field vary on very long time scales?
- How is the terrestrial atmosphere and climate influenced and what are the main mechanisms?
- Does the changing geomagnetic field affect terrestrial climate?
- Can solar and heliospheric variability affect human cultures?

For more on Space Climate research, interested readers are referred to the books ‘Solar Variability and its Effects on Climate’ (Geophysical Monograph Series, 2004), ‘‘The Sun, Solar Analogs and the Climate’’ (Springer, 2005) and the topical issue of the Solar Physics Journal containing papers presented at the ‘First International Symposium on Space Climate’ held at Oulu, Finland.

References

Burlaga, L. F. et al., Crossing the termination shock into the heliosheath: Magnetic fields. Science 309, 2027, 2005.

Burlaga, L. F., Ness, N. F., Acuña, M. H., Lepping, R. P., Connerney, J. E. P., Richardson, J. D. Magnetic fields at the solar wind termination shock, Nature 454, 75, 2008.

Decker, R. B. et al. Voyager 1 in the foreshock, termination shock, and heliosheath. Science 309, 2020, 2005.

Fahr, H. J. Global structure of the heliosphere and interaction with the local interstellar medium: three decades of growing knowledge. Adv. Space Res. 34, 3, 2004.

Ferreira S. E. S., Potgieter M. S., Scherer K. Modeling of the heliospheric interface, magnetic field, and cosmic-ray transport. Astrophys. J. 659, 1777, 2007.

Ferreira, S. E. S., Potgieter, M. S., Webber, W. R. Modulation of low-energy cosmic ray electrons in the outer heliosphere, Adv. Space Res. 34, 126, 2004.

Ferreira, S. E. S., Potgieter, M. S., Scherer, K. Transport and acceleration of anomalous CRs in the inner heliosheath, J. Geophys. Res. 112, A11101, 2007.

Ferreira, S. E. S., Scherer, K. Modulation of cosmic-ray electrons in the outer heliosphere. Astrophys. J. 616, 1215, 2004.

Fichtner, H. Cosmic rays in the heliosphere: progress in the modeling during the past 10 years. Adv. Space Res. 35, 512–517, 2005.

Fichtner, H., Scherer, K. 'The Heliosphere: A Brief Overview.' in 'The Outer Heliosphere: Beyond the Planets.' edited by K. Scherer et al. Copernicus Gesellenschaft, Lindau, 2000.

Frisch, P. C., Slavin, J. D. The Sun's journey through the local interstellar medium: the paleoLISM and paleoheliosphere. Astrophys. Space Sci. Trans. 2, 53, 2006.

Heber, B., Potgieter, M. S. Cosmic rays at high heliolatitudes, Space Sci. Rev. 127, 117, 2006.

Langner, U. W., Potgieter, M. S., Fichtner, H., Borrmann, T. Modulation of anomalous protons: Effects of different solar wind speed profiles in the heliosheath. J. Geophys. Res. 111, 1106, 2006.

Pogorelov, N. V., Zank, G. P., Ogino, T. MHD modeling of the outer heliosphere: Achievements and challenges, Adv. Space Res. 41, 306, 2008.

Scherer, K., Ferreira S. E. S. A heliospheric hybrid model: Hydrodynamic plasma flow and kinetic cosmic ray transport. ASTRA 1, 17, 2005.

Scherer, K., Fichtner, H., Borrmann, T., Beer, J., Desorgher, L., Flückiger, E., Fahr, H.-J., Ferreira, S.E.S., Langner, U.W., Potgieter, M.S., Heber, B., Masarik, J., Shaviv, N., Veizer, J. Interstellar-terrestrial relations: variable cosmic environments, the dynamic heliosphere and their imprints on terrestrial archive and climate. Space Sci. Rev. 127, 327, 2006.

Smith, E. J. and Wolfe, J. H., in M.A. Shea (ed.), Study of Travelling Interplanetary Phenomena, D. Reidel Publ. Co., Dordrecht, Holland, PP. 227-257, 1977.

Snyman J. L. Modelling of the heliosphere and cosmic ray transport. M.Sc. thesis, North-West University, South Africa. 2007.

Stone E. C. et al., An asymmetric solar wind termination shock, Nature 454, 71, 2008.

Stone E. C., Cummings, A. C., McDonald F. B., Heikkila B. C., Lal N., Webber W. R. Voyager 1 explores the termination shock region and the heliosheath beyond. Science 309, 2017, 2005.

Zank, G. P. and Müller, H-R. The dynamical heliosphere. J. Geophys. Res. 108, 7-1, 2003.

Zank, G. P. Interaction of the solar wind with the local interstellar medium: A theoretical perspective. Space Sci. Rev. 89, 413, 1999.

NIGERIAN JOURNAL OF SPACE RESEARCH **8**: 178 – 255, 2009 September 1

Electric Current Systems in the Earth's Environment

Christine AMORY-MAZAUDIER Ph.D.
CETP/CNRS, 4 Avenue de Neptune 94107 Saint-Maur-des-Fossés, FRANCE
Christine.mazaudier@cetp.ipsl.fr

Table of contents

1.0. General Introduction

In this paper the following items are presented:

1. The Large scale dynamos in the Sun Earth's System
2. The true electric currents systems in the Earth's environment
3. The equivalent electric current systems
4. The magnetic indices.

All these items are related: the large scale dynamo mechanisms in the Sun Earth's system generate electric currents in the Earth's environment. The circulation of these electric currents produces magnetic variations easily measured on spacecrafts or at ground level. Due to the lack of in situ measurements of electric currents in the ionosphere and the magnetosphere, magnetic variations are generally used to give an estimate of the true electric currents. By assuming geometrical properties of the real electric currents, as an infinite plane sheet or a ribbon of current, equivalent electric currents are deduced from ground or spacecraft magnetic field variations to approach the real 3D electric current systems. Magnetic indices are daily derived from the magnetic observatories in order to estimate geomagnetic activity which is related to the increase of electric current systems in the Earth's environment.

Large scale dynamos, real electric current systems, equivalent electric current systems and magnetic indices are related to the global Sun Earth electric current circuit. In this paper we are developing a global and synthetic view in order to understand the relations between all these physical phenomena or parameters. In the conclusion we give a bibliography of the main steps in the discovery of the large scale electric current in the close Earth's environment.

1.1 Large scale dynamos in the Sun Earth's system: Introduction

In the Robert dictionary a dynamo is defined as: 'Dynamoelectric machine', which transforms mechanical energy into electric energy'. The dynamo is the starting point of our study. Mechanical energy of various motions in the Sun Earth system is transformed into electric energy.

The Sun and the Earth are both magnetized bodies and internal dynamo process are invoked to explain the generation of both solar and terrestrial magnetic fields:

a) for the Sun: the interaction between differential rotation and convection generates an initially north-south (poloidal) magnetic field
b) for the Earth: an electrically conducting fluid in the core of the Earth which leads generates a dipolar magnetic field.

It is clear that dynamo processes are very important to understand the electromagnetism of the Sun Earth system. In the first section of this part we present the physical basis of dynamo mechanisms. The second section introduces historically the various dynamos of the Sun Earth's System. The conclusion recapitulates the characteristics of the large scale dynamos described in this section.

1.2 Dynamo mechanisms: Physical basis

In an ionized plasma in a magnetic field (this is the case for Solar and Earth environment), the charged particle motion is anisotropic. It is determined by the distribution of charged and neutral particles and the magnetic field.

Different forces may drive ions and electrons at different speeds and produce dynamo current $J_d = \sigma$ VxB in the direction perpendicular to the magnetic field. The space charge developed by this primary electric currents builds up a polarization electric field (E) and electric currents which tend to oppose the primary dynamo currents in order to make the total current ($J_t = \sigma$ (E + VxB)) divergence free everywhere. The current may modify the magnetic field. Therefore modified electric and magnetic fields change the ionization distribution and the anisotropic motions. Figure 1 from Paterno (2006), with Paterno's comments illustrates this complex series of actions and feedbacks.

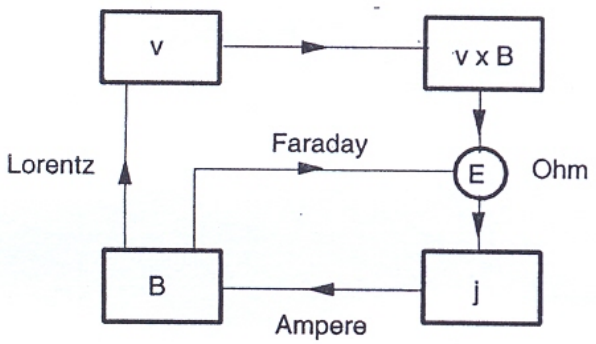

Figure 1: Schematic representation between plasma motion and magnetic field [after Paterno, 2006]. Comments by Paterno 'A motion v across a magnetic field B induces an electric field vxB, which produces an electric current J=σ (E + v×B) via Ohm's law where σ is the electric conductivity and E an electric field. This current produces in turn a magnetic field ∇ XB = μJ, where μ is the permeability. The magnetic field creates both electric field E through Faraday's law $\nabla \times$ E =-δB/δt and Lorentz force J×B which reacts on the motion v.

The basis equations for this study are the fundamental Laws of Electromagnetism:

MAXWELL 'S EQUATIONS

$div(\vec{j} + \varepsilon_0 \frac{dE}{dt}) = 0$ -> conservation of Electric field

$rotE = -\frac{\delta \vec{B}}{\delta t}$ -> induction -> FARADAY'S LAW

$rot\vec{B} = \mu_0 \vec{j}$ -> connection between density of current and magnetic field : AMPERE'S LAW

$div\vec{B} = \vec{0}$ -> conservation of magnetic flux

OHM'S law : $\vec{j} = \bar{\bar{\sigma}}(\vec{E} + \vec{V} \times \vec{B})$

BIOT and SAVART'S law : $B = \frac{\mu_0}{4\pi} \int (\frac{j \times \hat{r}}{r^2}) dV$

This law is used to compute the magnetic field generated by a **steady current**.

Where

j is the electric current density in A.m^{-2}

E is the electric field in V.m^{-1}

B is the magnetic field in T

$\bar{\bar{\sigma}}$ is the conductivity tensor in Ω.m^{-1}

ε_0 is the permittivity in free space in F.m^{-1}

ε_0 = 8.854187….x10 $^{-12}$ F.m^{-1}

μ_0 is the magnetic permeability in free space in H.m^{-1} , μ_0 = 4π. 10^{-7} H.m^{-1}

$c = \frac{1}{\sqrt{\varepsilon_0 \mu_0}}$ is the celerity of the light in m.s^{-1}

$c = 3.10^8$ m.s^{-1}

dV : differential element of volume

j : current density in this volume

$\hat{r}$: displacement unit vector in the direction pointing from the wire element towards the point at where the field is being computed

r : distance from the wire element to the point at which the field is being computed.

1.3 The different large scale dynamos: Historical approach

1.3.1 Solar dynamo: The 2 components

The discovery of sunspots is attributed to Galileo Galilei and Thomas Hariot around 1610. Later Christophe Scheiner and David Fabricius started the first observations in March 1611. The first publication is from Johannes Fabricius in autumn 1611. During several centuries, since 1610, sunspots were observed and compiled by scientists. On figure 2 is drawn the yearly average number of sunspots from 1610 to 2000. This diagram exhibits the well known sunspot cycle of ~11 years and also a solar cycle of ~80 years. We also observed the disappearance of the sunspots after 1645 until 1700. This period is called the Maunder minimum. Schwabe in 1851 discovered the sunspot cycle.

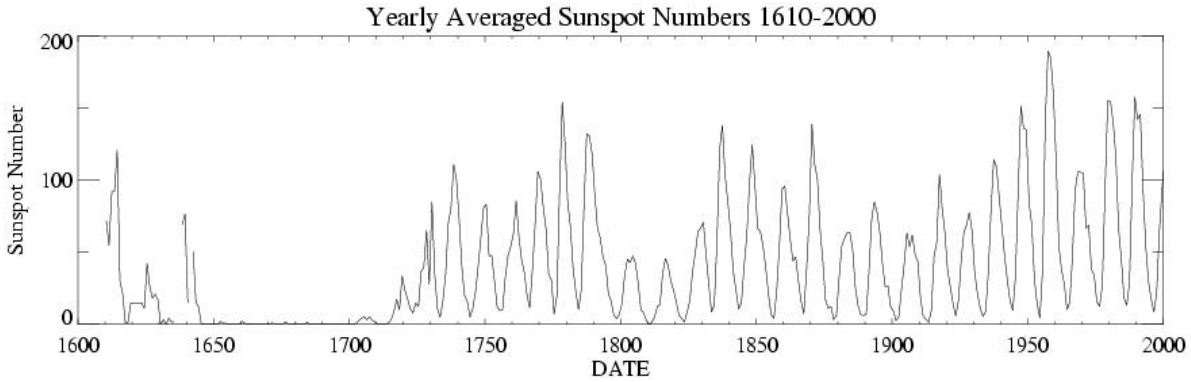

Figure 2: Sunspot cycles from 1610 until 2000

The regular and continuous observation of the Sun during centuries has revealed many morphological features:

- the migration of sunspots from the middle latitudes to the equator
- the reversal of the polar magnetic field from one sunspot cycle to another : 2 sunspot cycles of 11 years with reversed polar magnetic field constitute a 22 years cycle discovered by Hale.
- etc…

Observations of the sun revealed the 2 components of the solar magnetic field, poloidal and toroidal (sunspot cycle). Figure 3 shows the model of poloidal field proposed by Pneuman and

Kopp in 1971. This figure illustrates the trajectories of the particles of the solar wind flowing out of the sun. At equatorial latitudes there is the plasma sheet.

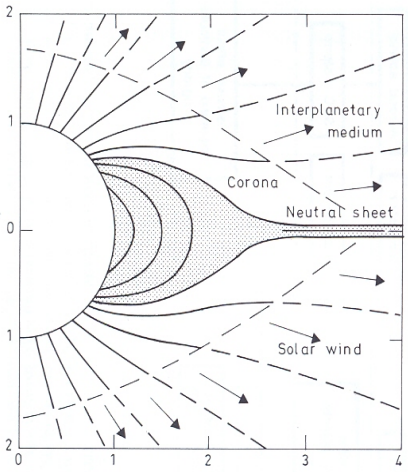

Figure 3: from Pneuman and Kopp, 1971: Model of the dipolar component of the Solar magnetic field

Figure 4 illustrates the linkage between the 2 components of the solar cycle. The reversal of the poloïdal component is clearly observed at the top and bottom of the figure by the colour change from yellow to blue. The butterfly diagrams with reversed polarity are the signature of the toroïdal component of the solar magnetic field, well known as the sunspot cycle. The poloidal solar magnetic field component is maximum when the toroidal component is minimum.

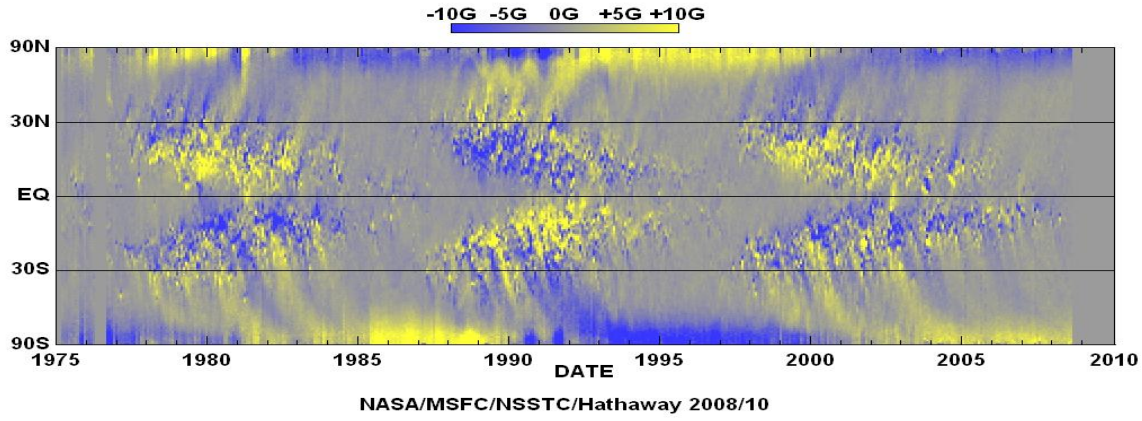

Figure 4: The two components of the solar magnetic field

Scientists have not yet understood all the morphological characteristics of the large scale components of the solar magnetic field. In particular they do not understand how the solar magnetic field changes from a dipolar to a multi-polar configuration (spots).

Recently, Paterno (2006) reviewed the solar dynamo phenomena and proposed a schematic view (figure 5c) to understand the solar dynamo machine in term of the coupling of 2 dynamos: the α dynamo (figure 5a) and the ω dynamo (figure 5b) related to different solar motions.

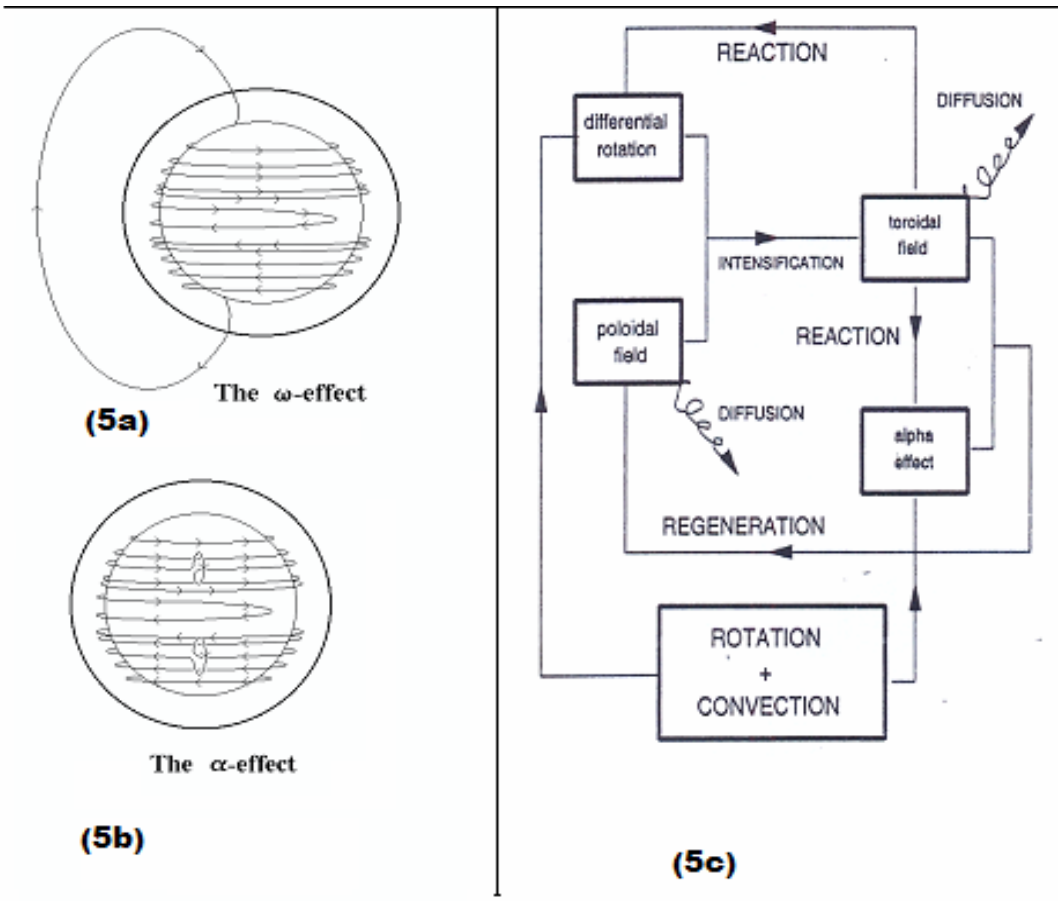

Figure 5: (a): Differential rotation, change in rotation as a function of latitude and radius within the Sun – poloidal component. (b): The twisting of the magnetic field lines is caused by the effects of the Sun's rotation – toroidal component. (c): Working scheme of the α–ω dynamo process. The basic ingredients are rotation convection and an initial poloidal magnetic field after[Paterno 1998]

At the beginning there is a poloidal magnetic field and rotation and convection motions. The differential rotation between the pole and the equator of the sun (~33 days at the pole and ~27 days at the equator) and the poloidal solar magnetic component (ω effect) lead to the intensification of the toroidal solar magnetic component and the twisting of the magnetic field lines (α effect) which both contribute to the regeneration of the poloidal solar magnetic component.

1.3.2 The Earth's dynamo

Long time before the Christian era, Chinese knew the existence the Earth magnetic field existence, but it was only at the beginning of the Middle Ages that the measurements of the Earth magnetic field started in Europe. During several centuries, sparse observations of the magnetic field declination and inclination were made over the world.

In 1600, Gilbert introduced the concept of the terrestrial magnet, allowing a global approach of the Earth's magnetic field. After Gilbert's work, all the sparse data were combined into a common picture (see figure 6).

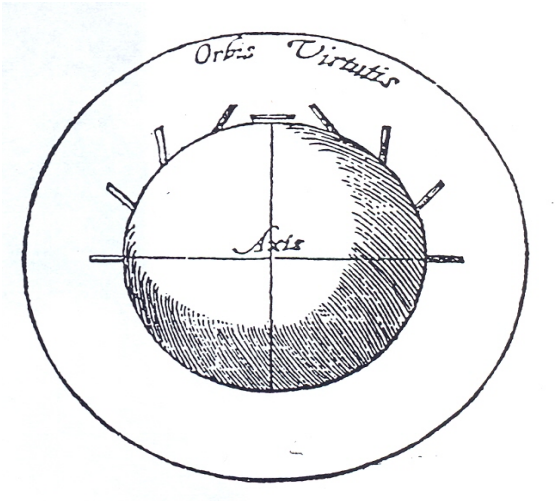

Figure 6: The magnet from Gilbert 1600

At the present time the magnetic field is measured onboard satellites and at ground level in many observatories over the world. Figure 7 presents the internal dynamo of the Earth. At first order the Earth's magnetic field is assumed to be a dipole. The mechanism invoked to explain the Earth's dynamo is the motion of an electrically conducing metallic fluid in the core of the Earth.

NIGERIAN JOURNAL OF SPACE RESEARCH **8**: 178 – 255, 2009 September 1

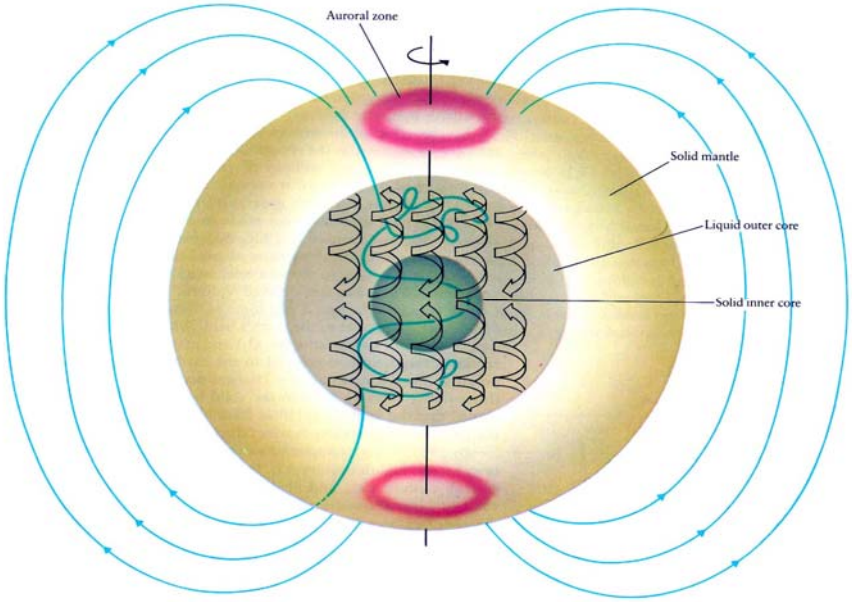

Figure 7: The earths magnetic dipole from Friedman, 1987: "a Model of the generation of a magnetic field by dynamo action in the Earth. Electrically conducting metallic fluid in the earth's core may circulate in screw like rollers. Lines of force are threaded through the rollers as shown here for a single line of force entering from the north and emerging from the south (heavy line)".

The systematic study of the Earth's magnetic field led scientists to establish different components of the Earth's magnetic field.

$$\mathbf{B = B_p + B_a + B_e + B_{in}}$$

B_p = *main field (~ 30000-60000nT)*

B_a = *magnetization field (~ 1-20 nT, due to the magnetization of the rocks in the Lithosphere)*

B_e = *external field (~ qqnT to 2000nT, due to external sources in the ionosphere and the magnetosphere)*

B_{in} = *induced field generated* by the external field B_e , is a percentage of B_e (Kamide and Brekke, 1975)

On the website : http://www.iugg.org/IAGA/iaga_pages/pubs_prods/igrf.htm, the IGRF model of the main field is available and presented as follows : "***The International Geomagnetic Reference Field (IGRF)*** *is a mathematical description of the Earth's main magnetic field used widely in studies of the Earth's deep interior, the crust and the ionosphere and magnetosphere.*

Production of the IGRF is an international collaborative effort relying on co-operation between magnetic field modellers and institutes and agencies responsible for collecting and publishing geomagnetic field data. The IGRF incorporates data from permanent observatories and from land, airborne, marine and satellite surveys. The latest version of the model - the 9th Generation IGRF - was finalised by IAGA's Division V Working Group MOD (formerly WG V-8) in July 2003 at the IUGG XXIII General Assembly in Sapporo, Japan. It includes models of the main field at five-year intervals from 1900 to 2000, and a secular variation model for 2000-2005."

Book recommended: Sun and Earth, Friedman, 1987

1.3.3 The Ionospheric Dynamo

Stewart in 1882 proposed the correct hypothesis to explain the regular variation of the Earth's magnetic field observed on all days on the sun side of the Earth. In the original paper B. Stewart proposed three mechanisms to explain the regular variations of the Earth's magnetic field. One of these mechanisms was the right one [Text of Balfour Stewart : " *It has been imagined that convection currents established by the sun's heating influence in the upper regions of the atmosphere are to be regarded as conductors moving across lines of the magnetic forces*."]

With the first transatlantic radio transmission performed by Marconi in 1901, started the studies of Ionosphere (ionized layers surrounding the Earth between ~ 90 and ~ 800km). From 1901 to 1925, many advances in understanding wave propagation in the ionosphere (Appleton and Hartree) were made and in 1925 the first measurements with the ionosonde technique were performed by Breit and Tuve, allowing measurement of the height profile of the electronic density created by the photo-ionization in the ionosphere.

From 1958 to 1965 new techniques were developed such as rocket flights (1960-1965) giving access to atmospheric tides (Siebert, 1954, 1956) and incoherent scatter sounders (1958-1966)

(Gordon, 1958; Dougherty and Farley, 1960) giving access to electric conductivity, electric field and current as well as atmospheric tides (Vasseur, 1969; Woodman, 1970; Brekke et al., 1974).

From 1960 up to now these in situ measurements were and still are used for developing empirical models of atmospheric parameters (Jacchia, 1964, 1971, MSIS 1986), neutral winds (Hedin et al., 1991), ionospheric electric fields (Richmond et al., 1980) and electric currents (Salah and Evans, 1977; Mazaudier and Blanc, 1982).

Now it is well established, by data and models, that the electric currents in the ionosphere at the origin of the daily variation of the Earth's magnetic field are mainly generated by the motion of the atmosphere which drags ions preferentially through the Earth's magnetic field lines in the E dynamo region (100km<h<150km) and causes a differential drift between ions and electrons.

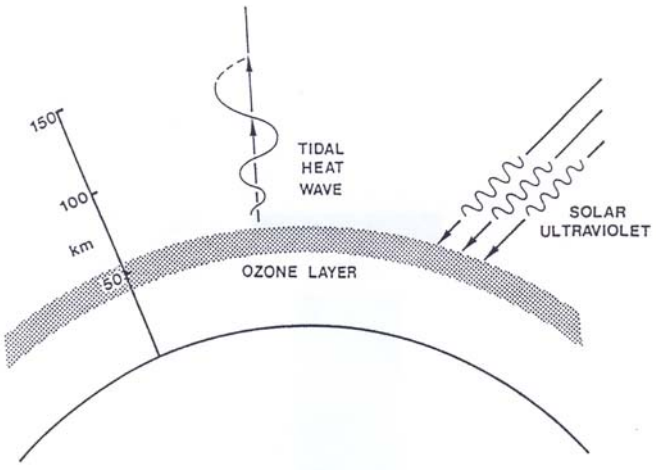

Figure 8a: Atmospheric tides from Evans 1978

On figure 8a from Evans (1978) is shown the absorption of solar radiation in the ozone layer at the origin of atmospheric tides which propagate in the upper atmosphere and are the main source of the atmospheric motions in the E dynamo layer. The figure 8b presents the height

density profile of the dayside ionosphere with the different layers D,E,F_1,F_2. These layers are created the solar radiations. The red arrow indicates the location of the main electric current flow on the dayside in the dynamo layer (90km<h<150km).We must recall here that gravity waves and lunar tides also contribute to the atmospheric motions and therefore to the ionospheric dynamo.

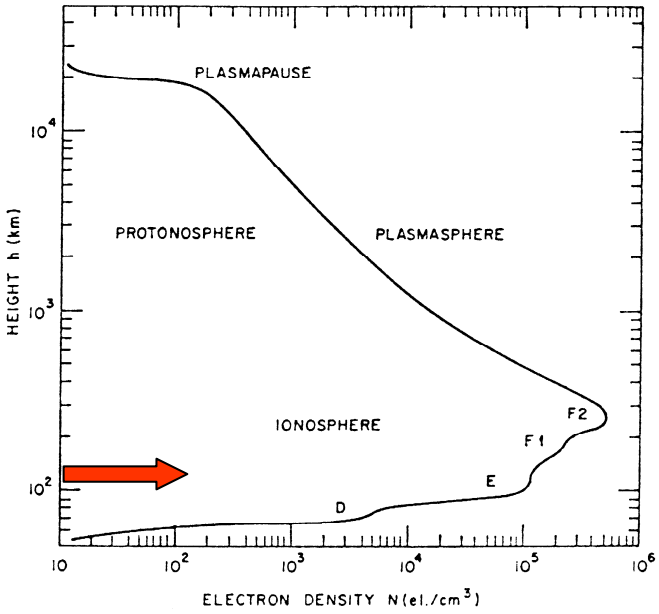

Figure 8b: Ionospheric layers

1.3.4 International Reference Ionosphere : http://modelweb.gsfc.nasa/ionos/iri.html

Brief Description*:The International Reference Ionosphere (IRI) is an international project sponsored by the Committee on Space Research (COSPAR) and the International Union of Radio Science (URSI). These organizations formed a Working Group (members) in the late sixties to produce an empirical standard model of the ionosphere, based on all available data sources (charter). Several steadily improved editions of the model have been released. For a given location, time and date, IRI describes the electron density, electron temperature, ion temperature, and ion composition in the altitude range from about 50 km to about 2000 km; and also the electron content. It provides monthly averages in the non-auroral ionosphere for*

magnetically quiet conditions. The major data sources are the worldwide network of ionosondes, the powerful incoherent scatter radars (Jicamarca, Arecibo, Millstone Hill, Malvern, St. Santin), the ISIS and Alouette topside sounders, and in situ instruments on several satellites and rockets. IRI is updated yearly during special IRI Workshops (e.g., during COSPAR general assembly). More information can be found in the workshop reports. Several extensions are planned, including models for the ion drift, description of the auroral and polar ionosphere, and consideration of magnetic storm effects.

Books or lectures recommended:

Introduction to Ionospheric Physics by Rishbeth and Gariott, 1969

Ionospheric Techniques and Phenomena by Giraud and Petit, 1978

Atmospheric Tidal and Planetary Waves by Volland, 1988

The Earth's Ionosphere, Academic Press, San Diego, by M.C. Kelley, 1989

Review on Ionospheric wind dynamo theory of Richmond 1979.

1.3.5 The solar wind/magnetosphere dynamo

The first satellite missions (Sputnik, Explorer, and Pioneer) and rockets revolutionized this field of research on the Earth electromagnetic environment. These new data provided direct measurements of ionospheric, magnetospheric or interplanetary parameters. In 1957, Van Allen obtained the first direct measurement of aurora radiation with rocket equipment. The following year in 1958 Van Allen discovered radiation belts in the Earth's environment which are now called the Van Allen belts (Van Allen ,1958; Gold, 1959b).

Gold (1959a) discovered the Magnetosphere, the region where the Earth's magnetic field dominates. Here is a part of the abstract of his paper called "Motion on the Magnetosphere of the Earth:" *The conditions determining the dynamical behavior of the ionized gas in the outer atmosphere of the earth are discussed. It is proposed to call this region in which the magnetic field of the Earth dominates the "magnetosphere". Observations by Van Allen and others*

indicate that this zone reaches out to between 5 and 10 earth radii, depending on the degree of magnetic disturbance. ".

Alfven first introduced the fundamental idea of the existence of an electric field $\vec{E}$ related to the solar wind speed $\vec{V}_s$ and the interplanetary magnetic field $\vec{B}_i$ to explain all the magnetospheric electric phenomena. It is the first presentation of the concept of the solar wind/magnetosphere dynamo. The solar wind flows continuously around the magnetosphere and its dynamic energy is transformed into an electric field applied to the magnetosphere:

$$\vec{E}c = -\vec{V}_s \times \vec{B}_i$$

$\vec{E}_c$ electric field called convection electric field (V/m ~ 10^{-3} V/m), V_s solar wind speed (m/s ~qq 100km/s) and $\vec{B}_i$: interplanetary magnetic field (T ~ qq 10^{-9}T). In 1961, Axford and Hines proposed the viscous interaction between the solar wind and the magnetosphere as a possible physical process involve in the solar wind/magnetosphere dynamo (see figure 9). Under the effect of the convection electric field the particles of the Magnetosphere move from the tail to the Earth. They needed a closed magnetosphere. Today the magnetosphere is considered as open.

Another mechanism is invoked to transfer energy from the solar wind to the Magnetosphere: the reconnection process (see figure 10). In the model of Dungey (1961) the magnetic field lines carried by the solar wind link up with the terrestrial magnetic field where the magnetic field lines are anti parallel. This second process is very strong during shock events/CME (Coronal Mass Ejection). Legrand and Simon (1989) worked on the relation between solar and geomagnetic activity. They found that 8.5% of the geomagnetic activity is due to shock events (mainly CME), 67% is due to the slow solar wind (V < 450km/s), 7.5% is related to high speed wind streams. They named fluctuating activity the 17% of solar activity which are not CME, slow solar wind or high speed wind streams.

Recommended books

Introduction to Space Plasma Physics by G.K. Parks

Introduction to Space Physics by Russell and Kivelson

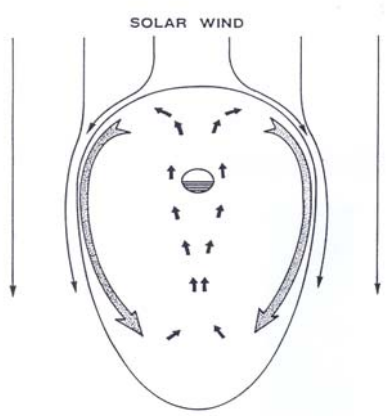

Figure 9: The viscous interaction between the Solar Wind and the magnetosphere [after Axford and Hines, 1961]

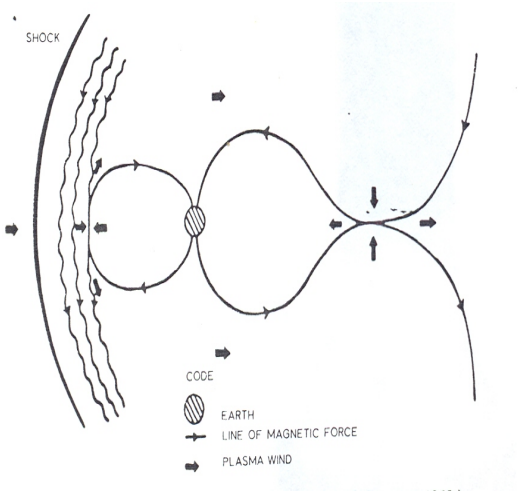

Figure 10: Reconnection model with shock [after Dungey, 1961]

1.4 Sub-conclusion

This first part briefly presents the various large scale dynamos involved in the Sun Earth's system. Four dynamos are invoked:

- the solar wind dynamo is generated by the solar rotation and convection motions and a primary poloidal magnetic field. The poloidal component of the solar magnetic field associated to the differential rotation of the sun create a toroidal solar magnetic field component known as the sunspot cycle. Scientists do not understand the complex relation between the 2 components (poloidal and toroidal) of the solar dynamo, which regenerate each other.
- the Earth's dynamo due to the motion of electrically conducting metallic fluid in the Earth's core.

- the solar wind/magnetosphere dynamo generated by the continuous flow of the solar wind around the magnetosphere,
- the ionospheric dynamo created by the motions of the atmosphere through the Earth's magnetic field lines.

Table 1 sets up together the characteristics (V, B) of the four large scale dynamos operating in the Sun Earth system.

Table 1: Dynamos in the Sun Earths system

Dynamo	Motions – V	Magnetic field B	Order of Magnitude
Sun dynamo	Sun Rotation and convection	Sun : 2 components Dipolar Toroïdal ~ sunspots	rotation speed : ~ 7280km/h at the equator Dipolar component : ~10 G Toroidal component ~3-5 KG
Solar wind/ Magnetosphere Dynamo component of Be	Solar wind	Interplanetary medium -> Bi	speed ~ [400km/s to 800km/s] Bi ~ qq 10 nT
Ionospheric dynamo Component of Be	Atmosphere	Earth's -> Bt	speed ~ 100m/s Bt ~ qq 10 000 nT Change with latitude and longitude
Earth's Dynamo inside the Earth Bp	Metallic core	Earth's -> Bt	No direct measurement of the velocity in the core material Indirect measurements deduced from the Earth's planetary magnetic field and the secular variation Velocity ~ qq km/year Bt ~ qq 10 000 nT Change with latitude and longitude

2.0 Large scale electric currents in the Earth's Environment: Introduction

This section is devoted to the large scale electric currents in the Earth's environment and organized in six paragraphs. The first 2.1 paragraph recall the basic equations and some generalities, and the five others the various electric current systems. We must distinguish three types of electric current systems:

- magnetospheric electric currents flowing in the magnetosphere
- field aligned currents which flow along the lines of the magnetic field and couple ionosphere and magnetosphere.

- ionospheric electric currents flowing in the ionosphere

2.1 Basic Physics and generalities

2.1.1 Basic equations

The Magnetosphere and Ionosphere are plasma, i.e, composed of electrons and ions. A branch of the physics, known as Plasma physics is used for our study. The main equations concerning electric currents are the following:

Equation of motion of the particle q

$$m\frac{d\vec{V}_q}{dt} = -\frac{1}{N_q}\vec{\nabla}.P_q + m_q g + q(\vec{E}+\vec{V}_q\times\vec{B}) - m_q\nu_{qn}(\vec{V}_q-\vec{V}_n) - m_q\nu_{qp}(\vec{V}_q-\vec{V}_p)$$

Inertia | **Pressure gradient** | **Gravity** | **Electric Field** | **Lorentz Force** | **Collisions with neutrals n** | **Collisions with charged particles p**

Where ν are the collisional frequencies

In the magnetosphere gravity and collisions with neutrals are negligible.

Equation of electric current density: $\vec{j} = \sum_q N_q e_q \vec{V}_q$

Nq : density number of particles by m³ ; eq : charge of the particle q; Vq : particle q drift m.s⁻¹

The electrical current density is divergence free

$\varepsilon_0 \frac{dE}{dt}$ -> displacement currents, $div\vec{j} = 0$

OHM's law: $\vec{j} = \bar{\bar{\sigma}}(\vec{E}+\vec{V}\times\vec{B})$

BIOT and SAVART' s law: $B = \frac{\mu_0}{4\pi}\int(\frac{j\hat{x}r}{r^2})dV$

Equation of continuity: $\frac{\partial N}{\partial t} = q - L - \vec{\nabla}(NV)$ -> N : particle density, V particle drift

The first term q is production of particles , the second term L is the loose of particles the third term is the transport of particles

2.1.2 Location of the different electric current systems.

Figure 11a illustrates the various current systems in the magnetosphere. In the front of the Magnetosphere are located magnetopause currents also called Chapman Ferraro currents (in

green on the figure). The magnetopause is the boundary between the solar wind and the Earth's magnetic field. The Earth's magnetic field is compressed by the solar wind pressure in the front and stretch as to the back of the magnetosphere. In the equatorial plane of the magnetosphere at a distance of several radii from the Earth circulates the ring current (violet in the figure). The tail currents flow in the magnetopause at a distance of ~ 15 to 20 Earth's radii, they are connected to the cross-tail current sheet (yellow on the figure) flowing in the plasma sheet in the equatorial plane of the magnetosphere. The field aligned currents are blue for current into the ionosphere and red for currents flowing away from the ionosphere. They correspond respectively to regions called region 1 and region 2 in the ionosphere.

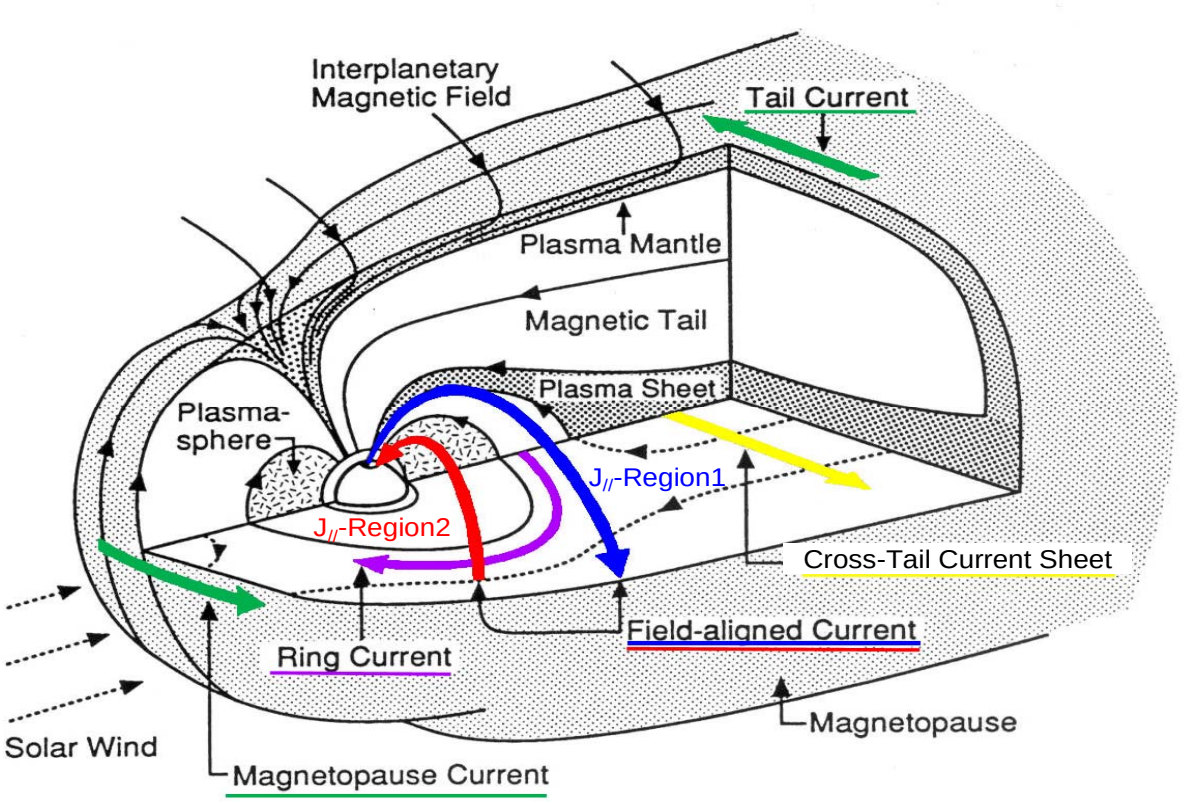

Figure 11a: Magnetospheric electric current systems

Figure 11b illustrates the various ionospheric electric current systems:

- the two auroral electrojets: the westward electrojet (blue) and the eastward electrojet (red),

- the equatorial electrojet (green),
- the middle latitude current sheet with current flowing anti clockwise (violet arrow)..

In the southern hemisphere there are similar auroral electrojets and a middle latitude current sheet but the currents flow in opposite direction.

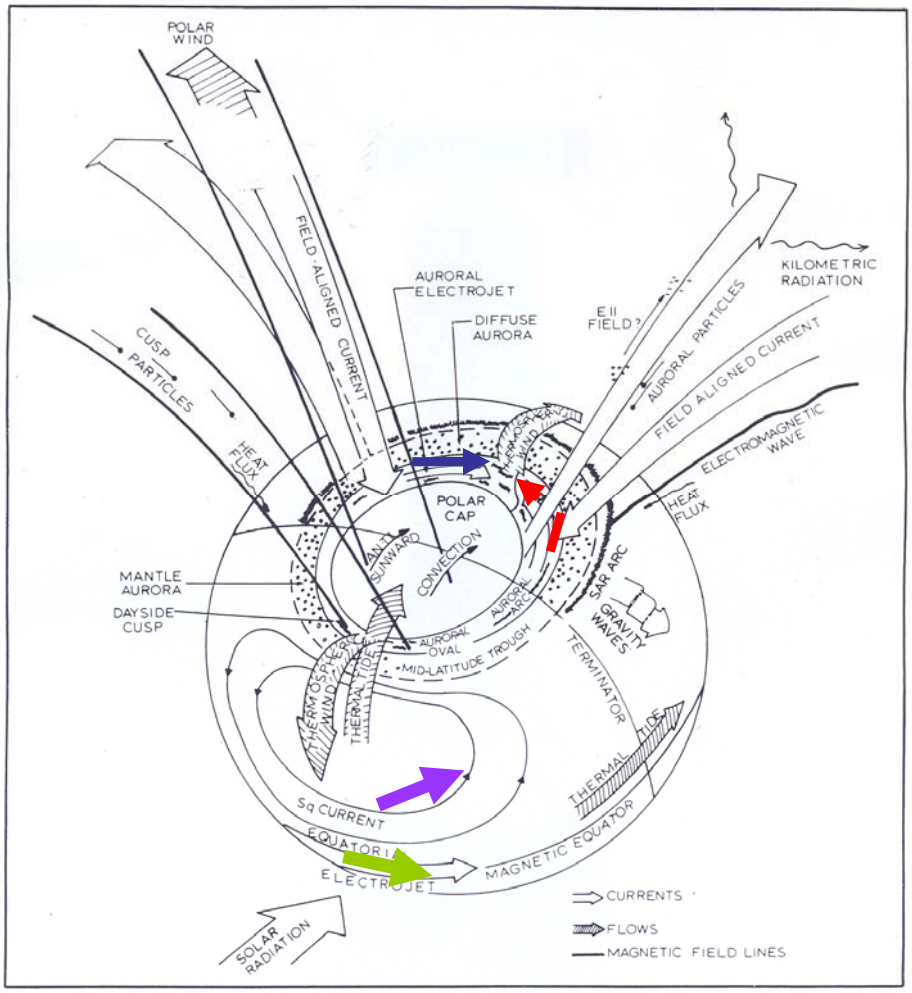

Figure 11b: Ionospheric electric current systems.

As we previously mentioned, there are very few in situ measurements of the real large scale electric current in the Earth's environment. The variations of the Earth's magnetic field lead the scientists to postulate the existence of large scale current systems. And the next sections will

present that fact. All the electric currents are evaluated through their effects on the Earth's magnetic field. To compare magnetic variation and electric current density we must know that 1 A/km~1 nT.

Amory-Mazaudier (1994) and Amory-Mazaudier (2002) listed the main steps in the study of electric currents The steps described in these papers correspond to advances in fundamental physics, as well as in technology, data interpretation and other factors. These papers cover the period from 1870 up to now. In annexe 1 we put three tables included in this paper:

- Table 2 from Chapman and Bartels, starting point of the 2 papers of Amory-Mazaudier
- Table 3 from Amory-Mazaudier (1994), corresponding to the main steps in the knowledge of the regular variation of the Earth's magnetic field
- Table 4 from Amory-Mazaudier (2002), corresponding to the main steps in the knowledge of the irregular variation of the Earth's magnetic field.

2.2 Chapman Ferraro currents

2.2.1 First concept

Chapman and Ferraro in 1935 explained magnetic storms by the interaction of a cloud of electrically neutral mixture of ions and electrons (today named plasma) approaching the Earth's dipole. When the cloud of 'plasma 'approaches the Earth, electric currents would be induced in it, producing magnetic disturbances. The cloud of matter was assumed to be a two-dimensional conducting sheet. Furthermore, if this sheet is a perfect electrical conductor, all the induced currents flow on the surface.

Maxwell had shown that when a perfectly conducting flat plane approached a dipole, its externally induced field was the same as the field of an equal 'image dipole' located symmetrically on the other side of the plane. Figure 12a from Chapman and Ferraro (1935) illustrates the meridian section of the interaction between the Earth's dipole and the current sheet, at the left is the Earth's dipole field and the image dipole at the right of the figure.

NIGERIAN JOURNAL OF SPACE RESEARCH **8**: 178 – 255, 2009 September 1

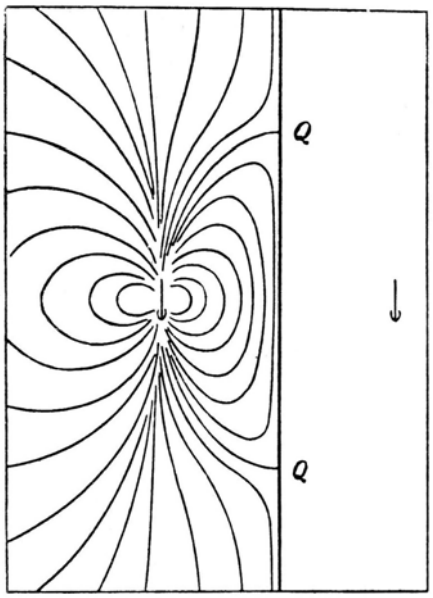

Figure 12a: Meridian section

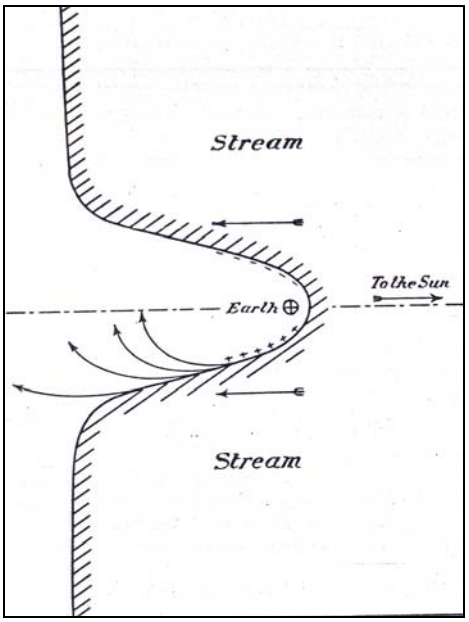

Figure 12b: equatorial section

As a feedback the Earth's magnetic field exerts a force on the induced currents. This force when the current sheet (cloud of plasma) approaches the Earth becomes strong enough to stop the frontal advance of the cloud of plasma toward the Earth. On the sides the flanks continue their advance. Thus is created a cavity enveloping the Earth and called the 'Chapman Ferraro cavity'. Under the influence of the Earth's magnetic the particles do not approach the Earth. Figure 12b (from Chapman and Ferraro, 1935) illustrates the formation of the Chapman-Ferraro cavity. The arrows trace the paths of the ions.

2.2.2 Physical mechanisms and estimation

The Chapman Ferraro currents flow in the Magnetopause layer, the boundary between the solar wind and the geomagnetic field. At the nose of the magnetopause the geomagnetic field pressure is balanced by the dynamic pressure of the solar wind

$$K_1 N_i m_i V_i^2 = \frac{B_{mp}^2}{2\mu_0}$$

{dynamic pressure of the solar wind ⇔ geomagnetic field pressure}

K_1 is the correction factor for flow deflection in magnetosheath and compression of B (Heelis, 2005). The order of magnitude of the Chapman Ferraro current is ~ 30 nT (Gosling et al. 1990).

Figure 13 illustrates the circulation of Chapman Ferraro currents (J) along the magnetopause boundary. At the frontier between the interplanetary medium and the magnetosphere ions and electrons are deflected in opposite direction, this leads to a circulation of electric currents along the magnetopause. We must recall here that the magnetic field in the solar wind is considered as nil, this is not really true, the magnetic field is small but not nil.

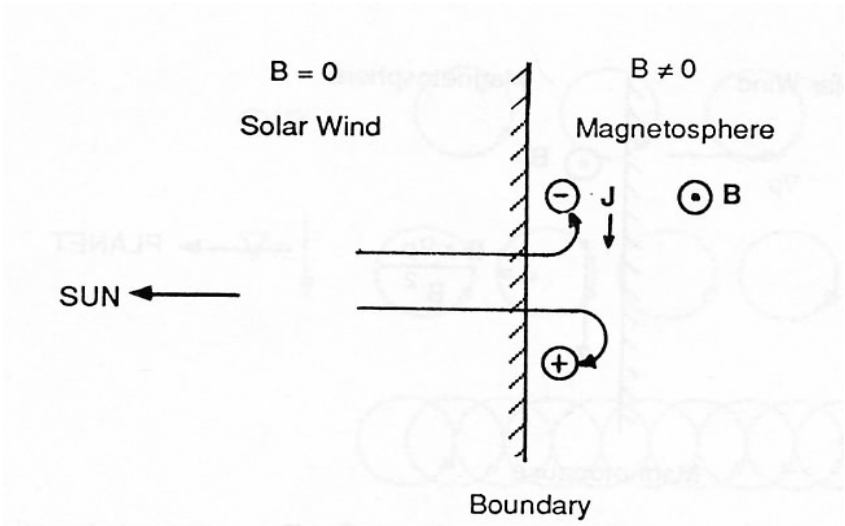

Figure 13: geometry

2.3 Ring current

2.3.1 First concept

Störmer (1907-1013) was the first to propose the existence of an electric current flowing in the equatorial plane of the Magnetosphere at several Earth's radii. Later in 1939 Alfven suggested the connection between the westward auroral electrojet and part of the ring current now called the partial ring current.

In 1966, Cummings developed an empirical model of partial ring current in order to interpret the daily variation of the low latitude disturbance. Figure 14a from Cummings (1966),

illustrates the partial ring current. This figure shows the drift currents flowing in the equatorial plane as well as the field-aligned currents connecting the drift currents to the auroral electrojets.

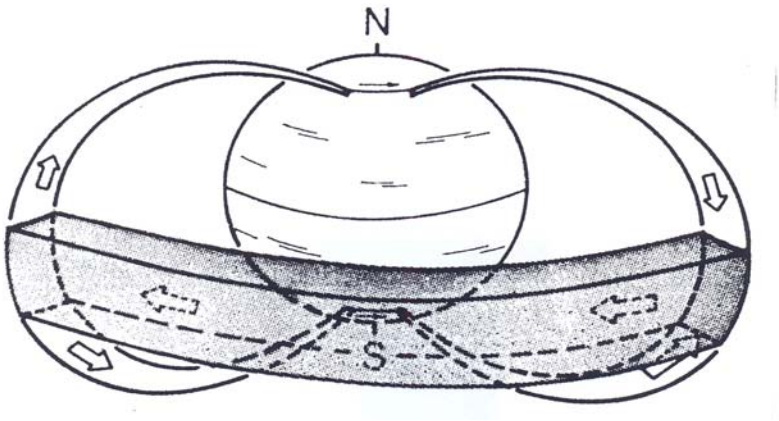

Figure 14a: Partial ring current [after Cummings, 1966]

An asymmetric ring current is equivalent to a symmetric ring current plus a superimposed partial ring current. This is shown on figure 14b from Fukushima and Kamide (1973).

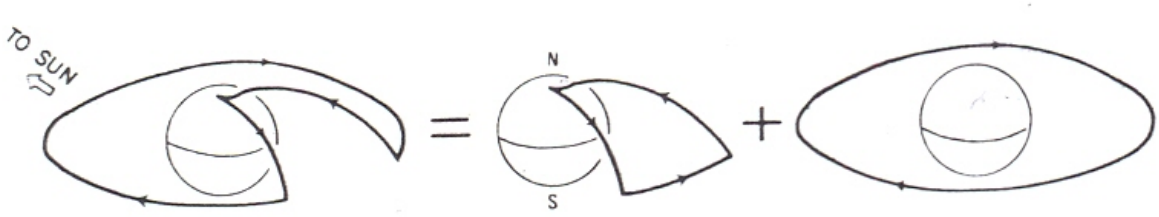

Figure 14b: Asymmetric ring current [after Fukushima and Kamide, 1973]

2.3.2 Physical mechanism and estimation

The solar wind flowing around the magnetosphere imposes a dawn dusk voltage drop difference to the magnetosphere. The hot magnetospheric particles are under the influence of the voltage drop difference and they follow trajectories from the tail of the magnetosphere toward the Earth. In the region where the curvature and gradient of the Earth's magnetic field are strong, particles are separated. The electrons are diverted to the morning side and the ions to the evening side, this leads to the formation of the ring current.

The charge space created by the ring current generates a secondary electric field which tends to oppose to the primary field. Before the installation of the secondary electric field the primary electric field influences the whole ionosphere.

There is direct extension of the magnetospheric convection toward middle and low latitudes. When the secondary electric field is established, it tends to diminish the effect of the primary electric field at middle and low latitudes: this is the shielding effect. Figure 15 illustrates this mechanism.

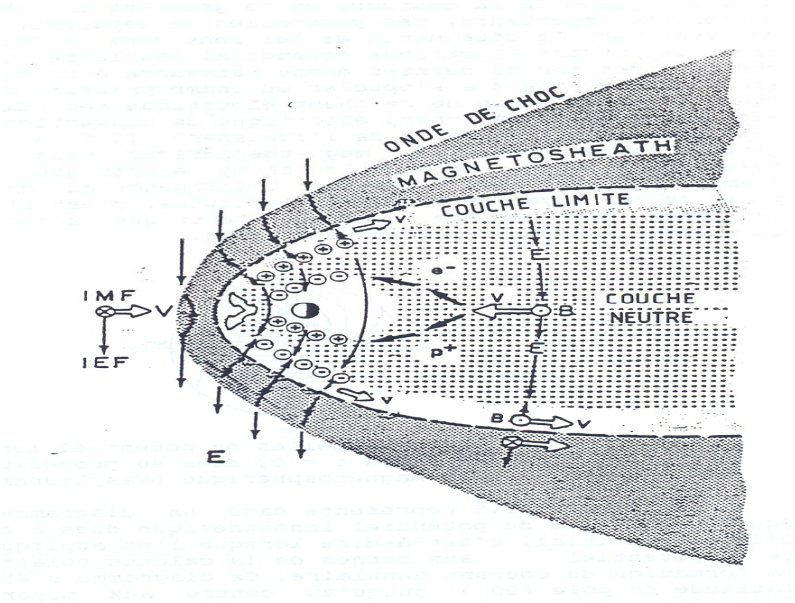

Figure 15: Formation of the ring current

The expression of the drift due to gradient and curvature and the resulting current is (Heelis, 2005):

$$\vec{V}_{gc} = \frac{1}{2} m V_{\perp}^2 \frac{B \times \nabla B}{qB^3} + m V_{LL}^2 \frac{B \times (b.\nabla)\hat{b}}{qB^2}$$

$$J_{gc} = NqV_{gc}^{ions}$$

This current is mainly carried by ions.

There is also an additional contribution of the magnetic moments of all particles:

$$\vec{M} = -N_i \frac{1}{2} \frac{m_i V_{i\perp}^2}{B} \hat{b} - N_e \frac{1}{2} \frac{m_e V_{e\perp}^2}{B} \hat{b}$$
$$\vec{J}_m = \nabla \times \vec{M}$$

The ring current keeps the pressure gradient and the Lorentz force in balance.

2.4 Tail Currents

2.4.1 First concept

Akasofu, in 1972, proposed that the tail currents flowing at the boundary of the plasma sheet are disrupted and deflected toward the Earth on the evening side. These currents via Birkeland (field aligned current) be converted to a westward electrojet. Figure 16 from Akasofu, 1972 illustrates this physical process.

2.4.2 Physical mechanisms and estimation

Figure 17a shows the magnetic field data from the ISEE2 satellite where a tail crossing is observed ~ 0830 UT. From the top panel we can estimate the tail current ~20 nT. Figure 17b from Heelis (2005) illustrates the geometry of the tail currents. Tails currents are closed through the neutral sheet current. The tail currents which enclose the magnetic field in tail lobes are under the control of the solar wind (Tsyganenko, 2000),

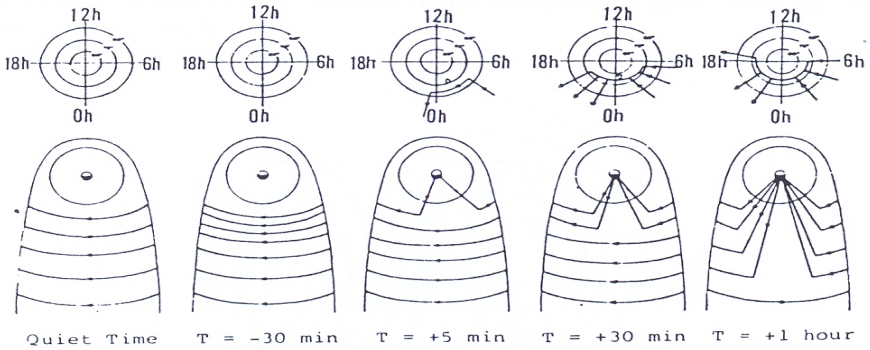

Figure 16: schematic diagrams showing the development of magnetospheric substorm as the conversion of magnetotail current to a birkeland and auroral electrojet [After Akasofu, 1972]

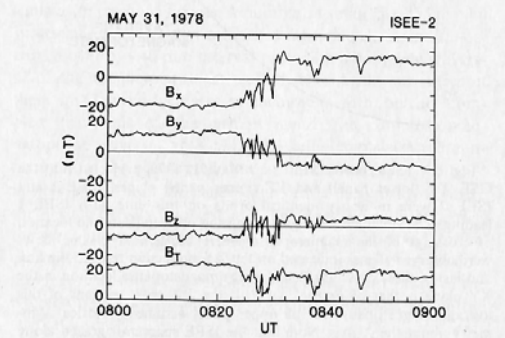

Fig. 2. Magnetic field data from ISEE 2 surrounding the ~0830 UT magnetopause crossing on May 31, 1978. From top to bottom the quantities plotted are the *x*, *y*, and *z* components (GSE coordinates) of the field and the total field magnitude.

Figure 17a: Tail crossing [after Gosling et al. 1986]

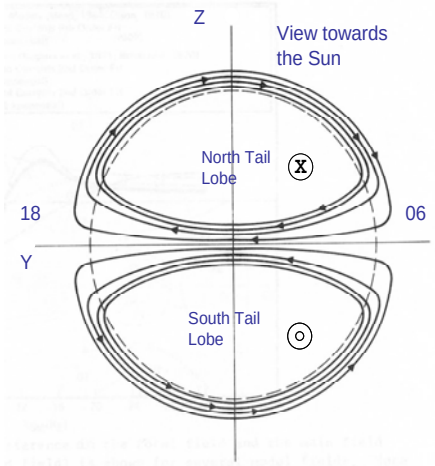

Figure 17b: Geometry of the tail current and comments [after Rod Heelis 2005]

2.5 Field aligned electric currents

2.5.1 First concept

It is at about the same time that K. Birkeland, a Norwegian scientist (1867-1917) organized polar expeditions to study aurora (Birkeland, 1908; Birkeland, 1913). Birkeland proposed a 3D system of electric currents to explain the magnetic disturbances. He was the first to suggest field-aligned currents closing in the ionosphere (Birkeland, 1908). Figure 18 shows the current system proposed by K. Birkeland. On this figure field aligned currents come into and out of the ionosphere. In the ionosphere field aligned currents are converted into an ionospheric electric current: the auroral electrojet.

2.5.2 Physical mechanisms and estimation

Satellite data were systematically used to determine the field-aligned currents essential to understand the closure of magnetospheric currents in ionosphere (Amstrong and Zmuda, 1970; Ijima and Potemra, 1978). Figure 18 and Figure 19 from Ijima and Potemra (1978) represents the distribution of field aligned currents which connect the auroral electrojets to the magnetospheric current systems. This amplitude of the magnetic field associated to field aligned current is ~100 nT.

NIGERIAN JOURNAL OF SPACE RESEARCH **8**: 178 – 255, 2009 September 1

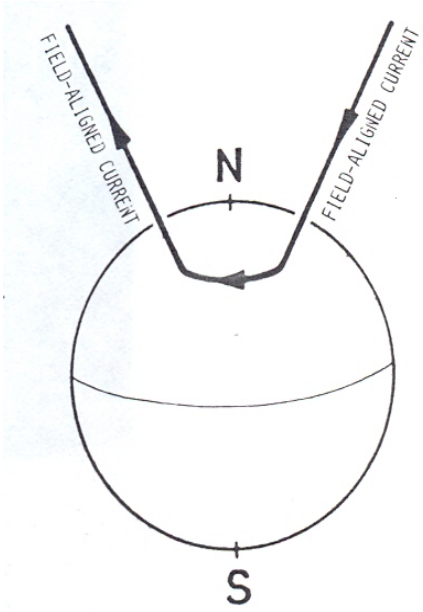

Figure 18: Field aligned current [after Birkeland, 1908]

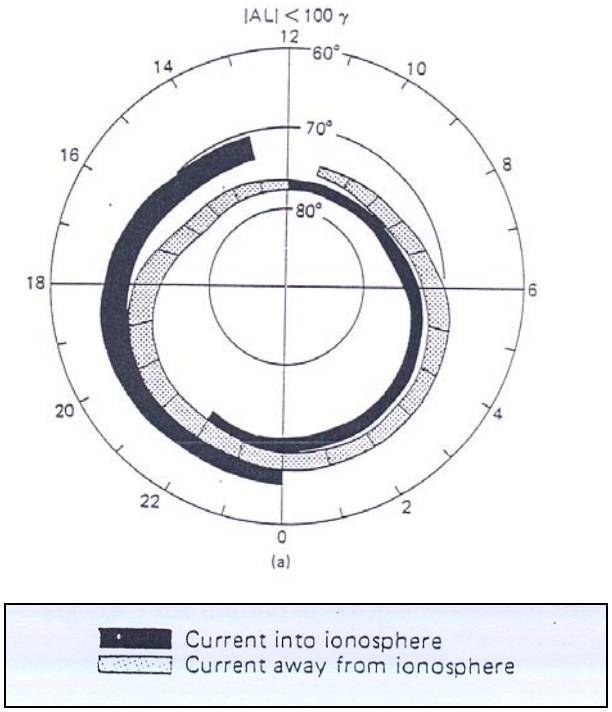

Figure 19: Distribution of the field aligned current system in the auroral zones [after Ijima and Potemra, 1978]

All the currents flowing in the ionosphere or magnetosphere must flow in closed loops. The Field aligned current assumed the coupling between the magnetosphere and the ionosphere. A divergence in the horizontal electric currents leads to a change in the field aligned current.

$$\nabla \vec{j} = \nabla_{\perp} \vec{j}_{\perp} + \nabla_{II} j_{II} = 0$$

The closure of the magnetospheric current loops requires field aligned currents flowing into and out of the ionosphere. The origin of the field aligned currents is near the equatorial edge of the magnetopause (region1), in the plasma sheet where the ring current is divergent (region 2) and at the magnetopause at high latitudes in the dayside.

2.6 Ionospheric electric currents

The ionosphere is a region of the Earth's environment where electric current flow is under the influence of various dynamos:

1) the ionospheric dynamo produces the daily regular variation of the Earth's magnetic field observed each day on the dayside
2) the solar wind magnetosphere/dynamo and reconnection processes in the magnetosphere generate disturbed ionospheric electric currents.

The existence of the electric current in the ionosphere depends on forces which induce motions of ions and electrons and determine the structure of the ionospheric electric conductivities.

In this section we first analyse the equations concerning the ionospheric plasma and then we present in situ measurements of the ionospheric electric or fields currents obtained with the techniques of rocket borne and incoherent scatter sounder and coherent radar.

2.6.1 Basis equations

In the Ionosphere the basic equations of electric current density in a plasma $\vec{j} = \sum_q N_q e_q \vec{V}_q$

reduces to: $\vec{j} = N_e.e(\vec{V}_i - \vec{V}_e)$ Where j is the electric current density (A.m^{-2}), e the charge of the electron (C) $\vec{V}_i$ and $\vec{V}_e$ the drift of the ions and of the electrons (m.s^{-1}) and N_e the electronic density (p.m^{-3})

The plasma is assumed quasi neutral $N_e \sim N_i$

Due to collisions there is a collective motions of ions.

The equation of motion of ions or electrons see paragraph 2.1.2 is:

$$m_i \frac{d\vec{V}_i}{dt} = -\frac{1}{N_i}\vec{\nabla}.P_i + m_i g + q(\vec{E} + \vec{V}_i \times \vec{B}) - m_i \nu_{in}(\vec{V}_i - \vec{V}_n) - m_i \nu_{ie}(\vec{V}_i - \vec{V}_e)$$

The ionospheric Ohm's law is expressed as:

$$\vec{j} = \bar{\bar{\sigma}}(\vec{E} + \vec{V}_n \times \vec{B})$$

$$div\vec{j} = 0$$

$$rot\vec{E} = 0 \Rightarrow \vec{E} = -\vec{\nabla}\Psi$$

Where $\bar{\bar{\sigma}}$ is the conductivity tensor ((Ω/m), $\vec{V}_n$ the neutral wind (m/s), $\vec{B}$ the Earth's magnetic field (T), $\vec{V}_n \times \vec{B}$ the dynamo electric field, $\vec{E}$ the electrostatic electric field due to the space charge (V/m).

If we consider large scale phenomena (space and time) we assume the quasi stationary state:

$$\frac{d\vec{V}_i}{dt} \sim 0$$

Following the direction perpendicular to the Earth's magnetic field, the equation of motion for ions reduces to the simplified expression:

$$e(\vec{E}_\perp + \vec{V}_i \times \vec{B}) - m_i \nu_{in} (\vec{V}_i - \vec{V}_n)_\perp = 0$$

Gravity, collisions between charged particles, and pressure gradients are negligible.
For the electrons the equation is similar except that the collisions with ions are not negligible.
If we divide by m_i

$$\frac{e}{m_i}(\vec{E}_\perp + \vec{V}_i \times \vec{B}) - \nu_{in} (\vec{V}_i - \vec{V}_n)_\perp = 0$$

If we introduce the gyrofrequency $\Omega_i = \frac{eB}{m_i}$, we obtain

$$\frac{1}{B}(\vec{E}_\perp + \vec{V}_i \times B) - \frac{\nu_{in}}{\Omega_i}(\vec{V}_i - \vec{V}_n) = 0$$

The ratio $\frac{\nu_{in}}{\Omega_i}$ is important and determines the existence of electric currents in the dynamo layer (E region).

On figure 20 from Richmond (1995) are plotted the collision frequencies and the gyrofrequencies as a function of the altitude. Above 160km the gyrofrequencies of both ions and ions are greater than the collisions frequencies. Below 100km in the direction perpendicular to the magnetic field the electron gyrofrequency reach the same order of magnitude as the

collision frequency between electrons and neutral atom, this is a good condition to have electric currents, but due to the weak electron density there is no electric current in this region. Below ~ 80 km the collision frequencies are all smaller than the gyrofrequencies for both ions and electrons. All the particles are moving with the neutral atmosphere.

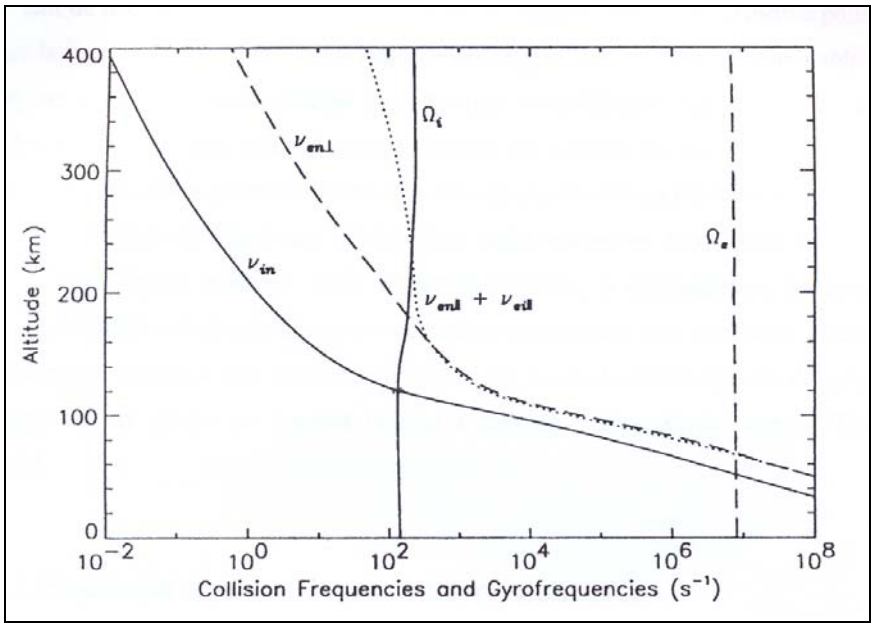

Figure 20: Altitude profile (0-400km) of the collisions frequencies and gyrofrequencies of the particles [after Richmond, 1995]

At altitudes above 160km $\Omega_e >> \nu_{en}$ and $\Omega_i >> \nu_{in}$ hence, the motion of the electrons and the ions is:

$\vec{V}_{e\perp} = \vec{V}_{i\perp} = \frac{\vec{E} \times \vec{B}}{B^2}$ (this drift is named EXB drift; pronounced "E cross B drift")

At altitudes between 100 and 160 km Ω_i and ν_{in} are of the same order of magnitude, the motion of the ions $\vec{V}_{i\perp}$ is influenced by the drag of the neutral atmosphere and by the electric field. The expression of the perpendicular ion drift is:

$$\vec{V}_{i\perp} = \frac{\vec{E} \times \vec{B}}{B^2} \frac{1}{1+r_i^2} + \frac{\vec{E}_\perp}{B} \frac{r_i}{1+r_i^2} + (\vec{V}_n \times \vec{B}) \frac{r_i}{1+r_i^2} + \vec{V}_{n\perp} \frac{r_i^2}{1+r_i^2} \quad \text{where} \quad r_i = \frac{\nu_{in}}{\Omega_i}$$

At the top of the E layer when r_i becomes small the first term is dominant $\vec{V}_{i\perp} = \frac{\vec{E} \times \vec{B}}{B^2}$

At the bottom of the E layer where r_i is large the last term is dominant and $\vec{V}_{i\perp} = \vec{V}_{n\perp}$ and the motion of the ions is equal to the motion of the neutral atmosphere.

In the direction parallel to the Earth's magnetic field:

$$V_{iII} = V_{nII} + V_{dII}$$

$$V_{eII} = V_{eII} + V_{dII} - \frac{j_{II}}{N_e.e}$$

V_{dII} is ambipolar diffusion drift under the influence of the pressure gradient and the gravity (neglected following the perpendicular direction).

The electrons are also accelerated by parallel field aligned currents not related to the diffusion. Below 180 km the diffusion is negligible therefore: $V_{iII} \cong V_{nII}$

2.6.2 Conductivities

Ohm's law can be expressed in a frame with the following directions

i) axis following the magnetic field $\vec{B}$ -> II

ii) axis perpendicular to $\vec{B}$ and parallel to the electric field $\vec{E}$

iii) axis perpendicular to $\vec{B}$ and $\vec{E}$

$$\vec{j} = N_e.e(\vec{V}_i - \vec{V}_e) = \overline{\overline{\sigma}}\vec{E}' = \sigma_{II} E'_{II} + \sigma_P E'_\perp - \sigma_H E'_\perp \times \hat{b}$$

where :

$$\vec{E}' = \vec{E} + \vec{V}_n \times \vec{B}$$

=> the electric field E' is the sum of the polarization electric field E and the dynamo field

σ_{II} is the parallel conductivity following the lines of the Earth's magnetic field $\vec{B}$

σ_P is the Pedersen conductivity in the direction of $\vec{E}$

σ_H is the Hall conductivity in the direction perpendicular to $\vec{B}$ and $\vec{E}$

$$\sigma_{II} = N_e e^2 \left(\frac{1}{m_e \nu e} + \frac{1}{m_i \nu_{in}}\right)$$

$$\sigma_H = \frac{N_e e^2}{B}\left(\frac{\Omega_e^2}{\nu_e^2 + \Omega_e^2} - \frac{\Omega_i^2}{\nu_i^2 + \Omega_i^2}\right)$$

$$\sigma_P = \frac{N_e e}{B}\left(\frac{\nu_e \Omega_e}{\nu_e^2 + \Omega_e^2} + \frac{\nu_i \Omega_i}{\nu_i^2 + \Omega_i^2}\right)$$

where

$$\nu_e = \nu_{en} + \nu_{ei} \quad , \nu_i = \nu_{in} + \nu_{ie}$$

$$\Omega_e = \frac{eB}{m_e}, \ \Omega_i = \frac{eB}{m_i}$$

The different components of the electric conductivities are drawn on figure 21 (from Richmond, 1995). This figure shows the large amplitude of the Hall and Pedersen components of the conductivity in the E region (100-150 km): the dynamo layer. Above the E region the Hall conductivity decreases more rapidly than the Pedersen conductivity. Above 90km, the parallel conductivity increases strongly.

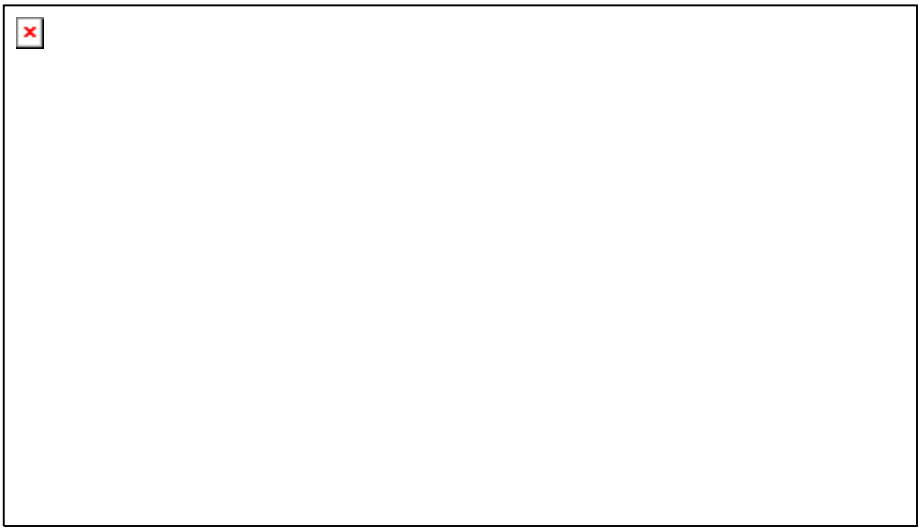

Figure 21: altitude profile of the different components of the ionospheric electric conductivity [after Richmond, 1995]

At the equator the electric current density is stronger than at middle latitudes due to geometry, B is horizontal. At the equator there is an enhanced conductivity called the Cowling conductivity given by the following equation : $\sigma_c = \sigma_P + \frac{\sigma_H^2}{\sigma_P}$ (see the book Onwumechili, 1997).

2.6.3 In situ measurements

It is important here to stress that there are very few in situ measurements of electric currents, neutral wind or electric fields made with incoherent scatter and rocket borne techniques, or electric fields measurement made with coherent radar. In this paragraph we will present observations made in the auroral zone, at middle latitudes and at equatorial latitudes.

Auroral zone

The auroral zone is located between the high latitudes ~65 °N to 75° N (in the northern hemisphere). It is a region where many phenomena take place :

- field aligned current close the magnetospheric loops of currents
- particles precipitate in the ionosphere producing enhanced conductivities
- the electric field generated by the solar wind/dynamo or other physical processes strongly influences the motion of particles
- the energy deposition (Joule heating $\vec{j}.\vec{E}$ and momentum transfer $\vec{j} \times \vec{B}$ produce motion of the neutral atmosphere, etc…=> see figure 10b paragraph 2.1.2.

All these auroral phenomena influence the circulation of electric currents in auroral zone (strong auroral electrojets exist) but also at middle and low latitudes. Two main physical processes are acting at a global scale to couple high and low latitudes through electrodynamic physical processes. The first process is called prompt penetration of the convection electric

field, first invoked by Nishida in 1968 (see the next section on equivalent current) and the second one the ionospheric disturbance dynamo (Blanc and Richmond, 1980).

On figure 22 are plotted the southward component of the electric field measured by the STARE radar (a coherent radar which was operating in Europe during the eighties) and the variation of the H component of the Earth's magnetic field measured in the observatory of Tromsö. The electric field is deduced from the EXB drift of electrons. We can notice the very good correlation between the two curves. The pattern of the horizontal component exhibits the signature of the 2 auroral electrojets: the westward one before 06.00 UT and after 21.00 UT and the eastward electrojet on the dayside between 12.00 UT and 18.00 UT. In the sector of longitude of Tromsö UT time equals LT time. The STARE radar measurements disappear between 06.00 and 12.00 UT and between 18.00 to 21.00 UT when the signal is not strong enough, i.e, when the motion of particles is too small.

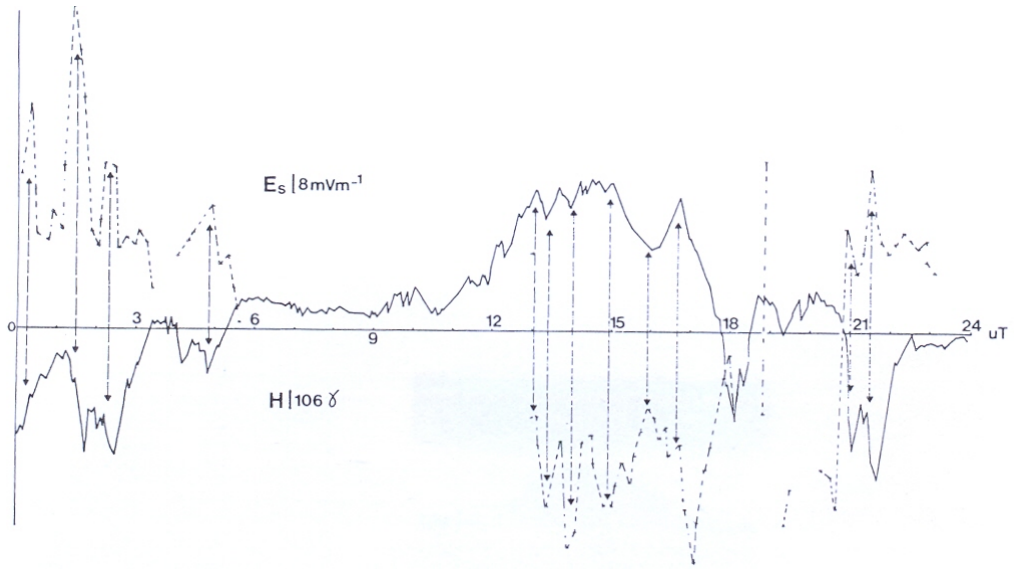

Figure 22: Southward STARE electric field and ground H component at Tromsö on March, 26, 1979 [after Mazaudier et al., 1987]

Figure 23 from Brekke et al. (1994) is composed of 4 panels. From the top to the bottom the panels show the D component of the Earth's magnetic field at College (American sector), the northward height integrated current density (⊥) , the H component of the magnetic field at College and the eastward height integrated current density (⊥). We can observe a good agreement for the whole day, between the H component and the eastward height integrated current density (⊥), the magnetometer and the incoherent scatter sounder capture the same phenomena of the amplitude of the auroral electrojet . On the contrary the agreement is bad between the D component and the northward height integrated current between 12.00 and 20.00 UT. The disagreement between the D component and the northward height integrated current density (⊥) is explained by the field aligned current.

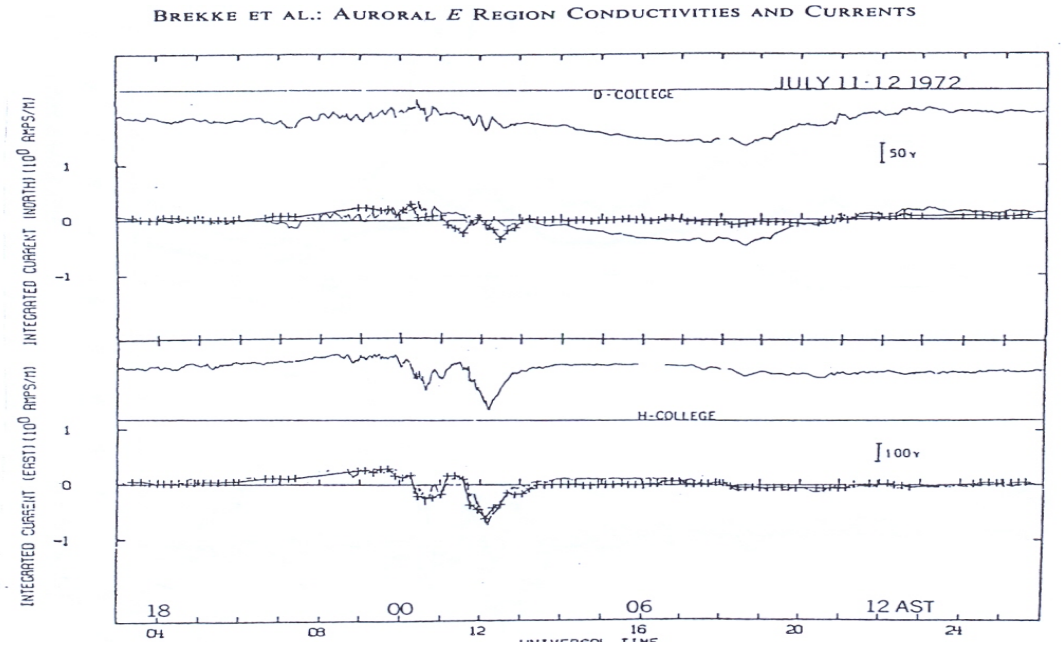

Figure 23: In situ measurements of electric height integrated electric current densities with the Chatanika incoherent scatter sounder and comparison with the variations of the Earth's magnetic field, on July, 11, 1972 [after Brekke et al., 1974].

Midlatitudes

Figure 24 selected to illustrate the direct in situ measurement of electric currents at middle latitudes is from Mazaudier (1982). This figure shows the altitude profile of the 2 components of the perpendicular electric current in the E. region measured with the incoherent scatter

sounder of Saint Santin which was operating from 1966 to 1987 in France (Europe). The order of magnitude of the electric current density is ~qq $\mu A.m^{-2}$. The integration of the altitude profile of the electric current density over the E region (~60 km) gives an eastward height integrated density with a magnitude of ~ 100 $A.km^{-1}$ which is comparable to the H component of the Earth's magnetic field ~100 nT.

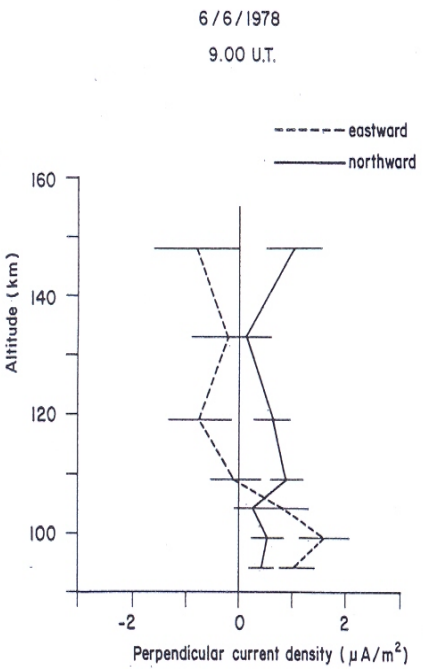

Figure 24: Typical altitude profile of the perpendicular eastward current density (dashed line) and the northward one (solid line).Such profiles are obtained every half hour [after Mazaudier, 1982]

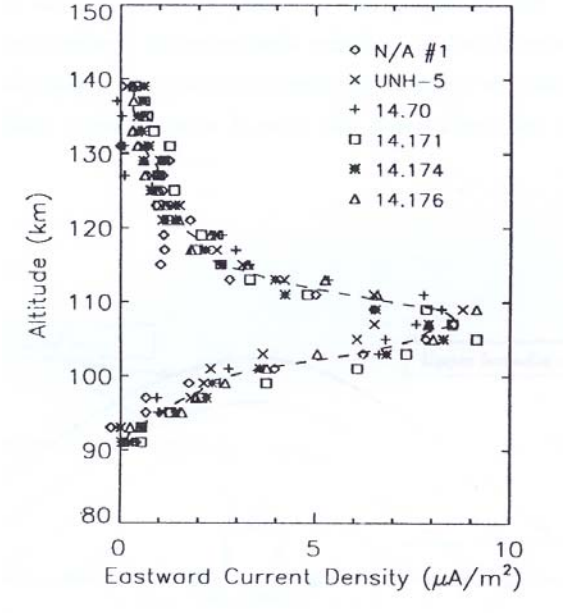

Figure 25: Vertical profiles of the current density at the magnetic equator (Peru). These profiles are derived from rocket flights. All the values are normalized with a magnetic variation at Huancayo of 100 nT [after Richmond, 1995]

Equatorial latitudes

Figure 25 is devoted to profile of vertical current density obtained with magnetometers on board rockets. These measurements are indirect in situ measurements. Richmond (1995) plotted together the results obtained by Shuman (1970), profile N/A#1, Maynard (1967) profile UNH-5. The other profiles 14.70, 14.171, 14.174 and 14.176 are from Davis (1967). All the current

densities derived from the different rocket flight are in good agreement. They all exhibit a maximum of 8 $\mu A.m^{-2}$ around 110 km. This is the signature of the equatorial electrojet.

2.7. Sub-conclusion

In this section we presented the different true electric current systems in the Earth's environment. Concerning the magnetospheric electric currents we just introduce the first original paper claiming the existence of a particular electric current and the physical processes invoked today to explain the observations which are mainly magnetic observations. We must recall here that Tsyganenko (1989, 1996)) proposed empirical models of magnetospheric magnetic field based of years of spacecraft data, magnetic indices and solar wind condition which is a tool to approach the large scale current systems in the Magnetosphere. The Rice University is also developing a model of magnetospheric convection.

Concerning ionospheric electric currents we presented the basic equations of the plasma physics of the ionospheric electric currents and also some in situ measurements obtained with incoherent scatter sounder coherent radar and rocket flights. We must recall that there are other large scale electric current generating by the F dynamo layer (Risbeth, 1997) and meridional electric current associated with the equatorial electrojet (Sugiura and Poros, 1969, Maeda et al., 1982).

The study of ionospheric electric currents at the planetary scale is now developed by using numerical simulations of the TIEGCM (thermosphere-ionosphere electrodynamics general circulation model) to complete the data analysis. The TIEGCM model is developed by the NCAR (National Center for Atmospheric Research). The work of Doumbia (2007) illustrates the actual tendency.

3.0 Equivalent electric current systems

3.1 Principles and generalities

Direct in situ measurements of electric currents in the Earth's environment, as we mentioned earlier are rare. On the contrary there are numerous observations of the Earth's magnetic field

in magnetic observatories or on board satellites. As a consequence the study of the real electric current is made by the step of the 'Equivalent current systems'. We derive from magnetic observations an 'equivalent current system' which approaches the 'true electric current system'. The 'equivalent current system' is based on assumptions on the 'real electric current geometry', the assumptions simplify the reality. Nevertheless the 'equivalent current system' helps to organize magnetic observations at a planetary scale, and to give a first rough approximation of the main component of the large scale 'true electric current'.

At the time scales of a second to the solar cycle the main field Bp is constant. The magnetization field B_a is also constant, therefore the transient variations of the Earth's magnetic field are mainly related to the external sources (B_e, B_{in}), see paragraph 1.2.2. When scientists started the systematic observations of the Earth's magnetic field they observed most of a daily regular variation all the days and on some days irregular variations superimposed to the regular one. They classification of days into classes base on the morphology and intensity of magnetic activity (very quiet days, quiet days moderate disturbed days, disturbed days, storm days) is discussed in detail in the next section which is devoted to magnetic indices.

The magnetic variation can be split in 2 parts the regular part (Q) and the Irregular part (D):

$$\Delta B = S_R + D$$

Where:

S_R is the daily regular variation of the Earth's magnetic field observed on an individual quiet magnetic day

D is the irregular variation observed superimposed the regular variation during magnetic disturbances.

S_q is the averaged regular variation of the Earth's magnetic field for the five magnetic quiet days of a month.

S_D is the averaged disturbed variation for the five most magnetic disturbed days of a month.

The disturbed D variation is the sum of the effects of the various electric current systems (Cole, 1966):

$$D = D_{CF} + D_R + D_T + D_I + D_G$$

D_{CF} : magnetic disturbance due to the Chapman Ferraro current (~ qq nT to 30 nT)

D_R : magnetic disturbance due to the ring current (~ qqnT to ~ 600nT)

D_T : magnetic disturbance due to the Tail currents (~ qq nT to 20 nT)

D_I : magnetic disturbance due to the ionospheric disturbed electric current (~qq nT to 2000 nT)

D_G : magnetic disturbance due to electric currents flowing in the ground related to external electric current systems (~30 % of the external electric current as the origin of the ground electric current).

The magnetic ionospheric disturbance D_I is also composed by the effects of various currents systems

$$D_I = DP_{1\,+} + DP_2 + D_{dyn}$$

DP_1 : polar/auroral magnetic disturbance associated to substorm

DP_2 : polar/auroral magnetic disturbance associated to the magnetospheric convection electric field

D_{dyn} : magnetic disturbance associated to the Joule heating in the auroral zone (Le Huy and Mazaudier, 2005 and 2008).

The two simple models of equivalent current systems to approach ‘true electric currents‘ are:
1) The model of the infinite ribbon of uniform current used for auroral or equatorial electrojet which is based on the H and Z components of the Earth’s magnetic field.
2) The model of an infinite plane sheet of uniform current over a plane Earth used to describe large scale phenomena, which is based on the H and D component of the Earth’s magnetic field.

It is important to recall here that an equivalent current system is made to qualify a phenomenon which exhibits particular morphological features.

3.2 The various equivalent current systems

This paragraph is devoted to equivalent current systems related to large space scale phenomena (regional to planetary), and long-period (> 10 minutes). The first map of equivalent current

system was proposed by Schuster in 1889 for the regular variation of the Earth's magnetic field, at that time the ionosphere was not discovered.

3.2.1 S_q^P ,DP_1, DP_2,

During magnetic quiet periods Nagata and Kokubun (1962) plotted the H and D components of the ground Earth magnetic field in several stations near the pole and in the auroral zone (figure). In their study they considered that all the electric currents flow in a spherical shell above the Earth's in the dynamo layer, they assumed that the currents in the shell are uniform. They found 2 cells of 'equivalent electric current' derived from the ground magnetic observations. These two cells are confined on the polar and auroral zone during magnetic quiet days. They called this equivalent current system S_q^P, this current system is presented on figure 26a.

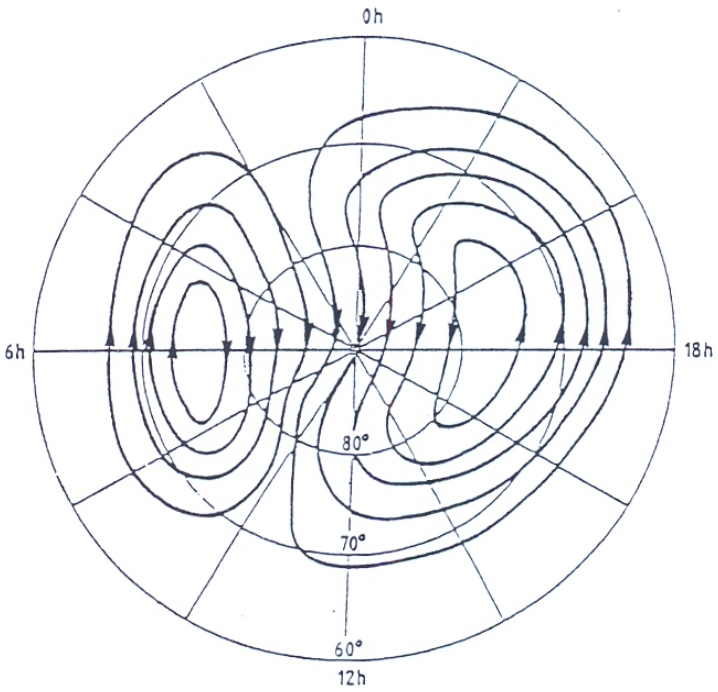

Figure 26a : S_q^P after [Nagata and Kokubun, 1962]

Nishida processed the magnetic data, as Nagata and Kokubun, during magnetic disturbed days Nishida (1968) observed magnetic perturbations occurring simultaneously from the pole to the equator. Nishida proposed to explain these observations by the transmission of an electric field:

the convection electric field related to the solar wind/magnetosphere dynamo ($\vec{E}c = -\vec{V}_s \times \vec{B}_i$ **)** first proposed by Axford and Hines (1961). Nishida plotted the components of the Earth's magnetic field for such perturbations and obtained the same pattern than for the S_q^P.equivalent current system. But during disturbed periods the 2 cells are not confined in polar and auroral zone they extend to equatorial latitudes. Nishida called this perturbation of the Earth's magnetic field DP_2. Figure 26b illustrates the DP_2 equivalent current system.

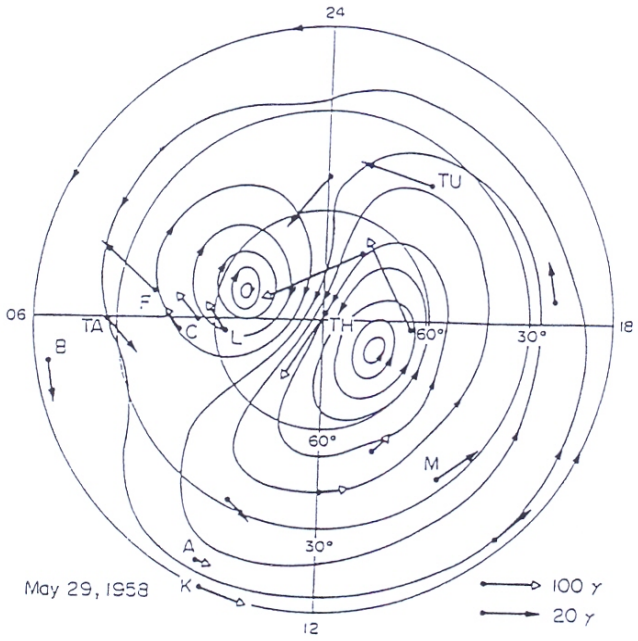

Figure 26b: DP_2 [After Nishida, 1968]

S_q^P, DP_2 are both related to the solar wind/magnetosphere dynamo, **S_q^P** is related to the slow solar wind flowing continuously along the magnetosphere and **DP_2** to high speed solar wind .

DP_1 is an equivalent current system which differs from **S_q^P** and **DP_2** as it is composed of one electric current cell located on the night side. In 1969, Rostoker presented a classification of Polar magnetic Disturbances. Following Rostoker: *"This current system (*DP_1*) is more related*

to large – scale perturbations of the magnetosphere called 'magnetospheric substorms' which are associated with a bay-type perturbations, which is termed the 'polar magnetic substorm."

On figure 27a , DP_1, is shown. This is the equivalent current system for a polar magnetic substorm which is derived from a dozen magnetic stations in the polar and auroral zones. The current system consists of one cell centered approximately on the (magnetic) midnight meridian.

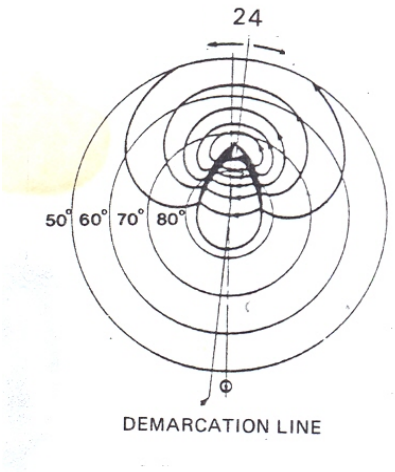

Figure 27a: Shematic equivalent current system for polar magnetic substorms [after Rostoker ,1967]

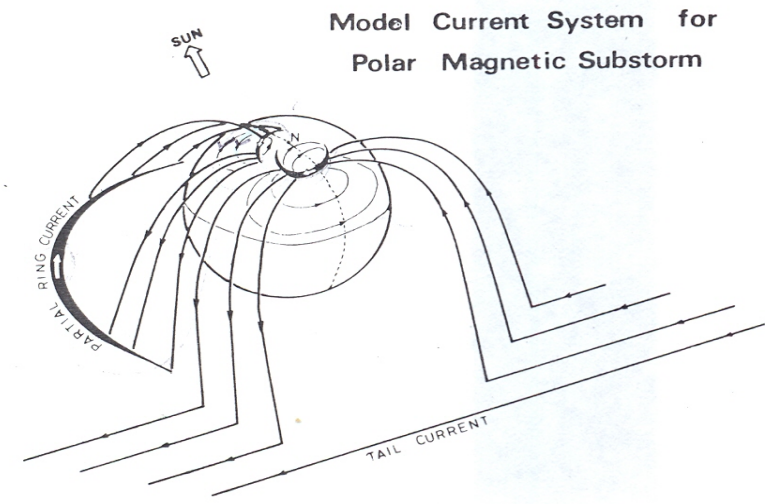

Figure 27b: Model of large scale electric current during substorms [after Kamide and Fukushima,1972]

On figure 27b, the model of ‘true electric current system” proposed by Kamide and Fukushima (1972) connects the tail current to the auroral westward electrojet on the nightside, and the partial ring current to the auroral eastward electrojet on the day side. The westward electrojet is strong and the eastward electrojet weak.

3.2.2 Sq/S_R and the Equatorial Electrojet EEJ

In paragraph 1.2.3 and paragraph 2.5 we have presented the ionospheric dynamo and the physics of ionospheric electric currents. The equivalent current systems Sq/S_R and the equatorial electrojet are related to the ionospheric dynamo and are easily observed during magnetic quiet days.

Figure 28 illustrates the various equivalent electric currents associated with the ionospheric dynamo. The Sq electric currents on the dayside. Electric currents flow anti-clockwise in the northern hemisphere (shown on this figure) and clockwise in the southern hemisphere. At the equator, the equatorial electrojet is a ribbon of current flowing toward the East. The ‘real electric currents’ are 3D with parallel currents connecting the 2 hemispheres.

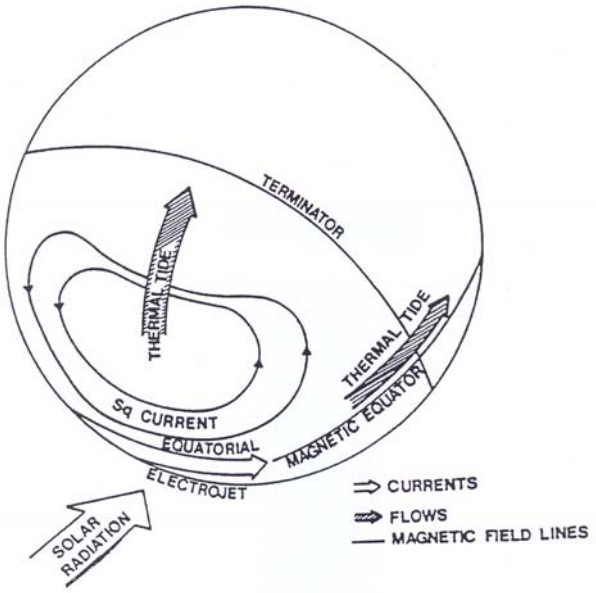

Figure 28: Equivalent electric current systems associated with the Ionospheric dynamo Sq and the equatorial electrojet

The Sq/S_R equivalent current system

The Sq equivalent electric current system (Chapman and Bartels, 1940) is based on the average magnetic data of the five quietest days of a month. The S_R equivalent electric current system is based on individual quiet days (Mayaud, 1965). Mayaud introduced the S_R when he observed that during some months, the magnetic activity was strong and contaminated the Sq. The S_R is necessary to study the day-to-day variability of the regular variation of the Earth's magnetic field.

On figure 29 is drawn the **Sq/S_R** equivalent current system.The model used is the model of a plane sheet above a plane Earth with uniform electric currents, therefore the currents are perpendicular to the magnetic field.. The electric current system is at fixed position related to the sun, the observation point during the day turns under the electric current system. The electric currents close separately on each hemisphere. On the right side of figure 29 are drawn the variations of the H and D component observed by the observer at the ground level by the cell of current.

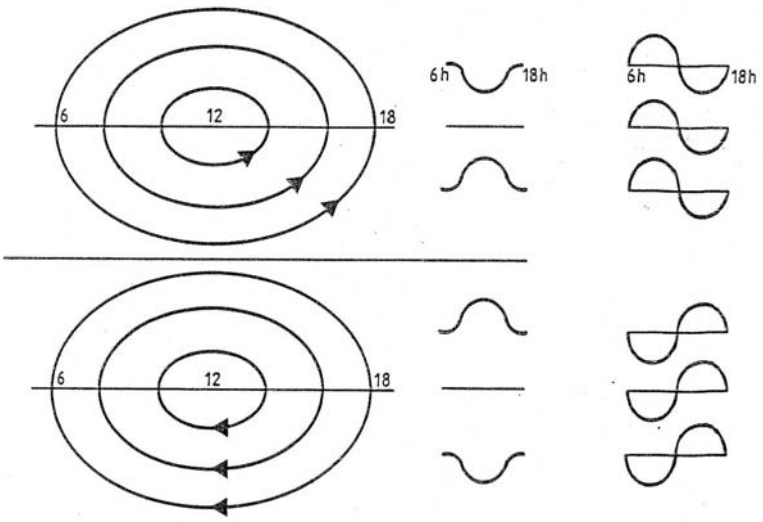

Figure 29: Equivalent electric current system Sq/S_R [After Amory-Mazaudier ,1983]

Whatever the latitudinal position of the observatory, the D component always exhibits the same variation; positive in the morning and negative in the afternoon. This corresponds in the

ionosphere to a southward current in the morning and a northward electric current in the afternoon. The H component is negative at latitudes above the focus of the Sq current system, nil at the focus and positive below the focus. In the ionosphere, this corresponds to westward electric currents above the focus and eastward electric currents below the focus. In the southern hemisphere the pattern is reversed.

Figure 30 illustrates the Sq variations of the H component and the D component of the Earth's magnetic field in three stations in the northern hemisphere (Memambetsu (Mb), Kanoya (Ky), and Kakioka (Ka)). The top panels are related to the H component and the bottom panels to the D component. The three magnetic seasons are December solstice 'd', equinox 'e' and June solstice 'j'.

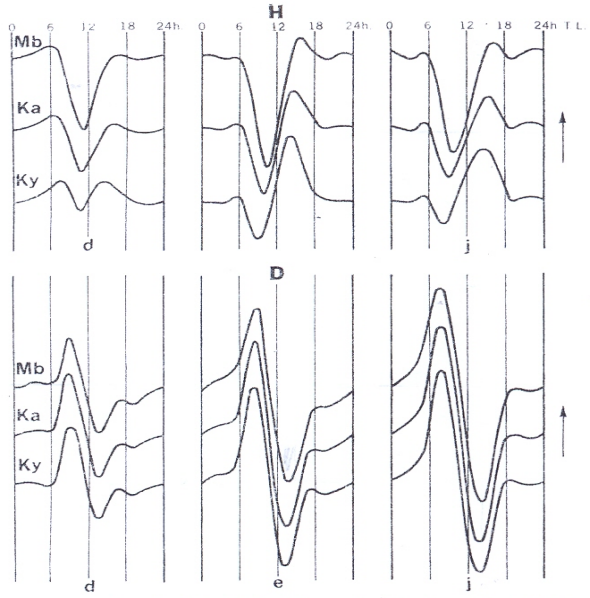

FIG. 20. — Courbes Sq de H et D pour les 3 saisons (*d* : solstice de décembre ; *e* : équinoxe ; *j* : solstice de juin) des années 1958-1959 à Memambetsu (Mb), Kakioka (Ka) et Kanoya (Ky). Échelle de 2 gammas/heure.

Figure 30: Sq of H and D for the 3 magnetic seasons in three stations of the northern hemisphere above the focus of the Sq system [after Mayaud, 1965]

Whatever the station and season, the main tendency for the D component is similar to the simple model of a uniform plane sheet of electric current flowing above the Earth. Concerning the H component the main tendency is also a negative variation of the H component during the

day for the three stations in winter. But for the other seasons there is a maximum in the afternoon that is weak at Memambetsu and Kakioka and very strong at Kanoya (Ky) which is at a lower latitude. This can be interpreted by the fact that Kakioka is above the focus in the morning and below in the afternoon.

There is finally a very rough agreement between the variation of the Earth's magnetic field predicted by the model of the plane uniform sheet of current (figure 29) and the data (figure 30). Equivalent current systems are a tool to approach the true electric currents.

Equatorial electrojet

At the equator the model used is the model of a ribbon of current circulating along the magnetic equator. We assume locally that the ribbon is straight line. We assume also that the electric currents are uniform. Figure 31 from Fambitakoye (1973) illustrates the H and Z components defined theoretically along a latitudinal chain below the ribbon of current. The H component is maximum at the equator and decreases with the distance to the equator. The Z component is nil at the equator and present 2 extrema at mid height relative to the observed H component.

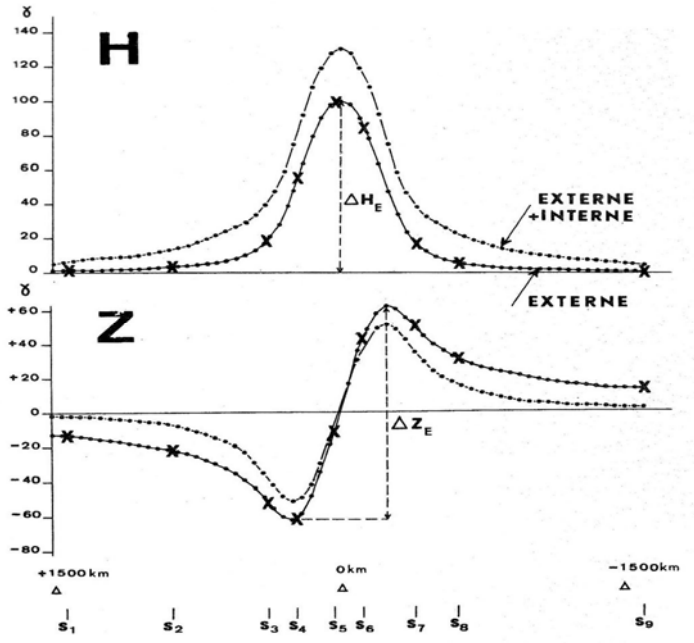

Figure 31: latitudinal profile of H and Z for a ribbon of current [after Fambitakoye, 1973]

On figure 31, Fambitakoye plotted the external part of the electric current (dashed line) as well as the sum of the external and internal part (see paragraph 1.2.2. the term $B_e + B_{in}$). This figure highlights the relation between the external source of electric current and the corresponding induced source of electric current. It is clear that the external part dominates particularly at the equator where the induced currents are very weak. The ribbon of current is defined as:

$$I(x) = I_o[1 - \frac{(x-c)^2}{a^2}]^2$$

Where I_0 is the current intensity at the centre *c* of the ribbon whose half width is *a* and length is infinite. The ribbon is assumed to be infinitely thin, and located at a height of 105 km.

Figure 32 gives real latitudinal profiles of the H and Z components of the Earth's magnetic field measured with a chain of magnetometers at various times and for 2 days, June 6, 1969 the 2 left panels and December 12, 1968, the two right panels.

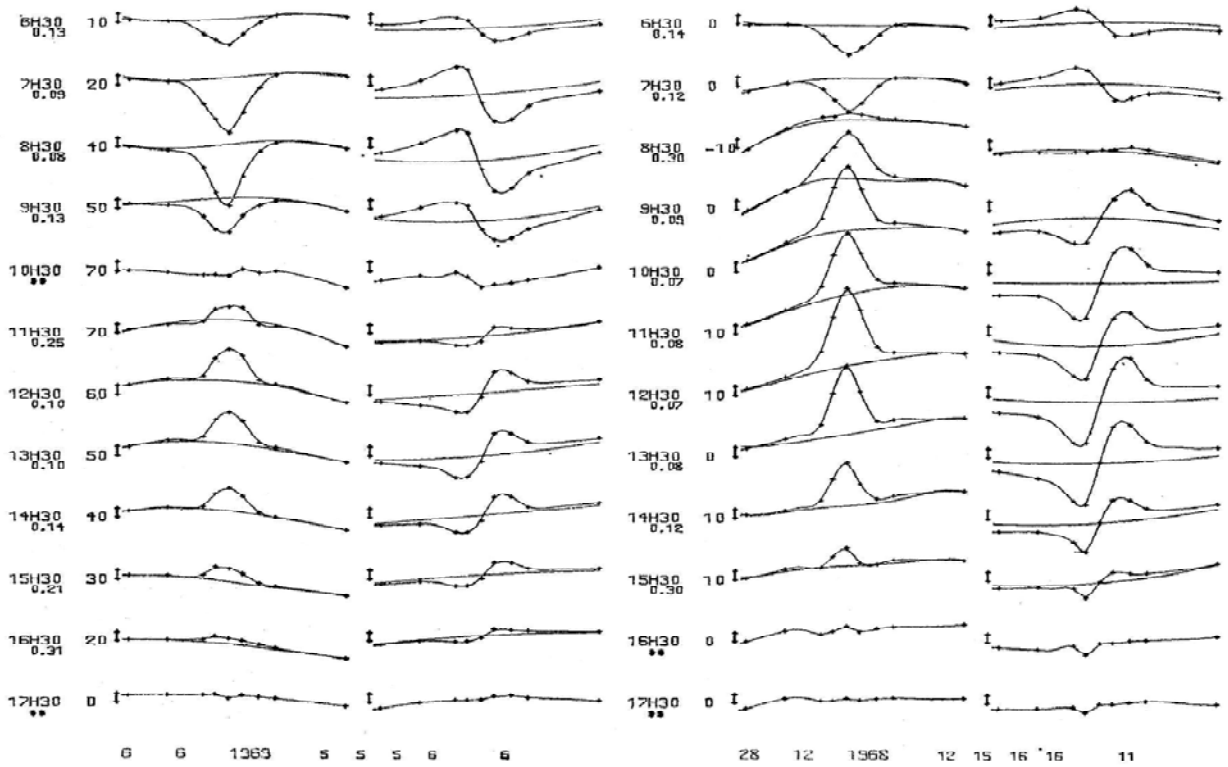

Figure 32: Latitudinal profile of the magnetic field along an experimental chain of magnetometers [after Fambitakoye, 1975]

On Figure 32, from Fambitakoye, 1975, we observe, on both days, in the morning a reversed circulation of the equatorial electrojet called the counter electrojet discovered by Gouin and Mayaud (1967). On December 28 the counter electrojet disappeared at 7.30 LT. On December 6, 1969, the counter electrojet is very strong and it affects the equatorial electrojet during the whole day. Nevertheless on December 28, 1968 from 09.30 LT to 15.00 LT, we can observe the pattern of the ribbon of current.

3.3 Sub-conclusion

In this section we present the principle of equivalent current. An equivalent current is a tool to approach the 'true electric current systems'. Different equivalent current related to various large scale dynamos are explained:

$\mathbf{S_q^P}$ **,DP$_1$**, and **DP$_2$** are currents related to the solar wind/magnetosphere dynamo. $\mathbf{S_q^P}$ and DP_2 . $\mathbf{S_q^P}$ is composed of 2 cells of current (one on the dayside and one on the night side)which are the signature of the regular effect of the solar wind/magnetosphere dynamo which affects directly the polar and auroral regions even during magnetic quiet days. During magnetic disturbed period the **DP$_2$** is observed, the 2 cells of current extend toward middle and low latitudes when the magnetospheric convection electric field influences the whole Earth. **DP$_1$** is composed by one cell centered on the nightside it is associated to substorm event.

Sq/S$_R$ and equatorial electrojet are produced by the ionospheric dynamo. **Sq/S$_R$** are composed of two cell of current, one on each hemisphere. The current flow anti clockwise in the northern hemisphere and clockwise in the southern one. The equatorial electrojet is represented by a ribbon of current circulating along the magnetic equator.

4.0 Magnetic indices

Since many decades magnetic indices are regularly computed by ISGI (International Service for Geomagnetic Indices) and available on internet:

http://isgi.cetp.ipsl.fr and http://spidr.ngdc.noaa.gov/spidr/index.jsp

Presentation of the ISGI service on the website:

"Geomagnetic indices and lists of remarkable geomagnetic events constitute data series aiming at describing at a planetary scale the magnetic activity, or some of its components. The data series are homogeneous since 1868 for aa and the list of ssc, 1932 for Kp, 1953 for the list of Sfe, 1957 for Dst and 1959 for am."

"The International Service of Geomagnetic Indices (ISGI) is in charge of the elaboration and dissemination of geomagnetic indices, and of lists of remarkable magnetic events with data provided by geomagnetic observatories."

In the IAGA (International Association for Geomagnetism and Aeronomy) a working group V-DAT is in charge of magnetic indices. This group prepare a new IAGA guide to geomagnetic indices derived from Earth surface data (Menvielle et al, 2008).

In this section we briefly recall some connections between some indices and the large scale current system in the Earth environment. We will not review all the geomagnetic indices available.

4.1 Principle: The K indices

Mayaud in 1980 was the first to establish a guide on Geomagnetic indices. Figure 33 from Mayaud illustrates how the K indices are computed The K index, for 3-H intervals, is determined as the difference between the extreme of the variation after eliminating the S_R. On this figure it is the record of a low latitude station Guam which is shown.

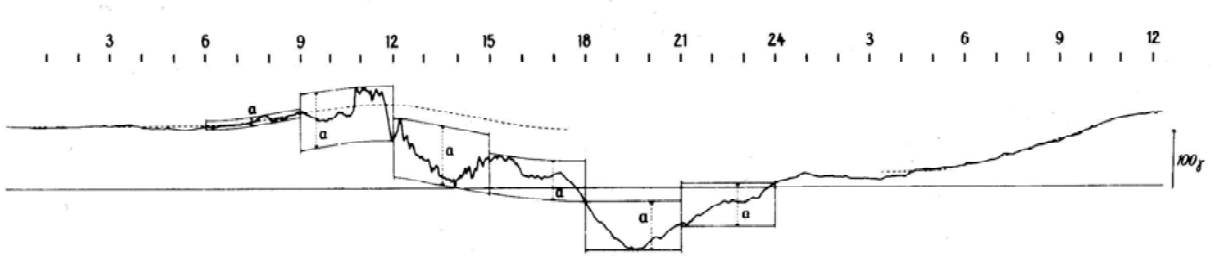

Figure 33: A record of the H component at Guam, a low latitude station. These figure illustrates how we determine the K index for 3-H intervals, as the difference between the extreme of the variation after eliminating the S_R.

"*An individual K index is an integer in the range 0 to 9 corresponding to a class that contains the largest range of geomagnetic disturbances in the two horizontal components during a 3-hour UT interval. The limits of these classes at a particular observatory are defined with the intent of producing a geomagnetic disturbance characterisation that does not depend significantly on the location of a sub-auroral, mid- or low- latitude observatory. K indices are assigned to successive 3-hour UT intervals (0-3 hr, 3-6 hr, ..., 21-24 hr UT) giving eight K indices per UT day.*

K indices can be hand-scaled from magnetograms by an experienced observer, or computer derived using one of the four algorithms that are acknowledged by IAGA. (Menvielle et al., 2008)"

4.2 On the use of magnetic indices

For all the scientific studies on Earth's environment it is a necessity to know the global geophysical context and the geomagnetic indices as well as solar wind parameters are essential.

Some geomagnetic indices are very useful for Magnetic storm studies other are useful to know the average level of geomagnetic activity.

4.2.1 Magnetic storms/ disturbed magnetic activity : AE, AU, AL, Dst.

The geomagnetic activity is very complex and the different magnetic indices are used to understand this complexity.

The AU, AL and AE magnetic indices are derived from stations located in the auroral zone in the northern hemisphere. Figures 34a and 34b (from Menvielle at al., 2008) show the stations used to compute these indices. Figure 34a gives the longitudinal distribution and figure 34b the latitudinal distribution (view from the pole). All the stations which are located in the auroral zone are under the influence of the auroral electrojets directly connected to the solar wind /magnetosphere dynamo. The AU index is a proxy of the eastward auroral electrojet which

flows on the dayside and the AL index is a proxy of the westward auroral electrojet which flows on nightside.

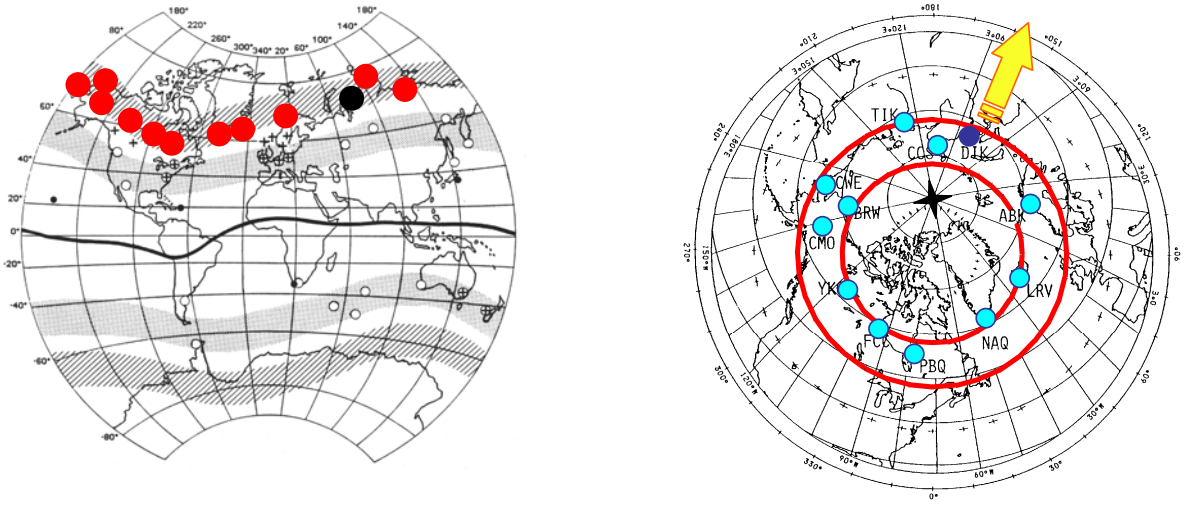

a b

Figure 34 : Distribution of the observatories using to compute the AU, AL and AE indices. The left panel show the longitudinal distribution, the right panel show a view from the pole.

"*The H magnetograms from the "AE" stations are superimposed: the upper envelope defines the AU index, and the lower envelope defines the AL index; AE = (AU+AL) / 2 and A0 = (AU-AL) / 2. From 2005 onwards, the AE indices are calculated from data from up to 12 sites in the northern auroral zone (see 34a)….AE is expressed in units of nT*" (Menvielle et al., 2008)

Figure 35a shows the stations used to compute the Dst : "*Dst is computed using 1-minute values from four low latitude observatories (Figure 35a)) the locations of which are sufficiently distant from the auroral and equatorial electrojets to inhibit noise from these two sources. Local Dst values are computed at each "Dst" observatory at one instant in time. Contributions to H from the background field (non-transient field of core and crustal origin) and the solar regular daily variation are first subtracted from the observed value of H. The local Dst value is deduced from the so-obtained residual D through normalization to the dipole equator. For each*

1-hour UT interval, the Dst index is the average of the local Dst hourly mean values at the four "Dst" observatories." (Menvielle et al., 2008).

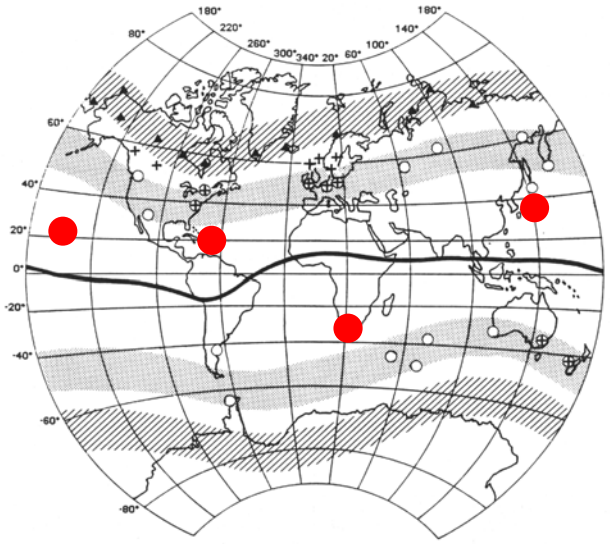

Figure 35: Distribution of the observatories used to compute the symmetric part of the Dst index;

The Dst is used for storm studies to approach the variation of the large scale ring current in the magnetosphere.

Figure 36 illustrates the variations of indices as Dst AU and AL, on September 19, 2001. From the top to the bottom there are the aa index (out of the scope of this paper), the Kp index (expressed in nT ~ Ap), the Dst and AU and AL index. On the figure the Dst exhibits the typical signature of a magnetic storm. The Dst index increases from 01.00 to 02.00 UT and decreases around 02.00UT until 05.00 UT and becomes negative. The AU and AL magnetic indices increase when the Dst decrease. This is the signature of the connection between the ring current in the magnetosphere with the auroral electrojets in the ionosphere. When the Dst increases it is the phase of compression of the storm: the Dst is the signature of the eastward magnetopause current. The Dst decreases from 02.00UT to 05.00 UT: it is the main phase of the storm. From 05.00UT the Dst slowly increases: it is the recovery phase of the storm. During the main phase and the recovery phase the Dst is the signature of the westward ring current.

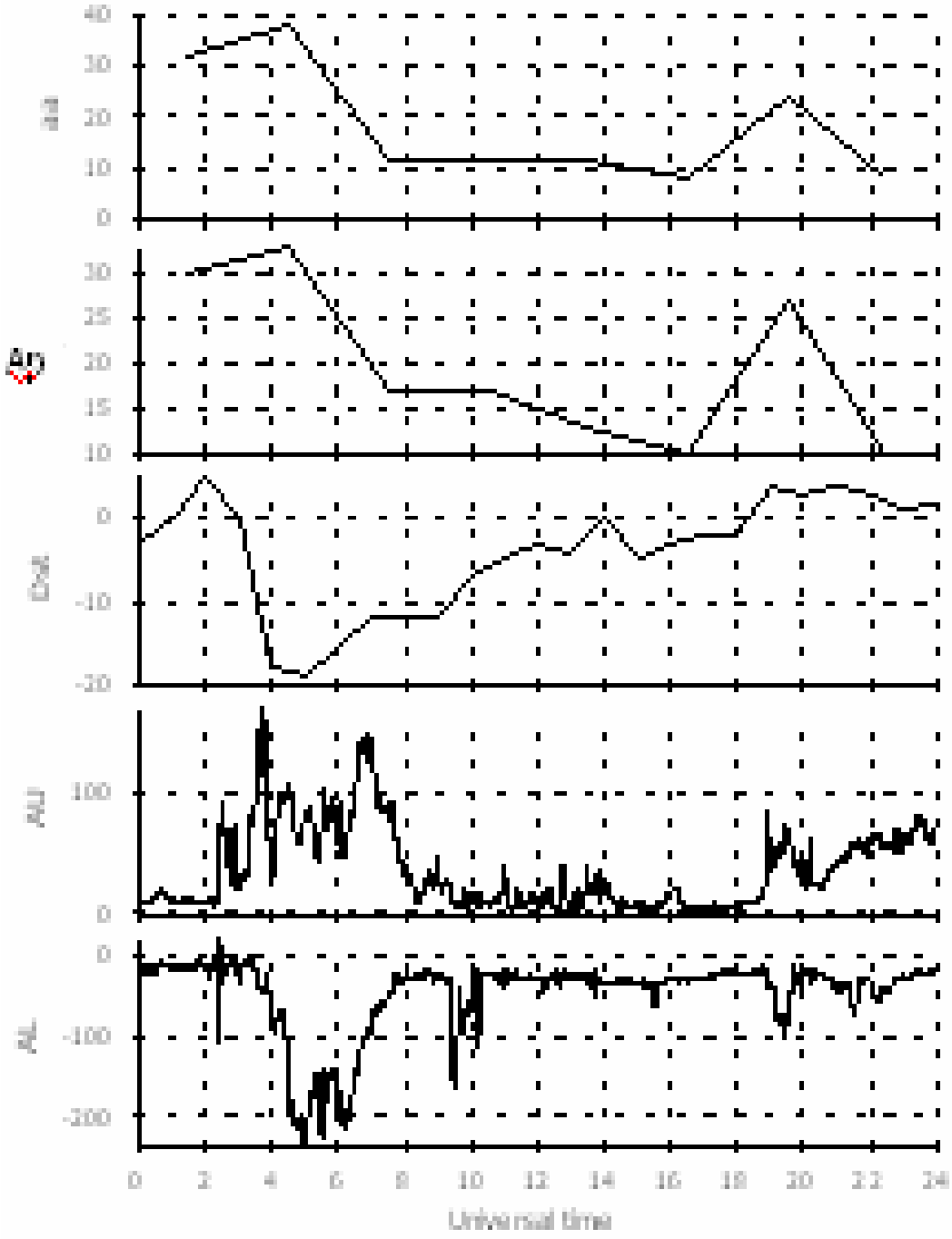

Figure 36: Diurnal variation of different magnetic indices, from the top to the bottom aa, kp, Dst, AU and AL on September, 19, 2001.

4.2.2 Average magnetic activity : Kp and Km

Figure 37a and 37b show the locations of the stations used to compute the Kp and Km magnetic indices.

"Kp is the arithmetic mean of the 3-hour standardized K-indices for the 13 "Kp" observatories (see Figure 37a). The standardization is achieved using "standardization tables" that have been defined by Bartels (IATME Bulletin 12, 97, 1949). They aim at removing the UT and seasonal variations in the geomagnetic disturbances. Kp is expressed in thirds of K units, which means that there are 27 possible values for Kp, from 0o to 9o: 0o, 0+, 1-, 1o, 1+, 2-,…, 8+, 9-, 9o." (Menvielle et al., 2008)."

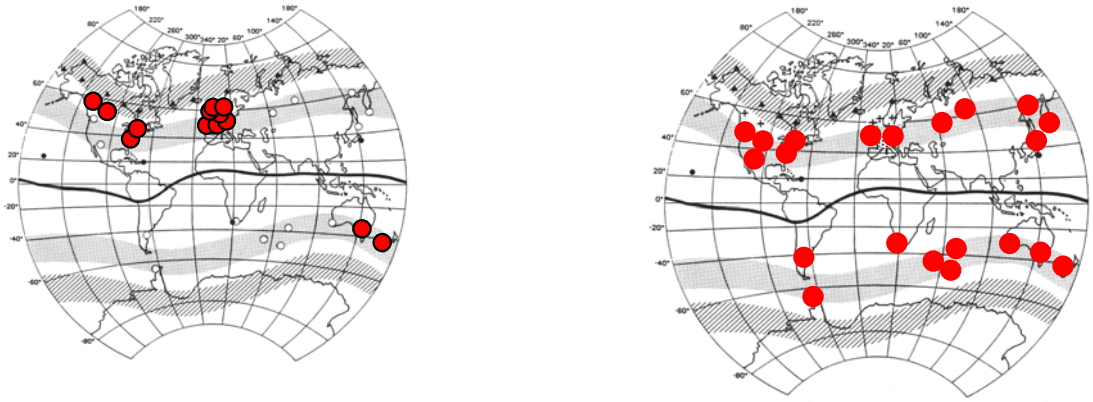

a b

Figure 37: Distribution of the observatories used to compute the Kp index (left panel), and to compute the Am index (right panel).

Km is like Kp the arithmetic mean of the 3-hour standardized K-indices for the 21 "Km" observatories.

Kp is computed from the K indices from 11 observatories, 9 in the northern hemisphere and 2 in the Southern one.

Km is computed from 21 observatories, 12 in the northern hemisphere and 9 in the Southern one. Km is defined for the Northern and the Southern hemispheres. Km index is more appropriate to study asymmetry between the 2 hemispheres.

4.3 Sub-conclusion

Magnetic indices developed are based on the morphological characteristics of the Earth magnetic field. They are essential to determine the level of geomagnetic activity and are available all the time, since many years. Three indices are related to the large scale electric current systems:

- the AU and AL indices respectively related to the eastward and westward auroral electrojet.
- the Dst which is the signature of magnetopause electric currents during the compression phase of magnetic storm and the signature of the ring current during the main phase and the recovery phase of a storm.

A new IAGA guide on magnetic indices is in preparation (Menvielle et al., 2008)

5.0. General conclusion

The main purpose of this presentation is to connect together different disciplines (solar, magnetospheric, ionospheric and atmospheric physics) in the frame of heliosphysics.

We demonstrate that dynamo process is able to help in the comprehension of large scale electric currents systems connecting Sun and Earth. Many studies were made separately and dynamo process unifies all these studies, therefore we are able to understand at a global scale the Sun Earth electrodynamics system.

In the first section we recall the morphological features of the 4 large scale dynamos of the Sun earth system which are : 1) the solar dynamo and its 2 components poloidal and toroidal, 2) the Earth’s dynamo, 3) the solar wind/magnetosphere dynamo and 4) the ionospheric dynamo. In the second section we briefly present the magnetospheric electric currents and field aligned currents and take more attention to the ionopheric electric current. We show ionospheric electric currents or fields obtained with in situ measurements made with coherent radar,

incoherent scatter sounder or rocket flights .The sections three and four are respectively devoted to the equivalent currents and to magnetic indices.

This presentation highlights that many physical processes occur in the transient variation of the Earth's magnetic field and today a large knowledge is necessary to progress in this field. In the study of the transient variations of the Earth's magnetic field our main recommendation concerning the data analysis is to look at some indicators in order to know the heliophysics context.

Here are these indicators

- Sun situation
  - Sunspot cycle and poloidal cycle
  - Solar event
- Solar wind parameters V,B
  - Solar wind magnetosphere dynamo
- Magnetic indices
  - AU and AL -> auroral electrojets
  - Dst (Hsym and H asym)-> magnetopause and ring current
  - Am -> Global magnetic context
- INTERMAGNET magnetograms
  - Planetary map of the transient variations of the Earth magnetic field.

We add in annex three tables :

- table 2 from Chapman and Bartels, which summarizes important events in history of geomagnetism up to about 1850,

- table 3 from Amory-Mazaudier (1994), corresponding to the main steps in the knowledge of the regular variation of the Earth's magnetic field

- table 4 from Amory-Mazaudier (2002), corresponding to the main steps in the knowledge of the irregular variation of the Earth's magnetic field.

The steps described in tables 3 and 4 correspond to advances in fundamental physics, as well as in technology, data interpretation and other factors. These papers cover the period from 1870 up to now. The historical bibliographical references of table 3 and 4 are given in the main bibliography.

6.0. Summary

This presentation is devoted to large scale electric current systems in the Earth's environment. We first present the dynamos involved in the generation of the electric current systems in section 1, then we describe the large scale electric current system, in section 2. The direct measurements of true electric currents are very rare and we approach the true electric currents by analysing the transient variations of the Earth's magnetic field. Equivalent current and magnetic indices are useful tools to understand the complex variations of the transient variations of the earth's magnetic field. We present these tools in section 3 and 4.

This first part briefly presents the various large scale dynamos involved in the Sun Earth's system. Four dynamos are invoked:

- the solar wind dynamo is generated by the solar rotation and convection motions and a primary poloidal magnetic field. The poloidal component of the solar magnetic field associated to the differential rotation of the sun create a toroidal solar magnetic field component known as the sunspot cycle. Scientists do not understand the complex relation between the 2 components (poloidal and toroidal) of the solar dynamo, which regenerate each other.
- the Earth's dynamo due to the motion of electrically conducting metallic fluid in the Earth's core,

- the solar wind/magnetosphere dynamo generated by the continuous flow of the solar wind around the magnetosphere. This dynamo is related to the solar wind.
- the ionospheric dynamo created by the motions of the atmosphere through the Earth's magnetic field lines. This dynamo is related to solar radiations.

Table 1 sets up together the characteristics (V,B)of the four large scale dynamos operating in the Sun Earth system.

In the second section we presented the different true electric current systems in the Earth's environment which are :

- magnetospheric electric current systems :
    - magnetopause electric currents, called also Chapman Ferraro currents, flowing on the frontier (called magnetopause) between the interplanetary medium and the Earth's magnetic field cavity called magnetosphere. On the magnetopause, the dynamic pressure of the solar wind is balanced by the geomagnetic field pressure.
    - Ring electric currents, flowing in the equatorial plane of the magnetosphere, they are mainly the result of the curvature and gradient of the Earth's magnetic field
    - The tail currents flowing in the tail of the magnetosphere and strongly related to the solar wind.
- ionospheric current systems
    - the auroral electrojets, flowing along the auroral oval in the eastward and westward directions directly related to the solar wind/magnetosphere dynamo
    - middle latitude electric current system composed mainly of one cell of current on each hemisphere generated on magnetic quiet days by the ionospheric dynamo and affected during disturbed magnetic days by the solar wind / magnetosphere dynamo
    - the equatorial electrojet, flowing along the magnetic equator in the eastward direction generated on magnetic quiet days by the ionospheric dynamo and

affected during disturbed magnetic days by the solar wind / magnetosphere dynamo

- field aligned current systems connecting the magnetospheric and ionospheric electric current systems.

Concerning the magnetospheric electric currents and field aligned currents we just introduce the first original paper claiming the existence of a particular electric current and the physical processes invoked today to explain the observations which are mainly magnetic observations.

Concerning ionospheric electric currents we presented the basic equations of the plasma physics of the ionospheric electric currents in order to understand the key role of the neutral atmosphere in the generation of these electric currents. We also presented some in situ measurements of ionospheric electric fields and currents obtained with incoherent scatter sounder coherent radar and rocket flights.

At the present time, progress in the study of large scale electric current systems needed large scale models. We must recall here some models :

- Tsyganenko (1989, 1996)) proposed empirical models of magnetospheric magnetic field based of years of spacecraft data, magnetic indices and solar wind condition which is a tool to approach the large scale current systems in the Magnetosphere.
- The Rice University is also developing a model of magnetospheric convection.
- The study of ionospheric electric currents at the planetary scale is now developed by using numerical simulations of the TIEGCM (thermosphere-ionosphere electrodynamics general circulation model) to complete the data analysis. The TIEGCM model is developed by the NCAR (National Center for Atmospheric Research) and produces 3D ionospheric electric currents.

In section three, we present the principle of equivalent current. An equivalent current is a tool to approach the ‘true electric current systems’.

Different equivalent current related to various large scale dynamos are explained:

- $\mathbf{S_q^P}$ **,DP$_1$, DP$_2$** , these currents are related to the solar wind/magnetosphere dynamo .
    - $\mathbf{S_q^P}$ is composed of 2 cells of current (one on the dayside and one on the night side)which are the signature of the regular effect of the solar wind/magnetosphere dynamo which affects directly the polar and auroral regions even during magnetic quiet days,
    - **DP$_2$** is observed during magnetic disturbed days and is composed of 2 cells of current extend toward middle and low latitudes when the magnetospheric convection electric field influences the whole Earth,
    - **DP$_1$** is composed by one cell centred on the nightside. It is associated to substorm event
- **Sq/S$_R$** and equatorial electrojet are produced by the ionospheric dynamo,
    - **Sq/S$_R$** are composed of two cell of current, one on each hemisphere. The current flow anti clockwise in the northern hemisphere and clockwise in the southern one.
    - The equatorial electrojet is represented by a ribbon of current circulating along the magnetic equator.

Section four is devoted to magnetic indices. Magnetic indices developed are based on the morphological characteristics of the Earth magnetic field. They are essential to determine the level of geomagnetic activity and are available all the time, since many years. Three indices are related to the large scale electric current systems:

- the AU and AL indices respectively related to the eastward and westward auroral electrojet.
- the Dst which is the signature of magnetopause electric currents during the compression phase of magnetic storm and the signature of the ring current during the main phase and the recovery phase of a storm.

A new IAGA guide on magnetic indices is in preparation (Menvielle et al., 2008)

Finally, this presentation connects together different disciplines (solar, magnetospheric, ionospheric and atmospheric physics) in the frame of heliosphysics.

We demonstrate that dynamo process is able to help in the comprehension of large scale electric currents systems in the Sun and Earth system. By the past many studies were made separately and dynamo process unifies all these studies, therefore we are able to understand at a global scale the Sun Earth electrodynamics system.

This presentation highlights that many physical processes occur in the transient variation of the Earth's magnetic field and today a large knowledge is necessary to progress in this field. In the study of the transient variations of the Earth's magnetic field our main recommendation concerning the data analysis is to look at some indicators in order to know the heliophysics context. Here are these indicators

- Sun situation
  - Sunspot cycle and poloidal cycle
  - Solar event
- Solar wind parameters V,B
  - Solar wind magnetosphere dynamo
- Magnetic indices
  - AU and AL -> auroral electrojets
  - Dst (Hsym and H asym)-> magnetopause and ring current
- INTERMAGNET magnetograms
  - Planetary map of the transient variations of the Earth magnetic field.

We add in annex three tables (Tables 2-4) which describes main steps in the study of ionospheric electric current from time immemorial to date.

ANNEXE : MAIN STEPS IN THE STUDY OF IONOSPHERIC ELECTRIC CURRENT

Table 2 : Summary of important events in history of geomagnetism up to about 1850 from CHAPMAN and BARTELS, 1940

A.D. 1030-93	The Chinese encyclopaedist Shon-Kua described the magnet pointing south

About 1187	Alexander Neckman of St. Albans described the magnetic compass
About 1450	Sun dials in Nuremberg showed marks for magnetic declination
About 1492	German roads maps containing the figure of a compass indicating the declination
1538-41	Joao de Castro, on a voyage to the East indes, made forty-three determinations of magnetic declination
1544	Letter by Georg Hartmann of Nuremberg, referring to the magnetic inclination
1576	Robert Norman *The Newe Attractive*
1600	William Gilbert, *De magnete*
1635	Henri Gellibrand discovered the secular variation of declination
1672	Daniel Tilas died (inventor of the Swedish mining compass for magnetic prospecting)
1698-1700	Halley's voyages in the Atlantic Ocean on the *Paramour Pink*
1701	Halley's sea chart of the whole world
1721	William Whiston's charts of inclination
1722	George Graham discovered non-secular time-variations
1741, April 5	**Simultaneous magnetic observations by Celsisus at Uppsala and Graham at London; discovery of the relation between magnetic disturbances and aurora**
1759	**Solar daily** variation found to be greater in summer than in winter (by Canton)
1770	**Wilcke observed that auroral rays are parallel to the magnetic inclination**
1782	Cassini found that the **daily variation** of the declination is independent of the daily variation of air-temperature
1799-1804	**A. von Humboldt's expedition to America Magnetic storm**
1819	Hansteen's *Untersuchungen über den Magnetismus der Erde*

1820-35	Arago's observations of the magnetic declination at Paris
1826	Poggendorff introduced readings by means of mirror and scale
1837	The earth inductor invented by Weber
1838	Gauss *Allgemeine Theorie des Erdmagnetismus*
1839	Llyod introduced the magnetic balance for recording the variations of the vertical intensity
1836-41	The Göttingen Magnetic Union
1839	Establishment of the British Colonial Observatories (Sabine)
1846	Charles Brooke constructed photographic apparatus recording magnetic variations
1850	Kreil found the lunar daily variation of declination at Prague
1851	Schwabe discovered the sunspot cycle
1852	Sabine found the effect of the sunspot cycle in the disturbances of declination at Toronto, 1841-48.

Table 3 : Summary of important events in the history of regular ionospheric electric current (S_R magnetic field) up to about 1993

1722	**George Graham discovered non-secular time-variations**
1873	Treatise on electricity, Maxwell *lecture of 1870 at the Cambridge University*
1882-1886	Concept of Atmospheric dynamo *lecture of B. Stewart*
1886-1907	Maps of external current systems (A. Schuster) Establishment of the dynamo theory mathematically *Lecture, figure*
1901	Radio beacon (Marconi) Ionosphere postulated by Kenelly and Heaviside
1905	Classification of the 5 international quiet days International Commission at the Innsbruck Conference
1919	Sq equivalent current system (S. Chapman)
1925-29	Wave propagation in the ionosphere (E.V. Appleton, Hartree)
1925-26	First measurements with ionosonde (G. Breit and M. Atuve, E.V. Appleton and M.A.F. Barnett)
1931	First observations of H component of the magnetic field at Huancayo -> equatorial electrojet (1951-S. Chapman)
1940	Application of theory dynamo to ionosphere (S. Chapman) (Maeda, Y. Kato)
1945	Conductivity in partially ionized gas (T.G. Cowling)
1950-65	Rocket flights, in situ measurement of atmospheric tides M. Siebert
1958-60	Theory of incoherent scattering of radio waves by a plasma W.E. Gordon, J.P. Dougherty, D.T. Farley

1960 -	Starting point for the development of atmospheric models Jacchia (1960) ----------> MSIS (1986)
1962	Asymmetries of the two hemispheres => J_{II} A.T. Price and G.A. Wilkins, D. Van Sabben, N. Fukushima
1962	equivalent current system S_q^P , Nagata and Kokubun
1965	concept of the S_R and its day-to-day variability
1970	Theory of atmospheric tides (S. Chapman , R.S. Lindzen)
1969-1976	Computation of ionospheric electric currents from available wind data, R.J. Stening, J.D. Tarpley, A. Richmond
1967-1970	Equatorial counter electrojet (Gouin and Mayaud)
1963-	Observations with incoherent scatter sounder network 1969 : neutral winds (G. Vasseur) 1970 : electric fields (R. Woodman) 1974 : electric currents (A. Brekke et al.)
1977-1982	Semi empirical models of quiet ionospheric electric current Salah and Evans 1977, Mazaudier and Blanc, 1982
1980-	Tri dimensional global simulations of ionospheric electric currents

Table 4 : Summary of important events in the history of disturbed ionospheric electric currents (DP magnetic field) up to about 2000

1733	Hypothesis of solar particles at the origin of aurora J-J. Dortous de Mairan
1741, April 5	**Simultaneous magnetic observations by Celsisus at Uppsala and Graham at London; discovery of the relation between magnetic disturbances and aurora**
1873	Treatise on electricity, J. Maxwell *lecture of 1870 at the Cambridge University*
1882	Concept of the Atmospheric dynamo *lecture by B. Stewart*
1887	relation between the magnetic perturbations and sunspots *E. Marchand*
1889	Maps of the magnetic potential on the surface of the Earth A. Schuster
1901	Radio beacon (Marconi) Ionosphere postulated by Kenelly and Heaviside
1908	Field aligned currents (Jll) *K. Birkeland*
1907- 1913	Field aligned currents and ring current *C. Störmer*
1911	Hypothesis of a flow of particles from the sun-> the solar wind, *K. Birkeland*
1925-29	Wave propagation in the ionosphere *E.V. Appleton, Hartree*
1925-26	First measurements with ionosonde *G. Breit and M. A. Tuve, E.V. Appleton and M.A.F. Barnett*
1931	Storm magnetospheric current model *S. Chapman and V.C.A. Ferraro*
1935	Electric currents systems of magnetic storms

S. Chapman

1937 Magnetic effects associated with bright solar eruptions
Mc Nish A.G.

1937 Terrestrial magnetic variations and the ionosphere
A.G. McNish

1939 A theory of magnetic storms and of Aurora
H. Alfven

1940 Geomagnetism
S. Chapman and J. Bartels

1942 Equivalent current system for geomagnetic bays
H.C. Silsbee and E. H. Vestine

1953 Equivalent overhead current system for the average disturbed field SD
N. Fukushima and T. Oguti

1957 Direct detection of auroral radiation with rocket equipment
J.A. Van Allen

1958 First satellite measurements

1958 Discovery of the radiation belts
J.A. Van Allen

1958-60 Theory of incoherent scattering of radio waves by a plasma
W.E. Gordon, J.P. Dougherty, D.T. Farley

1959 Discovery of the Magnetosphere Motions in the magnetosphere of the Earth, Origin of the radiation near the Earth
Gold T.

1961 Solar wind - magnetosphere dynamo : viscous interaction
W.I. Axford and C.O. Hines

1961 Reconnection between the interplanetary and the Earth's magnetic fields.
T.W. Dungey

1961 D = DR + DP+DCF+DT
S.I. Akasofu and S. Chapman

1962	equivalent current system S_q^P *T. Nagata and S. Kokubun*
1966	D = DR+DI+DCF+DT+DG *K. Cole*
1967-1968	Equivalent current system DP1 *G. Rostoker, T. Obayashi and T. Nishida*
1968	Equivalent current system DP2 *T. Nishida*
1969	In situ electric field measurements across the polar cap and auroral zones *Mozer and Serlin, 1969*
1969	First Observations with incoherent scatter sounder network for neutral winds *(G. Vasseur)*
1970	Theory of magnetospheric convection *V. M Vasyliunas*
1970	First observations with incoherent scatter sounder network electric fields (*R. Woodman/ L.A.Carpenter L.A J.H Kirchhoff*)
1972	Conversion of magnetotal current to Birkeland current and auroral electrojet, *Akasofu S-I*
1972	Connection of partial ring current and high latitudes magnetic bays *Y. Kamide and N. Fukushima*
1974	Satellite measurement of field aligned currents *J.C. Amstrong and A.J. Zmuda*
1974	First observations with incoherent scatter sounder network of electric currents (*A. Brekke et al*.)
1975	Thermospheric Response to Magnetic substorm *A.D. Richmond and S. Matshushita*
1978	Equivalent Field aligned currents *T. Ijima and T.A. Potemra*
Since 1980	Organization of large data base setting up together various satellite data or ground based measurements obtained since 1960,

	from various tools (NCAR, NASA, WORLD DATA CENTER) Organization of coordinated studies on specific events
1980-	Global simulations of ionospheric electric currents (Rice University, NCAR, etc....)
1980	The ionospheric disturbance dynamo *M. Blanc and A.D. Richmond*
1985	In situ measurements of Ionospheric disturbed Electric Currents Two type of disturbances : direct penetration of the magnetospheric convection and disturbed ionospheric dynamo, *C. Mazaudier*
1988	Mapping Electrodynamic features of the High latitude Ionosphere from localized observations technique, *A.D. Richmond , Y Kamide*
Since 1990	To progress in the knowledge of disturbed ionospheric electric currents need coordinated studies with : - use of large data sets of magnetic observations - use of in situ measurements - modelling - semi empirical existing models - Analytical models - Numerical simulations

Now -> Integrated Studies

1992	Solar Flares *J-J. Curto*
2000-2001	Electrodynamic coupling of high and low latitudes *A. Kobéa et al, C. Peymirat et al,*

Acknowledgments

I thank Gerard Vila for amending the English of this paper. I thank Art Richmond for scientific discussions and Michel Menvielle for figures and documents concerning the geomagnetic indices.

References

Akasofu, S.I., and S. Chapman., A neutral line discharge theory of the aurora polaris, Phil. Trans. Roy. Soc. London, Series A, 359-406, 1961.

Akasofu, S-I, Magnetospheric substorms : A model, in Solar Terrestrial Physics/Leningrad 1970, part 3 edited by E.R. Dyer and J.G Roederer, pp. 131-151, D. Reidel, Dordrecht, Netherlands, 1972

Alfven H., A Theory of magnetic storms and of aurorae, 1, Klg Sv. Vetenskapsakad. Handl, ser. 3, 18(3), 39pp., 1939 (Partial reprint, Eos Trans AAGU, 51, 181-193, 1970).

Alfven H., A theory of magnetic storms and aurorae, 2, , Klg Sv. Vetenskapsakad. Handl, ser. 3, 18(9), 39 pp., 1940 (Partial reprint, Eos Trans AAGU, 51, 181-193, 1970).

Amory-Mazaudier, C., Contribution à l'étude des courants électriques, des champs électriques et des vents neuters ionospheriques des moyennes latitudes, Variation régulière et variations perturnées : Etudes de cas à partir des observations du sondeur à diffusion incohérente de Saint-Santin, en relation avec les observations du champ magnétique terrestre, soutenue le 12 septembre, Université de Paris VI, France, 1983.

Amory-Mazaudier, C., On the electric current systems in the Earth's environment some aspects, Part I : external part/Ionosphere/Quiet variation, Geoacta, 21, 1-25, 1994.

Amory-Mazaudier, C., On the electric current systems in the Earth's environment, some historical aspects, Part II. : external part / ionosphere / disturbed variation, , Published in a book of Historical events and people in aeronomy geomagnetism and solar-terrestrial Physics, of geomagnetism and aeronomy, lectures from the IAGA Assembly in Hanoï 2001, collected and edited by W. Schröder, pp 154-190, Science edition AKGGKP, Bremen-Rönnebeck, Postdam, 2002.

Amstrong J.C. and A.J. Zmuda, Field aligned current at 1100 Km in the auroral region measured by satellite, J. Geophys. Res., 75, 7122-7127, 1970.

Appleton E.V., Proc Phys. Soc. London, 37, 16D, 1925

Appleton, E.V., M.A.F. Barnett, Local reflection of wire lea waves from the upper atmosphere, Nature, 115, 333-334, 1925.

Axford W.I., and C.O Hines, A Unifying theory of high latitudes geophysical phenomena and geomagnetic storms, Can. J. Phys., 39, 1433, 1961.

Birkeland K., The Norvegian aurora polaries expedition, 1902-1903, Aschlovg, Christania, Norvège 1908.

Birkeland K., The Norvegian aurora polaries expedition, 1902-1903, Aschlovg, Christania, Norvège 1913.

Blanc M. , A. D. Richmond, The ionospheric disturbance dynamo, J. Geophys. Res., 85, 1669-1686, 1980.

Breit, G., M. A. Tuve, A radio method of estimating the height of the conducting layer, Nature, 116, 257, 1925.

Brekke, A., J.R. Doupnik, P.M. Banks, Incoherent scatter measurement E region conductivities and currents in the auroral zone, J. Geophys. Res., 79, 3773, 1974

Brekke , A. A. Egeland, the Northern Light, Springer verlag, 1983

Carpenter, L.A. and V.W.J.H., Kirchhoff, Comparison f high and mid-latitude ionospheric electric fields, J. Geophys. Res., 80, 1810, 1975.

Chapman S., The solar and Lunar diurnal variations of Terrestrial Magnetism, Phil. Trans. of Roy. Soc. of London, A., 218, 1, 1919.

Chapman, S., V.C.A. Ferraro, new theory of magnetic storms, Terr. Magn. Atm. Elec., 36, 77, 1931.

Chapman, S. , the electric current systems of magnetic storms, terrestrial magnetism and Atmospheric Electricity, Vol.40, N°4, P. 349, 1935.

Chapman, S. and J. Bartels, Geomagnetism, Oxford University Press, New York, 1940.

Chapman, S., R.S. Lindzen, Atmospheric tides : thermal and gravitational, D. reidel publishing company/ Dordretch, Hollande, 1970.

Cole, K.D., Magnetic storms and associated phenomena, Space Science Reviews, 5, 699-770, D. reidel publishing Company, Dordrecht, Holland, 1966.

Cowling, T.G., Terrestrial Magn. Atmos. Elect, 47, 209, 1942.

Cowling, T.G., Proc. Roy. Soc., 183, 453, 1945.

Cummings, W.D., Asymmetric Ring Currents and the low-latitude disturbance daily variation. J. Gophys. Res., Vol 71, N°19, p. 4495, 1966.

Curto J-J. C. Amory-Mazaudier, J-M. Torta and M. Menvielle, Solar flare effects at Ebre and reversed solar flare effects, statistical analysis (1953 to 1985), a global case study and a model of elliptical ionospheric currents , J. Geophys. Res., Vol 99, N° A3, 3945-3954, March 1, 1994.

Curto J-J. C. Amory-Mazaudier, J-M. Torta and M. Menvielle, Solar flare effects at Ebre : Unidimensional integrated model, J. Geophys. Res., Vol 99, N° A12, 23289--23296, December 1, 1994.

Davis, T.N., K. Burrows and J.D. Stolarik, A latitude survey of the equatorial electrojet with rocket –borne magnetometers, J. Geophys. Res., 72, 1845-1861, 1967.

Dougherty, J.P. and D.T. Farley, A theory of incoherent scattering radiowaves by a plasma, Proc. Roy. Soc. London, A259, 79, 1960.

Doumbia, V., A. Maute and A.D. Richmond, Simulation of equatorial electrojet magnetic effects with the TIEGCM, J. geophys. Res., Vol 112, A09309, doi:1029/2007JA012308, 2007.

Dungey, T.W., Interplanetary magnetic field and the auroral zones, Phys. Rev. Lett. 6, 47, 1961.

Evans, J.V., Incoherent scatter contributions to studies of the dynamics of the lower thermosphere, Rev. Geophys. Space Phys, 16, 195, 1978.

Fambitakoye, O. Effets induits par l'electrojet equatorial au centre de l'Afrique, Annale de Geophysique, tome 29, numéro 2, avril-mai-juin, 1973.

Fambitakoye, O., Equatorial electrojet and regular daily variation S_R – I. A determination of the equatorial electrojet parameters., Journal of Atmospheric and Terrestrial Physics, Vol 38, pp 1-17, 1976.

Fambitakoye, O., Equatorial electrojet and regular daily variation S_R – IV. Special features in particular days, Journal of Atmospheric and Terrestrial Physics, Vol 38, pp 123 to 134, 1975.

Fejer, J., The effects of energetic trapped particles on the magnetosphere motions and ionospheric currents, Can. J. Phys., 39, 1409- 1417, 1961.

Friedman, H., Sun and Earth, Scientific American Library, ISBN 0-7167-5012-0, Scientific American Book, Inc. New York, 1986.

Fukushima, N. and T. Oguti, Polar magnetic storms and geomagnetic bays Appendix 1 : A theory of the SD-field, Rep. Ionos. Space. Res. Jap., 7, 137-146, 1953

Fukushima, N. Development and decay processes of the bay disturbances in geomagnetic field, J. Geomag., Geoelec;, 3, 59-76, 1951.

Fukushima, N., and Y. Kamide, Partial Ring Current Models for Worldwide geomagnetic disturbances, Reviews of Geophysics and Space Science, vol. 11, N°4, pp 795-853, November 1973.

Gauss, K.F., General theory of terrestrial magnetism, 1839.

Gilbert, W. De Magnete, 1600.

Giraud, A. and M. Petit, Ionospheric techniques and Phenomena, D. Reidel Company, Dordrecht Holland, Boston/USA and London/ England, 1978.

Gouin, O. and P. N. Mayaud, A propos de l'existence possible d'un contre-électrojet aux latitudes équatoriales, Ann. Geophys., 23, 41, 1967.

Gold, T., motions in the magnetosphere of the Earth , J. Geophys. Res., 64, 1219, 1959 (a).

Gold, T., Origin of the radiation near the earth discovered by means of satellites, Nature, 183, 355-358, 1959 (b).

Gordon, W.E., Incoherent scattering of radiowaves by free electrons with applications to space exploration by radar, P.I.R.E, 46, 1824, 1958.

Gosling, J.T., M.F. Thomsen, S.J. Bame and C.T. Russell, Accelerated Plasm Flows at te Near-tail Magnetopause, , Journal of Geophys. Research, Vol 91, N° A3, pp 3029-3041, 1986.

Gosling, J.T., M.F. Thomsen, S.J. Bame, R.C. Elphic and C.T. Russell, Plasma Flow Reversals at the Dayside Magnetopause and the Origin of Asymmetric Polar Cap Convection, Journal of Geophys. Research, Vol 95, N° A6, pp 8073-8084, 1990.

Graham - 1722

Greenwald, R.A., W. Weiss, E. Nielsen, N.R. Thomson, C. Haldoupis, STARE : A new radar auroral backscatter experiment in northern Scandinavia, radio Sci., 13, 1021-1039, 1978.

Hedin, A.E., A. Biondi, R.G. Burnside, G. Hernandez, R.M. Johnson, T.L. Killeen, C. Mazaudier, J.W. Meriwether, J.E. Salah, J. Sica, R.W. Smith, N.W. Spencer, V.B. Wickwar, T.S. Virdi, revised Global Model of Thermosphere Winds using satellite and Grond based bservation, J. Geophys. Res. Vol 96, N° A5, 7657-7688, 1991.

Heelis, R., Magnetospheric and Ionospheric currents, Wokshop CAWSES, Taiwan, 2005.

Ijima T., T.A. Potemra, Large scale characteristics of field-aligned currents associated with substorms, J. Geophys. Res., 83, 599-615, 1978.

Jacchia, L.G., revised static model of the thermosphere and exosphere with empirical temperatures profiles, Spec. rep., 332, Smithson Astrophys. Obs., 1971.

Kamide, Y. and N. Fukushima, positive Bays in evening high latitudes and their possible connection with partial ring current, Rep. ionos. Space Res. Jap., 26, 79-101, 1972.

Kamide, Y. and A. Brekke, Auroral electrojet densiy from the Chatanika radar and from the Alaska meridian chain of magnetic observations, J. geophys. Res. , 60, 587, 1975.

Kamide, Y., Electrodynamic processes in the Earth's ionosphere and magnetosphere, Kyoto Sangyo University press, Kyoto, japan, 1988.

Kato, S., Horizontal wind systems in the E region deduced from the dynamo theory of the geomagnetic Sq variation, 2. rotating Earth, J. Geomagn. Geoelectri., 8, 24, 1956.

Kelley, M.C., The Earth’s Ionosphere, Academic Press, San Diego, 1989.

Kobea, A., T., A.D. Richmond, B.A. Emery, C. Peymirat, H. Lürh, T. Moretto, M. Hairston, and C. Amory-Mazaudier, Electrodynamic coupling oh high and low latitudes : observations on May, 27, 1993, J. Geophys. Res, Vol 105, N° A 10, 22979-22989, 0ctober 1, 2000.

Legrand J-P. and P.A. Simon, Solar cycle and geomagnetic activity : A review for geophysicists Part I : the contribution to geomagnetic activity of shock waves and of the solar wind , Annales Geophysicae, 7(6), 565-578, 1989.

Le Huy, M. C. Amory-Mazaudier, Magnetic signature of the Ionospheric disturbance dynamo at equatorial latitudes : « Ddyn », Journal of Geophys. Res, Vol 110, A 10301, 2005.

Le Huy M., and C. Amory-Mazaudier, Planetary magnetic signature of the Storm wind disturbance Dynamo currents : Ddyn, Journal of Geophys. Res., Vol 113, A02312, doi:10.1029, 2008;

Maeda, H., Horizontal wind systems in the ionosphere E region deduced from dynamo theory of the geomagnetic S variation 1, Non rotating earth, J. Geomagn. Geoelec., 7, 127, 1955.

Maeda, H., T. Iyemoru, T. Araki and T. Kamei, New evidence of a meridional current system in the equatorial ionosphere, Geophys. Res. Lett., 9, 337-340, 1982.

McNish A.G., Magnetic effects associated with bright solar eruptions and radio fade-outs, Nature, 139, 244, 1937a.

Mc Nish, A.G., Terrestrial magnetic variations and the ionosphere, Nature, Journal of Applied Physics, Vol 8,p. 718, 1937b

McNish, A.G., Terrestrial Magnetic and Ionospheric effects associated with bright chromosperic eruptions , Terr. Magn. Atm. Elec., 42(2), 109-122, 1937c.

Mayaud, P.N., Analyse morphologique de la variabilité jour à jour de la variation journalière et régulière SR du champ magnetique terrestre, système C (régions non polaires), Ann. Geophys., 21, 514-544, 1965.

Mayaud, P.N., Derivation, Meaning and Use of Geomagnetic Indices, Geophysical Monograph series, Vol 22, AGU, Washington DC, 1980.

Maynard, N.C., Measurements of ionospheric currents off the coast Peru, J. geophys. Res., 72, 1863-1875, 1967.

Mazaudier, C., Electric current above Saint-Santin I. Data, J. geophys. Res., vol87, A4, p 2459-2464, 1982.

Mazaudier, C., and M. Blanc, Electric currents above Saint-santin 2. Model, J. Geophys. res., 88, A2, 981-987, 1982.

Mazaudier, C., Electric currents above Saint-Santin, 3. A preliminary study of disturbances, June 6, 1978, March, 22, 1979, March 23, 1979, Journal of Geophys. Res., vol 90, A2, 1355-1366, 1985.

Mazaudier, C., C. Senior and E. Nielsen, Global convection Electric Field and Current : comparisons between Model's predictions and Data from STARE, Saint-Santin and Magnetometers, J. Geophys. Res., Vol; 92, A6, 5591-5599, 1987

Maxwell, J., Introductive Lecture on Experimental Physics, at the Cambridge University, 1870.

Maxwell, J., electricity and Magnetism, Vol 2., 1873.

Menvielle, M., H. Mc Creadie, C. Barton, IAGA guide on geomagnetic indices derived from Earth surfec data, to appear in the publications of IAGA.

Mozer, F.S., and R. Serlin, Magnetospheric Electric fields measurements with balloons, J. Geophys. Res., 74, 4739, 1969.

Nagata, T., S. Kokubun, rep. Ionosph Space. Japan, 16, 250, 1962.

Nishida A., Coherence of geomagnetic DP2 fluctuations with interplanetary magnetic variations, J. Geophys. Res. 73, 5549, 1968.

Obayashi T. and T. Nishida, Large scale electric fields in the magnetosphere, Space Sci. Rev., 8, 3-31, 1968.

Onwumechili, C.A., Equatorial Electrojet, Gordon and Breach Science Publishers, Netherlands, 1997.

Paterno, L., C. R. Acad; Sci. Paris, série IIb, 326, 393-406, 1998.

Paterno, L., History of the Solar Cycle, Published in a book of Historical events and people in aeronomy geomagnetism and solar-terrestrial Physics, of geomagnetism and aeronomy, lectures from the IAGA Assembly in Hanoï 2001, collected and edited by W. Schröder, pp 261- 275, Science edition AKGGKP, Bremen-Rönnebeck, Postdam, 2002.

Peymirat, C., A.T. Kobea, A.D. Richmond, Electrodynamic coupling oh high and low latitudes : simulations of shielding: overshielding effects J. Geophys. Res, Vol 105, N° A 10, 22991-23003, 0ctober 1, 2000.

Pneuman, G.W. and R.A. Kopp, Gas-magnetic field interactions in the solar corona, Solar Phys., 18, 258-270, 1971.

Price, A.T. and G.A. Wilkins, new methods for the analysis of geomagnetic fields and their application to the Sq field of 1932-1933, phil. Trans. Roy. Soc. Lond. Series A, 256, 31-98, 1962.

Richmond A.D. and S. Matshushita, Thermospheric response to a Magnetic substorm, J. Geophys. Res., vol 80, N° 19, 2839-2850, July, 1975.

Richmond A.D., Ionospheric Wind Dynamo Theory : A review, J. Geomagn Geoelec, 31, 287, 1979.

Richmond, A.D., M. Blanc, B.A. Emery, R.W. Wand, B.G. Fejer, R.F. Woodman, S. Ganguily, P. Amayenc, R.A. Behnke, C. Calderon, and J.V. Evans, An empirical model of quiet day ionospheric electric fields at middele and low latitudes, J. Geophys. Res., 85, 4658, 1980.

Richmond, A.D., and Y. Kamide, Mapping electrodynamic features of the high-latitudes ionosphere from localized observations : Techniques, Journal of Geophys. res., Vol 93, N° A6, pp 5741-5759, 1988.

Richmond, A.D. Ionospheric Electrodynamics, in Handbook of Atmospheric Electrodynamics. Vol II (H. Volland, ed.) CRC Press, Boca Raton, Florida, 249-290, 1995.

Risbeth, H. and O.K. Gariott, Introduction to Ionospheric Physics, Academic Press, New York (111 Fifth Avenue New York, 10003 New York) and London (Berkeley Square House London W.1) , 1969.

Risbeth, H., Review paper : The ionospheric E-layer and F-layer dynamos, a tutorial lecture, Journal of Atmospheric and Solar Terrestrial Physics, Vol 59, n° 15, pp 1873-1880, 1997.

Rostoker, G. Classification of Polar magnetic disturbances, J. geophys. res., Space Physics, 74, N°21, 5161, 1969.

Rostoker, G., A determining factor in the form of the equivalent current system for geomagnetic bays, earths Planetary Sci. Letters, 2, 119, 1967.

Salah, J.E., and J.V. Evans, tests of electrodynamic consistency from daytime ionospheric electric fields and currents, J. Geophys. Res., 81, 6 2413-2418, 1977.

Schelgel, K., Coherent backscatter from ionospheric E region plasma irregularities, Journal of Atmospheric and Terr. Physics, Vol 58, N° 8/9, pp 933-941, 1996

Schröder, W., Some aspects of the History of Auroral Research, EOS, vol. 60, N° 51, pages 1035-1036, 1979.

Schröder, W., Behavior of Aurora in Germany, 1880-1964, J. Geophys. Res., Vol 77, N° 34, p. 6890, December 1972.

Schuman B.M., Rocket measurement of the equatorial electrojet, J. Geophys. Res., 75, 3889-3901, 1970.

Schunk, R.W. and A.F. Nagy, Ionospheres : Physics, Plasma Physics and Chemistry, Cambridge University Press, 2000.

Schuster, A., The diurnal variation of the Terrestrial Magnetism, Phil. trans. Roy. Soc. Lond., series A, 180, 467, 1889.

Schuster, A., the diurnal variation of Terrestrial Magnetism Phil. trans. Roy. Soc. Lond., series A, 208, 163, 1907.

Silsbee, H.C., and E.H. Vestine, Terr., Mag., 47, 195, 1942.

Siebert, M., Zur theorie der thermischen erregung gezeitenartiger Schwingungen der Endatmosphäre, Naturwissenchaften, 41, 446, 1954.

Siebert, M., Analyse des Jahresganges der 1/n- tagigen vatiationen des luftchuckes und der temperatur, Nach. Aksd. Wiss. Göttingen Math. Phys., K1, N6, 127-144, 1956.

Simon P. A. et J. P. Legrand, Solar cycle and geomagnetic activity : A review for geophysicists Part II. The solar sources of geomagnetic activity and their links with sunspot cycle activity. Annales Geophysicae, 7 , (6), 579-594, 1989.

Stening, R.J., An assessement of the contributions of various tidal wind to the Sq current system, Planet. space Sci., 17, 889, 1969.

Stern, D.P., Large-scale electric fields in the earth's magnetosphere, Rev. Geophys. Res., Sapce Phys., 15, 156, 1977.

Stewart B., Terrestrial magnetism, Encyclopaedia Britannica, 9th ed., Vol. 16, 159-184, 1882.

Stewart, B., On the cause of the Solar-diurnal Variations of the Terrestrial Magnetism, Communicated to the Physical Society, 1886.

Störmer , C. Sur les trajectoires des corpuscules électrisées dans l'espace sous l'action du magnétisme terrestre avec application aux aurores boréales Arch. Sci. Phys. Genève

(a) 24, p 5, 113, 121, 317 (1907)

(b) 32, 33, 163 pp (1911,2)

(c) 35, 483-8 (1913)

Sugiura, M., J.C. D.J. Poros, An improved model of equatorial electrojet with meridional current system, Journal of Geophysical Research, 74, 4025-4034, 1969.

Tarpley, J.D., the ionosphere wind dynamo, 2, solar tides, Planet. Space Sci., 18, 1091, 1970.

Tsyganenko, N.A. Magnetospheric magnetic field with a warped tail current sheet. Planet. Space Sci., 73, 5, 1989.

Tsyganenko, N.A., D.P. Stern, Modeling the global magnetic field of the large scale Birkeland current system, J. Geophys. Lett, 101, 27, 187-27, 198, 1996.

Tsyganenko, N.A., Solar wind control of the tail lobe magnetic field as deduced from Geotail, AMPTE/IRM and ISEEE-2 data, J. geophys. Res. 105, 5517, 2000.

Van Allen J.A., Direct detection of auroral radiation with rocket equipement, proc. Natl. Acad. Sci. U.A., 43, 57-92, 1957.

Van Allen, J.A., Ludwig, G.H., Ray E.C., McLlwain, C.E., Observations of High intensity radiation by Satellites 1958 Alpha and Gamma, IGY Bulletin, Transactions of the American Geophysical Union 39, 767-769, 1958.

Van Allen, J.A., The Geomagnetically Trapped Corspuscular Radiation, J. geophys. res., Vol 64, N°11, 1683-1689, Novemver 1959.

Van Sabben, D., North south asymetry of Sq, J. Atmos., Terr. Phys. 26, 1187, 1964.

Van Sabben, D., Magnetospheric currents associated with the N-S asymmetry of Sq, J. Atmos. Terr. Phys., 28, 965, 1966.

Vasseur, G., Dynamics of the F region observed with Thomson scatter -1. Atmospheric circulation and neutral winds, J. Atmos. terr. Phys., 31, 397, 1969b.

Vasyliunas, V.H., A Mathematical model of magnetospheric convection and its coupling to the ionosphere in " Particles and Fields in the Magnetospher", Edited by B.M. Cormac, D. Reidel, Hollant, 60, 1970.

Volland H., Atmospheric Tides and Planetary waves, Published by Luwer Academic Publishers, P.O. Box 17, 3300 A.A. Dordrecht, The Netherlands, 1988.

Woodman, R. F., Vertical drift velocities and east-west electric field at the magnetic equator, J. Geophys. Res., 75, 6249-6259, 1970.

NIGERIAN JOURNAL OF SPACE RESEARCH **8**: 256 – 281, 2009 September 1

Dynamo Processes

F. N. OKEKE Ph.D
Department of Physics and Astronomy
P.O. Box 3238, University of Nigeria, Nsukka, Nigeria.
e-mail: franciscaokeke@yahoo.com

Table of Content

Table of Content

1.0. Introduction

Dynamo, simply means, a device by which mechanical energy is converted into electrical energy. In earth's dynamo action, earth generates a magnetic field, in other words earth serves as magnet, the moving air serves as the armature while the conducting ionosphere serves as the windings. It has long been ascertained that the possible origin of the earth's magnetic field, is that of electric currents in the earth's interior, which set up a magnetic field by induction. This process is maintained by some magneto-hydrodynamic phenomenon, which we shall discuss later.

Dynamo theory, no doubt is a very complex concept that is why in most cases, many researches concentrates mostly on the kinematic dynamo theory, which involves the vector velocity field V. The discovery of dynamo theory has made serious contributions as to the correct origin of earth's magnetic field. Prior to it's discovery, there have been speculations as regards origin of earth's field, these include: Thermo Remnant Magnetization (TRM) of rocks. This simply means magnetization acquired by rocks cooling through their curie temperature in a magnetic field, and is common in igneous rocks, for sedimentary rocks do not acquire their magnetization by cooling, because, they are never hot (except those, by chance are heated by contact with igneous rocks). It was later discovered that most rocks do not get to their curie temperature; this led to dropping of TRM. Again, Chemical processes can also bring about magnetization, referred to as Chemical Remnant Magnetization (CRM). Furthermore, rocks acquire magnetism through naturally induced and artificially induced Isothermal Remnant Magnetization (IRM). It could also be acquired through Detrital Remnant Magnetization (DRM). The former takes place when ground is struck by lightening and its current sets up a varying magnetic field which leaves the rocks in the neighbor-hood magnetized after it has fallen to zero (Naturally induced IRM). On the other hand if a ferromagnetic mineral (Igneous Rock for example) is subjected to a varying magnetic field, so that it is taken round a hysteresis cycle, then when an external field returns to zero, the rock will remain magnetized (artificially induced IRM). Again rocks that are magnetized through alignment of magnetic grains, that is; rocks accumulating as grains of

sediment in water are found especially in the clays that settle in calm glacial lakes and in some sediments of the deep oceans.

In all of the above, it is important to note that each is peculiar to some rocks not all rocks, hence the need for further investigation which resulted in the discovery of dynamo action that answers the question.

*1.1 **Dynamo Action in the Earth's Core:***

Sir Joseph Harmer (1919) ascertained that the earth's core is a good conductor of electricity and a fluid in which motions can take place, ie it allows both mechanical motion and the flow of electric current, and the interaction of these could generate a self-sustaining magnetic field.

Dynamo theory established the fact that the magnetic field is ultimately produced and maintained by an induction process, the magnetic energy being drawn from the kinetic energy of the fluid motion in the core. It is possible that a group of particles moving at different speeds in the fluid may pull laterally on some magnetic lines of force, hence stretching them. During this stretching, they will gain energy, which is taken from the mechanical energy of the moving particles. The complexity of dynamo action involves both hydrodynamic and electromagnetic, Question: Is asymmetry of motion sufficient for dynamo action? Or asymmetry of structure important for dynamo action too?

Thus, the dynamo action within the core referred to, as the motion of the conducting liquid core relative to the magnetic field in the core, generates currents which maintain them. For this to be possible, the electrical conductivity of the core must be high enough and the core must be liquid with viscosity not too high. There must also be a source of energy to derive the movement of the liquid against the viscous and electromagnetic forces that resist it. The above is summarized by the word 'magneto- hydrodynamic phenomenon', this implies the motion of electrons in the fluid core which generated flow of current and in turn, magnetic field are set up which again as the flow continues, induces magnetism along the neighboring rocks.

It is good to note that other possible causes of electromotive force deep within the earth are the thermoelectric and chemical. It is remarkable to observe that for any of these to occur, there must be a major contact between dissimilar materials or between the same substances at notably different physical conditions. Hence Elsassar (1939) proposed that thermoelectric electromotive forces were due to inhomogeneities in the core material which are created and continuously regenerated by turbulent fluid motion. He then concluded that only a small fraction of the current generated by such a mechanism could be responsible for the surface magnetic field. While Runcorn (1954) suggested that thermoelectric currents are generated at the core-mantle boundary where there is a contact between two materials with different electrical properties.

1.2 ***Ionospheric Dynamo Action***

Ionosphere is that region of the atmosphere, from about 60 to 1000km above the earth's surface. In this region, free electrons exist in numbers sufficient to influence the transmission of electromagnetic waves at radio frequencies. Hence ionosphere could be regarded as ionized region of the upper atmosphere, which forms the inner boundary of the magnetosphere. The main reason for the existence of the ionosphere is because the solar radiation is absorbed by the upper atmosphere, thereby dissociating the molecules and liberating free electrons. It is important to note that earth's magnetic field affects the electron density motion at all heights, but with increasing importance at greater heights, where there are few molecules. Another important source of ionization at high latitudes is the precipitation of energetic charged particles. Onwumechili (1997) ascertained that in any part of the ionosphere, that the electron density Ne is determined by the equation of continuity for electrons

$$\frac{\partial N_e}{\partial t} = P(N_e) - L(N_e) - \nabla.(N_e V) \quad - - - - - - \quad 1.1$$

$P(N_e)$ is the rate of production of electrons, $L(N_e)$ is the loss of electrons, mostly through chemical processes, $\text{div}(N_e \mathbf{V})$ is the rate of outward transportation of electrons, and **V** is the mean velocity of electrons.

Hence, continuity equation for positive and Negative ions may be written respectively as;

$$\frac{\partial N_+}{\partial t} = P(N_+) - L(N_+) - \nabla.(N_+V) \quad - - \quad - \quad - \quad - \quad 1.2$$

$$\frac{\partial N-}{\partial t} = P(N_-) - L(N_-) - \nabla(N_-V) \quad - - \quad - \quad - \quad - \quad 1.3$$

Ionospheric dynamo action is likened to the dynamo action in the earth's core. The same fluid makes the action possible; the difference lies in the fact that, the fluid in the core is liquid while that in the ionosphere is air (wind). Ionospheric dynamo could be regarded as electric current system that flows in the ionosphere, where source of magnetic field exists. Hence, ionospheric dynamo is produced by movement of charged particles of the ionosphere across earth's main field.

Tidal forces due to the sun, the moon and the solar heating drive the motion of charged particles, through dynamo action and in turn produce a pattern of electric currents centered on the sun-earth line. As the earth rotates beneath the current system, magnetic observatories record a smooth daily variation in the geomagnetic field. Two parameters that control ionospheric dynamo are the distribution of winds and that of electrical conductivity in the ionosphere. In turn, these parameters are influenced by several other factors, namely; the solar cycle, solar flares, solar eclipses, the orbital parameters of the Earth, Sun and Moon. It has been observed by Du and Stening (1999) that changes in the position of the sun and the moon relative to the Earth as a result of orbital motions cause variation in distance. He also noted that this alters the strength of the tides and of solar heating, thereby changing ionospheric wind patterns. The changes are clearly seen (obvious) as a seasonal variation of the winds and hence of the strength of the current.

Electrical conductivity of the ionosphere is another parameter that controls the dynamo current, because any process that alters ionospheric conductivity changes the current (why?). It has long been known that the dominant source of ionization on the dayside of the Earth is sunlight. The angle at which the sunlight enters the atmosphere determines the amount of ionization, hence vertical incidences produces more ionization per unit volume than slant or inclined incidence. It has been proved that vertical (normal) incidence occurs in summer than in winter, then there exists strong seasonal variation of the dynamo current. The phase of the solar cycle also determines the degree of atmospheric ionization; this is true, because the 11 – year cycle of sunspot activity produces changes in the amount of ultraviolet radiation emitted by the sun. In effect, it could be seen that sunspots numbers are directly proportional to UV radiation and increased ionospheric conductivity, hence leading to stronger currents. For a shorter timescale, solar flares emit x-rays that penetrate deeper in the atmosphere, temporarily ionizing the D region, hence dynamo currents are produced in D – region by any amount of winds present in this region. These Parameters will be discussed in later chapters.

1.2.1. **Kinematic Dynamo Theory (KDT)**

It has already been noted that when a conducting fluid flows across an existing magnetic field, electric currents are induced, which then creates a separate magnetic field. If the original magnetic field is reinforced by this new magnetic field then a dynamo is created which sustains itself. A simpler version of dynamo theory is referred to as, kinematic dynamo theory – this involves the vector velocity field which does not vary, in accordance with the forces exerted upon the fluid. One of the basic assumptions made in applying the kinematic dynamo theory is that the magnetic field has to be very small so as not to affect the velocity field. The implication of this, is that long – term behaviour of dynamo system will not be taken into account.

The most functional feature of kinematic dynamo theory is that, it can be used to determine what fields or systems are, or are not dynamos (Wikipedia, encyclopedia, 2005)

A striking feature of KDT is its usefulness in determining what fields or systems that are not dynamos. An application of some velocity field to a small magnetic field reveals through observation whether the magnetic field tends to grow or not, in response to the applied flow. If the magnetic field grows, then the system is dynamo which can exhibit dynamo action. On the contrary, if it does not grow, then, the system is referred to as non-dynamo, incapable of exhibiting dynamo action.

1.2.2. None Linear Dynamo Theory (NLDT)

It is important to note that the assumptions and approximations made on KDT above become invalid as soon as magnetic field becomes strong enough to affect the fluid motions. When this is the situation, the velocity becomes affected by the Lorentz force and induction equation will no longer be linear in the magnetic field. In most cases this results in the stoppage of the amplitude of the dynamo. These dynamos are at times referred to as hydro- magnetic dynamos, these are common is astrophysics and geophysics.

1.3 Geomagnetic Variations

These variations are revealed from records of any magnetic observatory which show that geomagnetic field has spatial variation (from place to place) and temporal variation (from time to time).

1.3.1. Transient Variation

This refers to variation field which is related to sources in the upper atmosphere that are associated with induced currents in the earth. The main field has its origin deep inside the earth.

Contributions to the earth's field could be explained by atmospheric 'dynamo action', sometimes referred to as ionospheric dynamo action. The geomagnetic transient variation could be further classified as follows:

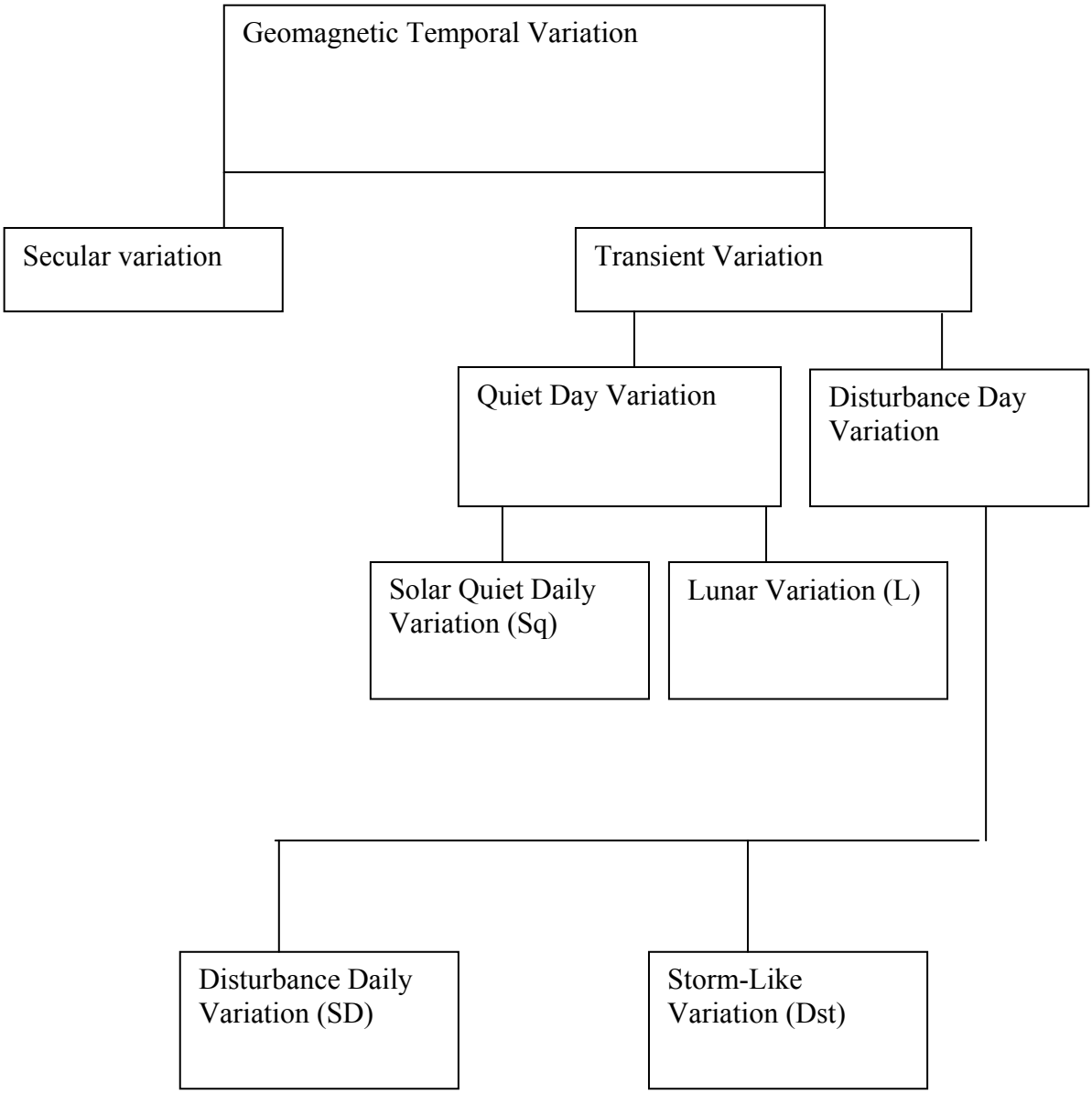

Fig. 1.1 Organogram of geomagnetic temporal variations

i. Daily mean variation: It is the mean of 24 hourly values from midnight to midnight

ii. Monthly (or annual) mean value: This is the daily mean values averaged over month (or year).

iii. Mean hourly value: This is mean of hourly values for each individual hour for all days of month or year or selected number of days.

iv. Mean daily inequality(s): This is monthly (or yearly) mean value subtracted from the mean hourly valued of month (or year), which gives a sequence of hourly departures called mean daily inequality.

v. S_q: This is mean daily inequality derived for five quietest days of month.

vi. L: This is lunar influence on geomagnetic variations.

vii. S_D: This is disturbance daily variation difference. (ie $S_d - S_q$, where S_d is mean daily inequality for five most disturbed days of the month).

viii. D_{st}: This is regular part of variation accompanying a magnetic disturbance (eg storm time) and is measured from beginning of storm.

ix. D_i: This is irregular part of variations accompanying a magnetic disturbance, not related to storm time.

NB: One Gamma (γ) $= 10^{-5}$ Gauss $= 10^{-9}$ Tesla

Characteristics of S_q:

(a) The amplitude changes phase at the latitude of $\sim 40^0$

(b) The amplitude of the variation is greatest during the light day hours (ie from 0080-1600 hours).

(c) The amplitude of S_q has an annual variation; it is greater in summer than in winter.

(d) The amplitude of S_q variation varies from day to day.

(e) The amplitude of S_q is greatest in years of sunspot maximum (but the average phase and form differ little from year to year).

It has been show that the transient S, L and D fields can be separated by spherical harmonic analysis into external and internal parts, which originate outside and within the earth

respectively. Just as one can use spherical harmonic analysis to represent potential at a point, Gauss, first used it and showed that Sq field is produced mainly by overhead currents (S_q^e) and there is a small contribution from currents in earth S_q^i field .

Four current systems exist; two in the Southern hemisphere and two in the Northern hemisphere and the amplitude is greater during day time than night time. The magnitude of amplitude of variation is of the order of 10^4 A.

Lunar Daily Variation (L)

The sun moves from 23^o N to 23^0 S, due to tilting of the earth. When mean monthly values of magnetic element is subtracted from values of magnetic element for each hour during the month, we are left with set of variations free from solar daily variation (Si). When L is much smaller that Sq (L < <Sq), L depends on the phase of the moon.

I lunar hour = 1 hour $2^1/_3$ min of solar day implies that lunar hour > solar hour .

Some characteristics of **L**

(i) **L** decreases in amplitude from summer to winter, and the ratio is greater for L than for S_q.

(ii) There is a slight dependence of **L** on sunspot number.

(iii) **L** increases with magnetic disturbances.

(NB, It has been observed that ¾ of L could be due to external cause, while ¼ of L could be due to internal cause.

1.3.2: ***Geomagnetic Components:***

Magnetic components: It has been internationally agreed that a set of names and symbols be used to describe the earth's field components. Geomagnetic force at a point could be expressed in terms of vector components known as geomagnetic elements. This could be specified by means of rectangular components X, Y, Z, of the total intensity F. Other common terms of specifying the geomagnetic intensity is by means of geomagnetic elements H, D and I.

H – Horizontal component (horizontal intensity of force along the magnetic meridian it is positive in Northerly direction).

D – Angle between the geographic and geomagnetic meridian.

Z – Vertical component (vertical intensity or force perpendicular to both X and Y, it is taken as positive downwards:

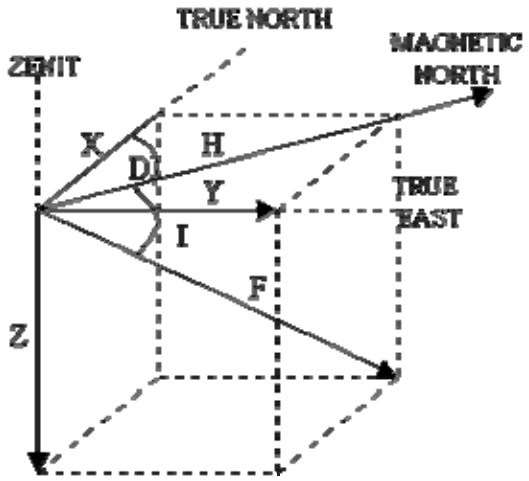

Fig. 1.2 Geomagnetic Components

Three elements are needed at a time to specify the magnitude and direction. Those whose records are regularly kept in magnetic observations are H, D and Z.

X – Northwards, Y – Eastward Z – downwards.

Easterly declination $D = \text{arc tan } (Y/X)$ - - - - - ----1.4

Horizontal intensity $H = (X^2 + y^2)^{1/2}$ -- - - - - ----1.5

Dip angle or inclination $I = \tan^{-1} (Z/H)$ - - - - - ----1.6

X Y Z and D H Z components are related as follows:

$X = H\cos (D)$, $Y = H \text{ Sin } (D)$, then, the total field F is given by,

$F = (X^2 + Y^2)^{1/2} = (H^2 + Z^2)^{1/2}$ - - - - - - - - ----1.7

It is important to note that main geomagnetic field ~ 6 x 10^4 ɤ near poles, 3 x 10^4 ɤ near the equator. Also quiet–time daily variations can be about 20ɤ at mid latitudes and 100ɤ at equatorial regions. Solar–terrestrial disturbance time variations, occasionally reach 1,000ɤ at the auroral region and 250ɤ at mid latitudes.

1.3.3. Effects of Solar radiation in the ionosphere and geomagnetic parameters.

The solar radiation ionizes the ionosphere and it behaves as a conducting medium. In the ionosphere, wind carries the ionized particles with velocity say, ω, across the lines of earth's magnetic flux B. This constitutes a conductor cutting of the magnetic lines, which then results in an induced emf. According to Faradays law of electromagnetic induction, there occurs the induction of electromagnetic force (emf) ie (ω x B). This emf causes current to flow in the conducting medium in the direction of (ω x B). Since in a given region, the direction of B is fixed, the wind needs to blow in closed curves for the current to complete its circuit, but the wind progresses instead of blowing in closed curves. Therefore, the current is divergent and cannot complete its circuit. In consequence, the current accumulates positive and negative charges that polarize the ionization. The polarized field is given by;

$$E = -\nabla \text{Ø} \quad - \quad - \quad - \quad - \quad 1.8$$

There exist now, two sources of electric field E, whose sum is;

$$E' = E + (\omega \times B) \quad - \quad - \quad - \quad 1.9$$

The total field E' sustains a current that completes the circuit, the current is non- divergent and $(\nabla J = 0)$, hence $J = \sigma E'$ - - - - 1. 10

Where J is current density and σ is tensor conductivity

Thus, the polarization electrostatic field E helps the dynamo induced field the drive a current that completes the circuit. The magnetic field of this dynamo current is that part of the geomagnetic transient variation whose origin is in the ionosphere this will be discussed later.

2.1 Electrical conductivity of the ionosphere

Although the ionosphere is not totally, but partially ionized, it is discovered that the ionization is strong enough to form plasma. Plasma is electrically neutral, implying that positive and negative charges are equal, (ie free ions and free electrons form ionosphere plasma). This ionospheric plasma is usually formed through dissociation by particle precipitation at high latitudes and by Energetic Ultraviolet (**EUV**) solar radiation at all latitudes. The neutral gas (Neutral atoms and molecules) is weakly ionized when its density clearly exceeds the plasma density.

In a magneto plasma (Plasma in a magnetic field) where there is no collision, charged particles gyrate round magnetic flux B with angular frequency w, given by

$$\omega = eB/m \quad \ldots\ldots\ldots\ldots\ldots\ldots\ldots\ldots\ldots\ldots\ldots\ldots\ldots\ldots\ldots\ldots \quad 2.1$$

where w is referred to as Larmor or gyro frequency e and m are the charge and mass of the particle respectively. It is important to note that in this state of gyration when there is no collision (collissionless), if electric field E is applied perpendicular to B, both electrons and ions drift with the same velocity V_d, given by;

$$\mathbf{V_d} = E \times B/B^2 \quad \ldots\ldots\ldots\ldots\ldots\ldots\ldots\ldots\ldots\ldots\ldots\ldots\ldots\ldots\ldots\ldots \quad 2.2$$

In the above motions, there is no flow of current because gyration does not involve any relative translation and in the E x B (electric drift), electrons and ions drift together without relative displacement. On the other hand, if collisions occur, there exist collisions between electrons and neutrals with collision frequency υ_{en}, and similarly for ions and neutrals, we have υ_{in}, electrons with ions have υ_e and that of ions be υ_{ei}. In general, we let the effective frequency of electrons with all particle types be donated by υ_e and that of ions by υ_i.

2.1.1 Electrical conductivity in magnetic field.

Let us first consider electrical conductivity in absence of magnetic field, it is seen that the particles having acquired velocity during collisions, it is accelerated in the electric field. The acceleration being given by; $a = q\,E/m$ $\ldots\ldots\ldots\ldots\ldots\ldots\ldots\ldots$ 2.3

In summary, the current density vector J is given by;

$$J = n_i \upsilon_i \, q_i + n_e \upsilon_e q_e = n_e^2 \left(\bar{\tau}_i / m_i + \bar{\tau}_e / m_e \right) E \qquad \ldots\ldots\ldots\ldots\ldots\ldots\ldots\ldots\ldots\ldots\ldots\ldots \quad 2.4$$

$\left(\text{but } \upsilon = \dfrac{1}{\tau} \right)$, then equation 2.3 becomes;

$$J = ne^2 \left(\frac{1}{m_i \upsilon_i} + \frac{1}{m_e \upsilon_e} \right) E \qquad \ldots\ldots\ldots\ldots\ldots\ldots\ldots\ldots\ldots\ldots\ldots\ldots \quad 2.5$$

$$NB \;\; ne^2 \left(1/m_i \upsilon_i + \frac{1}{m_e \upsilon_e} \right) \Rightarrow \sigma_o$$

(τ is time interval, n_i and n_e are ion and electron number density respectively).

Next, we consider conductivity in the presence of a magnetic field, here, it is important to divide the electric field vector into the component parallel (E_{11}), to the magnetic field (**B**) and that perpendicular ($E_\perp$) to **B**.

2.1.2 E parallel to magnetic field (E_{11})

No Lorentz forces act on a particle moving parallel to the magnetic field then,

$$J = \sigma_o E_{11} \qquad \ldots\ldots\ldots\ldots \quad 2.6 \text{ (a)}$$

σ_o is called parallel conductivity or direct conductivity but $J = n_e V = (n_e^2/mv)\, E = \sigma_o E$ hence

$$\sigma_o = n_e^2/m_e v_e + n_e^2/m_i v_i = n_e^2/m_e v_e \qquad \ldots\ldots\ldots\ldots\ldots\ldots \quad 2.6 \text{ (b)}$$

2.1.3 E perpendicular to the magnetic field

Here, because the collision frequency (υ) is greater than gygro frequency (ω), the frequent collisions impede the particles from gyrating round **B**. Ions move in the direction of E, while

electrons move along – E and current flows perpendicular to **B**. The conductivity associated with this is referred to as Pedersen conductivity ((σ_i), the this (σ_1) perpendicular to B and parallel to E, is given by;

$$\sigma_1 = n_e^2\left[\frac{1}{m_e}\frac{\upsilon_e}{(\upsilon_e^2 + w_e^2}+\frac{1}{m_i}\frac{\upsilon_i}{\left(\upsilon_i^2 + w_i^2\right)}\right]=\frac{ne^2}{m_i}\frac{\upsilon_i}{\left(\upsilon_1^2 + w_1{}^2\right)} \quad \ldots\ldots\ldots\ldots\ldots \quad 2.7\ (a)$$

Or $$\sigma_1 = \sigma_o\frac{\upsilon^2}{\upsilon^2 + w_2} \quad \ldots\ldots\ldots\ldots\ldots\ldots\ldots\ldots \quad 27(b)$$

When electrons and ions are subject to the electric drift E x B|B^2 and Hall current flows in the direction of **B x E**, then conductivity σ_2 for the current is called Hall conductivity. For a single type of charged particles $\sigma_2 = \frac{e^2 nw}{m(\upsilon^2 + w^2)} = \frac{e^2 n}{m\upsilon}.\frac{\upsilon w}{v^2 + w^2} = \sigma_o\frac{\upsilon w}{\upsilon^2 + w_2}$ …… 2.8

If we take into consideration the presence of electron, positive and negative ions, then the expression can be written for, σ_o, σ_1 and σ_2 as;

$$\sigma_o = e^2\left(\frac{n_e}{m_e\upsilon_e}+\frac{n_-}{m_-\upsilon_-}+\frac{n+}{m_+\upsilon_+}\right) \quad \ldots\ldots 2.9$$

$$\sigma_1 = e^2\left[\frac{n_e\upsilon_e}{m_e(\upsilon_e^2 + w_e^2)}+\frac{n_-v_-}{m_-(\upsilon_-^2 + w_-^2)}+\frac{n_+\upsilon_+}{m_+(\upsilon_-^2 + w_-^2)}+\frac{n_+\upsilon_+}{m_+(\upsilon_+^2 + w_+^2)}\right] \quad \ldots\ldots 2.10$$

$$and\ \sigma_2 = -e^2\left[\frac{n_e w_e}{m_e(\upsilon_e^2 + w_e^2)}+\frac{n_- w_-}{m_-(\upsilon_-^2 + w_-^2)}+\frac{n_+ w_+}{m_+(\upsilon_+^2 + w_+^2)}\right] \quad \ldots\ldots 2.11$$

It is interesting to note that these conductivities depends on the direction of flow of current, for examples parallel σ_o depends on the current flow along **B**, Pedersen σ_1 depends on current flow perpendicular to B,

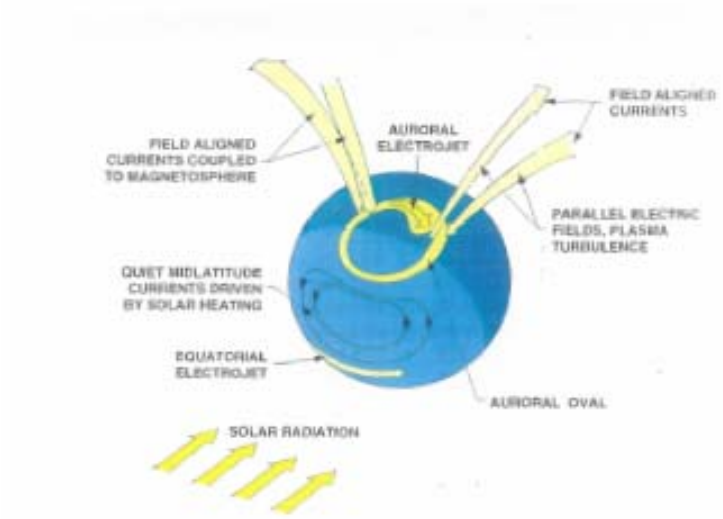

Fig. 2.1 Ionospheric Systems (Langel, 1989)

while Hall σ_2 depends on the current flow perpendicular to both **B** and **E**. Matsumoto (1962), noted that these conductivities are functions of altitude in the mid-latitudes. On the other hand, Forbes and Lendzen, (1976) showed that these conductivities are function of height during noon time, equatorial regions and average solar conditions.

Conductivities tensor

Maus (2006), noted that ohm's law for the ionosphere can be written using the anisotropic 3-D conductivity tensor σ as

$$J = \sigma E \text{ and } \sigma = \begin{pmatrix} \sigma_1 - \sigma_2 & \mathrm{O} \\ \sigma_2 & \sigma_1 & \mathrm{O} \\ \mathrm{O} & \mathrm{O} & \sigma_o \end{pmatrix} \quad \text{.....2.12}$$

We note that the coordinate system is chosen with Z in the direction of the magnetic field, **X** parallel to $E_\perp$, and **Y** perpendicular to **B** and perpendicular to $E_\perp$.

From equation 2.12, we can write;

$$\begin{Bmatrix} j_x \\ j_y \\ j_z \end{Bmatrix} = \begin{Bmatrix} \sigma_{xx} & \sigma_{xy} & \sigma_{xz} \\ \sigma_{yx} & \sigma_{y\,y} & \sigma_{y\,z} \\ \sigma_{zx} & \sigma_{zy} & \sigma_{zz} \end{Bmatrix} \begin{Bmatrix} E_x \\ E_y \\ E_z \end{Bmatrix} \quad \text{.....2.13}$$

From 2.13 Onwumechili (1997) defined elements of the tensor conductivity as;

$$\sigma_{xx} = \sigma_o Cos^2 I + \sigma_1 \sin^2 I \quad \text{.....2.13}a$$

$$\sigma_{xy} = -\sigma_{yx} = \sigma_2 \sin I \quad \text{.....2.13}b$$

$$\sigma_{xz} = \sigma_{zx} = (\sigma_o - \sigma_1)\cos I \sin \mathrm{I} \quad \text{..... 2.13c}$$

σ

$$\sigma_{yy} = \sigma_1 \quad \text{.....2.13}d$$

$$\sigma_{yz} = -\sigma_{zy} = \sigma_z \cos \mathrm{I} \quad \text{..... 2.13e}$$

$$\sigma_{zz} = \sigma_o \sin^2 + \sigma_1 \cos^2 \mathrm{I} \quad \text{..... 2.13f}$$

Where I is magnetic dip angle.

Cowling conductivity (σ_3) is the effective conductivity given by;

$$\sigma_3 = (\sigma_1^{\ 2} + \sigma_2^{\ 2})/\sigma_1 = \sigma_1 + \frac{\sigma_2^{\ 2}}{\sigma_1} \quad \text{.....2.14}$$

2.1.4 Currents in the ionosphere

The ionosphere consists of charged particles- ions and electrons. The motion due to mechanical forces and electric fields on these particles causes current to flow.

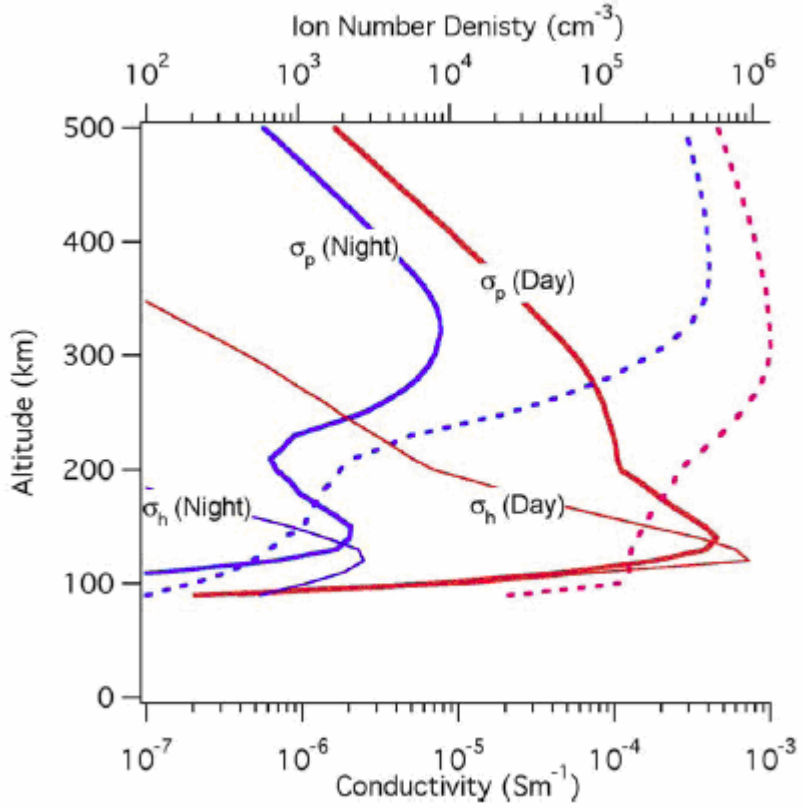

Fig. 2.2 Ionospheric conductivity at different latitudes (Heelis and Dallas, 2005)

The magnitude of the current produced depend on the conductivity of the ionized medium in which they flow.

These currents can be divided into

(i) Currents near a height of 110 km, driven by movement of the neutral air: - the atmospheric dynamo (has been earlier discussed).

(ii) Current near a height of 110 km in high latitude regions, driven by forces originating high in the ionosphere: the polar current system.

(iii) Currents in the ionosphere (magnetosphere) at a geocentric distance of about 4 earth radii: the ring current.

(iv) Currents in the magnetopause: resulting in a compression of the geomagnetic field.

It is known that current in the ionosphere originate from external polarization electric fields, that are delivered by field aligned currents. They also come from neutral winds as well as gravity.

It is important to discuss one of the above currents, the ring current, which is basically one of the major current systems in the earth's magnetosphere. Frank (1967), ascertained that ring current consists of geomagnetically trapped 10-200keV ions (mainly H^+, He^+ and O^+) and electrons that drift azimuthally around the earth at radial distances of about 2-7 Re (earth radii), overlapping the radiation belt region. In summary, a ring current could be defined as an electric current carried by charged particles trapped in a planet's magnetosphere. It is caused by the longitudinal drift of energetic (19-200KeV) particles (Wikipedia, 2006).

Martin (1994), noted that earth's ring current is responsible for shielding the lower latitudes of the earth from magnetospheric electric fields. It has large effect on the electrodynamics of geomagnetic storms. The main carrier of ring current energy (0.05 – 1 MeV)is ion, which majority are protons. Alpha particles, some percentage of O^+ oxygen ions, these mixture of ions suggests that ring current particles may have come from more than a source. It has also been observed that the formation of the storm-time ring current is due to two processes that have been suggested to explain the enhancement of the storm-time ring current which occurs at distance $L<4$. These processes include; (i) substorms particle injections i.e. injection of plasma into the inner magnetosphere during the expansion phase of magnetospheric substorms. (ii) transport and energization of plasma sheet particles by enhanced convection electric field Lyons and Schulz, (1989) ascertained that the latter process is more capable of delivery particles as deep as $L<4$, especially if there is electric field fluctuations. While Hamilton et al., (1988), noted that O^+ dominates over H^+ near the storms maximum phase.

Substorm processes have been of interest to many workers for some years now. For example; Lui et al. (1990), attributed the initiation of substorms to a kinetic instability due to particle drift across the magnetic field **B**. On the other hand, Roux (1991), attributed it to a ballooning

instability. Others like, Hones et al. (1973), Nishida et al. (1981), Cattle et al. (1986) attributed initiation to the formation of a magnetic neutral line within the cross-tait current sheet at a radial distance, ϒ ~15-20RE while Okeke, (1997), noted that substorm identification was not triggered externally but localized. Generally during a geomagnetic storm, the number of particles in the ring current increases, consequently there is decrease in the effects of geomagnetic field.

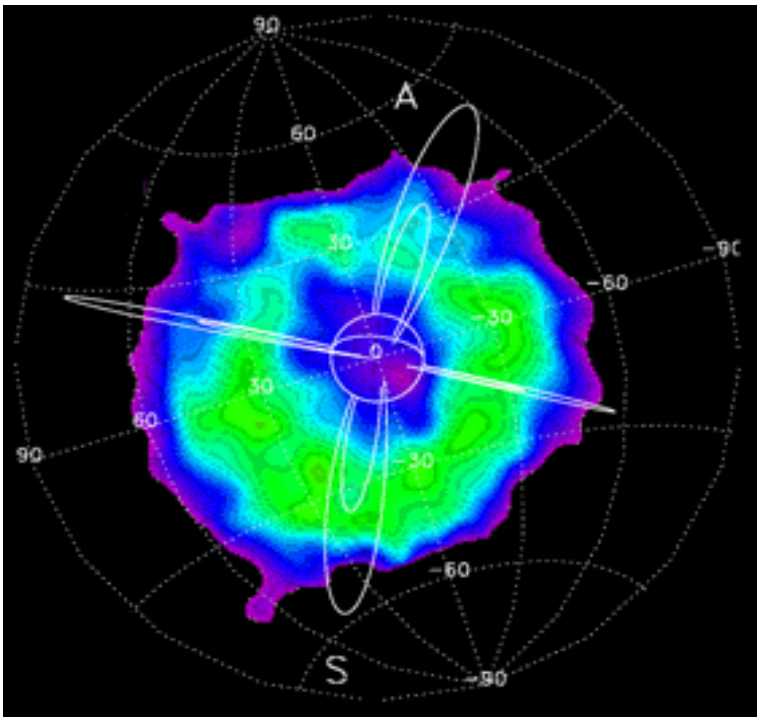

Fig. 2.3 Energetic neutral atom image of Earth's ring current during the recovery phase of a geomagnetic storm. (Rasinkangas, 1998)

As earlier stated, the current generated as a result of atmospheric dynamo is referred to as solar quiet day variation (Sq) current. Stewart and Tait (1865), noted that the solar radiation ionizes the upper atmosphere which then results in the over head currents as a result of the motions of the ionized particles across the magnetic field. The solar quiet day variation and lunar daily variation **(L**) are both as a result of large scale motions of air in the ionosphere. It has long been

noted that the primary sources of energy for the above two are solar heating and lunar tidal force. The next is equatorial electrojet current – this flows along the magnetic dip equator. (This will be discussed fully later).

In more general term, Heelis (2005) discussed currents in ionosphere with reference to low and high latitudes as well as the auroral zone and polar cap. He ascertained that horizontal currents originate in two places: the E-region and the F-region. In low and mid-latitudes, currents are driven by neutral winds and external potential applied at outer boundary. While in auroral zone and polar cap, currents are driven by neutral winds and external applied polarized fields.

Basically, there exist current drivers in the ionosphere, these include; neutral winds, zonal winds meridional winds and electric field-driven currents. Neutral winds are largely horizontal and the currents they drive are carried by ions. Heelis (2005) also noted that zonal winds drive vertical current in the F region and vertical and zonal current in the E region at equatorial latitudes but meridional winds are parallel to the magnetic field and do not contribute to the current.

It was equally noted that for the neutral wind driven currents at mid and high latitudes, that zonal wind drive a meridional currents in the F region and a meridional and zonal current in E-region, while meridional winds that have a component perpendicular to the magnetic field drive a zonal current in the F region and a zonal and meridional current in the E region.

Finally, Heelis (2005), noted that electric field driven current (EFDC) changes dramatically with altitude. In the F region, EFDC are in the direction of the electric field, while in the E region, they are in the direction of the electrical field near the peak in the Pedersen conductivity and in the direction opposite to the vector **E** x **B** near the peak in the Hall conductivity. He also observed that in the F region currents are weakly dependent on local time, only slightly smaller during the nighttime than during the day time. On the other hand, in the **E** region currents are strongly dependent on local time. (largest anywhere during the day).

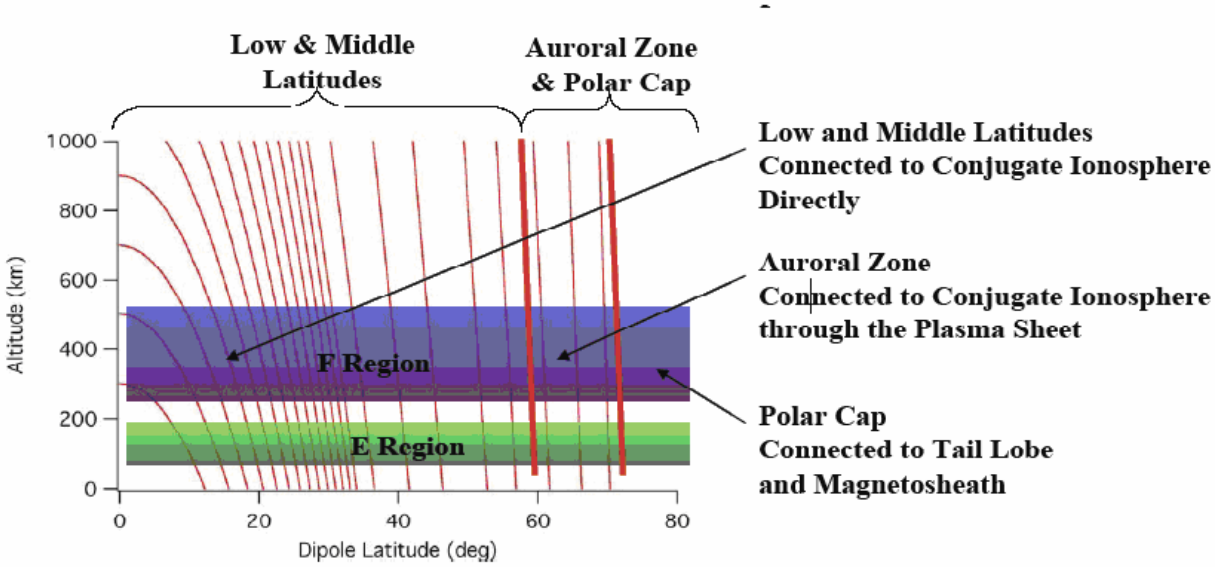

Fig. 2.4 Currents in the Ionospheric regions (Heelis and Dallas, 2005)

3.1 Equatorial electrojet (EEJ)

At the dip equator, where the magnetic dip angle I is equal to zero, the midday eastward polarization field generated by global scale dynamo action gives rise to a downward Hall current. A strong vertical polarization field is set up which opposes the downward flow of current due to presence of non-conducting boundaries. This field in turn gives rise to the intense Hall current which is called the EEJ. The basic reason for the existence of the EEJ is as a result of large value of hall polarization and hence large value of cowling conductivity at the dip equator where the earth's field is horizontal.

It is important to note that Cowling conductivity (σ_3) is the effective conductivity (σ_{yy}) applicable to the eastward equatorial electrojet over the dip equator, subject to the assumption that vertical current does not flow. EEJ stations lie within region of 4^o latitude, N or S of the magnetic equator.

3.2 EEJ conductivity model and altitude

With reference to mobility of electrons and ions, atmosphere is divided into three regions. These include;

(i) Region below 70km, here, collision frequency (f_o) of both ions and electrons are greater than gyro frequency ($f\omega$) of both ions and electrons.

[$f\upsilon_e > f_{we}$ and $f\upsilon_i > f\omega_i$], the implication is that there is no magnetic control, both ions and electrons move with the neutral air.

(ii) In the region, between 70 and 140km, here the collision frequency of ion is greater than the gyro frequency of ion ($f\upsilon_i > f\omega_i$) and collision frequency of electron is less than the gygro frequency for electron ($f\upsilon_e < fw_e$), then ions move with neutral air, but the electrons are controlled by the magnetic field.

Above 140km, in this region, both the collision frequency of ion and that of electron are both less than the gyro-frequency of both. The implication is that the motions are controlled by the magnetic field and collissional effects of the neutral gas are relatively unimportant.

Thus, at the equator, where the electric field during the day is primarily in the eastward direction and the magnetic field is in the northward direction, the electrons within 70 – 140 km drift upwards relative to ions and produce the Hall polarization field which in turn produces additional Hall current in the east direction.

4.0 Summary:

Dynamo, processes (actions) have been reviewed and it is seen that both dynamo action in the earth's core and in the ionosphere are similar. The principle of motor and generator both occur in the ionosphere. Both positive and negative ions are present in the ionosphere. The source of ions is sun's radiation and their movement is due to gravitational source, either by moon or by sun. It is also caused by thermal source – sun. We have the ions moving in the earth's magnetic field, and then current is induced as in dynamo. This current produces changes in the

magnetic field on the surface of the earth. That part of the ionosphere where the current is produced is referred to as atmospheric dynamo.

This current flowing in ionosphere – a conducting medium, is accompanied by an electrostatic field, which reaches other part of the ionosphere and causes current to flow there. This current also produces magnetic variations at the surface of the earth, the flow in turn, causes bodily movement of the atmosphere. This part of the earth is referred to as atmospheric motor. To first approximation the 'dynamo' is situated in E- region and 'motor' in F region, but motor effect is experienced in the dynamo region.

It is seen that current in the ionosphere could come from either external polarization electric fields or internal mechanical drivers. The former is often expressed in terms of direct (or parallel), Pedersen and Hall conductivity. The current drivers in the ionosphere are neutral, zonal and meridional winds, then, the electrical field. The driven current varies with latitudes; currents are weakly dependent on local time in F region, while in E region they are strongly dependent on local time.

EEJ occur because of large value of Hall polarization resulting in large value of Cowling conductivity at the dip equator. EEJ conductivity model reveals that in the first region i.e. below 70km, both ions and electrons move with the neutral air and there is no magnetic control. On the other hand, between 70 and 140km ions moves with neutral air but electrons are controlled by magnetic field. While above 140km, motions of ions and electrons are controlled by the magnetic field and collossional effects of the neutral air seizes to be important. Forbes et al. (2008), found quasi-biennial variations of order ± 10 – 15% in migrating diurnal and semidiurnal tidal amplitudes, still putting to tidal variability in the ionosphere dynamo region. More future research work is still being encouraged so as to still discover more on dynamo processes.

4.1 Conclusion

The ionospheric dynamo has been reviewed; charged particles of the ionosphere across the earth's magnetic field are necessary and very important tools for ionospheric dynamo process.

The tidal effects of sun and moon and solar heating drive the charged particles, in effect, the dynamo action is controlled by mainly the winds and the electrical conductivity.

It has been observed that driven currents by current drivers are latitude dependent. It is clearly evident from this work that dynamo action in the earth interior and that of the ionosphere are similar hence, causes of some changes in the earth interior could be explained from external current and verse versa. We are in a dynamic world not a static one, as such more current and future research on dynamo processes in both earth's interior and upper atmosphere should be intensified. Following the result of Forbe's et al. (2008), more complicated work will still yield new results in this area thereby revealing or unfolding hidden phenomena.

References

Caltel, C.A Mozer, F.S., Hones Jr, E.W. Anderson, E.R. and Sharp, R.D. 1986. ISEE Observations of the plasma sheet boundary, plasma sheet and neutral sheet, I Electric field, magnetic field, plasma and ion composition J., Geophys. Res. 74., p 5664-5679.

Elsasser, W.M. 1939. On the origin of the Earth's Magnetic Field, Phys. Rev. 55, 489, 233.

Forbes, J.M. and Lindzen, R.S. 1976. Atmospheric solar tides and their electrodynamic effects - 1. The global Sq current system, J. atmos. Terr. Phys.. 38, 897-910.

Forbes, J.M, Zhang x, Palo S., Russell, J, Mertens, C.J. and Mlynezak M. 2008. Tidal variability in the ionospheric dynamo region .J. of Geophysis res. 113, A02310, doi, :10.102a12007 JA 012737.

Frank, L.A. 1967. On the extraterrestrial ring current during geomagnetic storms, J. Geophys. Res., 72, 3753-3768.

Hamilton, D.C., Gloeckler, G., I pavich, F.M., Stiidemann, W., Wilken, B and Kremser, G. 1988. Ring current development during the great geomagnetic storm of February 1986, J. Gephys. Res 93, 14343-14355.

Heelis, R.A. 2004: Electrodynamics in the low and middle latitude ionosphere: a tutorial, J. Atmospheric and Territorial Physics, 66, P 825-838.

Heelis R and Dallas, U.T. (2005). Climate and Weather of the Sun-Earth System Conference Proceedings.

Hones Jr. E.W, Asbridge, J.R., Bame, S.J. and Singer 1973. Substorm variations of the magnetotail plasma sheet from XM-GR_e to XXM-60Re, J.Geophys. Res. 78, 109-121.

Junhu, Du and Stening, R.J. 1999. simulating the ionospheric dynamo-1 simulation model and flux tube integrated conductivities. J. of Atmos and solar Terres. Phys. 61,12, 913-923.

Larmor, J., 1919. How Could a rotating body such as the sun become a magnet? Rep. Brit. Assoc., 159, 232, 235.

Lui, A.T.Y., Mankofsky, A., Chang, C.L. Papadopoulos, K and Wu. C.S 1990. A current disruption mechanism in the neutral sheet: A possible trigger for substorm expansion, geophy. Res. Lett., 17, 745-749.

Lyon, L.R. and Schulz, M. 1989. Access of energetic particles to storm time ring current through enhanced radial diffusion, J. Geophys. Res. 94, 5491.

Martin S.F. Bilimoria R. and Tracadas P.W. (1994). Solar surface magnetism ed. R.J. Rutten & C.J.Schrijver (NATO AASI Ser. C, 433; Dordrecht: kluwer), 303.

Maus S. and Luhr H. (2006) A gravity-driven electric current in the earth's ionosphere identified in CHAMP Satellite magnetic measurement. Geophysical Research Letters Vol. 33, L02812, doi:10.1029/2005GL024436.

Matsumoto H. (1981) Beam-Plasma Interaction Experiment in the Magnetosphere by Emitting an Electron Beam from Satellite JIKIKEN (EXOS-B) Journal of Geomagnetism and Geoelectricity Vol. 33. P. 145

Nishida, A., Hayakywa, H and Hoones Jr. F.W., 1981. Observed signature of reconnection in the magnetotail J. Geophys./ resig 86, 1422-1437.

Okeke, F.N. 1999. The magnetospheric substorm of 29 April, 1997. IAJ, 26(1) 23-28.

Onwumechili, C.A. 1997. The equatorial electrojet, Gordon and Breach Science Publishers, Netherlands.

Rasinkangas, R. 1998. Oulu Space Physics Textbook, Publisher: Spaceweb

Roux, A. 1991. Plasma sheet instability related surge J. Geophys. Res. 95 17,669-17,708.

Runcorn, S. K. The earth's core, Trans. Am. Geophys. Union, 35, 49.

Stewart, B. and Tait, M.A. 1865. On the heating of a Disk by Rapid Rotation of Vacuo. Proc. of the Roy. Soc. of Lon. 19, 339-343.

Wikipedia, Contributor 2005: http://en:wikipedia.org/wiki/ring_current"

NIGERIAN JOURNAL OF SPACE RESEARCH **8:** 282 – 317, 2009 September 1

Planetary Ionospheres

Victor U. CHUKWUMA PhD
Department of Physics,
Olabisi Onabanjo University
P. O Box 351, Ago-Iwoye, Nigeria
Email: victorchukwuma@yahoo.com

Table of Contents

1.0. Introduction

In 1957 an international research effort, inspired by the International Polar Years of 1882-83 and 1932-33, was organized as the International Geophysical Year (IGY) to study global phenomena of the Earth and geospace. On the fiftieth anniversary of the International Geophysical Year an international program of scientific collaboration was conducted called the

International Heliophysical Year (IHY). The IHY focused on fundamental global questions of Earth and space science. The IHY involved thousands of scientists from over 70 nations, working at stations from pole to pole to obtain simultaneous, global observations on Earth and in space.

The goals of the IHY were, but not limited, to 1. Develop the basic science of heliophysics through cross-disciplinary studies of universal processes. 2. Determine the response of terrestrial and planetary magnetospheres and atmospheres to external drivers. 3. Promote research on the Sun-heliosphere system outward to the local interstellar medium - the new frontier. 4. Foster international scientific cooperation in the study of heliophysical phenomena now and in the future. 5. Communicate unique IHY results to the scientific community and the general public. The IHY promised to help us develop a deeper understanding of physical processes in the solar system through a program of comparative study of universal processes that affect the interplanetary and terrestrial environment.

Given that the overall objective of the IHY Regional School was to expose the students to the theories and advances in various aspects of heliophysics within the context of IHY. Our lectures on planetary ionosphere will derive from mainly from goal No. 2 as stated above which has come to be regarded as Space weather (Chukwuma, 2007a).

The term “Space weather” refers to conditions on the sun and in the solar wind, magnetosphere, ionosphere, and thermosphere that can influence the performance and reliability of space-borne and ground-based technological systems and can endanger human life or health. Adverse conditions in the space environment can cause disruption of satellite operations, communications, navigation, and electric power distribution grids, leading to a variety of socioeconomic losses (United States of America’s National Space Weather Program Strategic Plan, FCM-P30-1995).

The above-mentioned statement underscores the increasingly worldwide recognition of the importance of “space weather” research which has lead, in recent years, to the intensification of

investigations of geomagnetic storms. The main objective of space weather studies is to understand the solar and interplanetary causes of magnetic storms, and the ionospheric phenomena associated with these magnetic storms.

In terms of Space weather, one remarkable period of events was March 1989. This period was characterized by the great geomagnetic storm of March 13-14 (*Dst* ≈ -600 nT), which is one of the largest geomagnetic storms in the last 50 years. The March 13-14 storm had profound effects on Earth and in space. Power systems in Canada and New Jersey, USA failed as large electric currents were induced in power lines and tripped protective relays (Bolduc, 2002; Cliffswallow, 1993: Czech et al., 1992; Kappenman and Albertson, 1990). Increased atmospheric drag, resulting from the expansion of the Earth's outer atmosphere during the disturbance, altered the orbits of many satellites with the result that NASA lost track of some of them for a short period. Satellite navigation systems failed to operate and High Frequency (HF) communication systems were also out of action (Cliffswallow, 1993). Aurorae were sighted at quite equatorial latitudes. In this regards, investigations into the global ionospheric F2-region response during this geomagnetic disturbances became of considerable interest for the understanding of the morphology of ionospheric storms and solving of practical problems.

Chukwuma (2003a) studied the F2-region global response during this severe storm and showed that the depletion of *foF2* was simultaneously worldwide and extended to 12.4^{o} N. This result appears to imply that during intense storms, variations of *foF2* are characterized by universal time dependence. However the investigation of, another intense storm of lesser magnitude, the October 20-21, 1989 storm(*D st* ≈ -268 nT), showed that the depletion of *foF2* was restricted to the high and middle latitudes, lacked universal time dependence and simultaneity but diminished in amplitude towards the lower latitude (Chukwuma, 2003b).

The results of the aforementioned studies differing as they were required reconciliation which cannot be achieved without an understanding of the ionospheric phenomena; hence our study of the Earth’s ionosphere.

2.0. The ionosphere

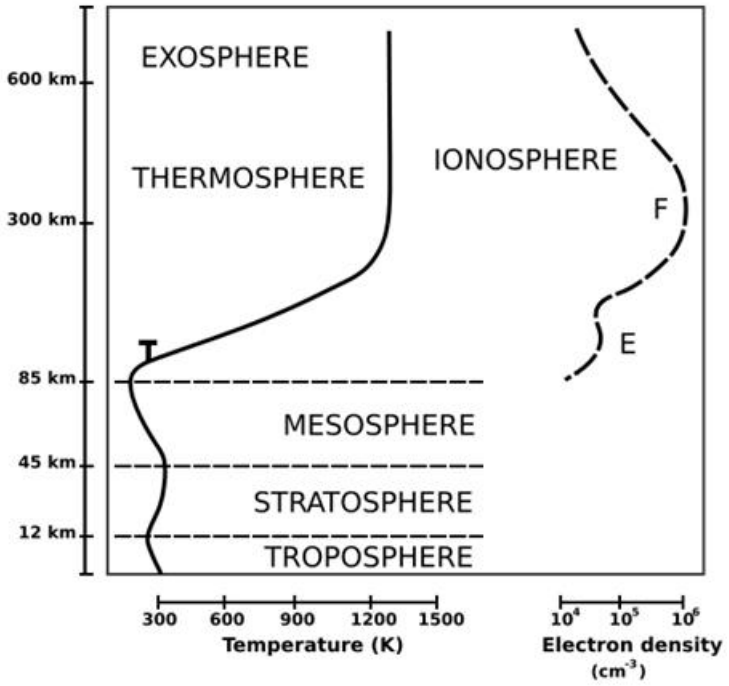

Figure 1. The atmosphere with the ionosphere

The earth's ionosphere is that part of the upper atmosphere in which free electrons exist in concentration which is sufficient to influence the propagation of radio waves. This region of the atmosphere is a major terrestrial sink of solar and magnetospheric events. According to Szuszewicz (1986) the atmosphere is an active element in the solar-terrestrial system, with its spatial distribution of ionospheric conductivity playing feedback roles in affecting magnetospheric plasma transport and the configuration of magnetospheric current systems in addition to being an important source of magnetospheric ions.

The ionosphere, which extends in altitude from about 60 to 600km, is a complex subsystem with intrinsic coupling networks. As a result, ionospheric studies have been divided into phenomena at low, middle and high geomagnetic latitudes where fundamentally different mechanisms can be associated with the degree of magnetic-field coupling to higher altitude

magnetospheric events. At low latitudes, where the geomagnetic field tends to be horizontal, the coupling to the higher altitude magnetosphere is largely through indirect effects (wind systems, electrojets current, electric fields etc). While at high latitudes the more vertical magnetic field promotes strong magnetospheric coupling and direct access of magnetic particles (Szuszczewicz, 1986).

The ionospheric regions are produced by solar extreme ultra violet (EUV) and X rays emitted as spectral lines and continuum radiation. According to Rishbeth (1989) the level in the ionosphere to which any wavelength λ penetrates depends on its absorption cross-section (or its 'hardness') and the gases it can ionize are those for which λ is shorter than the ionization limit (80nm for N_2, 91nm for O and H, 103nm for O_2 and 134nm for NO).

The free electrons in the ionosphere are known to have peak concentration at about the following altitudes; 110, 170, and 250km and are classified into the daytime into E, F1 and F2 region respectively. It must be pointed out that at night, the F1 region disappears resulting in a single F region, which lies above the E region. Also during the day, there exists another layer, which is below the E region. This region called the D region is below about 90km of altitude and has its peak electron density near 80km.

The ionosphere is of practical importance because of its role in radio communications. The ordinary wave critical frequency f_c of an Ionospheric layer is related to its peak density N_m by (Jaeger, 1947):

$$f_c^2 = \frac{N_{max} e^2}{4\pi^2 m} \tag{1.1}$$

There is also a slightly higher extraordinary wave critical frequency f_x, because of the double refraction of radio waves resulting from the earth's magnetic field. For simple Chapman layer in which electrons are produced according to the production function(Jaeger,1947; Rishbeth, 1989):

$$q = q_o \exp(1 - Z - e^{-z} \sec\chi)$$

and recombine according to the loss term

$$L(N) = \alpha N^2 \tag{1.2}$$

where α is the square –law loss coefficient, the critical frequency depends on solar zenith angle χ and mean sunspot number R, according to the formula (Rishbeth, 1989)

$$f_o = A(1 + aR)(\cos\chi)^n, n = 0.25 \tag{1.3}$$

where A and a are constants. It must be pointed out that because of complications like the variation of scale height H with height, and the effect of vertical drifts, the index n actually varies between about 0.2 and 0.35. Given that the solar flux that is incident on the ionosphere varies with the solar cycle, f_o therefore varies regularly with sunspot number.

The ionization of the ionosphere is important scientifically because charged particles are easier to detect experimentally than neutral gases, and thus act as useful tracers for studying the upper atmosphere. But despite its importance, the ionization of the ionosphere is a minor constituent of the upper atmosphere. Even in the main layers of the ionosphere less than 1% of the air is ionized.

The ionosphere as we know it has all along been divided into distinct layers with a specific ionization process responsible for each layer. But according to Bates (1974) when ionization is calculated as a function of altitude the results show that:

(i) The ionization rate profile passes through a single maximum at about 115km, where its value is great as $10^4 cm^{-3} sec^{-1}$.

(ii) Though ionization of all constituents by X radiation is very significant near the E-region, it is less important than photo- and pre-ionization of molecular oxygen by EUV radiation.

(iii) If only Lyman continuum contributed to ionization the maximum rate of photoionisation of atomic oxygen would occur at about 130km. Taking the solar emission lines into account raises the maximum to about 140km, which is still below F1 layer.

2.1 The D region

The D region of the ionosphere, which lies in the altitude range 60 to 90km, has a rather complicated structure caused by the existence of different ionizing sources. The dominant sources of ionization in the D region are the Lyman α (121.6nm), the 3.0 - 4.0nm and 0.1-0.8nm X- rays and galactic cosmic rays (Gnanalingam, 1974; Ratnasiri, 1977; Rishbeth, 1989). The Lyman α radiation ionizes NO and is the dominant source of electrons in the altitude range 70 to 80km, also the 3.0-4.0nm radiations ionizes O_2 and N_2 and exceeds by a factor of 2 the ionization produced by other radiations in the altitude range 88-94km at solar zenith angle less 30^o, while the 0.1-0.8nm radiations produces a broad maximum of ionization at altitudes less than 95km, the actual altitude depending upon the hardness of the spectrum (Gnanalingam , 1974; Rishbeth , 1989). The galactic cosmic rays are most important below about 62km , however, under quiet conditions 0.1-1.0nm radiations are only a minor source of ionization with the production function vanishing completely below about 70km, though under disturbed condition, their ionization could dominate the entire D region with values sometimes increasing by more than 100 fold (Ratnasri, 1977).

The free electrons produced in the D region ionization process are predominantly lost through one or more of the following process (Tarkar and Friedrich ,1988) : (i) Recombination with primary molecular ions such as O_2^+ or NO^+. These processes have only weak temperature dependence ($T^{-0.5}$), (ii) Recombination with heavier, mostly water cluster ions, which are formed by ion-chemical reactions of the primary ions with neutral atmospheric constituents. These ions then recombine with electrons faster than the primarily formed ions. The clustering process is strongly dependent on temperature (T^{-3} to T^{-5}) and on the concentration of minor species, mainly atomic oxygen, but also to a lesser extent on H_2O, NO, O_3 and CO_2 (iii)

Attachment to neutrals thus forming negative ions. This process is efficiently impeded by the presence of atomic oxygen and through photo-detachment by visible sunlight.

At altitudes below about 80km the presence or absence of negative ions constitutes a clear-cut difference between night and day times. The day/night variation of the concentration of atomic oxygen, which is most pronounced in the lower D-region, exerts an indirect influence on the recombination coefficient, because atomic oxygen breaks up H_2O clusters and inhibits the formation of negative ions (Tarkar and Friedrich, 1988).

It must be pointed out that in the D region the ratio of primary to cluster ion concentration increases when ion production is high as against the rate of clustering reactions. Also the concentration ratio of the primarily produced ions ($[NO^+] / [O_2^+]$) mainly depends on the type of the ionizing radiation, though according to Tarkar and Friedrich(1988) this has only a slight influence on the nature and behaviour of the secondary ions.

Direct measurements of the properties are scarce, only few rocket measurements have been carried out in Peru and India. Studies have shown that the D region electron density is the result of equilibrium between ion production rate and effective electron loss. Furthermore, according to Tarkar and Friedrich (1988) time dependence or transport phenomena only have to be considered at high altitudes or for fast temporal variations of production, as for example, encountered at sunset or sunrise, solar eclipse or fast varying fluxes of precipitating energetic charged particles.

Now using data from daytime rocket experiments conducted at Thumba during the period 1966 to 1978 Oyinloye (1989) has shown that electron density in the D region increases gradually from about 10 per cc at 60km to about 250 per cc at 70km and having a value of about 500-600 per cc in the altitude range 75-85km. There is a sharp increase in slope at about 82km, beyond which the electron density increases rapidly with altitude attaining a value of about 1.0×10^4 per cc at about 90km. Oyinloye (1989) has also shown that negative ions could be significantly larger in number than electrons at altitudes below about 75km. Furthermore, there is a diurnal

asymmetry in electron density between the heights of 85km and 100km. As such, a larger change in electron density is observed between $\chi = 50^o$ and 28^o (in the morning) than between $\chi = 28^o$ and 48^o (in the afternoon) below 100km. Also there is the solar control of the region of higher values of electron density at low values of χ for the height ranges 70-80km.

X -rays increase from sunspot minimum to sunspot maximum while Lyman α is nearly constant with solar activity. NO increases with solar activity while galactic cosmic rays decrease with solar activity. In effect, electron density is expected to increase with solar activity in the upper D region and decrease with increasing solar activity in the lower D region, the solar activity reversal in electron density being below about 70km. Also below about 70km there is a gradual loss of solar activity in the diurnal variations of electron density (Mitra and Rowe, 1974).

The D region plays an important part in LF/VLF propagation (Rishbeth, 1989). The attachment of electron to form negative ions at sunset and their detachment at sunrise, cause marked changes of LF/VLF reflection heights. At MF and HF the D region is important because of its probable radio wave absorption, which arises from the relatively high neutral density and consequent collision frequency between electrons and neutral molecules. D region absorption is known to show a fairly regular dependence of D region ionization on Cos χ. Also there is a diurnal asymmetry in the D region absorption such that for a given value of χ the radio wave absorption is greater in the afternoon than in the morning. Seasonal variation in the equatorial D region is semi-annual with equinoctial peaks and there are usually low values of absorption in the period May-August.

2.2 The E region

The E region of the earth's atmosphere occupies the altitude range of about 90-150km and is produced by different ionizing sources. According to Rastogi (1993) the E region is controlled by solar radiation flux. The principal radiations that produce the E region are the EUV 91-93nm

(Lyman β 102.6mm) and X- ray 1-17nm. The Lyman β radiation ionizes O_2, the peak ion-pair production occurring at 103km for overhead sun, while the 4.0-10.1nm radiation ionizes O_2 and N_2 substantially above 95km (Gnanalingam 1974).

The atmosphere in the E region is more rarefied than that of the D region, and only two- body collisions occur, so atomic ions cannot recombine easily (Rishbeth (1989). The overall result is that the positive ions are mostly molecular O_2^+ and NO^+. Some metal atoms (Fe, Mg, Ca) traces of which are deposited in the atmosphere by meteors become charged, giving long lived ions that are the main ionic component of mid latitude sporadic E layers.

The normal E region shows slight departures from idealized Chapman layer behaviour owing to complications such as the scale height gradient $\partial H/\partial h$ and drifts due to tidal electric fields (Rishbeth , 1989). Also in the lower E region, the shape of the electron density profile is largely controlled by the optical depth (Monroe et al, 1976).

The E region of the ionosphere exhibits asymmetries of electron density about local noon. Appleton (1953) discussed the differences in the time between the maximum ionization in the E region and the maximum production in terms of the sluggish of the ionosphere. According to Appleton et al. (1955), under quasi-stationary conditions such as are believed to obtain in the E layer, the maximum electron density N_m obeys the equation

$$\frac{dN_m}{dt} = q_0 Cos\,[\chi(1 - a^2)] - \alpha N_m^2 \qquad (1.4)$$

where a^2 is a quantity which can be estimated, but which is usually negligible compared with unity except where χ is large.

To Appleton et al (1955) an approximate solution of Eq (1.4) with "a" neglected suffices to express the theoretical variation of N_m over the central part of the day. This solution shows that N_m should generally be greater in the afternoon than in the morning. Also, the maximum of N_m should occur shortly after noon. Methods of determining α_{eff} the effective value of the

recombination coefficient can be based on each of these two effects (Appleton, 1937; 1953). In the first method, Appleton et al (1955) compared the value of N_m for similar values of χ before and after noon. The value of α_{eff} is then given by

$$\alpha_{eff} = \frac{\left|\frac{dN_m}{dt}\right|}{(\Delta N_m)} \cdot N_m \qquad (1.5)$$

Where $|d N_m /dt|$ and N_m are the numerical averages of forenoon and postnoon values, and ΔN_m is the amount by which the postnoon value of N_m exceeds the corresponding forenoon value. In the second method, Appleton et al (1955) used the theoretical relation expressing the delay (Δt) of the N_m maximum relative to noon. This is

$$\Delta t = \frac{1}{2\alpha_{eff} N_m} \qquad (1.6)$$

Now if the simple Chapman theory were applicable to the E layer it would be expected that α_{eff} as determined by (1.5) and (1.6) will be constant under all conditions. However, the result of the examination of a great wealth of diurnal data in relation to (1.5) and (1.6) leads to significant disagreement between experiment and theory, if α_{eff} is assumed constant. Indeed, estimates of the values of α_{eff} using (1.5) and (1.6) reveal relatively enormous variations of the quantity (Appleton et al, 1955). Given that it is clear (Appleton, 1953) that the value of the natural recombination coefficient α would not possibly vary by the amounts by which they found α_{eff} to exhibit, Appleton et al (1955) came to believe that the non-constancy of α_{eff} is an expression of the existence of some form of perturbation resulting from electron transport and thereby the continuity equation in the form

$$\frac{\partial N}{\partial t} = q(t) - \alpha N^2 - div(Nv) \qquad (1.7)$$

where ν is the velocity of electron transport.

To Appleton et al (1955), if electron transport occurs in the form of vertical drift, as suggested by Martyn (1947; 1949), it is possible to calculate theoretically (Appleton and Lyon, 1955) how

the height of maximum ionization, and the value of maximum ionization itself are altered under E region conditions.

Baker and Martyn (1953) had shown that in a given region of the ionosphere, the vertical drift of ionization depends entirely on the east-west current in that region. Now the east-west current is always small near the Sq current focus (say between latitude 25^o and 40^o) but at higher and lower latitudes it becomes large near noon, with opposite directions of flow.

In the light of the above Appleton et al (1955) reasoned that the perturbation due to the transport term in (1.7) must be small near Sq current focus. In harmony with this, they found that applications of (1.5) leads to sensibly constant values of α_{eff} over a considerably range of χ. In other words, the diurnal variation of E layer ionization appears to be most nearly Chapman-like near the Sq current focus where the vertical drift is a minimum.

In contrast Appleton and Lyon (1961) found that at Slough α_{eff} increases steadily from $2x10^{-9}cm^3s^{-1}$ near noon to about $8x10^{-8}cm^3s^{-1}$ near twilight instead of the value of $1.0x10^{-8}cm^3s^{-1}$ obtained by Appleton et al (1955), and attributed this result to the transport term of (1.7) having a perturbing effect, the phase of which is such that α_{eff} is raised in the morning and lowered in the afternoon.

It must be noted that while many attempts have been made to calculate the recombination rates using sluggishness of the ionosphere, it became apparent with modern laboratory measurements that the time constants were too small to account for the effect. Also the explanation of the phase differences must lie elsewhere (Monro et al, 1976). This position is strengthened by the studies using St. Santin incoherent scatter radar.

Monro et al (1976) in one such study investigated the behaviour of electron densities in the E region under the effect of tidal pressure changes and deduced that in direct conflict with what had been inferred from ionograms, electron density is greater in the morning than at the corresponding time in the afternoon. Also, Monro et al (1976) showed that the large differences

in the electron density at fixed altitudes between morning and afternoon are produced by tidal temperature and density changes in the neutral atmosphere. Senior et al (1981) went ahead to confirm the electron density asymmetry in the E region observed by Monro et al (1976) using measurements of the integrated Hall conductivity through E region, and suggested that electron density asymmetry is a nitric oxide effect. In their work, Senior et al (1981) recalled that Atmospheric Explorer measurements by Stewart and Cravens have shown that n [NO] in the lower E region increases throughout the greater part of day and by a factor of 2 at the equator. Senior et al (1981) pointed out that the resultant of this is that the charge transfer

$$O_2^+ + NO \rightarrow O_2 + NO^+ \qquad (1.8)$$

makes the concentration ratio of the primary produced ion ($[NO^+]$) / ($[O_2^+]$) to increase and hence the effective recombination (Bates, 1988)

$$\alpha_{eff} = \frac{1}{n_e\{n[O_2^+]\alpha(O_2^+) + n[N_2^+]\alpha(N_2^+) + n[NO^+]\alpha(NO^+)\}} \qquad (1.9)$$

also increases. Senior et al (1981) also estimated that the increase in α_{eff} causes electron density to decrease by about 10%. Also in confirmation of the work of Monro et al (1976), Gerard and Taieb (1986) have found that the morning values of electron density usually exceed the afternoon values by between 3% and 20%. According to Bates (1988) the asymmetry factor may indeed exceed that which would occur if there were only O_2^+ ions in the morning and only NO^+ ions in the afternoon showing that an effect other than the nitric oxide effect enters. It is important to note that the use of integrated conductivity by Senior et al (1981) is justified because integrated conductivity is proportional to maximum electron density in the E region (Rastogi, 1993).

The E region is probed with rockets, ground -based radar and HF sounding systems This situation has resulted as in the case of D region, in geographically localized studies of the E region, which are deficient in information on longitudinal and latitudinal variations greater than

ten to hundreds of kilometre. While not considered of major importance when viewed from a perspective of total electron content, it should be understood according to Szszczewicz (1986) that the E region can play an active interchange role with a number of F region irregularity processes and must be reckoned with in the development of any comprehensive model attempting to treat or predict ionospheric plasma distributions and transport. It is important to note that E region irregularities: sporadic E and equatorial electrojet, have a larger geomagnetic distribution than the corresponding F region irregularity morphology. It should also be recognised that an undisturbed E region is generally considered to exist only in daytime middle latitude and equatorial region.

2.3 The F region

The F region of the ionosphere lies on top of the E region at the height of about 140km and stretches into the exosphere. During the day, the electron density versus height profile for the F region shows a subsidiary bulge below the maximum of electron density. This is known as the F1 layer and it may occasionally attain an actual maximum (Budden, 1966). The main maximum above this F1 maximum is known as the F2 layer. According to Bradbury (1938) F1 and F2 layers have the same ionizing source with an upward-decreasing loss coefficient. According to Budden (1966), the Bradbury hypothesis proposes that the maximum ionization in the F2 layer results, not from a fast rate of production, but because of a slow rate of removal of electrons. To Budden, the formation of the whole F layer can be explained by a single ionizing agency which would form a single layer like a Chapman layer if the attachment coefficient were constant at all heights.

The dominant ionizing agency in the F1 layer is EUV17-80nm. According to Rishbeth (1989), there is no ionizing photon radiation that is strongly absorbed above the F1 layer. Hence the F1 and F2 layers must be formed by the same radiation and the greater electron density of the F2 layer is due to a smaller rate of loss of electron.

The major gases are ionized by EUV 17-80nm photons of the solar radiations giving predominately NO^+ and O_2^+ in the F1 layer and O^+ in the F2 layer plus electrons:

$$O + h\nu \rightarrow O^+ + e^- \quad (1.10)$$

$$N_2 + h\nu \rightarrow N_2^+ + e^- \quad (1.11)$$

Also ions collide with neutrals and undergo transfer reactions:

$$O^+ + O_2 \rightarrow O_2^+ + O \quad (1.12)$$

$$O^+ + N_2 \rightarrow NO^+ + N \quad (1.13)$$

$$N_2^+ + O \rightarrow NO^+ + N \quad (1.14)$$

The ions recombine with electrons and dissociate:

$$NO^+ + e^- \rightarrow N + O \quad (1.15)$$

$$O_2^+ + e^- \rightarrow O + O \quad (1.16)$$

$$N_2^+ + e^- \rightarrow N + N \quad (1.17)$$

The atoms produced in these recombination reactions are mostly in excited states. The excess energy is either lost in collision or is radiated as ultraviolet, visible or infrared airglow.

This scheme according to Rishbeth (1989) accounts for the otherwise puzzling facts:

(a) Despite the abundance of neutral N_2, there are very few N_2^+ ions; they are rapidly destroyed by reaction (1.14) as well as (1.17)

(b) NO^+ ions are very abundant although neutral NO is very scarce; NO^+ is being rapidly formed by reactions (1.13) and (1.14)

(c) Below about 200km, molecular ions dominate; this is because the O^+ are rapidly converted to NO^+ and O^+ by the relatively abundant N_2 and O_2

(d) Above about 200km, the relatively scarcity of N_2 and O_2 makes reactions (1.12) and (1.13) very slow. Once formed, however, the NO^+ and O_2^+ ions rapidly recombine with electrons by reactions (1.15) and (1.16). As a result O^+ is the dominant ion.

(e) The loss term L(N) in the continuity equation

$$\frac{\partial N}{\partial t} = q - L(N) - div\,(Nv) \tag{1.18}$$

takes the form αN^2 at heights where NO^+ and O^+ dominate, that is the F1 layer

(f) The loss term takes the form βN in the F2 layer where O^+ dominates

(g) The F1 layer, at the transition between (e) and (f) is seen as a distinct feature with its own critical frequency under certain circumstances (mainly summer and at sunspot minimum) but not at other times (eg winter)

(h) Above the F1 layer, the electron density increases upwards. This is because the loss coefficient β (which depends on N_2 and O_2 concentration) decreases upwards faster than the production rate q (which is proportional to O concentration)

It must be noted that whether or not F1 layer appears as a distinct layer depends on the ratio G which is evaluated and defined as

$$G = \frac{\beta^2}{\alpha q} \tag{1.19}$$

where β and α are attachment and recombination coefficients respectively. For the F1 layer, the effective square-law loss coefficient ($L=\alpha N^2$) is a combination of the values of α for the molecular ion present. The F1 layer is more prominent when G is large in summer (when β is large) and at sunspot minimum when q is small.

The F1 layer behaves like a Chapman layer and its distinctness depends on the shape of the F2 layer. It is important to note that the extra stratification of the F1 layer during a solar eclipse is largely due to the increase of the production function q and consequent increase of the ratio G.

In the F2 layer, the linear loss coefficient is given by

$$\beta = k \;\; n[O_2] + k'' n[N_2] \qquad (1.20)$$

where $k^{/}$ and $k^{//}$ are the rate coefficients in (1.12) and (1.13) respectively. The F2 layer does not vary regularly with cosχ, and shows many features that differ from those of a purely solar - controlled ionospheric layer (Rishbeth, 1989). Also the shape of the day/night variations of N_mF2 and h_mF2 is largely due to neutral air winds and, to a lesser extent, electric fields. De Franceschi et al (1993) confirmed this from the analysis of the planetary scale of the virtual height of the F layer. Also, the virtual height of the F layer is more sensitive to thermodynamic effects than to electrodynamic ones as is emphasised by the fact that seasonal variation is more pronounced for $h^{/}F$ than for geomagnetic records (De Franceshi et al ,1993).

In the F2 layer around sunset, the meridional component of the neutral wind changes equatorward to pole-ward and the resulting F2 layer drift changes from downward to upward. To Rishbeth (1989), this is a probable cause of the commonly observed N_mF2 in the late evening. Also the common predawn decrease of N_mF2 is probably connected to the poleward-to-equatorward wind reversal around that time.

At night, the F2 layer is maintained by:

(a) being raised by wind to height where the loss coefficient β is small

(b) inflow from the protonosphere

(c) EUV fluxes from the night sky

(d) energetic particles

The monthly mean noon critical frequency of the F2 layer exhibits anomalous seasonal variation which is attributed to the changes of the O/N_2 density ratio of the neutral air, which are an indirect consequence of the global circulation in the thermosphere, and which affect the loss coefficient β and to some extent the production rate q. According to Rishbeth (1989), there is also an annual variation, (which is largely due to the fact that the variation of the earth-sun distance modulates the flux of ionizing radiation), and a less well explained semi- annual variation, which is most pronounced in the southern hemisphere.

Beginning from F1 layer, the F region electron density increases according to the ratio q/β. Now this increase will stop in the F2 layer when gravity eventually controls the ion distribution. The F2 layer peak will therefore occur at the height where chemical control gives way to gravitational or diffusive control. According to Rishbeth (1989), at the F2 peak, the transport term in (1.18) is comparable to the production and loss terms respectively. Introducing the diffusion coefficient D for ions in Eq(1.18), at the F2 peak the following relations hold:

$$\beta_m \approx \frac{D_m}{H^2} \tag{1.21}$$

$$N_m \approx \frac{q_m}{\beta_m} \propto \frac{I_o n[O]}{(k' n[O_2] + k'' n[N_2])} \tag{1.22}$$

where the suffix ‘m’ denotes values at the peak height h_mF2 and the transport term in (1.18) has been simplified by omitting horizontal motion which has little contribution and including only the vertical drift velocity W in which case:

$$div(Nv) = \frac{\partial (NW)}{\partial h} \tag{1.23}$$

Thus N_m will depend on the atomic/molecular ratio of the neutral air. The height h_mF2, which is defined by (1.21), tends to lie at fixed pressure level in the upper atmosphere.

It is important to note that the height of the F2 peak is shifted by neutral air wind or electric field. A horizontal wind, which blows toward the equator, drives up the ionization up magnetic

lines, and raises the F2 peak, and increases the maximum electron density N_m. Opposite effects are produced by horizontal wind blowing towards the pole. Winds blowing towards the pole tend to occur at night while equatorial winds blow by the day.

3.0 Collision processes in the ionosphere

The determination of absorption suffered by radio waves transmitted through or reflected by the ionosphere requires the knowledge of electron collision frequency. A good knowledge of the electron collision frequency profile in the ionosphere is also important for specifying the conditions for radio wave propagation as well as understanding the geophysical phenomena in the ionosphere. For example in the middle ionosphere, the collision frequency between electrons and neutral molecules ν_{en} and the collision frequency between the electrons and ions $\nu_{ei,}$ which are the basic components of the effective collision frequency ν_{eff} are comparable, and as such neither of which can be neglected a' priori in the theoretical calculation of HF absorption (Serafimova and Serafimov, 1987).

The electron collision frequency in the ionosphere depends on the electron velocity distribution and collisions with both neutral molecules and ions. As an example, consider a set of charged particles $a_{i(i=1..n)}$,which have a Maxwellian velocity distribution and moving together in the x-direction with a bulk velocity ν_{ai}. Consider also another set of charged particles b_i, also with Maxwellian velocity distribution moving along the x-direction with a bulk velocity ν_{bi}. Now let there be a head-on collision between the particles of the two groups in which the transfer of bulk momentum is in the x-direction. For such a situation, a particle a_i would gain momentum:

$$2m_{ai}\, m_{bi}\, (\nu_{bi} - \nu_{ai}) / (m_{ai} + m_{bi})$$

and if it makes on the average ν_{aibi} head-on collision in unit time, it would gain momentum at an average rate:

$$F = \nu_{aibi}\, [2m_{ai}\, m_{bi}, / m_{ai} + m_{bi}]\, (\nu_{bi} - \nu_{ai}) \qquad (1.24)$$

However, the collisions are not actually all head-on and we can describe the average rate of change of momentum in terms of (1.24), and then ν_{aibi} is called the collision frequency for momentum transfer. If the particles a_i are electrons, b_i could be neutral molecules or ions. The magnitude of ν_{aibi} under any particular situation is either calculated theoretically or obtained experimentally. Experimentally determined values of collision frequency obtained by radio methods using the Appleton-Hartree magneto-ionic theory are referred to as the effective collision frequency ν_{eff}. This effective collision frequency is different from that of kinetic theory (Serafimov at al, 1985). It must be noted that the Appleton formula assumes mono-energetic electron and a collision frequency independent of velocity. This is not true because the probability of collision varies considerably with the velocity of the colliding electrons and depends upon the nature of the colliding molecule or ion (Phelps and Pack, 1959).

Examples of experimentally obtained collision frequency exist in literature. Baulch and Butcher (1985) determined collision frequency in the atmosphere by measuring differences in amplitude and group path of two closely spaced CW double-sided modulated signal which is reflected obliquely. Their method allowed collision frequency to be determined on a continuous basis. They found ν_{eff} to be about 1 - $5x10^4 s^{-1}$ for the E region and ~ $10^3 s^{-1}$ for the F region, and that daytime value of ν_{eff} increases towards midday while nighttime value of ν_{eff} decreases towards midnight. Also Newbury et al (1989) obtained collision frequency profiles from a method which inverts swept-frequency A1 absorption data mode on frequencies between 2.4MHz and 4.6MHz at intervals of 0.2MHz. In their procedure, the ionosphere was divided into a number of slabs, each with a mean collision frequency. The following set of equations describes the reflection coefficients for the frequencies at the top of the slabs:

$$-\ln\rho_n = 2A_D/(\omega_n \pm \omega) + (1/c)\sum \nu_n \int (\mu' - \mu)/1 + g)\, dh \qquad (1.25)$$

where A_D is absorption due to D region, μ' is the group refractive index, μ is the phase refractive index, and g is a function dependent on the same parameters as μ' and μ; ν is mean collision frequency. The results of Newbury et al (1989) show an overall decrease in collision frequency

with height, as well as an overall exponential variation of collision frequency profile in the F region. Also they indicate a smooth transition in collision frequency from the E region to the F2 region.

Several theoretical expressions of collision frequency exist in literature. These formulae are based on different assumptions of the electron-energy distribution and on how the electron collision frequency varies with velocity. The collision frequency in the generalized magneto-ionic theory by Sen and Wyller (1960) is adequate in that the range of electron energies in the ionosphere is taken into account. A Maxwellian electron distribution is assumed and we describe the variation of collision frequency by the law

$$\nu(g) = \nu \, . \, (g/g)^r \qquad (1.26)$$

where g is a measure of velocity; g corresponds to an averaged thermal velocity and ν is the transport collision frequency. The Sen and Wyller (1960) dispersion equation uses r=2 in agreement with laboratory experiments with electrons colliding with O_2 and N_2.

The collision frequency $\nu(g)$, averaged over the Maxwellian velocity distribution is given by:

$$\nu(g) = (5/2)\nu_m \qquad (1.27)$$

where ν_m is the electron collision frequency associated with the most probable velocity v_m and is given by Newbury et al (1989) as

$$\nu_m = n v_m q_D(v_m) \qquad (1.28)$$

where n is the concentration of the gas; and q_D is the momentum transfer cross section. Newbury et al (1989) have observed that in the Appleton-Hartree formula, it is not possible to use a single effective collision frequency ν_{eff}, across the entire radio frequency band. However, we do have the following approximations

$$\nu_{eff} = 1.5\,\nu_m \qquad \nu > \omega \qquad (1.29)$$
$$\nu_{eff} = 2.5\,\nu_m \qquad \nu < \omega$$

where ω is the angular frequency of the exploring wave. These approximations give

$$\nu_{eff} = 3/5\ \nu(g) \qquad \nu > \omega \qquad (1.30)$$

$$\nu_{eff} = \nu(g) \qquad \nu < \omega$$

In the lower ionosphere, up to at least, the E peak, collisions between electrons and neutrals mainly determine the collision frequency. In this regard Itakawa (1971) has given the most general theoretical derivative of collision frequency between electrons and neutral molecules as:

$$\nu_{en} = (4/3)n(8kTe/\pi m_e)^{1/2}Q_D \qquad (1.31)$$

where

$$Q_D = (m_e/2kTe)^3 \int v^5 q_D(v)\exp(-m_e v^2/2kTe)\, dv \qquad (1.32)$$

Banks (1966) has also derived Eq (1.31) as a measure of collisional effects in the energy transfer for thermal equilibrium. ν_{en} depends on variation of q_D with v.

Gregory and Manson (1969) gave the relation between gas pressure and the collision frequency for electron collision with neutrals, ν_{en} as

$$\nu_{en} = 6.4x10^5P \qquad (1.33)$$

where P is in millibars. While Serafimov et al (1985) gave it as

$$\nu_{en} = k\ .\ P \qquad (1.34)$$

where $k = (6.7 \pm 0.4) \times 10^5 s^{-1}/Pa$. According to Serafimov et al (1985) this value is recommended for future use in IRI.

Above the E peak the probability of electron-neutral collision decrease exponentially with height as:

$$\nu\ \alpha\ \exp - (z - z_o)/H$$

while electron-ion collision increase with height. With increasing altitude electron-ion collision begins to dominate. Considering collisions between electrons and ions in a similar way to electron-neutral collisions, Banks (1966) and Itakawa (1971) obtained

$$\nu_{ei} = (4/3)(2\pi)^{1/2}N_i\ (e^4 \ln\wedge)/(kTe)^{3/2}m^{1/2}_e \qquad (1.35)$$

where $\ln\wedge$ is the Coulomb logarithm. $\wedge$ according to Serafimov et al (1986) is given by:

$$\wedge = k^{3/2}/1.78z.e^3(T/\pi n_e)^{1/2}(T_i/zT_e + T_i)^{1/2} \quad (1.36)$$

where m and e are the mass and electron charge respectively. $N_i = N_e$ is the ion concentration and N_e the electron density, and T_e and T_i are the ion and electron temperatures respectively. z is the residual charge.

But Thrane and Piggot (1966) gave the electron-ion collision frequency as:

$$\nu_{ei} = [30+3.6\ln\{Te(Ti/N_i)^{1/2}\}] N_i T_e^{-3/2} \quad (1.37)$$

The value of Te and Ti are given by the International Reference Ionosphere (IRI) .

The collisions between other ionospheric constituents are equally important. The collision frequencies can also be computed using the expression given by Banks (1966) and taking into account the predominant ions present at each altitude.

From the base of E region up to 130km the predominant ions are O_2^+ and NO^+. Given that they have nearly the same frequency with neutral molecules, Dahau et al (1987) proposed a pseudo-ion with an ion mass of 31a.m.u corresponding to a mixture of 75% NO^+ and 25% O_2^+,(Brekke and Moen.1993), as being representative for the E region, and gave the expression for the collision frequency of this pseudo-ion as:

$$\nu_{31}^+ = [8.3n(O_2) + 9n(N_2) + 7.6n(O)] \times 10^{-8}s^{-1} \quad (1.38)$$

Above 170km, O^+ is the only major ion; its collision frequency with neutrals ν_o^+ is (Dahau et al, 1987):

$$\nu_o^+ = [n(O_2) + 1.1(N_2) + 1.9n(O)] \times (T_n/1000)^{0.3}]\times 10^{-9}s^{-1} \quad (1.39)$$

Owing to the quasi-neutrality condition, the concentration of this ion is equal to the electron number density, N_e. Between 130 and 170nm the density of O^+ is of the same order as that of O_2^+, and NO^+, and can be determined from N_e by taking into account the relation (Oliver, 1975):

$$p = n(O^+)/ N_e. \quad (1.39a)$$

and the quasi-neutrality condition, through the equation (Dahau et al, 1987)

$$n(O^+) = (1 - P)\, N_e. \qquad (1.39b)$$

Finally, the electron collision frequency is given in terms of the concentration of the neutrals and electron temperature as

$$\nu_e = [0.2n(N_2)(1-0.00012\, T_e)T_e + 1.8n(O_2) + (1 + 0.036\, T_e^{1/2})\, T_e^{1/2} + 2.8n(O)\, T_e^{1/2}\ ] \times 10^{-10} s^{-1} \qquad (1.40)$$

Values of the electron temperature could be determined by equating

T_e to T_i or using measured values of the electron concentration N_e

and the empirical relationship between T_e and N_e given by Brace and Theis (1978; 1981; 1984), Bailey et al (1987) and IRI 90.

Newbury et al (1989) compared experimental results with theoretical calculations of collision frequency based on Itakawa (1971) theoretical expression and found a large discrepancy between experimental and theoretical values. This discrepancy is considered with previous comparison between radio measurements of effective collision frequency and calculated values using expected ν_e and ν_{ei} (Thrane and Piggot, 1966; Baulch and Butcher, 1988).

Finally, it is important to note that ν_{ei} has solar-cycle , seasonal and diurnal variations because of its dependence on T_e, T_i, and N_i while ν_{en} depends only on month and latitude because it is mainly pressure dependent.

4.0. Electrical Conductivity of the Ionosphere

4.1 Preamble

Ionospheric electrical conductivities are important parameters in ionospheric electrodynamics and magnetosphere-ionosphere coupling. Under many circumstances (eg when dealing with field aligned current closure by Perdersen current or Ohmic energy dissipation or ground

magnetic field signatures of ionospheric currents) the knowledge of height-integrated conductivities is sufficient and simplifies calculations considerably (Watermann et al,1993).

Senior et al (1981) used measurements of integrated Hall conductivity through the E region to confirm that in direct conflict to what had been deduced from ionograms electron density is greater in the morning than at the corresponding time in the afternoon. Earlier Perdersen (1927) had pointed out in connection with radio measurements of electron density, that the geomagnetic field renders the electrical conductivity of the ionosphere anisotropic.

In his influential Bakerian lecture, Appleton (1937) took a similar approach as Perdersen (1927) and applied the Chapman theory to derive ionization profile to support his radio wave data. He then used the data to calculate the Perdersen conductivity, which is perpendicular to the geomagnetic field. He also showed that Perdersen conductivity is proportional to radio wave absorption. Given the works of Perdersen (1927), Appleton (1937), Senior et al (1981) and the fact that our work is based on absorption of radio wave in the ionosphere, it is necessary we comment briefly on the conductivities of the ionospheric plasma.

4.2 Motions Due to Winds and Electric Fields

Let us consider the simplified equations of motion for singly charged positive ions and electrons. Rishbeth and Garriott (1969) have shown that:

$$m_i \, d\mathbf{V_i}/dt = m_i \mathbf{g} + e\mathbf{E} + e\mathbf{V_i} \times \mathbf{B} + m_i \nu_i (\mathbf{U} - \mathbf{V}) - \nabla p_i / N \qquad (1.41)$$

$$m_e \, d\mathbf{V_e}/dt = m_e \mathbf{g} + e\mathbf{E} + e\mathbf{V_e} \times \mathbf{B} + m_e \nu_I (\mathbf{U} - \mathbf{V}) - \nabla p_e / N \qquad (1.42)$$

According to Rishbeth (1989), the acceleration terms ($d\mathbf{V_i}/dt$, $d\mathbf{V_e}/dt$) are negligible for the large scale motions which come under consideration in the ionosphere, so the sum of the forces acting on the particle can be set equal to zero. The relevant forces are due to gravity **g**, the electrostatic field **E**, the geomagnetic field **B**, frictional drag by the neutral air and the gradient of the ions or electrons own partial pressure p_i , p_e.

The basic equations (1.41) and (1.42) can be greatly simplified and we can write for any charged particle acted on by electric and magnetic fields

$$0 = e\mathbf{E} + e\mathbf{V} \times \mathbf{B} - m\nu(\mathbf{V} - \mathbf{U}) \tag{1.43}$$

In a Cartesian coordinates system (ε, η, ξ) in which **B** is directly along the ξ-axis, we have

$$\begin{aligned} 0 &= F_\varepsilon - m\nu V_\varepsilon + eV_\eta B \\ 0 &= F_\eta - m\nu V_\eta - eV_\varepsilon B \\ 0 &= F_\xi - m\nu V_\xi \end{aligned} \tag{1.44}$$

where

$$\mathbf{F} = e\mathbf{E} + m\nu\mathbf{U} \tag{1.45}$$

is the applied force. The solution of (1.44) can be written in terms of the tensor k which satisfies the equation $\mathbf{V} = k \bullet \mathbf{F}$

$$k = \begin{bmatrix} k_p & \pm k_H & 0 \\ \pm k_H & k_p & 0 \\ 0 & 0 & k_o \end{bmatrix} \tag{1.46}$$

In (1.46), the upper sign apply to positive ions, the lower sign to the electrons. Each component of k is the ratio of a velocity to a force and is therefore a “mobility per unit charge”. The parameters k_p ,k_H, k_o are essentially positive. Rishbeth and Gariott (1969) gave expressions for them as :

Direct, longitudinal ($||\mathbf{B}, ||\mathbf{E}$), $k_o = 1/m\nu = 1/eB.\omega/\nu$

Transverse, Pedersen ($\perp\mathbf{B}, ||\mathbf{E}$), $k_p = 1/m\nu \,.\, \nu^2/(\nu^2 + \omega^2)$

$$= 1/eB.\ \nu\omega/(\nu^2 + \omega^2) \tag{1.47}$$

Hall ($\perp\mathbf{B}, \perp\mathbf{E}$)$k_H$, $= 1/m\nu.\omega\nu/(\nu^2 + \omega^2)$

$$= 1/eB.\ \nu\omega/(\nu^2 + \omega^2)$$

At any height in the ionosphere ω/ν is different for ions and electrons.

Rishbeth and Garriott (1969) and Rishbeth (1989) used (1.47) to illustrate how charged particles move in response to an applied electric field for which $\mathbf{F} = e\mathbf{E}$ and a neutral wind for which $\mathbf{F} = m\nu\mathbf{U}$ as follows:

(i) ***Electric field and Neutral wind Parallel to the Magnetic Field***

An electric field would cause a drift $eE/m\nu$, opposite in sense for positive ions and electrons. This electric current is along **B** (and is carried mainly by electrons, for which k_o is greater than for ions).

A wind causes a drift $F/k_o = m\nu U/m\nu = U$. Hence, at all heights both ions and electrons are driven along a field line at a velocity equal to the wind component parallel to **B**.

(ii) **Electric Field and Wind Perpendicular to the Magnetic Fields.**

The direction of motion of electrons and positive ions will depend on the ratio of collision frequency ν(with neutral molecules) to the gyro-frequency $\omega = eB/m$. Now given that ν decreases exponentially upwards, while ω is almost constant, the ratio ν/ω will fall off rapidly with height; it is different for ions and electrons. The most important cases are:

(a) Up to 100km for ions, and 60km for electrons, $\nu >> \omega$ and $k_p = k_o >> k_H$. In this region, the magnetic field is of no importance; an electric field moves ions parallel and electrons anti parallel to itself but only slowly because of the high collision frequency, so the conductivity is low.

(b) At about 125km for ions, and 75km for electrons, $\nu \approx \omega$ and $k_p \approx k_o$, a wind or an electric field drives ions and electrons in directions inclined to the applied field. The angle is given by arc tan (ω/ν) and is thus 45^o at the level where $\nu = \omega$.

(c) Above 150km for ions and 90km for electrons $\nu << \omega$ and $k_p << k_H \sim 1/eB$, and k_H is almost independent of height . An electric field causes both electrons and ions to drift in the same direction (**E** x **B**) with speed E/B: this is the electromagnetic drift velocity or Hall drift of speed (ν/ω)**U,** in the direction (**U** x **B**) for positive ions and the opposite direction for electrons.

It is important to note that when drift velocities for ions and electrons are equal, they are referred to as plasma drift velocity. And at any height, the field aligned component of plasma drift velocity due to wind can be written vectorially as

$$\mathbf{V}_W = (\mathbf{U} . \mathbf{B}) \mathbf{B}/B^2 \qquad (1.48)$$

Also the Hall drift is written vectorially as

$$\mathbf{V}_E = \mathbf{E} \times \mathbf{B}/B^2 \qquad (1.49)$$

4.3 The Electrical Conductivity

When positive ions and electrons move at different velocities as they do at ionospheric heights where the ratio ν/ω is different for ions and electrons, an electric current flows, of density

$$\mathbf{j} = Ne (\mathbf{V}_i - \mathbf{V}_e) \qquad (1.50)$$

where N is the electron and ion concentration. This result may be expressed through a tensor relationship

$$\mathbf{j} = \sigma . \mathbf{E} \qquad (1.51)$$

The conductivity tensor has components which follow the definition and expression for k (1.46):

$$\sigma = \begin{bmatrix} \sigma_p & -\sigma_H & 0 \\ \sigma_H & \sigma_P & 0 \\ 0 & 0 & \sigma_o \end{bmatrix}$$

(i) **Longitudinal conductivity σ_o**: This is the ratio of the electric current and electric field components parallel to the geomagnetic fields. Thus conductivity current is carried almost entirely by the electrons, as they are more mobile than the ions.

$$\sigma_o = ne^2 (K_{oe} + K_{oi}) \qquad (1.52)$$

(ii) **Transverse or Pedersen Conductivity σ_p**: The Pedersen conductivity relates the electric field $\mathbf{E}_\perp$ (normal to **B** to the current in that direction. The Pedersen current is carried by the ions, and according to Rishbeth (1989) peaks around 125km. Some Pedersen current flows in the F layer,

$$\sigma_p = ne^2 (K_{pe} + K_{pi}) \tag{1.53}$$

(iii) **Hall Conductivity σ_H** : The Hall conductivity relates to the current in the direction normal to both **B** and **E**. The Hall current, carried by electrons is the main part of the total ionospheric conductivity.

The electrical conductivity in the ionosphere is directly proportional to the electron density, and also depends on collision and gyro-frequency (Baker and Martyn, 1952; Chapman, 1956). For the purpose of deriving instantaneous values of ionospheric conductivities. Brekke and Moen (1993) expressed Pedersen and Hall conductivities as following:

$$\sigma_p (z) = N_e e /B [\omega_e \nu_{en} /(\omega^2_e + \nu^2_{en})+ \sum P_{ij} \omega_{ij} \nu_{ijn} /(\omega^2_{ij} + \nu^2_{ijn})] \tag{1.54}$$

$$\sigma_H (z) = N_e e / B [\omega^2_e /(\omega^2_e + \nu^2) - \sum P_{ij} \omega_{ij} / (\omega^2_{ij} + \nu^2_{ij})] \tag{1.55}$$

where N_e = electron density (m^{-3}), e = electron charge, B =magnetic field (Wb/m^2), ω_e ,ω_{ij} = electron and ion gyro-frequencies, ν_{en} , ν_{ij} = electron and ion collision frequencies and $P_{ij} = N_{ij}/ N_e$ = relative number densities for ion species j.

The expressions in parenthesis in (1.54) and (1.55) are referred to as the mobility coefficients. For practical purposes, the collision frequencies in (1.54) and (1.55) are either computed using the expressions given by Dahau et al (1987) or those of Brekke and Hall (1988):

$$\nu_{en} = 2.33 \times 10^{-17} n (N_2)*(1 - 1.2 \times 10^{-4} T_e) + 1.86 \times 10^{-16} n (O_2)* (1 + 3.6 \times 10^{-2}(T_e)^{1/2})(T_e)^{1/2} - 8.9 \times 10^{-16} n (O)* (1 + 5.7 \times 10^{-4} T_e)(T_e)^{1/2} \tag{1.56}$$

where T_e is the electron temperature in K and n is the density of neutral species in m^{-3}.

$$\nu_{i1n} = [4.23. n (N_2) + 4.18. n (O_2) + 2.38. n (O)] \times 10^{-16} \tag{1.57}$$

$$\nu_{i2n} = [6.82.\, n\,(N_2) + 6.66.\, n\,(O_2) - 3.42.\, n\,(O).\,(T_t.)^{1/2}\,(1.08 - 0.139)\log T_t)^{1/2} + 4.51 \times 10^{-3} .(\log T_t)^2]\times 10^{-16} \quad (1.58)$$

where $T_t = (T_i + T_e)/2$ and T_i and T_e are the ion and neutral temperatures respectively. ν_{i1n} is the collision frequency for a pseudo-ion with an ion mass of 30.5 a.m.u corresponding to a mixture of 75% NO and 25% O, the assumed average to be representative for the situation in the E region, while ν_{i2n} is the collision frequency for O^+ (Brekke and Moen, 1993). As can be seen from (1.56), (1.57) and (1.58), the collision frequencies depend on Te , Ti as well as Tn. To compute instantaneous values of the conductivities would require in principle simultaneous and independent observations of all these temperatures together with electron density, if all other factors are assumed to be known. As all these temperatures are difficult to measure simultaneously, there will be a need to fall back on some model values. The neutral temperatures are believed to be less variable and therefore its models are usually applied (Brekke and Moen, 1993)

The use of neutral temperature is based on the usual hypothesis that electron and neutral temperatures are equal, but according to Dahau et al (1987), electron temperature at E-region heights is greater than neutral temperature even in geo-magnetically quiet conditions. Analysis of the influence of different ion species to the conductivities do indicate that these are minor and therefore that the ions can be well represented by the pseudo-ion with a mass of 30.5 a.m.u (Moen and Brekke, 1990). The presence of O^+ ions can be ignored as they dominate at altitudes well above the main conducting region. The Hall and Pedersen conductivities are therefore well represented by the formulas given by (1.56), (1.57) and (1.58) when only one ion species is assumed (Moen and Brekke, 1990).

It must be pointed out that the most important factor in (1.54) and (1.55) is the electron density. The electron density varies most strongly and rapidly and its profile mainly determines the vertical profile of the electrical conductivity (Dahau et al, 1987). Combining the conductivities

gives a general relation between electric field and current density, which is the Ohm's law for the ionosphere

$$\mathbf{j} = \sigma_o \mathbf{E}_{||} + \sigma_p \mathbf{E}_{\perp} + \sigma_H (\mathbf{B} \times \mathbf{E}_{\perp}) / \mathbf{B} \qquad (1.59)$$

Now given that the ionosphere is always nearly electrically neutral, the current cannot produce any appreciable density of electric charge, but must be non divergent

$$\text{div}\, \mathbf{j} = 0 \qquad (1.60)$$

5.0 The Equatorial Electrojet

Several theoretical models of the dynamics of the equatorial E region exist. The starting point is the set of hydromagnetic equations.

$$\nabla . \mathbf{j} = 0 \qquad (1.61)$$

$$\nabla . \mathbf{E} = 0 \qquad (1.62)$$

$$\mathbf{j} = \sigma (\mathbf{E} + \mathbf{U} \times \mathbf{B}) \qquad (1.63)$$

where **j** is the current density, σ is the conductivity tensor, **U** is the neutral velocity, **B** is the geomagnetic field and **E** the electric field.

Theoretical models of the equatorial E region under thin shell approximations are shown to be inadequate by Untiedt (1967) and Richmond (1973).This is due to the fact that the peak current density seem to be underestimated and the vertical and latitudinal extent of the elelctrojet is neglected (Forbes and Lindzen, 1976; Kelly, 1989). It must be pointed out that without vertical currents at the equator which is neglected in the thin shell approximation, it is very hard to satisfy the divergence requirement

$$\partial j_x / \partial x + \partial j_y / \partial y = 0 \qquad (1.64)$$

given that the electrojet varies in latitude but only slowly in longitude (Kelley, 1989). The more realistic models (Untiedt, 1967; Richmond, 1973) assumed that the longitudinal extent of the electrojet is so great in comparison with its width that it is very possible to neglect longitudinal gradients of the electric field conductivity and current and therefore failed to take

into account local time variations. To improve on the shortcomings of the models, Forbes and Lindzen (1976) applied the full three-dimensional global dynamo solution within the equatorial electrojet and found that inclusion of vertical currents could actually increase the electrojet intensity predicted by the thin shell dynamo model. For example, the equatorial currents at the equator is simply given by

$$j_x = \sigma_p E_x + \sigma_H E_z \quad (1.65)$$

$$j_z = -\sigma_H E_x + \sigma_p E_z \quad (1.66)$$

Eliminating E_z yields

$$j_x = \sigma_c E_x + (\sigma_H/\sigma_p) j_z \quad (1.67)$$

for the zonal (positive eastward) electrojet current where σ_c is the Cowling conductivity. Thus positive (negative) vertical current act to enhance (reduce) the thin-shell ($j_x = 0$) value of the electrojet intensity (Forbes and Lindzen, 1976).

To explain the physics of vertical current, Forbes and Lindzen (1976) assumed that the maintenance of non divergent current flow associated with global scale dynamo action causes a zonal polarization field E_x to exist at the Equator during midday. Referring to equations (2.65) and (2.66), this results in a zonal Pedersen current ($\sigma_p E_x$) and a downward Hall current ($-\sigma_H E_x$). As their first approximation the E region dynamo is considered as a thin conducting shell bounded above and below by insulating layers, such that a vertical polarization field due to surface charges is built up to completely inhibit any vertical flow. As such the vertical Perdesen current must exactly cancel the Hall current. This implies that

$$\sigma_H E_x = \sigma_p E_z$$

which yields

$$E_z = (\sigma_H / \sigma_p) E_x \quad (1.68)$$

since $\sigma_H > \sigma_p$, the vertical field component considerably exceeds the zonal electric field component. In addition, E_z (z) has the same dependence as the function: $\sigma_p(z)/ \sigma_H(z)$. The current is now given by Kelly, (1982)

$$j_x = \sigma_H E_z + \sigma_p E_x \quad (1.69)$$

$$j_x = [\sigma^2_H)/\sigma^2_p) + 1]\,\sigma_p E = \sigma_c E_x$$

where σ_c is the so-called Cowling conductivity, The Cowling conductivity is very high, and the reduction of the expression for j_x to the form $j_x = \sigma_c E_x$ at the magnetic equator accounts for the existence of the equatorial electrojet which is imagined to be a ribbon of strong current and few hundred kilometres wide. It must be noted that the local neutral wind does not enter the calculations for j_x at all; the electrojet is set up by the global tidal winds that create the diurnal zonal electric field component measured at the equator.

According to Forbes and Lindzen (1976), the high Cowling conductivity owes its existence to the large vertical polarization field which exists at the magnetic equator (I = 0), for it is the Hall component of ($\sigma_H E_z$) of j_x which comprises most of the electrojet. When magnetic field lines are not horizontal (I ≠0) charges are relatively free to spiral along the highly conducting magnetic lines of forces, thus preventing such large charge separation and vertical polarization fields to exist away from the magnetic equator.

The intense electrojet currents and the geometry of electric and magnetic fields at the magnetic equator give rise to some interesting plasma instability phenomena. These instabilities cause electron density fluctuations (Forbes and Lindzen, 1976).

References

Appleton, E.V (1937) Regularities and Irregularities in the ionosphere-1. *Proc. Roy. Soc. Lond.,* 162, 451.

Appleton, E. V. (1953) A note on the "sluggishness" of the ionosphere. *J. Atmos. Terr. Phys.,3,* 282.

Appleton, E. V., Lyon, A. J., and Pritchard, A. G (1955) The detection of the Sq. current system in the ionospheric radio sounding.*J. Atmos. Terr. Phys.,7,* 292.

Baker, W. G., and Martyn, D. G (1953) Electric currents in the ionosphere 1- The conductivity. *Phil Trans. R. Soc.* A246, 281.

Bates, D. R. (1974) Radiative and Collision processes in the ionosphere. *J. Atmos. Terr. Phys.,36,* 2287.

Bates, D. R. (1988) Recombination in the Normal E and F layers of the ionosphere. *Plant. Space Sci.* 36(1) 55.

Baulch, R.N.E and Butcher, E.C (1988) Effective electron collision frequency measurements in the E- and F-regions. *J. Atmos. Terr. Phys.* 50(1), 45.

Bourne, I. A. and Hewitt, L.W.(1968) The dependence of ionospheric absorption of MF radio waves at mid-latitudes on planetary magnetic activity. *J. Atmos. Terr. Phys.* 30, 1381.

Brace, L.H and Theis, R. F (1978). An Empirical model of the interrelationship of electron temperature and density in the daytime thermosphere at solar minimum. *Geophys. Res. Lett.* 5,275.

Brace, L.H and Theis, R. F (1984). Solar cycle effects upon the relationship of N_e and T_e in the F region.*Adv. Space. Res* 4, 89

Bradbury, N. E. (1938). Ionization, negative ion formation and recombination in the ionosphere. *Terr. Magn. Atmos. Elect.* 43 55.

Brekke, A. and Hall C. (1988) Auroral ionospheric quiet summer time conductances *Ann. Geophys.* 6, 361

Brekke, A and Moen, J. (1993) Observations of high latitude ionospheric conductances *J. Atmos. Terr. Phys.* 55, (11/12) 1493.

Bolduc, L., 2002, *GIC observations and studies in the Hydro-Quebec power system*, J. Atmos. Sol.Terr. Phys., **64**, 1793-1802.

Budden K. G (1966) *Radio waves in the ionosphere.* Cambridge University Press, London.

Chapman, S. (1956). The electrical conductivity of the ionosphere: a review. *Nouvo Cimento* 4, 1385.

Chukwuma, V.U., 2003a, On *F2 response to geomagnetic storm*, Acta Geod. Geoph. Hung., **38**, 1-7.

Chukwuma, V.U., 2003b, *Interplanetary Phenomenon, geomagnetic and Ionospheric response associated with the storm of October 20-21, 1989*, Acta Geoph. Polonica, **51**, 459-472.

Chukwuma V. U., 2007, *On positive and negative ionospheric storms*. Acta Geod. Geophy. Hung., **42(1)**, 1-21.

Chukwuma, V. U., 2007a, Ionospheric Phenomena and Processes: Introductory notes, Publisher: BIB PRESS NIG. LTD, Ibadan. pp 42. ISBN: 978-978-086-374-6.

Cliffswallow, W., 1993, *Region 5395 of March 1989*, NOAA Technical Memorandum ERL SEL-82, National Oceanic and Atmospheric Administration, Boulder, USA, 1-40.

Czech, P., Chano, S., Huynh, H., and A. Dutil, 1992, *The Hydro-Quebec system blackout of March 13, 1989: system response to geomagnetic disturbance*, EPRI Report, TR- 100450. In: Proceedings of Geomagnetically Induced Current Conference, Millbrae, California, USA, November 8-10, 1989, 19.1-19.21.

De Franceschi, G Bianchi, C. Gregori, G. P Zolesi, B. and Pau, S. (1993). 10yr analysis on the planetary scale of the virtual height of the F-layer. *J. Atmos. Terr. Phys.* 55, 1553.

Duhau, S, De la Vega, M. and Azpiazu, M. C. (1987) Effect of the electron temperature in the number density and dynamics of the equatorial E region. *Planet. Space. Sci.* 35, 1.

Forbes M. and Lindzen, R.S. (1976). Atmospheric solar tides and their electrodynamic effects-II. The equatorial electrojet. *J. Atmos. Terr. Phys.,38*, 911.

Gerard, J.-Cl, and Taieb, C. (1986) the E-region electron density asymmetry at Saint Santin: observations and role of nitric oxide. *J. Atmos. Terr. Phys.,* 48, 471.

Gnanalingam, S. (1974) Equatorial ionospheric absorption during half a solar cycle (1964-1970). *J. Atmos. Terr. Phys.,* 36, 1335.

Gregory, J. B. and Manson, A. H.(1969) Seasonal variations of electron densities below 100km at mid latitudes-I. Differential absorption measurements., *J. Atmos. Terr. Phys.,*31, 703.

Jaeger, J.C. (1947) Equivalent path and absorption in an ionospheric region. *Proc. Phys. Soc. Lond.* 59, 43.

Kappenman, J.G., and V. D. Albertson, 1990, *Bracing for the geomagnetic storms*. IEEE Spectrum, March 1990, 27-33.

Kelly, M.C.(1989). *The Earth's Ionosphere: Plasma physics and Electrodynamics.* Academic Press, Inc. San Diego

Mitra, A. P. and Rowe, J. N. (1974). Ionospheric constraints of mesospheric nitric oxide. *J. Atmos. Terr. Phys.,* 36, 1797.

Monro, P.E; Nisbet, J. S. and Stick, T.L. (1976). Effects of tidal oscillations in the neutral atmosphere on electron densities in the E-region *J. Atmos. Terr. Phys.,* 38, 523.

Newbery, S. M.; Dyson P.L and Singh, A. (1989) An inversion procedure for obtaining collision frequency profiles from swept-frequency absorption measurements. *J. Atmos. Terr. Phys.,* 51, 425.

Oyinloye, J.O (1975) Radio-wave absorption in the equatorial ionosphere. *J. Atmos. Terr. Phys.,* 37, 1.

Oyinloye, J.O (1978) On the seasonal variation of absorption of radio waves in the equatorial ionosphere. *J. Atmos. Terr. Phys.,* 40, 793.

Oyinloye, J.O (1987) *Handbook on Radio Propagation For Tropical and Subtropical Countries.* URSI. 27

Pedersen, P. O. (1927) The propagation of radio waves., *Danm. Naturvid. Samf.,* A15, a/b

Rastogi, R. G. (1993) Geomanetic field variations at low latitudes and ionospheric electric fields. *J. Atmos. Terr. Phys.,* 55(10), 1375.

Ratnasiri, P.A.J.(1977) D region processes at equatorial latitudes. *J. Atmos. Terr. Phys.,* 39, 999.

Richmond, A.D (1973). Equatorial electrojet 1. Development of a model including winds and instabilities. *J. Atmos. Terr. Phys.,* 35, 1105.

Rishbeth, H. and Garriott, O.K (1969). *Introduction to Ionospheric Physics.* Academy Press, New York

Rishbeth, H. (1974) Ionospheric dynamics 1945-1970. *J. Atmos. Terr. Phys.,* 36, 2309.

Rishbeth, H. (1988) Basic Physics of the Ionosphere: A Tutorial Review: *J. IERE.* 58(6), s207.

Sen, H. K. and Wyller, A. A. (1960) On the Generalization of the Appleton-Hartree Magnetoionic Formulas *J. Geophys. Res.* 65, 3931.

Senior, C., Bauer, P., Taieb, C. and Petit, M. (1981) The effect of nitric oxide on the variation of the electron density in the E region with solar zenith angle. *C. r. Acad. Sci. Paris* 292, 1195.

Serafimova, M.K. (1986) Determination of vertical distribution of collision frequency in multi-frequency radio absorption measurements. *C. r. de I'acad. Bulgare Sci* 39(9), 71.

Serafimova, M. K. and Serafimov , K. B (1987) Determination of collision frequency from N_e(h)-profiles in the middle and bottom side ionosphere. *C. r. de I'acad. Bulgare Sci* 40(2), 39.

Szcuzczewicz, E.P. (1986) Theoretical and experimental aspects of ionospheric structure: A global perspective on dynamics and irregularities. *Radio Sci.,* 21, 351.

Tarkar, K. M. and Friedrich, M (1988) Empirical electron recombination coefficients in the D- and E- regions. *J. Atmos. Terr. Phys.,* 50(8) 749.

Thrane, E. V. and Piggott, W. R. (1966) The collision frequency in the E- and D- regions of the ionosphere., *J. Atmos. Terr. Phys.,*28 703.

Untiedt, J (1967) A model of the equatorial electrojet involving meridional currents. *J. Geophys.Res.,* 72, 5799.

Watermann, J., De la Beaujardiere, O. and Rich, F.J (1993) Comparison of electrical conductances inferred from coincident radar and spacecraft measurement and Photo-ionization models., *J. Atmos. Terr. Phys.,*55(7), 1513.

NIGERIAN JOURNAL OF SPACE RESEARCH **8:** 318 – 348, 2009 September 1

Planetary Atmospheres

Lawrence B. KOLAWOLE Ph.D.
Department of Physical Sciences
Redeemer's University,
km 46, Lagos-Ibadan Expressway,
Mowe, Nigeria
Email: proflkb@yahoo.com

Table of Contents

1.0 Planets

The recently adopted IAU resolution states that "planets" and other bodies in our Solar System be defined into three distinct categories in the following way:

i. A "planet" is a celestial body that:

a) is in orbit around the Sun,
b) has sufficient mass for its self-gravity to overcome rigid body forces so that it assumes a hydrostatic equilibrium (nearly round) shape, and
c) has cleared the neighbourhood around its orbit.

ii. A "dwarf planet" is a celestial body that:
a) is in orbit around the Sun,
b) has sufficient mass for its self-gravity to overcome rigid body forces so that it assumes a hydrostatic equilibrium (nearly round) shape,
c) has not cleared the neighbourhood around its orbit, and
d) is not a satellite.

iii. All other objects, except satellites orbiting the Sun, shall be referred to collectively as "Small Solar-System Bodies".

So by this official definition there are exactly **eight** planets - **Mercury, Venus, Earth, Mars, Jupiter, Saturn, Uranus and Neptune.** Ceres, Pluto, and Eris (2003UB313) are now classified as *dwarf planets.* A potentially large number of additional objects may fall into this category in the near future.

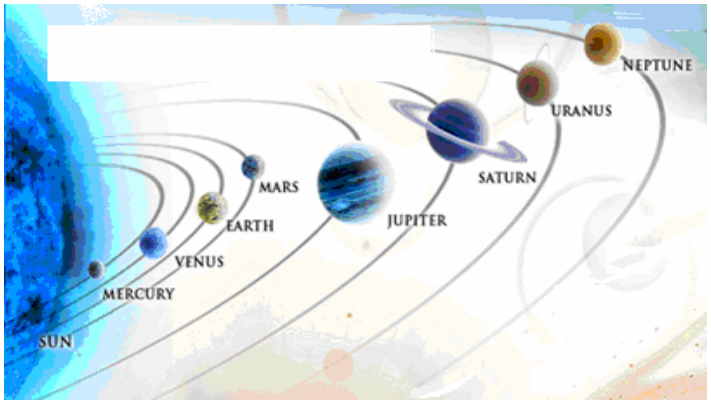

Fig. 1. The Planetary System

The four planets closest to the Sun (Mercury, Venus, Earth, and Mars) are called the ***terrestrial planets*** because they are like the Earth: small rocky worlds with relatively thin atmosphere.

The four giant planets beyond Mars (Jupiter, Saturn, Uranus, Neptune) are called the ***Jovian planets*** because they are like Jupiter: large, mostly liquid worlds with thick atmosphere.

Planets are nearly perfect spheres. Gravity compresses the planets to the most compact shape possible, a sphere, but the rapidly-spinning ones bulge slightly at the equator. This is because the inertia of a planet's material moves it away from the planet's rotation axis and this effect is strongest at the equator where the rotation is fastest (Jupiter and Saturn have easily noticeable equatorial bulges).

2.0 Atmosphere

An atmosphere is a layer of gases that may surround a material body of sufficient mass. The gases are attracted by the gravity of the body, and are retained for a longer duration if gravity is high and the temperature of the atmosphere is low. Some planets consist mainly of various gases, and therefore have very deep atmospheres. The atmosphere of a planet enables it to shield its surface from harsh radiation from the Sun and also moderate the amount of energy lost to space from the planet's interior.

All planets started out with atmospheres of hydrogen and helium. The inner four planets – Mercury, Venus, Earth and Mars – lost their original atmospheres. The atmospheres they have now are from gases released from their interiors, but Mercury and Mars have even lost most of their secondary atmosphere. The outer four planets – Jupiter, Saturn, Uranus and Neptune – were able to keep their original atmospheres. They have very thick atmospheres with proportionally small solid cores while the inner four planes have thin atmospheres with proportionally large solid parts.

The thickness of a planet's atmosphere depends on the planet's gravity and the temperature of the atmosphere. A planet with weaker gravity does not have as strong a hold on the molecules that make up its atmosphere as a planet with stronger gravity. The gas molecules will be more

likely to escape the planet's gravity. If the atmosphere is cool enough, then the gas molecules will not be moving fast enough to escape the planet's gravity.

2.1 Escape Velocity

The escape velocity, $\mathbf{V}_e$, is the initial velocity needed to escape a massive body's gravitational influence. It is given by

$$V_e = \sqrt{\frac{2G\,M_p}{d}} \qquad \text{…..2.1}$$

where G = the gravitational constant,

M_p = planet mass

d = distance measured from the planet centre

We note that the escape velocity increases as the mass increases. A more massive planet will have stronger gravity and, therefore, a higher escape velocity. On the other hand, the escape velocity decreases as the distance increases. The escape velocity is lower at greater heights above the planet's surface. The planet's gravity has a weaker hold on the molecules at the top of the atmosphere than those close to the surface, so those high up molecules will be the first to "evaporate away'.

2.2 Temperature

The temperature of a material is a measure of the average kinetic (motion) energy of the molecules in the material. Therefore, the particles in a hotter gas are moving quicker than those in a cooler gas of the same type. The kinetic theory of gases shows that the average gas molecule speed, V_a, is given by

$$V_a = \sqrt{\frac{3kT}{m_g}} \qquad \text{…2.2}$$

where k is a universal constant called the Boltzmann constant, T is temperature, and m_g is mass of gas molecule.

It follows from the equation above that the more massive molecules will move slower on average than the lighter gas molecules. For example, carbon dioxide molecules move slower on average than hydrogen molecules at the same temperature. Because massive gas molecules move slower, planets with weaker gravity (e.g., the terrestrial planets) will tend to have atmospheres made of just massive molecules. The lighter molecules like hydrogen and helium will have escaped.

The dependence of the average speed of the molecules on their mass also explains the compositional structure observed in planet atmospheres. Since the distance a gas molecule can move away from the surface of a planet depends only on how fast it is moving and the planet's gravity, the lighter gas molecules can be found both close to the surface and far above it where the gravity is weaker. The gas molecules high up in the atmosphere are most likely to escape. The massive gas molecules will stay close to the planet surface. For example, the Earth's atmosphere is made of nitrogen, oxygen, and water molecules and argon atoms near the surface but at the upper-most heights, hydrogen and helium predominate.

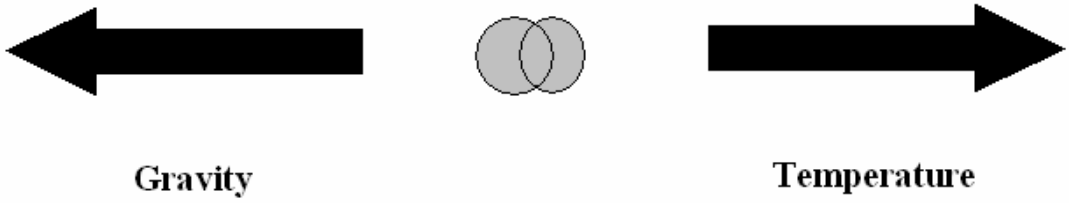

Fig. 2. Effect of Gravity and Temperature

The effects of gravity and temperature work opposite to each other. A higher temperature tries to dissipate an atmosphere while higher gravity tries to retain an atmosphere. If the particle's average speed is close to the escape velocity, then those types of gas particles will not remain for billion of years. The general rule is: if the average gas molecule speed for a type of gas is

less than 0.2 x (the escape velocity), then more than a half of that type of gas will be left after one billion years. If the average speed is greater that that critical value then more than ½ of that type of gas will be gone after one billion years.

Because the Jovian planets are massive and cold, they have thick atmospheres of hydrogen and helium. On the other hand, the terrestrial planets are small in mass and warm, so they have thin atmospheres made of heavier molecules like carbon dioxide or nitrogen.

2.3 Densities and Composition

An important property of a planet that tells what a planet is made of is its density. A planet's density is how much material it has in the space the planet occupies: density = mass/volume.

The four planets closest to the Sun (Mercury, Venus, Earth, Mars) are called the terrestrial planets because they are like the Earth: small rocky worlds with relatively thin atmosphere. Terrestrial planets have overall densities = 4-5 (relative to the density of water) with silicate rocks on the surface. Silicate rock has density = 3 (less than the average density of a terrestrial planet) and iron has a density = 7.8 (more than the average density of a terrestrial planet). Since terrestrial planets have average densities greater than that for the silicate rocks on their surface, they must have denser material under the surface to make the overall average density what it is. Iron and nickel are present in meteorites (chunks of rock left over form the formation of the solar system) and the presence of magnetic fields in some of the terrestrial planets shows that they have cores of iron and nickel. Magnetic fields can be produced by motion of liquid iron and nickel. Putting these facts together leads to the conclusion that the terrestrial planets are made of silicate rock surrounding a iron-nickel core.

The four giant planets beyond Mars (Jupiter, Saturn, Uranus, Neptune) are called the Jovian planets because they are like Jupiter: large, mostly liquid worlds with thick atmosphere. Jovian (Jupiter-like) planets have overall densities = 0.7-1.7 (relative to the density of water) with light

gases visible on top. Gases and light liquids (like hydrogen and helium) have densities lower than water. Using reasoning similar to before, you conclude that the Jovian planets are made of gaseous and liquid hydrogen, helium and water surrounding a possible relatively small rocky core. Spectroscopy says the Jovian planets have hydrogen, helium, methane, ammonia, and water gas in their thick atmosphere sot the predictions are not too far off track.

Planets can have a wide range of sizes and masses but planets made of the same material will have the same density regardless of their size and mass. For example, a huge, massive planet can have the same density as a small, low-mass planet if they are made of the same material.

2.4. Magnetic Fields

A moving charge will produce a magnetic field. The liquid conducting material in a planet's interior can be made to swirl about if the planet is rotating quickly enough. The faster a planet rotates, the more the material gets stirred up and, therefore, the stronger the generated magnetic field. If the liquid interior becomes solid or if the rotation slows down, the magnetic field will weaken. So in summary what a planet needs in order to produce a strong magnetic field is

- a liquid conducting (metallic) interior and
- rapid rotation to get the conducting material moving about.

Some planets have magnetic fields that act like there is a giant bar magnet in the centre of a planet. The magnetic field can be aligned differently from the rotational axis. For example, the Earth's magnetic field is tilted by about 18^{o} with respect to the Earth's rotational axis.

A planet's magnetic field forms a shield protecting the planet's surface from energetic, charged particles coming from the Sun and other places. The Sun is constantly sending out charged particles called the ***solar wind***, into the solar system. When solar wind particles run into a magnetic field, they are deflected and spiral around the magnetic field lines.

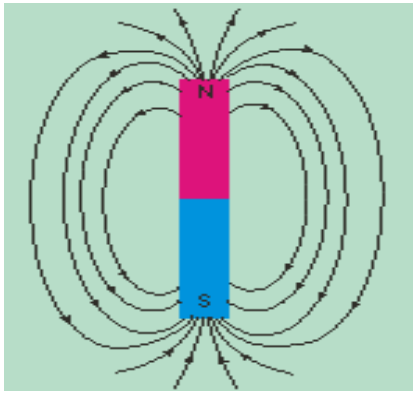

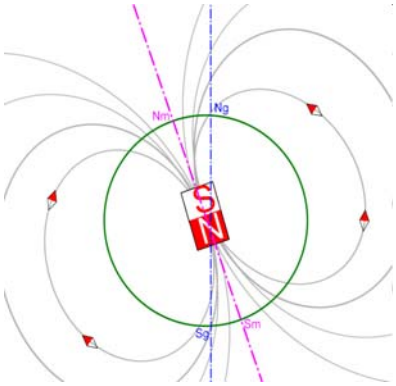

(a) (b)

Fig 3 (a) Magnetic field of a bar magnet (b) Approximate geomagnetic field

There isn't really a giant magnet at the centre of a planet. We recall from basic physics that that a magnetic field can be produced by circulating electrical charges. A theory called ***the magnetic dynamo theory*** says that the magnetic field is produced by swirling motions of liquid conducting material in the planet interiors. Materials that can conduct electricity have some electrical charge that is free to move about. Such materials are called ***metallic*** and are not necessarily shiny solids like copper, aluminum, or iron. Jupiter and Saturn have a large amount of hydrogen that is compressed so much it forms a liquid. Some of that liquid hydrogen is in a state where some of the electrons are squeezed out of the atoms and are free to move around.

For the terrestrial planets, plate tectonics may also play a role. Plate tectonics cool the planet's mantle, creating a large enough temperature difference between the core and mantle to produce convection in the metallic core needed to make a magnetic field

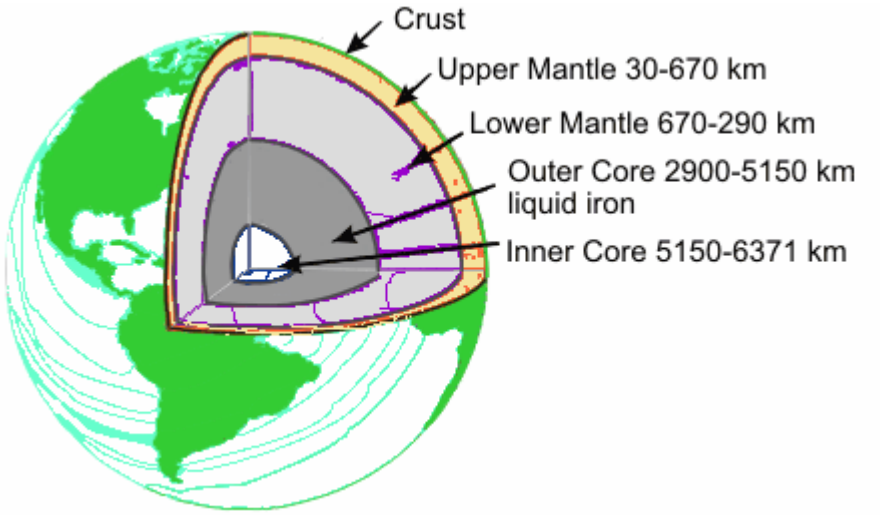

Fig 4. The Earth's Interior

Let's see how this theory explains the presence or lack of a magnetic field on some of the planets:

1. Venus has no magnetic field (or one so weak, it hasn't been detected yet). It probably has a liquid conducting interior for a couple of reasons:

   Since it is almost the size of the Earth, its interior should still be very warm. Larger planets lose their heat from formation and radioactive decay more slowly than small planets. A planet with a larger volume than another planet of the same composition will start off with a larger supply of heat energy. In addition, the heat in a large planet's interior has a great distance to travel to reach the planet's surface and the cold outer space.

   The rate of heat loss increases with the surface area. A planet with a larger surface area than another planet with the same internal temperature will have a larger rate of heat loss. The time it takes for a planet to cool off depends on the total amount of heat stored/rate of heat loss or (its volume)/(its surface area). Recall from the planet volume section that the volume increases as the diameter^3. The surface area increases as only the diameter^2, so the

planet's cooling time increases as diameter^3/diameter. Even though its heat loss rate is greater, a larger planet has a much larger amount of energy stored in it and, thus, it will take longer to cool off than a smaller planet. Venus should have a iron-nickel core that is still liquid like the Earth's.

High resolution radar imaging of Venus' surface by the Magellan spacecraft shows several places where volcanoes have erupted recently and produced large lave flows.

The reasons Venus does not have a global magnetic field are that it spins very slowly (about once every 243 Earth days!) and the absence of convection in the liquid core, (probably because of the lack of plate tectonics for the past half billion years).

2. Mars has an extremely weak magnetic field but for a different reason than Venus. Mars is about half the diameter of the Earth and has about 1/10th the Earth's mass, so its internal heat should have disappeared to space long ago. So even though Mars spins quickly (once every 24.6 hours), its metallic core is solid --- the charges are not able to swirl about. Mars' crust is also probably too thick for plate tectonics to occur even if the core had not cooled.

3. Earth has a strong magnetic field because it spins fast (*once every 23.93 hours*). It has a liquid conducting core made of liquid iron-nickel, and it has plate tectonics.

4. Jupiter has a HUGE magnetic field. Jupiter has a large amount of hydrogen that is super-compressed to form the strange liquid called liquid metallic hydrogen. This material cannot be produced on the Earth because the super-higher pressures needed to squeeze some o the electrons out of liquid hydrogen cannot be produced. Jupiter also spins very quickly – one rotation in under 10 hours!

Jupiter's magnetic field is so large that from the Earth it has an angular size over four times the size of our moon. One of the first radio sources detected from space was Jupiter. Solar wind particles spiraling around magnetic field lines can produce electromagnetic radiation in many different frequency bands. For Jupiter a lot of this energy is in the form or radio.

5. Mercury is a bit surprising because it has a weak magnetic field. Mercury is the smallest of the terrestrial planets, so its interior should have cooled off long ago. Also, Mercury spins slowly - once every 58.8 days. Mercury's high density tells us that it has a proportionally large iron nickel core. Its magnetic field implies that Mercury's interior is probably partially molten. In mid-2007, astronomers announced independent evidence in favour of a molten core for Mercury. Using very careful observations of Mercury's rotation, they found that Mercury's core could not be solid.

Mercury's situation was a major challenge to the magnetic dynamo theory. In true scientific fashion, the theory made a testable prediction: Mercury should have no magnetic field or one even less than that of Mars because its core should be solid. Observation, the final judge of scientific truth, contradicted the prediction. Should we have thrown out the magnetic dynamo theory then? Astronomers were reluctant to totally disregard the theory because of its success in explaining the situation on the planets and the lack of any other plausible theory.

So we must take a more conservative route; either modifying the magnetic dynamo theory or investigating Mercury more closely to find out what is so unusual about its interior to produce a magnetic field despite our expectations. Is their reluctance a violation of the objectivity required in science? Perhaps, but past experience has taught that when confronted with such a contradiction, nature is telling you that you forgot to take something into account or you overlooked a crucial process.

Mercury's magnetic field is just one of the puzzles of Mercury the *Messenger* mission will be exploring when it finally begins orbiting Mercury in March 2011. The careful observations of Mercury's spin may have solved part of the problem (the core is at least partially molten), but how has the core remained molten and convecting (even partially) despite Mercury's small size?

One example of this conservative route is the discovery of the planet Neptune. When its near twin planet, Uranus, was discovered, astronomers were very confident in Newton's gravity theory because of its over-a-hundred-year success rate in explaining the motions of many different types of objects. So they applied Newton's gravity theory to Uranus' orbit. Rather than throwing out Newton's gravity theory, astronomers used the contradiction to predict the presence of another planet beyond Uranus. Within a couple of years, Neptune was discovered at the position predicted! Might the same sort of thing be happening with the magnetic dynamo theory and Mercury's magnetic field? Perhaps one thing is for sure scientists love a good puzzle and will work hard at trying to solve it.

2.5. Saturn Rings

In 1655 Christann Huygens proposed that Saturn was surrounded by a solid ring, "*a thin flat ring, nowhere touching, and inclined to the ecliptic."* As time went on, more and more observations were made and theories proposed. It took until the mid 1800s before the notion that the ring was made out of small particles rather than being solid became the prominent theory.

In 1979 ***Pioneer 11*** became the first spacecraft to fly past Saturn and take pictures of the planet and rings. Although the pictures are of low resolution by today's standards, they were better than any previous photos taken through telescopes. In 1980 and 1981 ***Voyager 1 and Voyager 2*** flew past the planet and took numerous high-resolution images of Saturn and its rings. The next

major milestone was in 2004 when the ***Cassini*** spacecraft arrived at Saturn. Cassini was the first spacecraft to go into orbit about the planet.

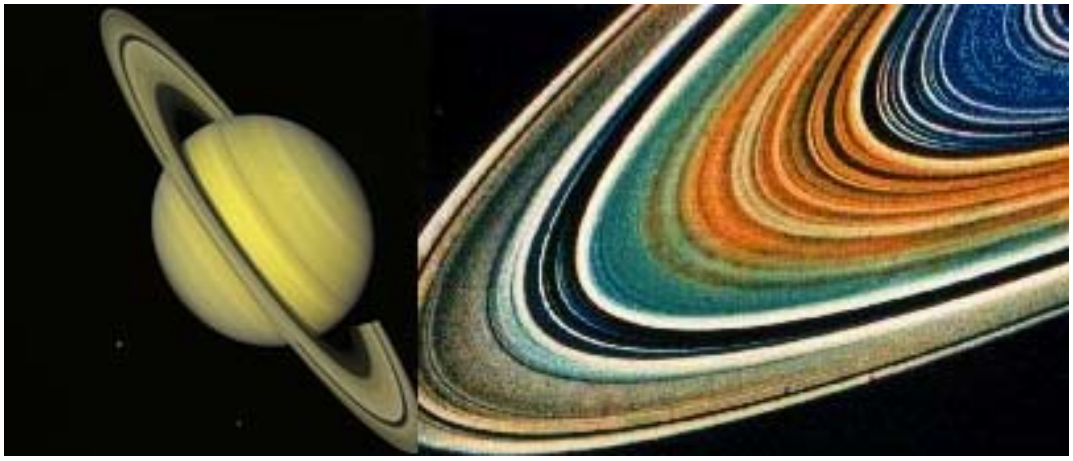

Fig. 5 Saturn Rings

Saturn's ring system is divided up into 7 major divisions with alphabetic designators in the order of discovery (See Figure 5 and Table 1). From the innermost ring to the outermost ring the designators are D, C, B, A, F, G and E. Each major division is further subdivided into thousands of individual ringlets. The F and G rings are very thin and difficult to see while the A, B, and C rings are broad and quite visible. Between the A and B rings is a gap called the Cassini division named after Giovanni Cassini who discovered the Gap in 1676. Between the A and F rings lies the Keeler (Encke) gap.

2.6 Appearance and Colours of the Atmospheres

Most of the planet atmospheres reflect enough of the visible sunlight that only the upper layers of their atmosphere can be seen. Only the Earth and Mars have atmospheres transparent to most of the visible light so that we can see what lies below their atmospheres.

Table 1. Properties of Saturn Rings

Name	Distance* (km)	Width (km)	Thickness (km)	Optical Depth	Mass (g)	Albedo
D	66,000 - 73,150	7,150	?	0.01	?	?
C	74,500 - 92,000	17,500	?	0.05 - 0.35	1.1×10^{24}	0.12 - 0.30
Maxwell Gap	87,500	270				
B	92,000 - 117,500	25,500	0.1 - 1	0.8 - 2.5	2.8×10^{25}	0.5 - 0.6
Cassini Div	117,500 - 122,200	4,700	?	0.05-0.15	5.7×10^{23}	0.2 - 0.4
A	122,200 - 136,800	14,600	0.1 - 1	0.4-0.5	6.2×10^{24}	0.4 - 0.6
Encke gap	133,570	325				
Keeler gap	136,530	35				
F	140,210	30 - 500	?	0.01-1	?	0.6
G	164,000 - 172,000	8,000	100 - 1000	10^{-6}	10^{20}	?
E	180,000 - 480,000	300,000	1,000	10^{-5}	?	?

* The distance is measured from the planet center to the start of the ring.

In visible light, Venus is a bland, yellow-white planet. Venus' atmosphere is 96 percent carbon dioxide but it is the thick cloud layer of sulfuric acid droplets that reflects back about 70 percent of the sunlight and make Venus brighter than any other object in our sky besides the Moon and the Sun (in fact Venus can be seen in broad daylight if the Earth's atmosphere above you is very clear).Venus' cloud layer extends from 30 kilometers to 60 kilometers above the surface. Below 30 km Venus' atmosphere is clear because the high temperature near the surface evaporates any cloud droplets that drop too far. What sunlight that makes it through the clouds, has an orange tinge to it because the blue colors are absorbed by the clouds. The sulfuric acid

may be from sulfur compounds, possibly from volcanoes, that chemically react with the trace amounts of water vapor left in the atmosphere.

The structures of the clouds are revealed in ultraviolet light. It is the ultraviolet images that most astronomy books will use to show what Venus looks like. To see what lies below the surface, astronomers use the long wavelengths of radio. The rocky surface of Venus has been mapped using imaging radar by spacecraft orbiting Venus, such as the spectacular Magellam spacecraft that surveyed Venus in the early 1990's.

Earth's atmosphere is mostly transparent to visible light with a blue tint caused by the preferential scattering of blue sunlight by the nitrogen and oxygen molecules. Up to about 10 km above the surface, clouds of water droplets and ice crystals form. The droplets and crystals are large enough to reflect all wavelengths of visible equally, so the clouds have a white color. Because of the *Coriolis Effect*, the clouds form spiral patterns.

Mars' carbon dioxide atmosphere is also mostly transparent to visible light. Its thin white clouds are mostly water ice crystals. Some clouds have a yellow color because they are composed of fine dust particles a few micrometers across. Astronomers expected Mar's sky to have a deep blue color as seen from the surface because the atmosphere is only one percent the thickness of the Earth's atmosphere. However, pictures from the Mars surface Landers show the Martian sky to be pink from sunlight bouncing off dust particles blown off Mars' red surface.

Jupiter's atmosphere is very dynamic and colorful and Saturn's atmosphere is a muted version of Jupiter's. Even though their atmospheres are primarily hydrogen and helium, the clouds of ammonia ice crystals in their upper atmospheres give the planets their appearance. The strong Coriolis effect from their rapid rotation deflect the clouds into bands parallel to their equators.

The bright zones on Jupiter are regions of upwelling convection cells in the upper atmosphere with more ammonia clouds than the darker bands. The dark bands are where we see to the warmer clouds made of ammonium hydrosulfide ice crystals about 20 to 30 kilometers below the ammonia cloud deck. Clouds of water ice crystals are thought to exist about 100 kilometers below the ammonia cloud deck, but the Galileo probe that plunged through Jupiter's clouds in early December of 1995 found no water layer. However, this may because the Galileo probe descended through an unusually dry and cloud-free part of the atmosphere.

Saturn's layer of clouds is about twice as thick as Jupiter's because of the colder temperatures and lower gravity compression on Saturn. The strong jet streams in their atmospheres create turbulent eddies of swirling clouds, some several thousands of kilometers across. One spectacular example is the Great Red Spot on Jupiter – a hurricane twice the size of the Earth that has lasted for over 300 years. Such storms and the belted patterns on the Jovian planets can last so long because there is no solid surface for the storms to expand their energy.

What is puzzling about the clouds is their color. The ammonia ice clouds should be white, yet they have a variety of red, orange, yellow and brown colours. Sunlight striking the clouds causes photochemical reactions with the molecules in the clouds. The resulting organic compounds, or trace amounts of sulfur and phosphorus may be responsible for the colours in the clouds.

Uranus and Neptune also have thick cloud decks but Uranus' atmosphere does not have the prominent bands and storms seen on the other Jovian planets. This is because Uranus does not have an extra internal heat source like the other jovian planets, so it does not have the convective motions in its atmosphere. Neptune's clouds are deflected to form bands parallel to its equator because of its rapid rotation. Neptune can also have turbulent eddies form in its atmosphere. When the Voyager spacecraft flew by Neptune in 1989, it found a large dark storm, called the Great Dark Spot (very original, yes?), that was about the size of Jupiter's

Great Red Spot. However, recent Hubble Space Telescope photographs show that the Great Dark Spot seems to have dissipated.

Uranus and Neptune both have a blue color. Instead of ammonia clouds, their clouds are made of frozen methane crystals because they are much colder than Jupiter and Saturn. The red and orange colors of sunlight are absorbed by the methane in their atmospheres while the blue colors are scattered back out, producing the blue color with a faint greenish tinge.

3.0. The Earth's Atmosphere

The **Earth's atmosphere** is a layer of gases surrounding the planet Earth that is retained by the Earth's gravity. It contains roughly (by molar content/volume) 78.08% nitrogen, 20.95% oxygen, 0.93% argon, 0.038% carbon dioxide; trace amounts of other gases, and a variable amount (average around 1%) of water vapor. This mixture of gases is commonly known as air. The atmosphere protects life on Earth by absorbing ultraviolet solar radiation and reducing temperature extremes between day and night.

There is no definite boundary between the atmosphere and outer space. It slowly becomes thinner and fades into space. Three quarters of the atmosphere's mass is within 11 km of the planetary surface. Usually, people who travel above an altitude of 80.5 km are designated astronauts. An altitude of 120 km marks the boundary where atmospheric effects become noticeable during reentry. The *Karman line*, at 100 km, is also frequently regarded as the boundary between atmosphere and outer space.

3.1. Temperature and Layers

The regions of the atmosphere are named according to various schemes based, in particular, on temperature, composition, and state of mixing.

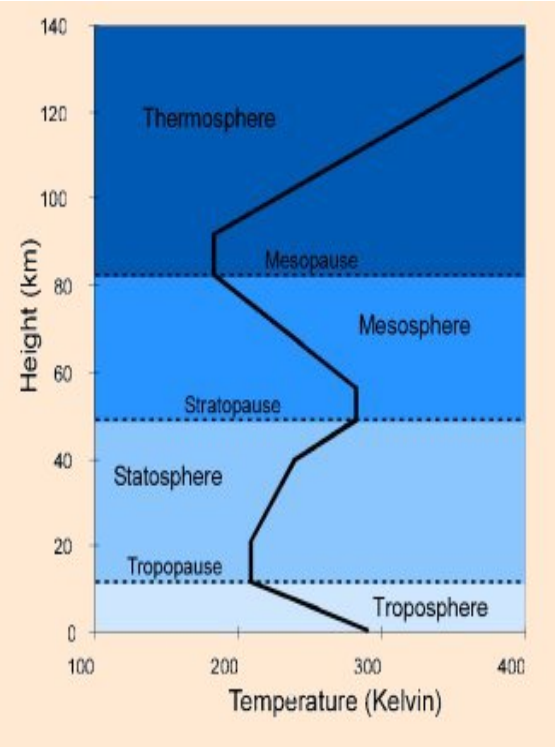

Fig. 6. Earth's Atmospheric layers

Fig.6. illustrates the nomenclature that is in most common use. The primary classification is by temperature. In this system individual temperature regions are named *sphere* and each upper boundary is called a *pause.* Thus, the troposphere, in which the temperature fall off at a rate of 10 K km^{-1} or less, is bounded by the tropopause at a height of 10 -12 km. The stratosphere above that was originally thought to be isothermal but in fact is a region of increasing temperature.

The temperature of the Earth's atmosphere varies with altitude; the mathematical relationship between temperature and altitude varies among five different atmospheric layers (ordered highest to lowest, the ionosphere is part of the thermosphere). A maximum due to ozone absorption appears at about 50 km and this is the stratopause. The temperature decreased again in the mesosphere (or middle atmosphere) to the temperature minimum at the mesopause at 80-85km. With the temperature around 180 K this is the coldest part of the atmosphere. Above the

mesopause, dT/dh remains positive, and this is the thermosphere. Eventually the thermosphere temperature becomes constant with altitude at a value which changes with time but is usually over 1000 K, the hottest part of the atmosphere.

The temperature classification is generally the most useful one, but scheme based on the state of mixing, the composition and the state of ionization are also indispensable in their respective contexts. The well mixed part of the atmosphere in which the composition does not change with height can be called the turbosphere or the homosphere.

The upper region where mixing is absent and the composition changes with height is the heterosphere. The boundary between the regions, at about 1000 km, is the turbopause. Within the heterosphere there are regions where the dominant gas is helium or hydrogen, and these regions are the heliosphere and the protonosphere respectively. At the highest levels, above about 600 km, individual molecules can escape the Earth's gravitational attraction and this region is the exosphere. The base of the exosphere is the exobase or the baropause. For reasons that will become clear in the next section, the lower region below the baropause, is the barosphere.

- **Exosphere**: from 500 -1000 km (300 – 600 mi) up to 10,000 km (6,000mi), free moving particles that may migrate into and out of the magnetosphere or the solar wind. (*Exobase boundary)*

- **Ionosphere**: the part of the atmosphere that is ionized by solar radiation. It plays an important part in atmospheric electricity and forms the inner edge of the magnetosphere. It has practical importance because, among other functions, it influences radio propagation to distant places on the Earth. It is located in the thermosphere and is responsible for auroras. We should take note of the difference between the *ionosphere and the magnetosphere*, the first applying to the ionized regions (above about 70 km) and the second to the outermost

part where motions are controlled by the geomagnetic field. The outer termination of the geomagnetic field, at distances of the order of 10 earth radii, is the magnetopause. (*Thermopause boundary)*

- **Thermosphere**: from 80 – 85 km (265,000 – 285,000 ft) to 640 + km (400 + mi), temperature increasing with height. *(Mesopause boundary)*

- **Mesophere:** From the Greek word "*μεσος*" meaning middle. The mesosphere extends from about 50km (160,000 ft) to the range of 80 to 85km (265,000 – 285,000 ft), temperature decreasing with height. This is also where most meteors burn up when entering the atmosphere. *(Stratopause boundary)*

- **Stratosphere**: From the Latin word "stratus" meaning a spreading out. The stratosphere extends from the troposphere's 7 to 17 km (23, 000 – 60,000 ft) range to about 50 km (160,000 ft). Temperature increases with height. The stratosphere contains the ***ozone layer***, the part of the Earth's atmosphere which contains relatively high concentrations of ozone. "Relatively high" means a few parts per million – much higher than the concentrations in the lower atmosphere but still compared to the main components of the atmosphere. It is mainly located in the lower portion of the stratosphere from approximately 15 to 35 km (50,000 – 115,000 ft) above Earth's surface, though the thickness varies seasonally and geographically. (*Tropopause boundary)*

- **Troposphere**: From the Greek word ""*τρεπω*" meaning to turn or change. The troposphere is the lowest layer of the atmosphere; it begins at the surface and extends to between 7 km (23, 000 ft) at the poles and 17 km (60,000 ft) at the equator, with some variation due to weather factors. The troposphere has a great deal of vertical mixing because of solar heating at the surface. This heating warms air masses, which makes them less dense so they rise. When an air mass rises, it does work against gravity. This work changes some

of the thermal (kinetic) energy into gravitational potential energy, so the temperature of the air mass decreases. As the temperature decreases, water vapor in the air mass may condense or solidify, releasing latent heat that further uplifts the air mass. The process determines the maximum rate of decline of temperature with height, called the ***adiabatic lapse rate***. The troposphere contains roughly 80% of the total mass of the atmosphere. Fifty percent of the total mass of the atmosphere is located in the lower 5 km of the troposphere.

The average temperature of the atmosphere at the surface of Earth is 15^0C (59^0F).

3.2 Atmospheric Pressure

The four basic properties of the upper atmosphere are pressure (P), density (ρ), temperature (T) and composition. These properties are not independent, but are related by the gas law PV = RT for one mole of gas (R being the gas constant) or PV = NRT for N moles. Also, since R = N_0k, where N is Avogadro's number (6.02 x $10^{23}g^{-1}$ mol^{-1}) and k is Boltzmann's constant (1.38 x 10^{-16} erg $^0K^{-1}$), and ρ = NM/V, where M is the molecular weight, the gas law can also be written in the useful form.

$$P = nkT \qquad \text{----------} \qquad 3.1$$

where n is the number of molecules per unit volume. 'n' is properly called the concentration, but it may also be termed the number density or, particularly if referring to free electrons or ions, simply density.

The average atmospheric pressure, at sea level, is about 101.3 kilopascals (about 14.7 psi); total atmosphere mass is 5.1480 x 10^{18} kg. Atmospheric pressure is a direct result of the total weight of the air above the point at which the pressure is measured. This means that air pressure varies with location and time, because the amount (and weight) of air above the earth varies with location and time. However the average mass of the air above a square meter of the earth's surface is known to the same high accuracy as the total air mass of 5148.0 teratonnes and area of the earth of 51007.2 mega-hectares, namely 5148.0/510.072 = 10.093 metric tones or 14.356

lbs (mass) per square inch. This is about 2.5% below the officially standardized unit atmosphere (1 atm) of 101.325 kPa, and corresponds to the mean pressure not at sea level but at the mean base of the atmosphere as contoured by the earth's terrain.

Were atmospheric density to remain constant with height the atmosphere would terminate abruptly at 7.81 km Instead it decreases with height, dropping by 50% at an altitude of about 5.6 km. For comparison; the highest mountain, Mount Everest, is higher, at 8.8 km, which is why it is so difficult to climb without supplemental oxygen. This pressure drop is approximately exponential, so that pressure decreases by approximately half every 5.6 km (whence about 50% of the total atmospheric mass is within the lowest 5.6 km) and by I/ℓ = .368 every 7.64 km, the average height of Earth's atmosphere below 70km. However, because of changes in temperature, average molecular weight, and gravity throughout the atmospheric column, the dependence of atmospheric pressure on altitude is modeled by separate equations for each of the layers listed above.

Even in the exosphere, the atmosphere is still present (as can be seen for example by the effects of atmospheric drag on satellites).

3.3. Hydrostatic (Barometric) Equation

The most basic physical feature of the atmosphere is the decrease of pressure and density with increasing height. The height variation is described by the hydrostatic equation, derived as follows.

If a gas contains n molecules, each of mass m, per unit volume, a cylinder of unit cross-section contains total mass nm.dh, where dh is the height of the cylinder. Under gravity the cylinder experiences a downward force nmg.dh which, in static equilibrium, is balanced by the net upward force due to the difference of pressure between the top and bottom faces:

$$(p + dp) - p = nmg \, . \, dh$$

Therefore $\frac{dp}{dh} = nmg$

But, by the gas law, p = nkT.

Hence

$$\frac{1}{p}.\frac{dp}{dh} = -\frac{mg}{kT} = -\frac{1}{H} \quad \text{----------} \quad 3.2$$

where $H = \frac{kT}{mg}$ is defined as the scale height. If H is constant, Equation 3.2 is integrated to give:

$$p = p_o \exp(-h/H) \quad \text{----------} \quad 3.3$$

where p_o is the pressure at a height h = 0

The scale height is the vertical distance in which p changes by a factor *e.*

Even if g, T and m are not independent of height, H can be defined by Equation 3.2 in terms of the relative rate of change of concentration with height.

In the terrestrial atmosphere H increases with height from about 5 km at height 80 km, to 70-80 km at 500 km. A useful approximate formula, accurate to about 10% over the height range 200-900 km is

$$H(\text{km}) \sim T(\text{K}) / M(\text{mass units}) \quad \text{----------} \quad 3.4$$

Instead of Equation 4.3, it is sometimes convenient to put

$$\frac{p}{p_0} = \exp\left[-\frac{h-h^0}{H}\right] = e^{-z} \quad \text{----------} \quad 3.5$$

where $p = p_o$ at $h = h_o$, and z is the reduced height defined by $z = (h-h_o)/H$. The hydrostatic equation can also be written in terms of density (ρ) or concentration (n), since $n/n_o = \rho/\rho_0 = p/p_o$, if T, g and m are constant. The ratio k/m can be replaced by R/M, where R is the gas constant and M the molecular weight.

Whatever the height distribution of a gas, its pressure p_o at height h_o is just the weight of a gas in a column of unit cross-section above h_o. Hence

$$p_o = \frac{N_T n_o k T_o}{mg} = n_o H_o \quad \text{----------} \quad 3.6$$

where N_T is the total number of molecules in the column above h_o, and n_o and T_o are the concentration and temperature at h_o. Hence

$$N_T = \frac{n_o k T_o}{mg} = n_o H_o \quad \text{----------} \quad 3.7$$

H_o being the scale height at h_o. Equation 3.7 means that if the entire atmosphere above h_o were compressed until it had the density of the real atmosphere at h_o, it would occupy a column of one scale height. Note also that Equation 3.6 implies that the total mass of the atmosphere above unit area of the Earth's surface is equal to the surface pressure divided by g.

The equations of pressure by altitude above can be used directly to estimate atmospheric thickness. However, the following published data are given for reference [4]

- 50% of the atmosphere by mass is below an altitude of 5.6 km
- 90% of the atmosphere by mass is below an altitude of 16 km. The common altitude of commercial airliners is about 10 km.
- 99.99997% of the atmosphere by mass is below 100 km. The highest X-15 plane flight in 1963 reached altitude of 354,300 ft (108,000 m)

Therefore, most of the atmosphere (99.99997%) is below 100 km, although in the rarefied region above this there are auroras and other atmospheric effects.

4.0 The Earth's Magnetic (Geomagnetic) Field

The Earth's magnetic field (and the surface magnetic field) is approximately a magnetic dipole, with one pole near the North Pole and the other near the geographic South Pole *(see section 2.4 Fig. 3(b)).* An imaginary line joining the magnetic poles would be inclined by approximately 11.3° from the planet's axis of rotation.

Magnetic fields extend infinitely, though they are weaker further from their source. The Earth's magnetic field, which effectively extends several tens of thousands of kilometers into space, is called the *magnetosphere*.

The Earth's magnetic field is an ever-changing phenomenon that influences human activity and the natural world in a myriad of ways. The geomagnetic field changes from place to place, and on time scales ranging from seconds to decades, to eons. These changes can affect human health, safety, and economic well-being. The geomagnetic field, along with its associated phenomena can both assist and degrade navigation and surveying techniques; it can impede geophysical exploration; it can disrupt electric power utilities, and pipeline operations; and it can influence modern communications systems, spacecraft, and more.

The Earth's magnetic field is a vector quantity; at each point in space it has strength and a direction. To completely describe it we need three quantities. These may be:

- three orthogonal strength components (**X**, **Y**, and **Z**);
- the total field strength and two angles (**F**, **D**, **I**); or
- two strength components and an angle (**H**, **Z**, **D**)

The relationship between these 7 elements is shown in Fig. 7.
D and **I** are measured in degrees. All other elements are measured in nanotesla (nT; 1 nT = 10^{-9} Tesla). The seven elements are related through the following simple expressions.

$$D = \tan^{-1}\left(\frac{Y}{X}\right); \qquad X = H\cos(D); \qquad I = \tan^{-1}\left(\frac{Z}{H}\right);$$

$$Y = H\sin(D); \qquad H = \sqrt{X^2 + Y^2}; \qquad F = \sqrt{X^2 + Y^2 + Z^2};$$

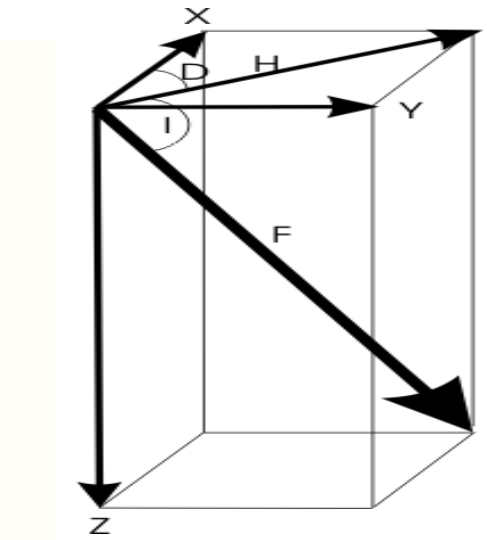

Figure 7: Magnetic elements

Table 2. Geomagnetic elements

Geomagnetic elements	*Description*
F	the total intensity of the magnetic field vector
H	the horizontal component of the magnetic field vector
Z	the vertical component of the magnetic field vector; by convention Z is positive downward
X	the north component of the magnetic field
Y	the east component of the magnetic field
D	magnetic declination, defined as the angle between true north and the horizontal component of the field measured eastward from true north
I	magnetic inclination, defined as the angle measured from the horizontal plane to the magnetic field vector; downward is positive

4.1. Magnetic reference field models

Magnetic reference field models provide an easy way to calculate magnetic declination and other components of the magnetic field. A reference field model is a mathematical algorithm

whose parameters are based on an analysis of magnetic observations either over the entire world or a part of the world. Spherical harmonic analysis is the most common method used for producing global models. The International Geomagnetic Reference Field (IGRF) and the World Magnetic Model (WMM) are the most commonly used models for navigational purposes. Models are traditionally updated every five years.

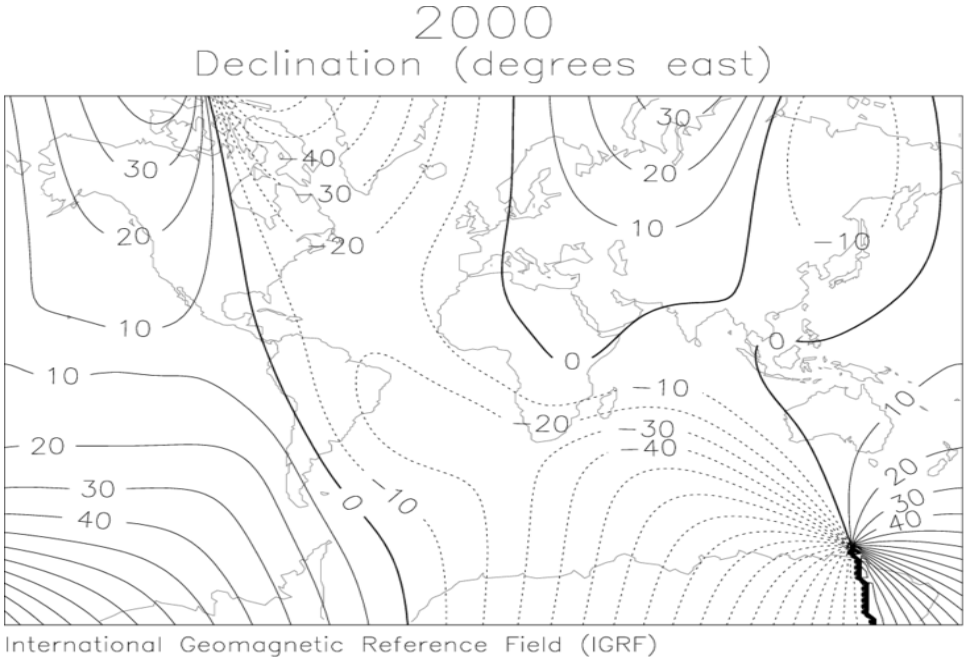

Fig. 8 Magnetic Declination (degrees east) 2000

4.2. Spherical Harmonics

In 1838 the German mathematician and magnetician Frederick Gauss developed a method of representing the magnetic field in terms of a converging series whose terms were functions of latitude, longitude and radial distance from the centre of the earth. In modern notation, the representation is:

$$V = a \sum_{n=1}^{N\max} \left(\frac{a}{r}\right)^{n+1} \left[g_n^m \cos(m\phi) + h_n^m \sin(m\phi)\right] P_n^m(\theta)$$

where

φ refers to longitude

θ refers to latitude

r is the radial distance

n is the degree of the term

m is the order of the term

V is called the scalar potential

The P_n^m are called associated Legendre polynomials which look very much like distorted sine waves. The g_n^m and h_n^m are called Gauss coefficients which are determined through a least-squares analysis of a world-wide distribution of magnetic observations.

In theory the series goes to infinity; in practice some maximum degree, *Nmax* is chosen so that the series is able to reproduce the observed field to the desired resolution and accuracy. For example, for the IGRF, *Nmax = 10*. To reproduce the field originating within the core of the Earth requires *Nmax* = 15. To reproduce crustal anomalies visible in magnetic data at satellite altitudes requires *Nmax* = 80.

The magnetic field components (X, Y and Z) can be calculated from the scalar potential through the following derivatives:

$$X = \frac{1}{r}\frac{\partial V}{\partial \theta} \qquad Y = \frac{1}{r\sin\theta}\frac{\partial V}{\partial \phi} \qquad Z = \frac{\partial V}{\partial r}$$

The International Association of Geomagnetism and Aeronomy (IAGA) released the 10th Generation International Geomagnetic Reference Field (IGRF) — the latest version of a standard mathematical description of the Earth's main magnetic field and used widely in studies of the Earth's deep interior, its crust and its ionosphere and magnetosphere. The coefficients for this degree and order 13 main field model were finalized by a task force of IAGA in December 2004. The IGRF is the product of a collaborative effort between magnetic field modellers and

the institutes involved in collecting and disseminating magnetic field data from satellites and from observatories and surveys around the world.

The IGRF is a series of mathematical models of the Earth's main field and its annual rate of change (secular variation). In source-free regions at the Earth's surface and above, the main field, with sources internal to the Earth, is the negative gradient of a scalar potential V which can be represented by a truncated series expansion:

$$V(r,\theta,\lambda,t) = R\sum_{n=1}^{n_{max}}\left(\frac{R}{r}\right)^{n+1}\sum_{m=0}^{n}\left(g_n^m(t)\cos m\lambda + h_n^m(t)\sin m\lambda\right)P_n^m(\theta)$$

where r, θ, λ are geocentric coordinates (r is the distance from the centre of the Earth, θ is the colatitude, i.e. 90° - latitude, and λ is the longitude), R is a reference radius (6371.2 km); $g_n^m(t)$ and $h_n^m(t)$ are the coefficients at time t and $P_n^m(\theta)$ are the Schmidt semi-normalised associated Legendre functions of degree n and order m. The main field coefficients are functions of time and for the IGRF the change is assumed to be linear over five-year intervals. For the upcoming five-year epoch, the rate of change is given by predictive secular variation coefficients. For more details on main-field modeling, see Chapman and Bartels (1940).

The strength of the field at the Earth's surface ranges from less than 30 microteslas in an area including most of South America and South Africa to over 60 microteslas around the magnetic poles in northern Canada and south of Australia, and in part of Siberia. It should be noted that although we have assumed the field is similar to that of a bar magnet, this similarity is superficial. The magnetic field of a bar magnet, or any other type of permanent magnet, is created by the coordinated spins of electrons and nuclei within the atoms. The Earth's core, however, is hotter than 1043 K, the Curie point temperature at which the orientations of spins within iron become randomized. Such randomization causes the substance to lose its magnetic field. Therefore the Earth's magnetic field is caused not by magnetized iron deposits, but mostly by electric currents in the liquid outer core.

Convection of molten iron within the outer liquid core, along with a Coriolis effect caused by the overall planetary rotation, tends to organize these "electric currents" in rolls aligned along the north-south polar axis. When conducting fluid flows across an existing magnetic field, electric currents are induced which in turn, creates another magnetic field. When this magnetic field reinforces the original magnetic field, a dynamo is created which sustains itself. This is called the "Dynamo Theory" and it explains how the earth's magnetic field is sustained. Another feature that distinguishes the Earth magnetically from a bar magnet is its magnetosphere. At large distances from the planet, this dominates the surface magnetic field. Electric currents induced in the ionosphere also generate magnetic fields. Such a field is always generated near where the atmosphere is closest to the Sun, causing daily alterations which can deflect surface magnetic fields by as much as one degree..

References

Annual Review of Earth and Planetary Science, 1988 16 p.435 Time Variations of the Earth's Magnetic Field: From Daily to Secular by Vincent Courtillot and Jean Louis Le Mouel

Chapman, S., and Bartels, J., (1940), *Geomagnetism, Vol. 1* and 2, Oxford UniversityPress.

Deutschlander, M., Phillips J, Borland S. (1999) The case for light-dependent magnetic orientation in animals. Journal of Experimental Biology 202(8): 891-908

Earth's Radiation Balance and Oceanic Heat Fluxes

(http://oceanworld.tamu.edu/resources/oceanography-book/radiationbalance.htm)

Early Earth atmosphere favourable to life: study

(http://newrelease.uwaterloo.ca/news.php?d=4348)", University of Waterloo (2005-2007)

Friedson, A.J. (2005). Water, ammonia, and H_2S mixing ratios in Jupiter's five hot spots: A dynamical model. Icarus 177, 1-17.

Friedson, A.J., A-S Wong, Y.L Yung (2002). Models for polar haze formation in Jupiter's stratosphere. Icarus 158, 389-400.

Herndon, J. Marvin (1996) Substructure of the inner core of the Earth Vol. 93, Issue 2, 646-648, January 23, 1996, PNAS

Hollennbach, D.F. and J.M. Herndon (2001) Deep-Earth reactor: Nuclear fission, helium, and the geomagnetic field. Published online before print September 18, 2001, 10.1073/pnas.201393998.

Hulot, G., Eymin C, Langlais B, Mandea M, Olsen N. (2002) Small-scale structure of the geodynamo inferred from Oersted and Magsat satellite data. Natufe 416 (6881): 620-3

Vercheval, J The thermosphere: a part of the heterosphere (http://www.oma.be/BIRA-IASB/Public/Research/Thermo/Thermotxt.en.html))

Lutgens, Frederick K. and Edward J. Tarbuck (1995) The Atmosphere, Prentice Hall, 6th ed., pp14-17, ISBN 0-13-350612-6.

Neil, F. C., (2001) Discovering the Essential Universe

Towle, J.N. (1984). The Anomalous Geomagnetic Variation Field and Geoelectric Structure Associated with the Mesa Butte Fault System, Arizona. In: Geological Society of America, Bulletin, 95:221, 1984.

NIGERIAN JOURNAL OF SPACE RESEARCH **8**: 349 – 390, 2009 September 1

A Review of MAGDAS/CPMN Project During IHY

Kiyohumi YUMOTO Ph.D., and the MAGDAS/CPMN Group
Space Environment Research Center, Kyushu University,
6-10-1 Hakozaki, Higashi-ku, Fukuoka 812-8581, Japan
Email: yumoto@serc.kyushu-u.ac.jp

Table of Contents

1. Introduction

In 1957–58, more than 66,000 scientists and engineers from 67 nations participated in the International Geophysical Year (IGY). Fifty years on, the International Heliophysical Year (IHY) again drew scientists and engineers from around the globe in a coordinated campaign to observe the heliosphere and its effects on planet Earth. For the benefit of scientists and

engineers from developing nations, the United Nations Office for Outer Space Affairs, through the United Nations Basic Space Science Initiative (UNBSSI), assisted scientists and engineers from all over the world in participating in the activities of IHY 2007–2009 (United Nations, 2006).

The IHY was an extensive international program undertaken to study the universal physical processes in the heliospace in order to gain a better understanding of the Sun-heliosphere system (Yumoto et al., 2009b). Particular attention was paid to the neutral and ionized matter in the heliospace from the Sun to the atmospheres of Earth and the other planets and throughout the interplanetary medium. The IHY continued the legacy of the IGY by extending the geophysical studies performed 50 years ago to the combined system of the Sun and the planets. IHY also extended the physical realm from geospace to heliospace, recognizing the enormous progress made over the past 50 years. There were four key elements of IHY: 1) science (coordinated investigation programs conducted as campaigns to investigate specific scientific questions, 2) instrument development (the IHY/UNBSS program), 3) public outreach (to communicate the beauty, relevance and significance of space science to the general public and students), and 4) the IGY Gold Club program (to identify and honor the scientists who participated in the IGY program).

In June of 2006, the Science Council of Japan formally recognized the STPP (Solar Terrestrial Physics Program) subcommittee for International Affairs, Committee on Earth and Planetary Sciences, as the IHY National Steering Committee for Japan. The committee was chaired by Kiyohumi Yumoto and promoted the followings (see the details of Yumoto et al., 2009b)

(1) satellite missions launched or to be launched by Japan,
(2) international network observations,
(3) public outreach,
(4) international and domestic workshops, and
(5) nomination of Japanese scientists as IGY Gold Club members.

On the other hand, one purpose of the Solar Terrestrial Physics (STP) research in the twenty-first century is to support human activities from an aspect of fundamental study. The scientific new aim for the STP society is a creation of new physics; (1) couplings of the complex and composite systems and (2) multi-scale couplings in the Sun-Earth system. The goals for the attainment of the purpose are to construct Network Stations for observations and Modeling Stations for simulation/ empirical modeling. In order to understand the Sun-Earth system and its effects to human lives, the international LWS (Living With Star) and CAWSES (Climate And Weather of Sun-Earth System) programs started from 2004. The International Heliophysical Year (IHY) program also started in 2007.

For space weather study on the complexity in the Sun-Earth system, the Space Environment Research Center (SERC), Kyushu University started to construct a new ground-based magnetometer network, in cooperation with about 30 organizations around the world from 2004 (Yumoto et al., 2006 and 2007, Otadoy, et al., 2009). The SERC is conducting the MAGDAS (MAGnetic Data Acqusition System) observations along 210° magnetic meridian (MM) and along the magnetic equator in the CPMN (Circum-pan Pacific Magnetometer Network) region (Yumoto et al., 2009c and 2009d), and the FM-CW (Frequency Modulated Continuous Wave) radar observations along the 210°MM (Ikeda et al., 2008 and 2009, Yumoto et al., 2009e), in order to understand dynamics of plasmaspheric changes during space storms, responses of magnetosphere-ionosphere-thermosphere to various solar wind changes, and penetration mechanisms of DP2-ULF range disturbances from the solar wind region into the equatorial ionosphere. From 2008, MAGDAS-II magnetometers have been installed along the 96° magnetic meridian in Africa to understand the longitudinal dependence of long-, short-term Sq variations, DP-2, sc, si, and of Ultra Low Frequency (ULF) waves (Maeda G. et al., 2009, Rabiu et al., 2009a and 2009b). On the other hand, electromagnetic phenomena, e.g., ULF, ELF and VLF waves are recognized as useful diagnostic probes of the solar wind-magnetosphere-

ionosphere- atmosphere coupled system for space weather studies. These waves convey information about the dynamics and morphology of the coupled system.

In the present review paper, at the first we will introduce our real-time data acquisition and analysis systems of MAGDAS/CPMN and MAGDAS-II, and scientific results obtained by these systems during the IHY (2007-2009); (1) the global 3-dimensional current system to understand the electromagnetic coupling of high-latitude, Sq, and EEJ current systems and their long-term variations, and (2) global characteristics of ULF waves (Pc 3, 4, and 5, and Pi 2) in geo-space to know magnetospheric environment changes during storms and substorms. In the second, we will show the FM-CW radar systems along the 210°MM to deduce electric field variations from the ionospheric plasma Doppler velocity. From 24hr measurement of the ionospheric drift velocity with 3 and/or 10-sec sampling rate by the FM-CW radar observation, (3) we can understand how the polar electric field penetrates into the equatorial ionosphere.

2. MAGDAS/CPMN network

2.1. Motivation

The MAGnetic Data Acquisition System (MAGDAS) group at the Space Environment Research Center (SERC) of Kyushu University, Fukuoka, Japan seeks to deploy around the world in a strategic fashion a new generation of tri-axial fluxgate magnetometers (called MAGDAS) that transfer the digitized data to a central SERC server in real-time for space weather study and application during the IHY period (2007–2009). The strategy is to put the magnetometers in well-defined ‘‘bands’’ on the globe that are useful for scientific exploration.

The first band is the strip that goes north and south of Japan—up to Siberia and down to the Antarctic. In our geo-space field, this north–south band is also known as the ‘‘210 Magnetic Meridian’’ and became famous in this field of geospace research (Yumoto and the 210MM Magnetic Observation Group, 1996a). After the international solar terrestrial energy program (STEP) period (1990–1997), 1-sec magnetic field data from coordinated ground-based network stations made it possible to (1) study magnetospheric processes by distinguishing between

temporal changes and spatial variations in the phenomena, (2) clarify global structures and propagation characteristics of magnetospheric variations from polar to equatorial latitudes, and (3) understand the global generation mechanisms of various solar-terrestrial phenomena (Yumoto and the CPMN group, 2001). In this north–south band, the average spacing of magnetometers is 500 km. The most northern magnetometer is at Cape Schmidt in northern Russia. The most southern magnetometer is located at Davis Station of AAD (Australian Antarctic Division).

The second band is the geo-magnetic ‘‘dip’’ equator. SERC has completed most of the installations along this band (see Yumoto and the MAGDAS Group, 2007) (One big gap however is the Pacific Ocean; we are still searching for a suitable island in the middle of it). The third band runs up and down the continent of Africa; SERC has already completed one installation in South Africa (at the Hermanus Magnetic Observatory) and one in Egypt near Cairo. The fourth band runs up and down the Americas; SERC has completed several MAGDAS installations in North and South America. Figure 1 is a map of MAGDAS and MAGDAS II stations.

With scientifically significant real-time data arriving at SERC from over 40 identical magnetometers (and identically calibrated magnetometers, and which are sensitive down to the nT level), SERC seeks to conduct socially beneficial space weather forecasting. SERC also has a policy to establish an important new research tool for the geospace community: Our EE-index (EDst, EU, and EL) in sub-session 3.3. is being proposed to monitor transient and long-term variations of the Equatorial Electrojet by using MAGDAS/CPMN real-time data (Uozumi et al. 2008).

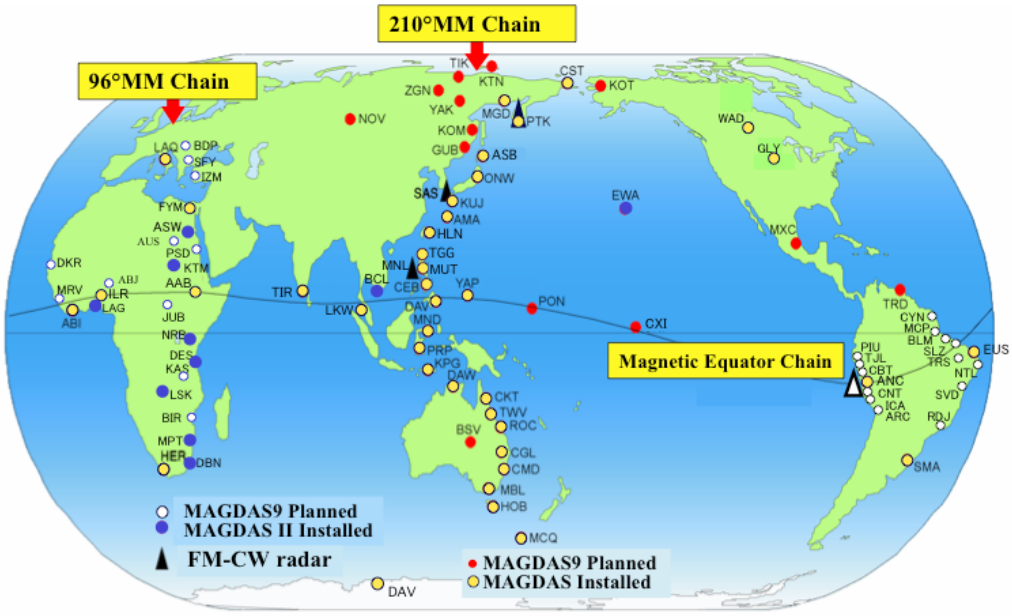

Fig. 1. MAGDAS/CPMN (MAGnetic Data Acquisition System/Circum-pan Pacific Magnetometer Network). The non-blue dots are installed or soon-to-be installed MAGDAS magnetometers. They are concentrated in four bands. The black triangles are SERC FM-CW radars (for ground-based observation of the ionosphere). The blue dots are MAGDAS II magnetometers but whose discussion go beyond the scope of this paper (Colour online)

With scientifically significant real-time data arriving at SERC from over 40 identical magnetometers (and identically calibrated magnetometers, and which are sensitive down to the nT level), SERC seeks to conduct socially beneficial space weather forecasting. SERC also has a policy to establish an important new research tool for the geospace community: Our EE-index (EDst, EU, and EL) in 3.3. sub-session is being proposed to monitor transient and long-term variations of the Equatorial Electrojet by using MAGDAS/CPMN real-time data (Uozumi et al. 2008).

2.2. Description of MAGDAS

The MAGDAS system is divided into two portions: MAGDAS-A and MAGDAS-B. MAGDAS-A is a real-time magnetometer unit installed at Circum-pan Pacific Magnetometer

Network (CPMN) stations, while MAGDAS- B is a data acquisition and monitoring system installed at SERC. MAGDAS-A as a whole consists of a sensor unit, data logger/transfer units, and power supply (Fig. 2). The sensor unit of MAGDAS-A system consists of tri-axial ring-core sensors, two tilt-meters and a thermometer (Fig. 3). Magnetic field digital data (H+dH, D+dD, Z+dZ, F+dF) are obtained with the sampling rate of 1/16 s, and then the 1-sec averaged data are transferred from each overseas station to SERC, Japan, in real time (Yumoto and MAGDAS Group 2006). To facilitate installation in just about any spot on the globe, MAGDAS-A was specially designed to be portable (hand-carried suitcase) and lightweight (just 15 kg). Visible in Fig. 2 are all vital components. The required power is just 20 W. The best way for SERC to get the data in real-time from this instrument (we have found out from sheer experience) is via the Internet. (The machine was designed with other options.) However, for redundancy, the data is stored onto a high-capacity compact flash semiconductor memory card (1.0 or 0.5 GB). The cord for the GPS antenna is about 25 m. This antenna is usually placed on the roof of the building in which the main case resides. The sensor is placed in a separate structure to be away from building-related noise (e.g., noise from electric motors). To allow ample separation, the sensor cable is 70 m in length. In Fig. 2a, the cable is wound up on the reel (to allow for delivery from SERC to the final site overseas). The component of MAGDAS is described in Fig. 2b.

The sensor's analog data is continuously digitized. The ambient magnetic fields, expressed by horizontal (H)-, declination (D)-, and vertical (Z)-components, are digitized by using the field-canceling coils for the dynamic range of ±64,000nT/16bit. The magnetic variations (dH, dD, dZ) subtracted from the ambient field components (H, D, Z) are further digitized by a 16-bit A/D converter. Two observation ranges of ±2,000 nT and ±1,000 nT can be selected for high- and low-latitude stations, respectively.

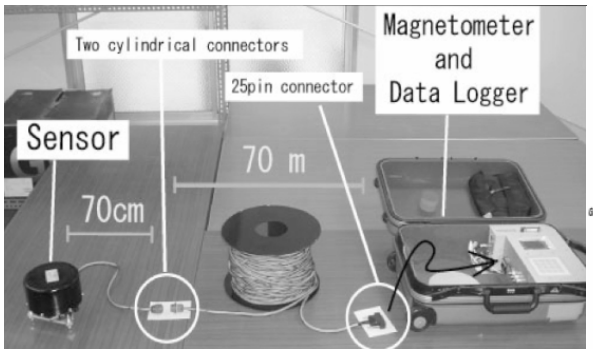

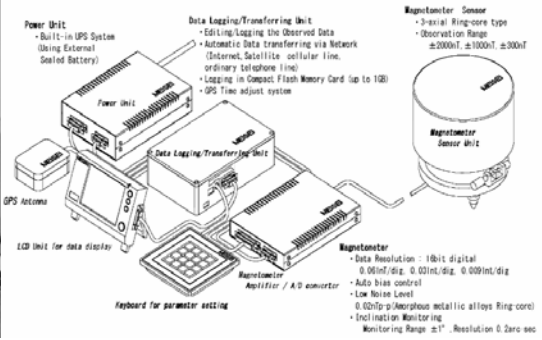

Fig. 2a **Fig. 2b**

Fig. 2a. This is photo of MAGDAS Unit 08 (taken at SERC by G. Maeda). Easily visible are the: (1) grey AC power cord, (2) round and black sensor with its 1-meter cable, (3) the 70-meter cable reel, (4) main case (modified travelers suitcase), and (5) GPS antenna with 25-meter cord. The output of the sensor is analog. The electronics inside the main case converts this analog data into digital data, which is sent to SERC via the Internet and is stored locally on a CF card for redundancy. Fig. 2b. The component of MAGDAS/CPMN magnetometer system for real-time data acquisition.

The total field (F + dF) is estimated from the H + dH, D + dD, and Z + dZ components. The resolution of MAGDAS data is 0.061nT/LSB and 0.031nT/LSB for the ±2,000 nT range and ±1,000 nT range, respectively. About 1.5 MB of data is generated each day as a result. Data from all MAGDAS units flow into a central server at SERC. This raw data must be processed to become scientifically useful. All the processing takes place here at SERC. This data can be accessed by anyone via the Web (http://magdas.serc.kyushu-u.ac.jp/), with some conditions attached.

Installation of the sensor (see Fig. 3) is complicated because it must be carefully aligned in three ways. First, it must be pointed exactly north with precision threading. Second, it must be perfectly level (resulting in two orthogonal adjustments). This levelness is achieved with the precision threading of a tripod base. The long-term inclinations (I) of the sensor axes can be measured by two tilt-meters with resolution of 0.2 arc-sec. The temperature (T) inside the sensor unit is also measured. GPS signals are received to ‘‘keep correct’’ the standard time

inside the data logger/transfer unit. These data are recorded on to the compact flash memory card as data backup.

Fig. 3 This is the MAGDAS sensor with the round and black cover removed. The two brass-colored devices are precision tiltmeters. The rest form a tri-axial fluxgate magnetometer. This photo was taken at SERC by G. Maeda last year when the magnetometer had to be repaired (Colour online)

2.3.Calibration for temperature drift of MAGDAS

For quantitative analysis of various geomagnetic phenomena, which are observed in wide longitudinal and latitudinal area (e.g., as shown in Fig. 1), it is necessary to analyze precise and standardized magnetic field data. For instance, the stability of the base magnetic variation and the absolute sensitivity are very important for the study of the Equatorial Electrojet (EEJ) and Counter Electrojet (CEJ) (e.g., Uozumi et al., 2008), Sq (e.g., Yamazaki et al., 2009b), SC/SI (e.g., Kitamura et al., 1998, Yumoto et al., 1996b and 2009e) and ULF (e.g., Yumoto et al., 1996 and 20001, Uozumi et al., 2004 and 2009b; Abe et al., 2006, Tokunaga et al., 2007). It is also indispensable to grasp the accuracy of the data to be analyzed, because this matter critically limits the quantitative validity or reliability of analyses. Thus, Uozumi et al. (2009a) have investigated and developed a calibration technique for the MAGDAS/CPMN ground magnetic field data, which is obtained by MAGDAS fluxgate magnetometer made by the Meisei Electric Co., Ltd. They have also evaluated quantitatively the suitability of the method, and estimated the expected accuracy of the calibrated MAGDAS magnetic data. The result

provides fundamental information on the accuracy limit of MAGDAS magnetic data, and would be standard of the reliability on all geophysical results derived by the MAGDAS data.

The thick curves in Figure 4 plot the raw (original) magnetic field (*H*, *D*, *Z*, *F*) and the sensor-head temperature (*T*), which was observed at Sasaguri station (GGLAT=33.64°, GGLON=130.51°) during the period of September 7-18, 2007 in JST (UT+9hour). Sasaguri Station is the observatory for experimental tests and calibration of MAGDAS/CPMN magnetometer system, and is located in the suburban area near SERC (about 8km distance). As shown in Fig. 4, nighttime variations of the *H*, *D*, *Z* and *F* tend to increase/decrease as *T* decreases. Dashed lines indicate the trend of the variation for each component around midnight. The thin curves in Fig. 4 represent the corrected data. It is well known that the base nighttime magnetic variation traces close to straight line for the first approximation, except the time of active geomagnetic situation such as magnetic storm (e.g., Matsushita and Campbell, 1967). Thus magnetic variation, which is correlated with temperature variation, is considered as not geomagnetic phenomena but artificial variation. The artificial component of the magnetic variation is well correlated with the temperature variation. Thus, they assumed that the artificial component of the magnetic variation is proportional to the temperature variation. They called this type of magnetic variation as “temperature drift”. Based on this assumption, they developed a correction technique of the MAGDAS magnetic field data. Magnetic field variation, which was observed by MAGDAS magnetometer of the serial number 6 (SN06) during the period of September 7-18, 2007, was used as test data for developing the correction method. The detail of the correction method is explained in the paper of Uozumi et al. (2009a). The corrected data represent that the nighttime variation traced almost a constant value. On the other hand in daytime, daily magnetic variation, so-called Sq (solar quiet) variation is usually observed. The real geomagnetic variation should be estimated by correcting the original data. They confirmed that the raw magnetic field data can be corrected by subtracting the temperature drift component, which will be estimated by the derived factor. Theye evaluated the quantitative

validity of the correction method. The correction method is concluded to be suitable for practical use.

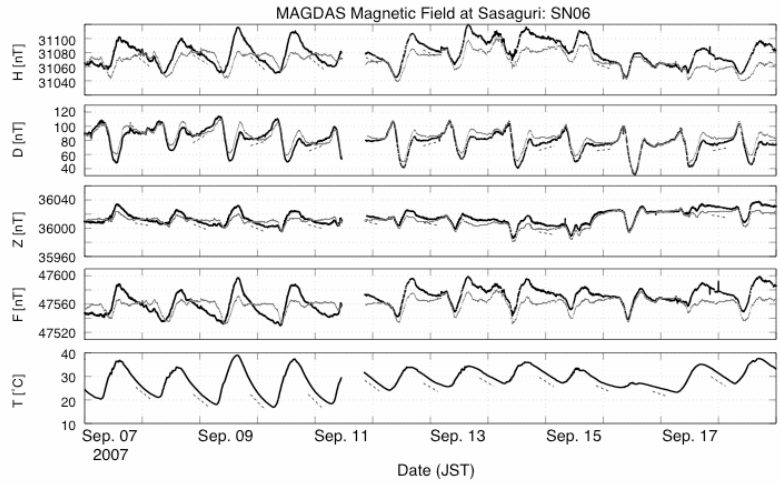

Fig. 4. Thick curves plot the MAGDAS raw (original) magnetic field (H, D, Z, F) and the sensor-head temperature (T) observed at Sasaguri during the period of Sep. 7-18, 2007 (JST). Thin curves plot corrected magnetic field data of each component. Dashed lines indicate the trend of the variation for each component around midnight.

4.0. Scientific objectives and recent MAGDAS results

In order to establish the space weather studies, we have to clarify dynamics of geospace plasma changes during magnetic storms and auroral substorms, the electro-magnetic response of iono-magnetosphere to various solar wind changes, and the penetration and propagation mechanisms of DP2-ULF range disturbances from the solar wind region into the equatorial ionosphere. Figure 5 shows one example of amplitude-time records of 3-component ordinary (upper) and induction-type (bottom) magnetograms observed at the Kujyu station in Oita, Japan, during 24 hrs. The ordinary data (i.e. MAGDAS data (1)) can be used for studies of long-term variations, e.g. magnetic storm, auroral substorms, Sq, etc., while the induction-type data (i.e. MAGDAS data (2)) will be useful for studies of ULF waves, transient and impulsive phenomena. By using these new MAGDAS data, we can conduct a real-time monitoring and modeling of (1) the

global 3-dimensional current system and (2) the ambient plasma density for understanding the electromagnetic and plasma environment changes in the geospace.

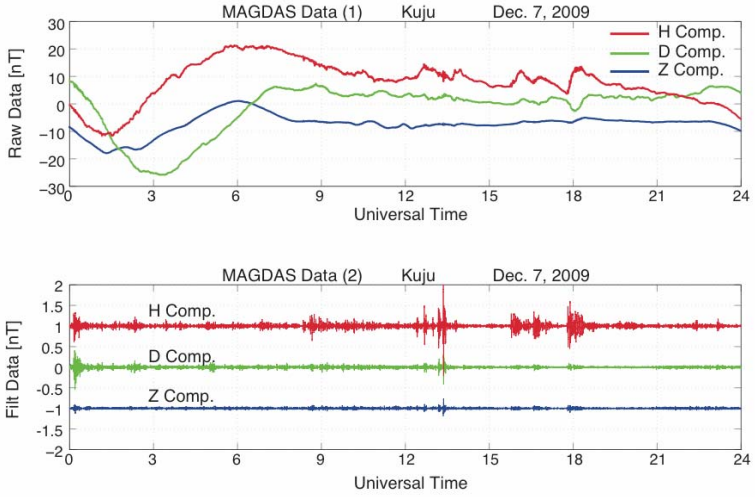

***Fig. 5**. An example of amplitude-time records of ordinary (upper; MAGDAS data (1)) and induction-typ.*

3.1. Imaging of global 3-D current system

The left panel of Figure 6 indicates the ionospheric equivalent current pattern obtained from the CPMN stations along the 210°magnetic meridian during a northern summer. Each ionospheric current vector was estimated by the horizontal magnetic fields observed at each CPMN station at every hour. We will make the ionospheric equivalent current pattern every day using the MAGDAS data (1) as shown in Fig. 5. The right panel of Fig. 6 shows the global 3-dimensional currents and electric potential, with the currents illustrated by ribbons and the potential with + and – (Richmond and Thayer, 2000). At high latitudes the ionospheric currents are joined with **f**ield-**a**ligned **c**urrents (FAC) from the solar wind region into the magnetosphere, and the electro-dynamics is dominated by the influences of solar wind-magnetosphere interaction processes. The total current flows is of the order of 10^7 A. On the other hand, the ionospheric current at middle and low latitudes is generated by the ionospheric wind dynamo, which produces global current vortices on the dayside ionosphere, i.e., counterclockwise in the

northern hemisphere and clockwise in the southern hemisphere. The total current flow in each vortex is order of 10^5 A.

There are strong electric fields at high latitudes, on the order of several tens of millivolts per meter or more depending on the magnetic activity. At middle and low latitudes electric fields are considerably smaller, typically a few millivolts per meter during magnetically quiet periods. During magnetic active periods the part of strong electric fields at high latitude can penetrate into middle and low latitudes, and then the global ionospheric current pattern must be re-organized strongly. In reality the current and electric fields at all latitudes are coupled, although those at high, and middle and low latitudes have been often considered separately. By using the MAGDAS ionospheric current pattern as shown in the left panel of Figure 6, the global electromagnetic coupling processes at all latitudes will be clarified during the ISWI period (2010-2012).

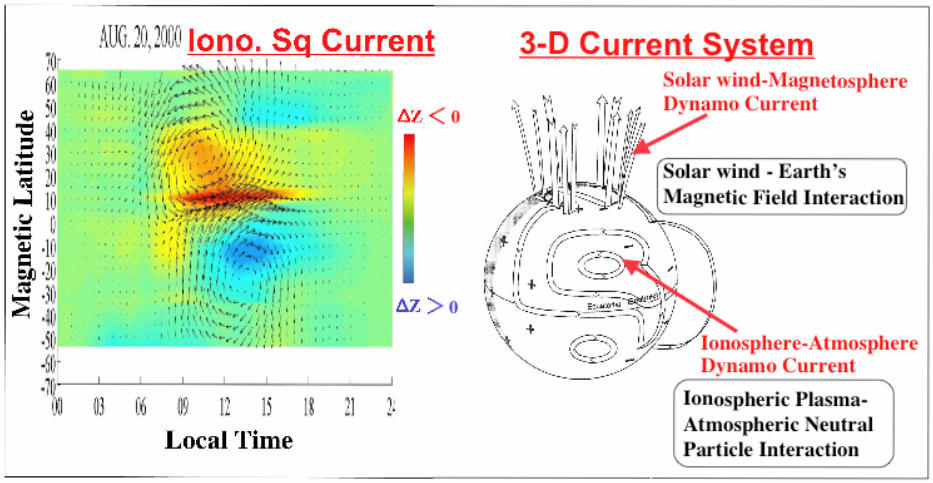

Fig. 6. *(Left) The ionospheric equivalent current pattern obtained from the MAGDAS/CPMN data. (Right) Global 3-dimensional current system cased by magneto-spheric field-aligned currents at high latitude and the ionospheric dynamo at middle and low latitudes.*

Figure 7a shows equivalent ionospheric current patterns obtained from the MAGDAS Data (1) on September 25, 2005 (Kohta et al., 2005). The vertical axis indicates magnetic latitudes of the MAGDAS stations, and the horizontal axis is the local time of the 210° magnetic meridian

stations. The arrows indicate the current vectors obtained from the H and D components, and the color code indicates the negative and positive magnetic Z component. The equatorial electrojet can be seen at the dayside dip equator. There are twin vortices of Sq current, i.e., counter-clockwise and clockwise in the northern and southern hemisphere, respectively. The centers of Sq current patterns are sometime not consistent with the maximum and minimum points of the Z component. Figure 7b is one example of Sq equivalent current pattern obtained by the CPMN data on July 15, 2000, during a disturbed day. The vertical axis indicates geographic latitudes of the CPMN stations, and the horizontal axis is the local time of the 210^{o} magnetic meridian stations. A clear Sq current vortex, equatorial electrojet, auroral electrojet, and ring current patterns can be identified in the figure. It is newly found a current flowing from the northern hemisphere into the southern hemisphere around 06 hr local time during magnetic storm.

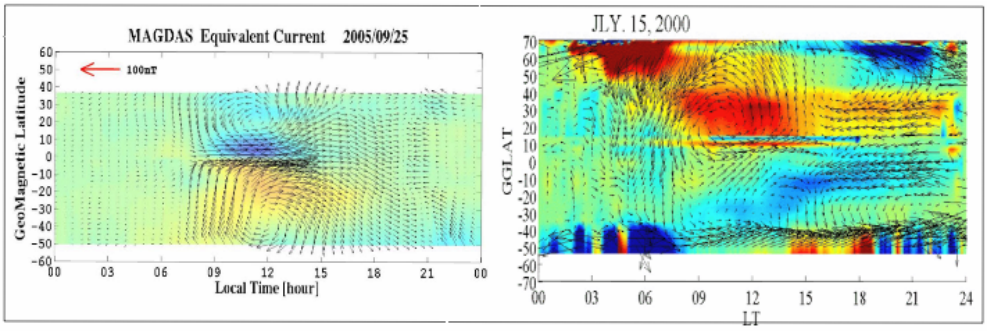

Fig. 7a and 7b. *MAGDAS Sq current pattern on September 5, 2005 during magnetic quiet day (left), while CPMN Sq current pattern on July 15, 2000 during magnetic disturbed day (right) (Kohta et al., 2005).*

3.2. Annual and semi-annual Sq current variations

Yamazaki et al. (2009b) analyzed ground magnetometer data for the 10 International Quiet Days during 1996-2007. The data were obtained from 19 stations along 210◦ Magnetic Meridian (MM) of the Circum-pan Pacific Magnetometer Network (CPMN) covering both the northern and southern hemispheres. From the daily variations of the geomagnetic field, we deduced the latitude-local time (LAT, LT) diagram of the equivalent Sq current system, which can be regarded as the superposition of the following three current systems: **Sq0**, **Sq1** and **Sq2**

current systems. The **Sq0**, **Sq1** and **Sq2** current systems are equivalent current systems for the yearly average, annual variation and semi-annual variation of the Sq field, respectively. We have examined temporal and spatial features of these current systems. The principal features are as follows: (1) the total current intensity of the **Sq1** and **Sq2** current systems are about 35% and 15% of the **Sq0** current system, respectively. (2) the **Sq0** and **Sq2** current systems have a dayside vortex in each hemisphere, while the **Sq1** cur rent system has a single vortex centered at the equatorial region in the morning sector (~ 10 LT).

They analyzed hourly data of the daily variation of the geomagnetic field components ΔH and ΔD, where the Δ symbol represents the deviation of the geomagnetic field value from the zero level which is defined as the mean of the nighttime values (i.e., the values at 0000, 0100, 0200, 2200 and 2300 L.T.). The data of 10 International Quiet Days during 1996-2007 (as given by German Research Center for Geosciences (GFZ)) were selected. As is often pointed out, the International Quiet Days are not necessarily 'quiet' days but are just 'quietest' days for each month [e.g., Hibberd, 1981]. Consequently, the data for the International Quiet Days sometimes include severe effects from the magnetospheric and auroral activity, which can make irregular variations comparable to or larger than Sq variation range. Therefore, any visually-disturbed days which include irregularity obviously larger than Sq variation range were eliminated. The period of the analysis (i.e., 1996-2007) covers almost one solar cycle. The solar activity is known to control amplitudes of the Sq variation (ΔH, ΔD and ΔZ) [Rastogi et al., 1994]. Therefore, in order to reduce the solar-activity effect on the Sq amplitudes (ΔH and ΔD), the selected quiet days were divided into two levels of the solar activity (i.e., "high" and "low") based on the daily F10.7 solar flux data. They note that our distinction between "high" and "low" solar activity does not depend on the time of solar cycle. The data with $150 \leq F10.7 < 250$ were classified as the data for the "high" solar activity period. On the other hand, the data with $50 \leq F10.7 < 150$ were classified as the data for the "low" solar activity period. ΔH and ΔD are analyzed as a function of station latitude Φ, day of year d, local time LT and solar activity SA ("high" or "low"), i.e., ΔH(Φ, d,LT, SA) and ΔD(Φ, d,LT, SA), respectively. For a

given Φ, LT and SA, ΔH(d) is represented by the sum of the following three components, namely, stationary component (ΔH0), annual component (ΔH1) and semi-annual component (ΔH2) as follows:

$$\Delta H(d) \sim \Sigma \Delta Hi(d) = \Delta H0 + \Delta H1(d) + \Delta H2(d) \qquad (1).$$

In the same manner, ΔD(d) is represented.

Figure 8 shows the LAT-LT diagram of the **Sq**0 current system (i.e., the equivalent current system for the yearly average of the Sq field) for the ”high” and ”low” solar activity period. It is seen that the **Sq**0 current system is composed of two dayside vortices with clockwise direction in the southern hemisphere and counter-clockwise in the northern hemisphere. Figures 9 and 10 show LAT-LT diagrams of the **Sq**1 and **Sq**2 current systems (i.e., the equivalent current systems for the annual and semi-annual variations of the Sq field), respectively, for different seasons of the ”high” solar activity periods. This is the first time that the equivalent current systems of the annual and semi-annual Sq variations are derived. The morphology of the **Sq**1 current system is characterized by a single vortex pattern centered at the equatorial region in the morning sector (~ 10 L.T.), on the other hand, the **Sq**2 current system is composed of two dayside vortices like the **Sq**0 current system.

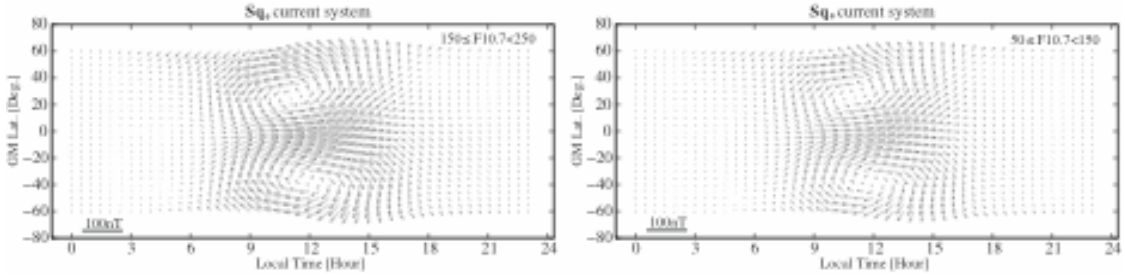

Fig. 8. The LAT-LT diagram of the Sq0 current system (i.e., the equivalent current system for the yearly average of the Sq field) during the ”high” solar activity period (left panel) and ”low” solar activity period (right panel). See the section 2 of Yamazaki et al.(2009) for the construction details of the LAT-LT diagram.

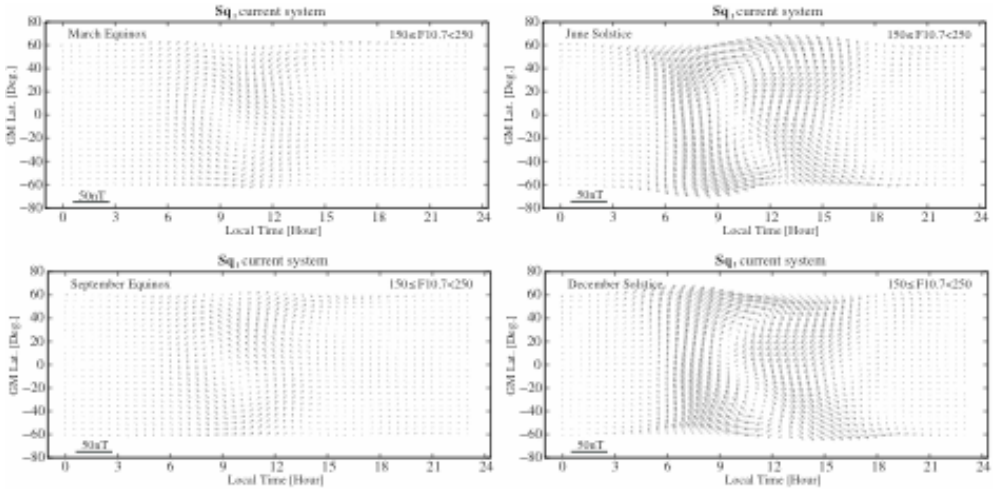

Fig. 9. The LAT-LT diagram of the Sq1 current system (i.e., the equivalent current system for the annual variation of the Sq field) for March equinox (D.O.Y. = 80, upper left), June solstice (D.O.Y. = 172, upper right), Spring equinox (D.O.Y. = 264, lower left) and December solstice (D.O.Y. = 355, lower right) during the "high" solar activity period.

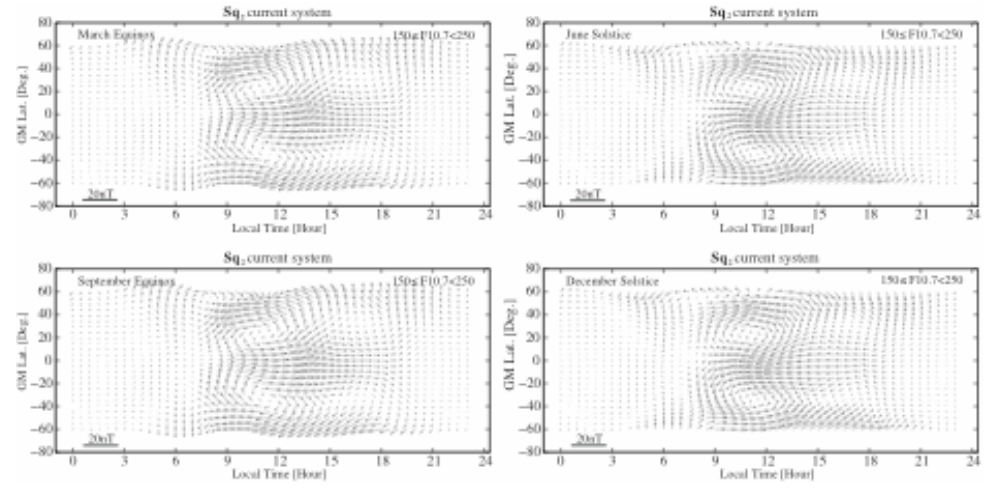

Fig. 10. The LAT-LT diagram of the Sq2 current system (i.e., the equivalent current system for the semi-annual variation of the Sq field) for March equinox (D.O.Y. = 80, upper left), June solstice (D.O.Y. = 172, upper right), Spring equinox (D.O.Y. = 264, lower left) and December solstice (D.O.Y. = 355, lower right) during the "high" solar activity period.

They compared the yearly-averaged total current intensities among the **Sq**0, **Sq**1 and **Sq**2 current systems. For each current system, the total current intensities from DOY = 1 to DOY = 365 was calculated and were averaged. It was found that the yearly-averaged total current

intensity of the **Sq**0 current system is the largest of the three. The ratio of the yearly-averaged total current intensity of the **Sq**1 current system to that of the **Sq**0 current system (**Sq1**/**Sq0**) is 0.31 for the ”high” solar activity period and 0.38 for the ”low” solar activity period. On the other hand, the **Sq2**/**Sq0** is 0.15 and 0.16 for the ”high” and ”low” solar activity periods, respectively. They also examined phases of the **Sq**1 and **Sq**2 current systems. The phase is given by the day number d of the first peak in the total current intensity of the **Sq**1 and **Sq**2 current systems. The phase of the **Sq**1 current system appears on d = 186 (July 5) and d = 185 (July 4) for the ”high” and ”low” solar activity periods, respectively, which are about 10 days after the June solstice (June 21). On the other hand, the phase of the **Sq**2 current system appears near the March equinox (March 21) on d = 87 (March 28) and d = 83 (March 24) for the ”high” and ”low” solar activity periods, respectively.

3.3. A new EE-index and its long-term variation

A new index, EE-index (EDst, EU, and EL), is proposed by Uozumi et al. (2008) to monitor temporal and long-term variations of the equatorial electrojet by using the MAGDAS/CPMN real-time data. The mean value of the H component magnetic variations observed at the nightside (LT = 18–06) MAGDAS/CPMN stations along the magnetic equatorial region is found to show variations similar to those of Dst; we defined this quantity as EDst. The EDst can be used as a proxy of Dst for the real-time and long-term geospace monitoring. By subtracting EDst from the H component data of each equatorial station, it is possible to extract the Equatorial Electrojet and Counter Electrojet components, which are defined as EU and EL, respectively.

Figure 11a shows a superposed plot of the relative magnetic variation of the H component data ERS(m) (definition given just below) obtained for 1 month (Dec. 1–31, 2006), at the MAGDAS equatorial stations: Addis Ababa (AAB: Dip Lat. = 0.57◦; GMLON = 110.47◦), Davao (DAV: −0.65◦; 196.54◦), Ancon (ANC: 0.74◦; 354.33◦) and Eusebio (EUS: −7.03◦; 34.21◦). The “S” and “m” in “ERS(m)” refer to a station and a point of time in UT, respectively. In order to

obtain ERS(m), the median value of the H component data, which is determined for the period from the start time of the observation to the end time of ERS(m), was subtracted from the original magnetic data for each station. It was found (not shown) that the median value, which was calculated from all the data in the abovestated interval, could estimate the non-disturbed nighttime ambient level. The determination by shorter-period data might cause some jumps in the base level among different periods (it might occur in particular during disturbed times when large magnetic storms occurred frequently). Thus the median value was calculated for the period from the start time of the observation to the end of the ERS(m). In the future the subtracting offset value will be corrected by taking into account the secular variation of the base level, though the value is currently determined as a constant.

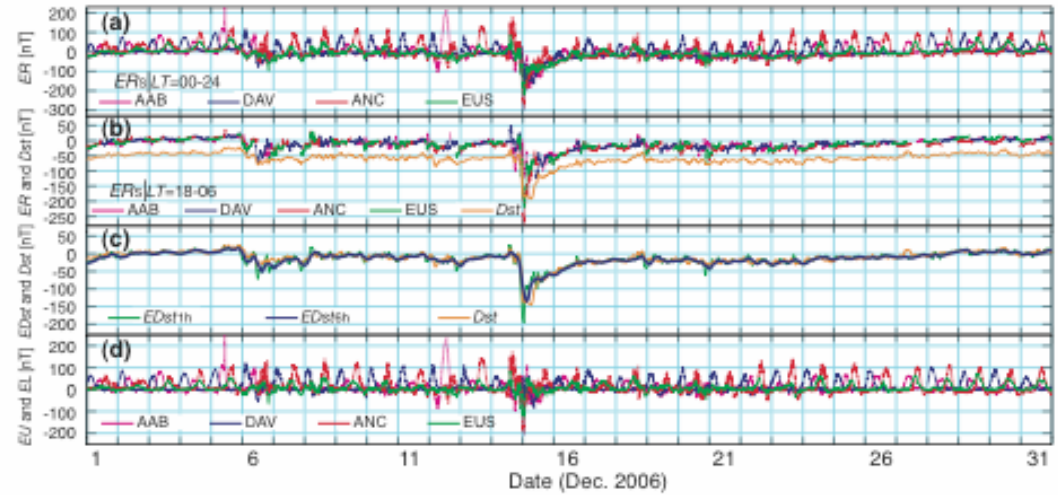

Fig. 11. One month plot of (a) relative magnetic variation of the H component (ERS |LT=00–24) observed by MAGDAS/CPMN equatorial network stations, (b) relative night time (LT=18–06) variation of the H component (ERS |LT=18–06) and the real-time Dst, (c) EDst1h, EDst6h and the real-time Dst, and (d) EU and EL for MAGDAS/CPMN equatorial network stations, during one month of December 2006.

Figure 11b plots the superposed H component perturbation field data that was observed during the night time (LT = 18–06) at each station: ERS(m) |LT=18–06. The solid thick curve (orange) in Fig. 11b is the Dst value for the same plot interval. This Dst was provided in real-time on the website of the World Data Center for Geomagnetism, Kyoto (http://swdc234.kugi.kyoto-

u.ac.jp/dst realtime/). In this figure, Dst was graphically shifted downward so as to avoid overlap with MAGDAS/CPMN data. It is noticed that the nighttime variation of each station was almost aligned with each other and formed a common base magnetic variation. On the other hand, by comparing Fig. 11a and 11b, it can be confirmed that the daytime EEJ component of each station bulged out independently from the base magnetic variation. With this presentation, it is evident that the base magnetic variation ERS(m) |LT=18–06 varies closely with the traditional Dst (Sugiura, 1963). This similarity will be further examined later in this section. "EDst1h" is one-hour average of EDst1m. In Fig. 11c, EDst1h is plotted the green curve. The blue and orange curves in Fig. 11c are 6-h running averages of EDst1h (labeled EDst6h) and the real-time Dst, respectively. Dst is shifted +42 nT to adjust the base level. It is confirmed that the EDst and Dst exhibited the similar temporal variation. It is noticed that EDst6h is less deviated from Dst than EDst1h. Correlation coefficients between EDst6h and Dst, and that between EDst1h and Dst, which were calculated for the 1-month period of December 2006, were 0.93 and 0.88, respectively. It is also found that the correlation coefficient between the low-pass-filtered EDst6h and the low-pass-filtered Dst with the cut-off-period of 2 days was 0.98 is larger than the above-mentioned 0.93.

Figure 11d shows the relative magnetic perturbation of each station, which was calculated by subtracting EDst6h from the H component data. In this calculation, EDst6h was converted to 1-min resolution data by interpolating the original EDst6h through application of the FIR (finite duration impulse response) low-pass interpolating method. It is considered that the positive and negative deviations represent the EEJ and CEJ components, respectively. Uozumi et al. (2008) define those two component as EUS(m) and ELS(m), respectively. For example, when the EU and EL components are derived for the DAV station, those values are expressed as EUDAV(m) and ELDAV(m), respectively. Inspection of these data reveals that the EEJ intensity varies from day to day; moreover, the peaks and dips of each station are not in-phase with other stations. For example, the intensity of EEJ at the DAV station (blue line) and at the ANC station (red line) attained local maxima on Dec. 6 and 8, respectively. The mechanism of the 2-

day separation is one of the open questions concerning EEJ. In some cases, it will be necessary to correct the secular variation of a base level to determine EDst6h for properly extracting the EU and EL component.

Uozumi et al.(2008) estimated the power spectrum of the subtracted H component data at DAV; (DAV H) −(Dst) during the period from July 1, 2005 to March 4, 2006. It is recognized that there are at least three dominant peaks at 7.5, 14.5, and 35.3 day (these dominant peaks were visually identified in the figure). Table 1 shows the list of dominant period peaks of various parameters. In the tables, (DAV H) refers to the original (without Dst subtraction) H component data at DAV. IMF (BX , BY , BZ and BT), VSW, TSW, and NSW are the interplanetary magnetic field, solar wind velocity, temperature, and number density, which were observed by the ACE spacecraft. PD and ε are the dynamic pressure and the epsilon-parameter, respectively (Perreault and Akasofu, 1978) calculated by using the ACE solar wind data. F10.7 represents the flux of the solar radio emission at 10.7 cm wavelength. The data of F10.7 was provided at the website of the Herzberg Institute of Astrophysics (http://www.draoofr. hia-iha.nrc-cnrc.gc.ca/icarus/www/archive.html).

Jul. 1, 2005 - Mar. 4, 2006

Variable	Peak Period [day]
(DAV H) - (Dst)	7.5, 14.5, 35.3
(DAV H)	7.7, 9.2, 11.2, 14.5, 17.6, 22.5, 27.4
Dst	7.7, 9.2, 11.2, 17.6, 22.5, 27.4
Kp	9.2, 27.4
IMF Bx,y,z	9.2, 13.7, 27.4
Vsw	9.2, 13.0, 27.4
Tsw	9.2, 13.0, 27.4
Nsw	9.2, 11.2, 27.4, 35.3
P_D	9.2, 11.2, 27.4, 35.3
ε	9.2, 22.5
F10.7	22,5 35.3

Table 1. Dominant peak periods detected in the power spectrum for various parameters during the period from July 1, 2005 to March 4, 2006.

It is noteworthy that the above-stated dominant period peaks of 7.5 and 14.5 days, which appeared in the spectrum of (DAVH)−(Dst), did not have their roots in the geomagnetic activity

indices of Dst and Kp nor any parameters such as IMF, VSW, TSW, NSW, PD, ε, and F10.7, although the peak at 35.3 days was also identified in NSW, PD, and F10.7. On the other hand, the original H component data contained the same spectrum component as geomagnetic activity indices and solar wind parameters, except 35.3 day.

3.4. Estimation of plasma mass density

The field line resonance (FLR) oscillations in the Earth's magnetosphere are excited by external source waves, and are so-called as ultra low frequency (ULF) waves (cf. Yumoto, 1988). The amplitude of H-component magnetic variations observed at the ground stations reaches a maximum at the resonant point, and that its phase jumps by 180 degrees across the resonant point (see Yumoto, 1985). The eigen-frequency of FLR oscillations is dependent upon the ambient plasma density and the magnetic field intensity in the region of geospace threaded by the field line, and the length of the line of force. The left of Figure 12 shows f-t diagrams obtained at MLB and HOB stations in Australia, phase difference between the two station, and the H-component amplitude ratio of MLB/HOB. The right panel shows the relation among the FLR, eigen-period, length of line of force and the plasma mass density, and the schematic illustration of plasmasphere. When we observe the eigen-frequency of FLR and assume models for the latitude profiles of the magnetic field and the plasma density (with the equatorial density as a free parameter), we can estimate the plasma mass density in the magnetosphere. Therefore, the FLR oscillations are useful for monitoring temporal and spatial variations in the magnetospheric plasma density. By using ground-based network observations, we can identify the FLR phenomena and measure the fundamental field-line eigen-frequency by applying the dual-station H-power ratio method (Baransky et al., 1985) and the cross-phase method (Baransky et al., 1989, Waters et al., 1991), which have been established to identify the FLR properties (Abe et al., 2006, Takasaki, et al., 2006, Maeda N. et al., 2009).

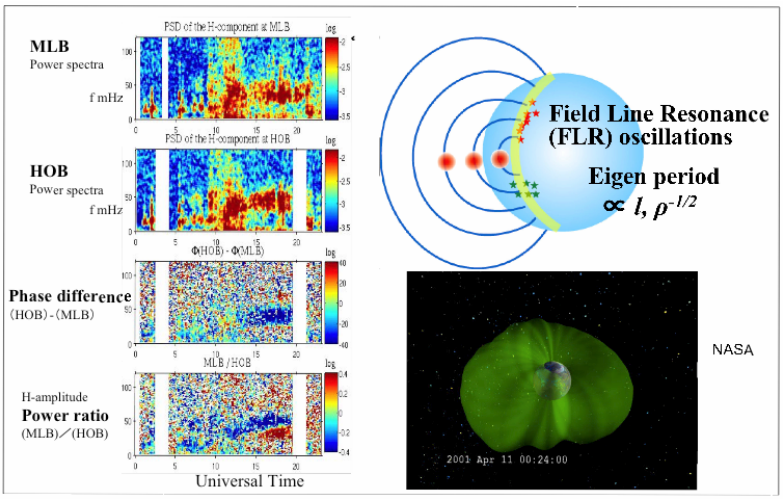

Fig. 12. (left) f-t diagrams of ULF waves observed at MLB and HOB stations in Australia, phase difference between the two station, and the H-component amplitude ratio of MLB/HOB. (right) the relation among the FLR, eigen-period, length of line of force and the plasma mass density, and the schematic illustration of plasmasphere.

By applying the cross-phase method and the amplitude-ratio method to magnetic field data obtained from two ground stations located close to each other, Maeda N. et al. (2009) determined the frequency of the field line resonance (FLR), or the field line eigenfrequency, for the field line running through the midpoint of the two stations. From thus identified FLR frequency they estimated the equatorial plasmamass density (q) by using the T05s magnetospheric field model (Tsyganenkoet al., 2005) and the equation of Singer et al. (1981). They further compared the plasma mass density (q) estimated from magnetometer data at two stations in the CPMN (Circum-pan Pacific Magnetometer Network) chain, Tixie (TIK, geographic coordinates: 71.59^{o}N, 128.78^{o}E, L~ 6:05) and Chokurdakh (CHD, geographic coordinates: 70.62^{o}N, 147.89^{o}E, L~ 5:61), with the plasma electron number density (Ne) observed by the WHISPER (Waves of High frequency Sounder for Probing the Electron density by Relaxation) instrument onboard the Cluster satellites. For the interval of January 1, 2001–December 31, 2005, they have identified 19 events in which the Cluster spacecraft were located on the field line running through the midpoint of TIK and CHD when they observed FLR, and statistically compared the simultaneously observed q and Ne, although the number of

events are limited (19). In 15 out of the 19 events the ratio of q to Ne is found to fall into a realistic range. It is also suggested that the contribution of heavy ions tends to increase when the magnetosphere is disturbed.

Takasaki et al. (2006) discussed temporary variations of the plasma mass density by using the two methods during magnetic storm. From ground-based observations at L~1.4 they found a significant decrease in the FLR frequency at during a large magnetic storm as shown in Figure 13. During 28 - 31 October, 2003, a series of coronal mass ejections hit the magnetosphere and triggered two consecutive large storms. Three ground magnetometers at L = 1.32~1.41 recorded field-line resonances (FLRs) during this interval. The FLR frequencies decreased from 0600 LT on 31 October 2003 during in the main phase of the second storm until 12 LT when the recovery phase of this storm began. After the decrease, the FLR frequencies increased to its value before the storm started at 0600 LT on 31 October in a few hours. The measured decrease in FLR frequency might indicate a relative increase in mass density along the field lines during the magnetic storm. On the other hand, the plasma number density in the ionosphere estimated from TEC values was similar in magnitude taken during quiet time. A possible explanation for the increase in mass density would be an outflow of the heavy ions (e.g., O^+) from the ionosphere to the plasmasphere.

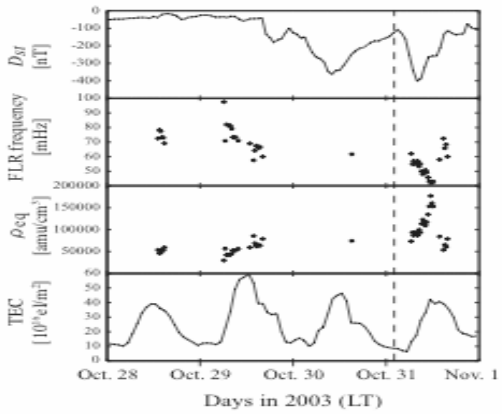

Fig. 13. (From top to bottom) Dst index, FLR frequencies derived from ground observations at L~1.4, ρ_{eq} estimated from data in the second panel, and the total electron content (TEC). The dashed vertical line marks the beginning of the second magnetic storm (Takasaki et al., 2006).

Abe et al. (2006) have applied the dual-station H-component power ratio method, which identifies the field-line eigen-frequency, to eleven-months magnetometer data obtained at two ground stations TIK (L=5.98) and CHD (L=5.55) that belong to the Circum-pan Pacific Magnetometer Network (CPMN). As a result, they have identified two patterns in the frequency dependence of the power ratio (TIK/CHD); one is an increase-then-decrease pattern (named Type 1), and the other is a decrease-then-increase pattern (named Type 2). Type 1 is observed where the Alfv´en velocity (V_A) decreases with increasing L, and it has often been reported in literature. In the paper, they mainly studied the Type 2 events w hich have rarely been reported for the area near L=5.7 (midpoint of TIK and CHD); Type 2 is expected to be observed where V_A drastically increases with increasing L. Their statistical analysis shows that the Type 2 events were observed more frequently in the afternoon sector (especially in 15~18 hr LT) than in the morning sector as shown in Figure 14. The geomagnetic condition was usually quiet when the Type 2 events were observed. These features are consistent with the interpretation that their Type 2 events were observed at the footpoint of the plasmapause layer, as follows. The plasmapause is the only location around L=5.7 where V_A drastically increases with increasing L, leading to Type 2. L of the plasmapause is smaller than 5.7 at all LT during geomagnetically active times (meaning Type 1 at L=5.7) while it is larger than 5.7 only on the late-afternoon sector during quiet times.

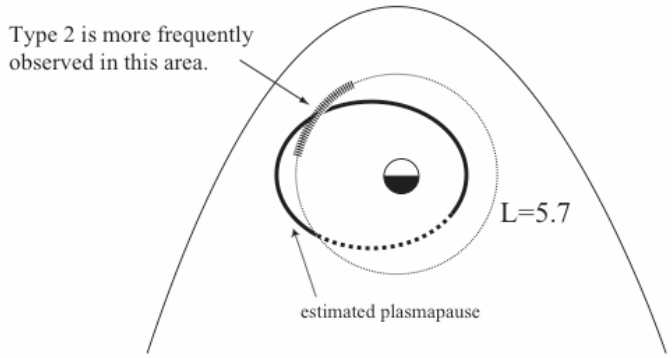

Fig. 14. *Schematic picture of the plasmapause location (view from above the north ple). The place where mant Type 2 FLR events were observed is shown by the thick line, and the estimated plasmapause is shown by the black ellipse (Abe et al., 2006).*

3.5. Latitudinal dependence of Pc 3-4 amplitudes along 96^o MM and Pi 2 along 210^o MM

In order to investigate Pc3-4 magnetic pulsations with periods of 10-45 sec and 45-150 sec, respectively, at equatorial and very low latitudes up to mid latitudes, Takla et al. (2009) analyzed geomagnetic data simultaneously obtained from MAGDAS II African stations for more than three and a half months from 4th of October 2008 up to 22nd of January 2009. During this period they selected 21 Pc3 events for studying the latitudinal dependence of Pc3 amplitude and 25 events in case of Pc4. All of the selected events were in daytime ranging from 6 am up to 6 pm local time. Figure 15 shows latitudinal dependence of Pc 3-4 magnetic pulsations observed at the MAGDAS II stations in the African 96^o magnetic meridian.

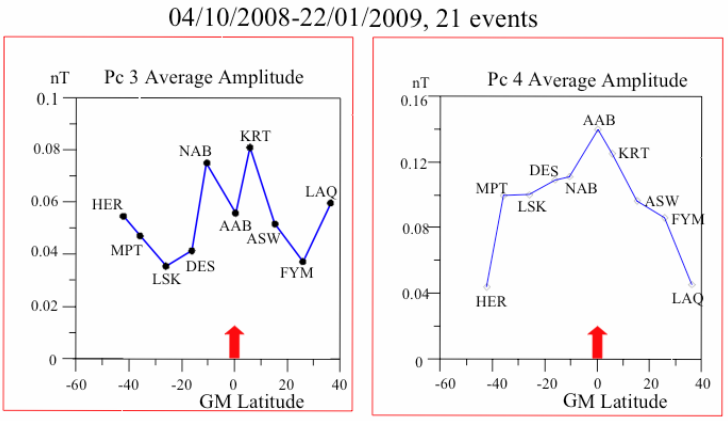

Fig. 15. Latitudinal dependence of equatorial and low-latitude Pc 3-4 amplitude along 96^o MM.

As shown in Fig. 15, they found that the Pc3 amplitudes showed a peak at low latitudes stations with a depression at the dip equator (represented by Addis Ababa station). While the Pc4 amplitudes showed a peak at dip equator and started to decrease by increasing latitude up to mid latitudes. This decrease of the Pc3 amplitudes at magnetic dip equator may be explained as a result of the ionospheric shielding effect on short-period (10-45 sec) hydro-magnetic wave, while the enhancement of Pc 4 amplitude with 45-150 sec period maybe driven by the enhanced equatorial current at magnetic dip equator. Therefore, they conclude that the equatorial Pc3 is originated from the upstream wave, which is propagating as a magnetosonic mode across the ambient magnetic field into the equatorial ionosphere (cf. Yumoto et al., 1985). On the other

hand, the equatorial amplitude enhancement of Pc4 may be explained by the penetration of wave electric field of Pc4 range filed-line resonance oscillation, coupled at higher latitudes with surface wave, into the magnetic equator.

On the other hand, Pi 2 magnetic pulsations, impulsive hydromagnetic oscillations with a period of 40–150s, occur globally at the onset of magnetospheric substorm expansion phase. From the long term accumulation of the observations, it has been found that Pi 2 pulsations observed on the ground are a superposition of several different components [e.g., Yumoto and the CPMN Group, 2001]. Ground Pi 2 pulsations are mixtures of several components reflecting (1) propagations of fast and shear Alfve´n wave, (2) resonances of plasmaspheric/magnetospheric cavity and magnetic field lines, and (3) transformations to ionospheric current systems. However, it has been unclear how they coupled with each other and how their signals are distributed at different latitudes. The present work is intended to pilot the future possibilities whether we can identify the global system of Pi 2 pulsations by Independent Component Analysis (ICA).

Tokunaga et al. (2007) have applied the ICA to the observed CPMN data based on the ICA mode. The dimension of vector x was twenty (i.e., m = 20), the number of source signals was unknown. In this case, they assumed that the observed data was composed of seven independent components and reduced the dimension of the vector to seven via PCA (so the dimension of matrix W become 7 x 20). And then, seven Independent Components (ICs) were calculated by updating the iteration. They made waveforms of ICs estimated by the FastICA. Since the propagation time was ignored in the ICA model, they had to take into account the possibility that these ICs were separated excessively. Thus, they decided to classify these ICs into some groups depending on their waveforms and kurtosis. Kurtosis, which is a classical measure of non-Gaussianity, is defined as $\mathrm{kurt}(x) = E\{x^4\}/[E\{x^2\}] - 3$, whose x is the normalized random variable. kurt(x) becomes 0 if has a Gaussian distribution and positive (negative) if has a super-Gaussian (sub-Gaussian) distribution. Kurtosis of each IC were as

follows: IC 1: 19.11, IC 2: 19.26, IC 3: 6.89, IC 4: 3.53, IC 5: 2.80, IC 6: 0.56, IC 7: -0.38. Since the kurtosis of IC 6 and 7 were quite close to 0, each was regarded as noise (especially, IC 7 seem to be strongly affected by periodic noise of ZYK data). Next, IC1, IC2, IC3, IC4 and IC5 were classified into two groups: IC1, IC2 were classified into Group (A), IC3, IC4, IC5 were classified into Group (B).

Tokunaga et al. (2007) have successfully decomposed an isolated Pi 2 event on a quiet day observed at the CPMN stations into two components. One was the global oscillation that occurs from nightside high to equatorial latitudes with the common waveform and has an amplitude maximum at nightside high latitude. Another component was localized at nightside high latitudes. Its amplitudes were quite weak at low latitudes, but were enhanced near dayside dip equator. Figures 16a and 16b show Pi 2 components plotted as a linear combination of ICs classified into group (A) and group (B), respectively. They call them Pi 2 component (A) and Pi 2 component (B) in the following descriptions. As shown in Figure 16a, it was found that Pi 2 component (A) distributed globally at nightside high, low and equatorial latitudes. Although they seemed to be coherent of each other at low latitudes, there was a phase reversal between CHD and ZYK. In addition, it is recognized that there is a phase shift between TIK and CHD. While, as shown in Figure 16b, it was found that Pi 2 component (B) locally distributed mainly at nightside high latitudes. Although they were hardly seen at nightside low latitudes, at ANC, which was located near dayside dip equator, there was the variation whose waveform was similar to those at KTN. In addition, there was no phase lag between the two stations. As shown in Figure 16a, the amplitudes of Pi 2 component (A) were largest at TIK and one order larger. They decreased exponentially from nightside higher to lower latitudes but were enhanced at ANC, which was located near dayside dip equator.

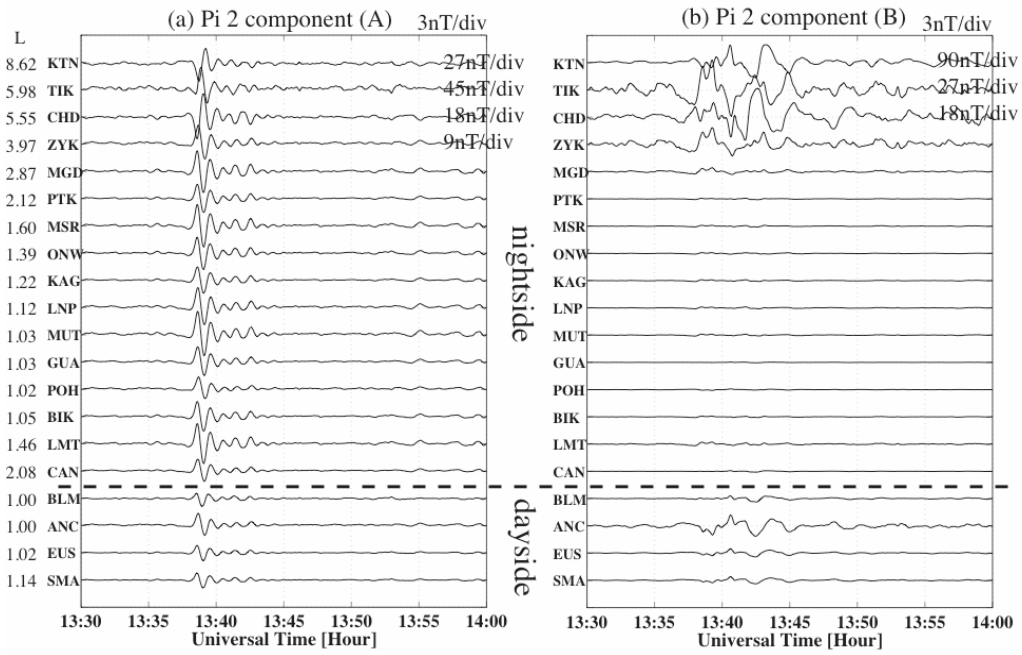

Fig. 16. (a) Separated Pi 2 component (A) plotted as a linear combination of IC 1 and IC 2. (b) Separated Pi 2 component (B) plotted as a linear combination of IC 3, 4 and 5. (see Tokunaga et al., 2007)

4. Ionospheric electric field observations by FM-CW radar

In order to investigate penetration mechanisms of the ionospheric electric fields from the polar to the equatorial ionosphere, SERC has installed a FM-CW (Frequency Modulated Continuous Wave) radar array at Paratunka, Russia (PTK: Magnetic Latitude = 45:8^{o}, Magnetic Longitude = 221:6^{o}, LT = UT + 10.5 hrs), Sasaguri, Japan (SSG: M. Lat. = 23:2^{o}, M. Lon. = 199:6^{o}, LT = UT + 9.5 hrs) as shown in Figure 17, and Manila, Philippines (MNL:M. Lat. = 4:19^{o}, M. Lon. = 192:4^{o}, LT = UT + 8.5 hrs) (see Ikeda et al., 2009). The height of dipole antenna is 26 m. HF radio wave of 2~42 MHz is emitted in the vertical direction with 20 w power for ionosonde mode, while radio waves of central frequencies (f_0; 2.5 and 8 MHz) for Doppler mode are emitted during night (09 – 21 UT=18 – 06 LT) and day time, respectively. The speed of sweep frequency and the sampling frequency are 100~1000 kHz/sec and 2000~20,000Hz/sec, respectively. This system can measure the Doppler frequency (Δf) of reflected radio wave from

the ionized layer and the height of reflection layer with 10-sec sampling rate (Ikeda et al., 2008, Yumoto et al., 2009e).

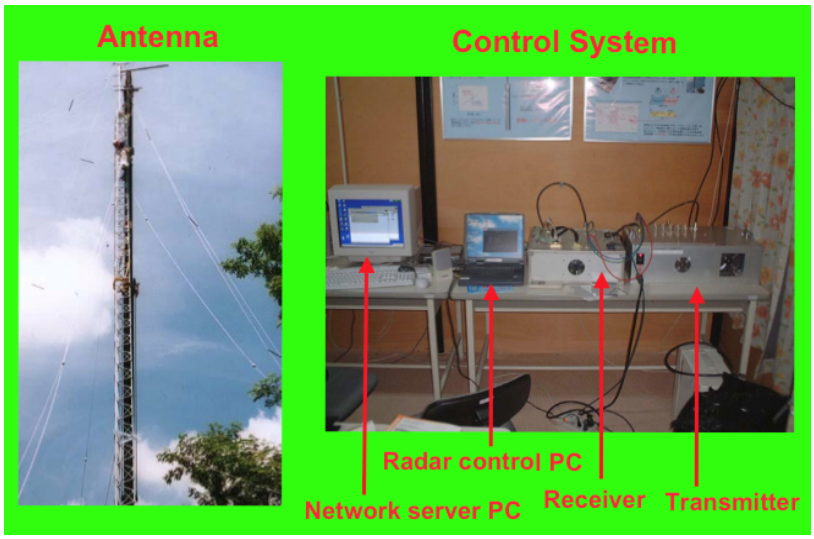

Fig. 17. FM-CW radar system at Sasaguri. 26m dipole antenna (left) and control system including network server, radar control, radio-wave transmitter and receiver (right).

From the observed vertical plasma drift velocity ($v = - c\Delta f/2f_0$), we can deduce east-west component of electric field (**E**) in the ionosphere, i.e. **E**= - **v** x **Bo**, where Bo is the ambient magnetic field at the HF radar stations.

We have performed correlation analysis between ionospheric Doppler data obtained at the FM-CW stations and geomagnetic variations observed at the MAGDAS/CPMN stations, and focus on DP2 type magnetic variations, SC, Pi 2 and Pc 5 magnetic pulsations, which show equatorial enhancements of magnetic field variations at the dip equator. Figure 18 shows H-component DP 2 magnetic variation observed by MAGDAS near ANC during local daytime, and ionospheric DP 2 electric field measured by FM-CW radar at PTK at mid-latitude during nighttime. The equatorial enhancement of dayside DP 2 magnetic variation at ANC can be driven by an ionospheric eastward electric field, while the observed ionospheric westward electric field during the nighttime is synchronized with the DP 2 magnetic variation during daytime. This observation can be interpreted by a scenario in which the IMF Bz variation drives

a dawn-to-dusk electric field in the solar wind, which penetrates into the polar region and transmits into both the day- and night-sides of the low-latitude ionosphere. It is noteworthy that the H-component DP 2 magnetic variation observed near the magnetic equator during the nighttime indicates roughly in-phase relation with those during daytime, as shown in Fig. 4. However, it cannot be explained by using the decline in conductivity during the nighttime ionosphere with the ionospheric DP 2 dawn-to-dusk electric field observed at PTK as shown in Fig 18. A new generation mechanism of DP 2 is needed to understand the globally coherent, DP 2 magnetic variations near the magnetic equator.

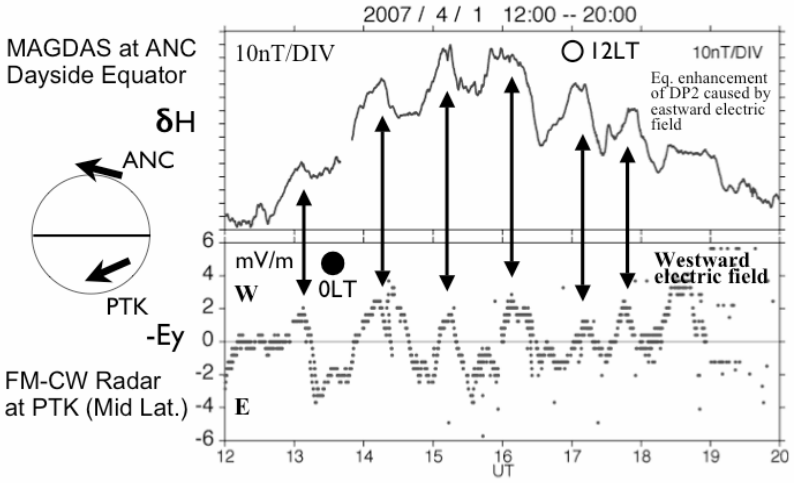

Fig. 18. H-component magnetic DP2 variation observed by MAGDAS at ANC during daytime, and ionospheric electric DP 2 field observed by FM-CW radar at PTK during nighttime on 1 April 2007.

The upper panel of Fig. 19 shows SC magnetic variations at KUJ during daytime and at SMA during nighttime, and the associated ionospheric electric field observed at SSG during daytime on 4 November 2003. We can see eastward ionospheric electric field with 0.69mV/m peak-to-peak intensity at SSG and step-like magnetic field variations of about 60 nT amplitude at both KUJ on the dayside and SMA on the nightside. The bottom panel of Fig. 19 shows the SC magnetic variation at KUJ and the ionospheric electric field at SSG observed during nighttime on 21 January 2005. In this case, westward ionospheric electric field of 1.15mV/m peak-to-peak intensity was observed at SSG with step-like magnetic variation of 80 nT at KUJ. Yumoto

et al. (2009e) selected 40 SC events that were identified using magnetic data from KUJ and the FM-CW radar data during the period of 2002–2005. At first, they examined step-function-like magnetic changes, and then read the peak-to-peak intensity of the ionospheric electric fields during the SC events. It was found that the ionospheric electric fields denote the direction eastward during daytime (06–20 LT) and westward during the nighttime (17–07 LT). The averaged peak-to-peak intensity of observed electric fields is also found to be 0.5mV/m during the daytime and 1.0mV/m during the nighttime. This daytime and nighttime asymmetries of observed ionospheric electric fields cannot be interpreted using only the penetration model of polar dawn-to-dusk electric field into the day- and night-side lower ionosphere during the SC events. The scale size of changes in the solar wind is too large in comparison to that of the globe; therefore, the day–night asymmetry of the ionospheric electric fields must not be related to the solar-wind conditions. It is needed to study dditional electric field component or a local time-dependence of the penetration efficiency of the polar electric fields into the low-latitude ionosphere. At the onset time of SC preceded by PRI on November 4, 2003, the initial change in the ionosphere was observed simultaneous with the geomagnetic initial change in the accuracy of ±6.4s at 0625UT as shown in Figure 19. Simultaneous observations of the initial changes are not contradictory to the result of the past reports, and approve of the instantaneous penetration of the electric fields to the equatorial latitude. At the same time, it proves the quality of the FM-CW radar as a useful tool for detection of ionospheric electric fields.

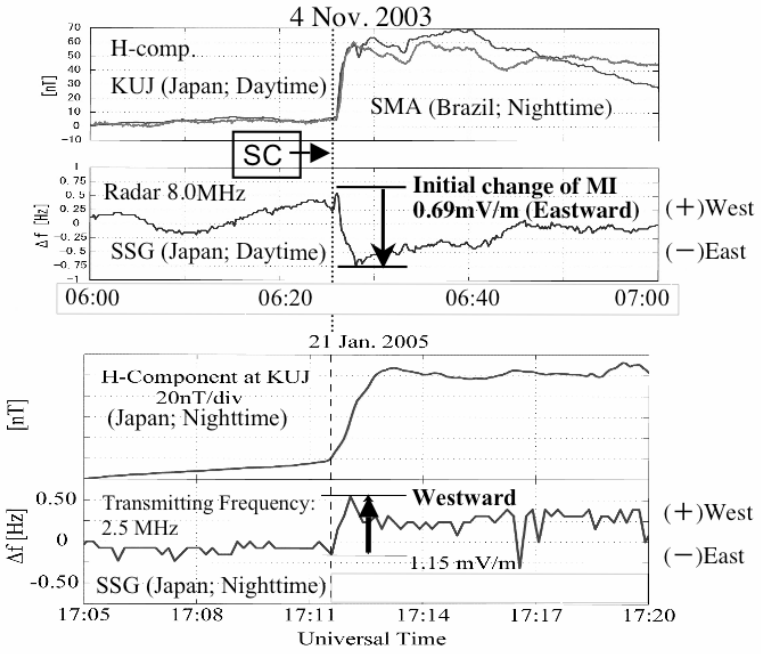

Fig.19. (Upper) Dayside ionospheric electric SC field at SSG with magnetic variations at KUJ during daytime and at SMA during nighttime on 4 Nov. 2003. (Bottom) Nightside ionospheric electric SC field at SSG with magnetic variation at KUJ during nighttime on 21 Jan. 2005.

Figure 20 shows a nighttime Pi 2 (40-150 seconds) event observed by an FM-CW radar and a MAGDAS magnetometer at PTK on 19 October 2007. During this event, the FM-CW radar observed the altitude of about 250 km (virtual height) at 3.0 MHz. The ground magnetic H and D components obtained at PTK (L = 2.05, LT = UT + 10.5 hrs) and Ashibetsu, Japan (ASB; M. Lat. = 34:7_, M. Lon. = 209:6_, L = 1.48, LT = UT + 9.5 hrs), and Ey at PTK are plotted in Figure 20. The thick lines indicate H components and the thin lines indicate D components. We can see that Pi 2 pulsations were observed simultaneously in H and Ey. They started around 1644 UT and attained their peak around 16:48 UT (see the H component at PTK). The dominant frequency was 15.4 mHz for all waves. The peak-to-peak amplitude of H at PTK, D at PTK, H at ASB, D at ASB, and Ey at PTK are 3.3 nT, 1.4 nT, 2.5 nT, 1.2 nT, and 0.43 mV/m, respectively. The ground magnetic perturbation was dominant at H components rather than at D components. Ikeda et al.(2009) calculated the cross correlation between Ey at PTK and geomagnetic field data. As a result, the maximum correlation coefficients were 0.95 for Ey-

H (PTK), 0.95 for Ey-H (ASB), 0.79 for Ey-D (PTK), 0.72 for Ey-D (ASB). Thus the correlation coefficient of Ey-H is higher than that of Ey-D. In addition, the correlation coefficient of Ey-H (ASB) is higher than that of Ey-H (PTK).Pi 2 pulsations are well known as the signal for the onset of magnetic substorms. Moreover low-latitude Pi 2 pulsations are explained in terms of the plasmaspheric cavity mode, Takahashi et al. (1995).

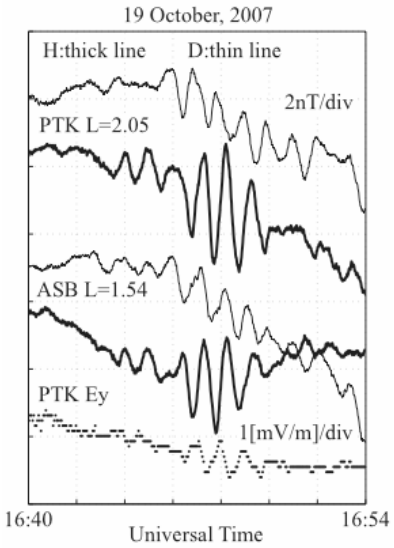

Fig.20. Pi 2 pulsations on 19 October 2007. H and D components at PTK and ASB and Ey at PTK. The thick lines are H components and the thin lines are D components. The transmitting frequency of the FM-CW radar was 3.0 MHz.

The electric field variations (period of about 5 min) associated with Pc5 magnetic pulsations (150-600 sec period) were also observed at the low-latitude ionosphere at Sasaguri (geomagnetic latitude θ=23.2°) during the recovery phase of severe magnetic storm on October 30-31, 2003 as shown in Figure 21. The top and bottom panel show amplitude-time records of H-component magnetic field observed at the MAGDAS/CPMN station at KUJ (M. Lat. = 23:6^{o}, M. Lon. = 203:2^{o}, LT = UT + 8.7 hrs) and Yap (M. Lat. = 0:42^{o}, M. Lon. = 209:9^{o}, L = 1.00, LT = UT + 9.2 hrs) near the magnetic equator, and the Doppler shifted frequency of HF radio wave measured by FM-CW radar at Sasaguri, respectively, during the period of 00:30-03:30 UT on October 30, 2003. During this event, the FM-CW radar at SAS recorded an altitude of 300 km at 8.0 MHz. The peak-to-peak amplitude of Ey at SAS was about 1.0 mV/m. The

magnetic Pc 5 pulsation at YAP was larger than that at KUJ. The peak-to-peak amplitude at YAP was more than 100 nT. This would be due to equatorial enhancement because of the high ionospheric conductivity in the equatorial region. Inspecting the vertical dashed lines in Fig. 21, the peaks of H at YAP almost corresponds with that of Ey at SAS. The positive peaks of Ey correspond with positive peaks of the H. The oscillation of Ey at SAS corresponds with the H at YAP without significant time delay. This result suggests that the ground Pc 5 was excited by the ionospheric electric fields which drive ionospheric currents. The source of Ey for Pc 5 would be caused by the polar dawn-to-dusk electric fields which are excited by the DP 2 type current system (see, Motoba et al., 2004). This is the evidence of Pc5 magnetic pulsations produced by DP2-type current system in the low latitude ionosphere. In this case, the phase delay of geomagnetic variations was found to be about 10-40 second to the ionospheric variations. We can not ignore the self-inductance effect of enhanced ionospheric current caused by the Cowling conductivity to understand the phase delay of geomagnetic variations observed at the dip equator in daytime (Shinohara et al., 1997).

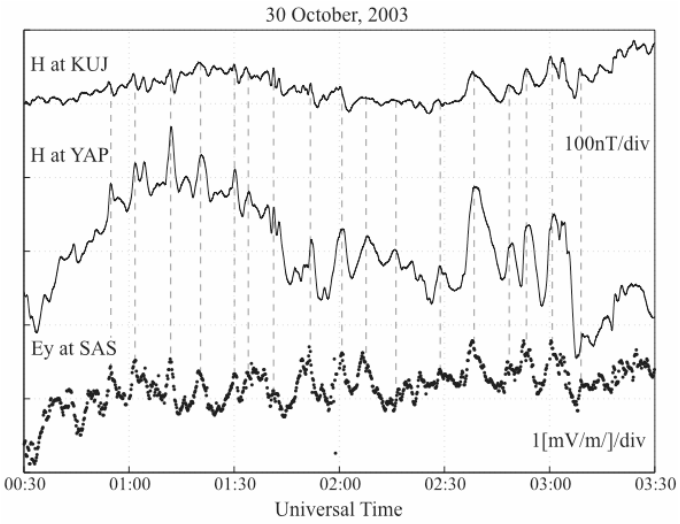

Fig. 21. *Amplitude-time records of H-component magnetic field observed at the CPMN station at Yap near the magnetic equator (top), and the Doppler shifted frequency of HF radio wave measured by FM-CW radar at Sasaguri (bottom) during the period of 00:30-03:30 UT on October 30, 2003.*

5. Summary and Conclusion

MAGDAS/CPMN magnetometers were installed at 40 stations along the 210° MM and the magnetic dip equator in 2005 - 2007, including East Asia, Pacific Ocean and Micronesian Islands, and South America and Africa. MAGDAS II system was installed mainly in Africa in 2008. After corrections of the obtained MAGDAS data at SERC, at the first MAGDAS collaborators (the host scientists and others) can access to the SERC server, in which the corrected data are stored, and get 1-min digital data. The corrected 1-sec data will be open for the collaborations with the host scientists at the oversea stations and SERC. Kyushu Univ. SERC also provide the corrected MAGDAS data to the scientific community for collaborative works.

By using the MAGDAS/CPMN system, we can conduct the real-time monitoring for space weather study, and modeling of the global 3-dimensional current system and the plasma mass density variations for understanding electromagnetic and plasma environment changes in the geospace, especially, during the solar flare, coronal mass ejection, magnetic storms, and auroral substorms. Using FM-CW radar array, we are also able to investigate how solar-wind electric fields and polar electric fields of DP-2, sc, Pi2, Pc 5 and other disturbances can penetrate into the equatorial ionosphere. In the present paper, we reviewed the recent results obtained by MAGDAS/CPMN and FM-CW radar system; (1) Imaging of global 3-D current system, (2) Annual and semi-annual Sq current variations, (3) A new EE-index and its long-term variation, (4) Estimation of plasma mass density, (5) Latitudinal dependence of Pc 3-4 amplitudes along 96^{o} MM and Pi 2 along 210^{o} MM, and (6) Ionospheric electric field observations by FM-CW radar.

By using newly established observation systems (such as orbiting satellites and ground-based networks), we can now study the universal physical processes in the “heliospace” – from the Sun to the atmospheres of Earth and the other planets, and throughout the interplanetary medium. During IHY (2007-2009), many developing nations were invited to join the space

science community by attending IHY workshops (such as the IHY Tokyo Workshop in 2007), hosting ground instrumentation (such as MAGDAS), and hosting regional IHY schools (such as the IHY Africa School in Nigeria in 2008). But this was only the first step. The next logical step is to continue the nurturing of young scientists in these countries by (1) training them how to do scientific observations and how to use the results, (2) internationally exchanging students and young researchers, and (3) organizing international scientific workshops on their behalf. However, to effectively achieve these goals, we believe there must be regular international scientific conferences that (1) cover the entire region from the Sun to the Earth and the other planets and (2) bring into this discussion the scientists and engineers working in developing countries (who have been neglected in the past). Because of the international scope of this agenda, we suggest that the United Nations coordinate these important plans by initiating an appropriate "post-IHY", i.e., International Space Weather Initiative (ISWI) program.

6. Acknowledgements

The PI of MAGDAS/CPMN project, K. Yumoto, SERC, Kyushu University gratefully acknowledge the strong support received from key members of the IHY community: Prof. Hans Haubold (United Nations Office for Outer Space Affairs), Dr. Joseph Davila (NASA), Dr. Nat. Gopalswamy (NASA), and Dr. Babatunde Rabiu (MAGDAS Coodinator of Africa). The PI also gratefully acknowledges the dedicated work of his staff at SERC and students at Department of Earth and Planetary Sciences, Kyushu University, and all the MAGDAS/CPMN stations located around the world. They made the MAGDAS/CPMN Project possible and successful. Financial supports were provided by Japan Society for the Promotion of Science (JSPS) as Grant-in-Aid for Overseas Scientific Survey (15253005, 18253005) and for publication of scientific research results (188068). The IHY Organizer in Japan, K. Yumoto (SERC, Kyushu Univ.) would like to thank the following Japanese IHY Coordinators for their tireless efforts and contributions to the IHY Program in Japan: Secretary of Japan IHY, Dr. S. Watari (NICT), Prof. T. Sakurai (Natl. Astron. Obs. of Japan), Prof. M. Kojima (STE Lab.,

Nagoya Univ.), Prof. K. Shibata (Kwasan/Hida Obs., Kyoto Univ.), Prof. M. Fujimoto (JAXA/ISAS).

7. References

Baransky, L.N., Y. E. Borovkov, M. B. Gokhberg, S. M. Krylov and V. A. Troitskaya. (1985): High resolution method of direct measurement of the magnetic field line eigen-frequencies. Planet. Space Sci., 24, pp. 1369-1376.

Baransky, L.N., S. P. Belokris, Y. E. Borovkov, M. B. Gokhberg, E. N. Fedorov, and C. A. Green, (1989). Restoration of the meridional structure of geomagnetic pulsation fields from gradient measurements. Planet. Space Sci., 37, p. 859.

Hibberd, F. H. (1981): Day-to-day variability of the Sq geomagnetic field variation. Aust.310 J. Phys., **34**, 81-90.

Huang C-S, K. Yumoto, S. Abe and G. Sofka (2008): Low-latitude ionospheric electric and magnetic field disturbances in response to solar wind pressure enhancements, J. Geophys. Res., Vol. **13**, A08314, doi:10.1029/2007JA012940, 2008.

Ikeda Akihiro, Kiyohumi Yumoto, Manabu Shinohara, Kenro Nozaki, Akimasa Yoshikawa, Atsuki Shinbori (2008) : SC-associated Ionospheric Electric Fields at Low Latitude : FM-CW Radar Observation, Memoirs of the Faculty of Sciences, Kyushu University, Series D Earth and Planetary Sciences, Volume XXXII, No. 1, pp.1-6.

Ikeda, A., K. Yumoto, M. Shinohara, K. Nozaki, A. Yoshikawa, M.G. Cardinal, B.M. Shevtsov, V.V. Bychkov, Q.M. Sugon, Jr. and D. McNamara (2009): Ionospheric observation using FM-CWradar array, Submitted to WSPC.

Huang C-S, K. Yumoto, S. Abe and G. Sofka (2008): Low-latitude ionospheric electric and magnetic field disturbances in response to solar wind pressure enhancements, J. Geophys. Res., Vol. **13**, A08314, doi:10.1029/2007JA012940, 2008.

Kitamura, K., Yumoto, K., and the 210^{o} MM Magnetic Observation Group. (1998) Nothern/southern hemisphere asymmetry of sc/si in the nighttime sector, Proc. NIPR Symp., Upper Atmos. Phys.,12, 108-114.

Kohta, H., T. Uozumi, K. Kitamura, A. Yoshikawa, M. Shinohara, MAGDAS group and K. Yumoto, “MAGDAS preliminary report: real-time monitoring of global current structure”, Abstract of 118th SGEPSS Fall Meeting, held at Kyoto Univ., on September 28, 2005, B41-08.

Maeda, G., K. Yumoto and the MAGDAS Group (2009); Progress report on the deployment of MAGDAS, Earth Moon Planet, doi 10.1007/s11038-008-9284-5, vol.104, pp.271-275.

Maeda, N., S. Takasaki, H. Kawano, S. Ohtani, P. M. E. Decreau, J. G.Trotignon, S. I. Solovyev, D. G. Baishev, and K. Yumoto (2009), Simultaneous observations of the plasma density on the same field line by the CPMN ground magnetometers and the Cluster satellites, *Advances in Space Research* (J. Adv. Space Res.), **43**, doi:10.1016/j.asr.2008.04.016, p.265-272.

Matsushita, S., and Campbell, W.H. (1967), Physics of Geomagnetic Phenomena, 2 volumes(International Geophysics Series, Vol. 11), Academic Press, New York and London.

Motoba, T., T. Kikuchi, T. F. Shibata, and K. Yumoto (2004), HF Doppler oscillations in the low-latitude ionosphere coherent with equatorial long-period geomagnetic field oscillations, J. Geophys. Res., 109, A06214, doi:10.1029/2004JA010442.

Otadoy, R.E.S., D. McNamara, K. Yumoto, and MAGDAS group (2009); Proposal to use theMAGnetic Acquisition System(MAGDAS) of the Circum Pan-Pacific Magnetometer Network (CPMN) to study the equatorial electrojet: A Philippine contribution to the International Heliophysical Year, *Earth Moon Planet*, doi 10.1007/s11038-008-9271-x., vol. 104, pp. 167-172.

Rabiu, A.B., I.A. Adimula, K. Yumoto, J.O. Adeniyi, G. Maeda, and MAGDAS/CPMN project group (2009a); Preliminary results from the magnetic field measurements using MAGDAS at Ilorin, Nigeria, *Earth Moon Planet*, doi 10.1007/s11038-008-9290-7, vol. 104, pp. 173-179.

Rabiu A.B., Yumoto K., Shiokawa K., and Fujimoto A. (2009b); Equatorial electrojet parameters along 210◦ magnetic meridian using a thick shell model format: Preliminary results, *Proc. of the Workshop on Equatorial Atmosphere*, Research Institute for Sustainable Humanosphere, Kyoto University, 159-166.

Rastogi, R. G., S. Alex and A. Patil (1994): Seasonal variations of geomagnetic D, H and Z fields at low latitudes. J. Geomag. Geoelectr., **46**, 115-126.

Rastogi R.G. and K. Yumoto (2007): Equatorial electrojet in the East Brazil anomaly region, Earth Planet Space, 59, No.2, 103-106.

Rastogi R.G., H. Chandra, M.E. James, Kentarou Kitamura and K. Yumoto (2008): Characteristics of the Equatorial Electrojet current in Central South America, Earth Planets Space, **60**, 623-632.

Richmond, A. D. and J. P. Thayer, "Ionospheric electro-dynamics: A Tutorial", in Magnetospheric Current Systems, S.-I. Ohtani et al., Eds. AGU, Washington, DC, 2000, p. 131-155.

Sastri J.H., Yumoto K., Rao J.V., and Ikeda A (2008): Summer-winter hemisphere asymmetry of the preliminary reverse impulse of geomagnetic storm sudden commencements at

midlatitudes: J. Geophys. Res., Vol.113, A05302, 2007JA012968.

Shinohara, M., K. Yumoto, A. Yoshikawa, O. Saka, S. I. Solovyev, E. F. Vershinin, N. B. Trivedi, J. M. Da Costa and the 210°MM Magnetic Observation Group, "Wave characteristics of daytime and nighttime Pi 2 pulsations at the equatorial and low latitudes", Geophys. Res. Lett., Äi0vol. 24, pp. 2279-2282, 1997.

Singer,H.J., Southwood, D.J., Walker, R.J., and M.G. Kivelson (1981); M.G. Alfven wave resonances in a realistic magnetospheric magnetic field geometry, J. Geophys. Res. 86 (A6) 4589–4596.

Sugiura, M., Hourly values of equatorial Dst for the IGY, Goddard Space Flight Center, Greenbelt, Maryland, NASA Rept., X-611-63-131, June, 1963.

Takahashi, K., S.-I. Ohtani, and B. J. Anderson (1995), Statistical analysis of Pi2 pulsation observed by the AMPTE CCE spacecraft in the inner magnetosphere, J. Geophys. Res.,100, 21,929-21,941.

Takla E. M., K. Yumoto, S. Abe, A. Fujimoto, A. Ikeda, T. Tokunaga, Y. Yamazaki, T.Uozumi, M. G. Cardinal, A. Mahrous, G. Mengistu, T. Afullo, A. Macamo, L. Joao, N.Mwiinga, C. Uiso, P. Baki, C. Kianji, K. Badi, S. Malinga, A. Meloni and E. Ghamry (2009); Preliminary Results of Latitudinal Dependence of Pc3-4 Amplitudes at 96º MM Stations in Africa, Submitted to J. Atmos. Solar-Terres. Phys.

Takasaki, S., H. Kawano, Y. Tanaka, A. Yoshikawa, M. Seto, M. Iijima, Y. Obana, N. Sato and K. Yumoto (2006); A significant mass density increase during a large magnetic storm in October 2003 obtained by ground-based ULF observations at L □ 1.4, Earth Planets Space, **58**, 617-622.

Tanaka Y-M., Yumoto K., Yoshikawa A., Itonaga M., Shinohara M., Takasaki S. and Fraser B.J. (2007): Horizontal amplitude and phase structure of low-latitude Pc3 pulsations around the dawn terminator: J. Geophys. Res. 112(A11): A11308.

Tokunaga, T., H. Kohta, A. Yoshikawa, T. Uozumi, and K. Yumoto (2007); Global features of Pi 2 pulsations obtained by Independent Component Analysis, Geophys. Res. Lrtt., Vol. 34,L14106, doi:10.1029/2007GL030174.

Tsyganenko, N.A., and M.I., Sitnov (2005); Modeling the dynamics of the inner magnetosphere during strong geomagnetic storms, J. Geophys. Res. 110, A03208.

United Nations, New York, (2006) Putting the "I" in the IHY, Comprehensive overview on theworld-wide organization of the International Heliophysical Year 2007.

Uozumi, T., H. Kawano, A. Yoshikawa, M. Itonag, and K. Yumoto (2007); Pi 2 source region in the magnetosphere deduced from CPMN data, Planet. Space Sci., 55, 849-857, doi:10.1016/j.pss. 2006.03.01.

Uozumi, T., K. Yumoto, K. Kitamura, S. Abe, Y. Kakinami, M. Shinohara, A. Yoshikawa, H. Kawano, T. Ueno, T. Tokunaga, D. McNamara, J. K. Ishituka, S.L.G. Dutra, B. Damtie, V.

Doumbia, O. Obrou, A.B. Rabiu, I.A. Adimula, M. Othman, M. Fairos, R.E.S. Otadoy, and the MAGDAS Group (2008): A new index to monitor temporal and long-term variations of the Equatorial Electrojet by MAGDAS/CPMN real-time data: EE-Index, *Earth Planets Space*, **60**, 785-790.

Uozumi, T., Yumoto, K., Kitamura, K., Abe, S., Omoto, T., and MAGDAS Group,(2009a); A Calibration Technique for Temperature Drift of MAGDAS Magnetometer Data. *Memoirs of the Faculty of Sciences, Kyushu University, Series D, Earth and Planetary Sciences,* **32(2),** 95-104.

Uozumi, T., S. Abe, K. Kitamura, T. Tokunaga, A. Yoshikawa, H. Kawano, R. Marshall, R.J. Morris, B.M. Shevtsov, S.I. Solovyev, D.J. McNamara, K. Liou, S. Ohtani, M. Itonaga, and K. Yumoto (2009b), Propagation characteristics of Pi 2 pulsations observed at high- and low-latitude MAGDAS/CPMN stations: A statistical study, J. Geophys. Res., 114, A11207, 1-16.

Waters, C.L., F. W. Menk, and B. J. Fraser, "The resonance structure of low latitude Pc3 geomagnetic pulsations", Geophys. Res. Lett., (1991); vol. 18, pp. 17547-17551.

Yamazaki, Y., K. Yumoto, A. Yoshikawa, S. Watari, and H. Utada (2009a); Characteristics of counter-Sq SFE at the Dip equator1 (SFE*) observed by CPMN stations, J. Geophys. Res., vl.114, A05306, doi:10.1029/2009JA014124, pp. 1-5.

Yamazaki, Y., K. Yumoto, T. Uozumi, A. Yoshikawa, and M.G. Cardinal (2009b); Equivalent current systems for the annual and semi-annual Sq variations observed along the 210o MM CPMN stations, J. Geophys. Res., Vol. 114, in press.

Yoshikawa, A., Nakata, H., Nakamizo A., Uozumi, T., Itonaga, T., and Yumoto, K., (2009); A new magnetosphere-ionosphere coupling scheme for temporal and global magnetospheric MHD simulations. *Memoirs of the Faculty of Sciences, Kyushu University, Series D, Earth and Planetary Sciences,* **32(2),** 87-94.

Yumoto, K. (1985); Characteristics of localized resonance coupling oscillations of the slow magnetosonic wave in non-uniform plasma, Planet._Space_Sci., 33, 1029-1036.

Yumoto, K. (1988); External and internal sources of low-frequency MHD waves in the magnetosphere --- A review, J._Geomag._Geoelectr., 40, 293-311.

Yumoto, K., and the 210^{o} MM Magnetic Observation Group (1996a); The STEP 210^{o} magnetic meridian network project, J. Geomag. Geoelectr., 48, 1297-1309.

Yumoto, K., H. Matsuoka, H. Osaki, K. Shiokawa, Y. Tanaka, T.-I. Kitamura, H. Tachihara, M. Shinohara, S.I. Solovyev, G.A. Makarov, E.F. Vershinin, A.V. Buzevich, S.L. Manurung, Obay Sobari, Mamat Ruhimat, Sukamadradjat, R.J. Morris, B.J. Fraser, F.W. Menk, K.J.W. Lynn, D.G. Cole, J.A. Kennewell, J.V. Olson, and S.-I. Akasofu (1996b); North/south asymmetry of sc/si magnetic variations observed along the 210o magnetic meridian, J. Geomag. Geoelectr., 48, 1333-1340.

Yumoto, K, and the CPMN Group (2001); Characteristics of Pi 2 magnetic pulsations observed at the CPMN stations: A review of the STEP results, Earth Planets Space, 53, 981-992.

Yumoto, K., and the MAGDAS Group (2006); MAGDAS project and its application for space weather, Solar Influence on the Heliosphere and Earth's Environment: Recent Progress and Prospects, Edited by N. Gopalswamy and A. Bhattacharyya, ISBN-81-87099-40-2, pp. 399-405.

Yumoto K. and the MAGDAS Group (2007): Space weather activities at SERC for IHY: MAGDAS: Bull. Astr. Soc. India 35, 511-522

Yumoto, K., S. Ikemoto, M.G. Cardinal, M. Hayakawa, K. Hattori, J.Y. Liu , S. Saroso, Ruhimat M., M. Husni , D. Widarto, E. Ramos., D. McNamara, R.E. Otadoy, G. Yumul, R. Ebora and N. Servando (2009a): A new ULF wave analysis for seismo-electromagnetics using CPMN/MAGDAS data, *Physics and Chemistry of the Earth* (J. Phys. Chem. Earth), doi:10.1016/j.pce.2008.04.005, 34, 360-366.

Yumoto, K., and STPP Sub-committee (2009b); International heliophysical year activities in Japan, *Data Science Journal*, Vol. 8, 30 March 2009, pp. S14-S23.

Yumoto, K. H. Kawano, and MAGDAS group (2009c); MAGDAS for geospace environment monitoring, , *26th ISTS-ISTS Special Issue of JSASS On-Line Journal*, *Trans. JSASS Space Technology Japan*, Vol.7, No. ists26, pp. Tr_2-Tr_2_4.

Yumoto, K., G. Maeda, S. Abe, T. Uozumi, A. Fujimoto, A. Ikeda, T. Tokunaga, Y. Yamazaki, T. Ueno, Y. Hitayama, B. Rabiu, C.B.S. Uiso, P. Baki, K.M. Badi, L. B. Kolawole, T. Afullo, A. Macamo, H. Mweene, and MAGDAS/CPMN Group (2009d); Progress report on the global deployment of MAGDAS, *Sun and Geosphere*, in press.

Yumoto K., A. Ikeda, M. Shinohara, T. Uozumi, K. Nozaki, S. Watari, K. Kitamura, V. V. Bychkov, and B. M. Shevtsov (2009e): Electric and Magnetic Field Variations at Low and Equatorial Latitudes During Sc, DP2, and Pi2 Events, *Advances in Geosciences*, Vol. **14**, Solar Terrestrial, Eds. Marc Duldig et al., World Sci. Publ. Comp. in press.